Two-Dimensional Materials for Water Treatment

James Martin Exley

School of Civil Engineering

University of Leeds

Submitted in accordance with the requirements for the degree of

Doctor of Philosophy

NOVEMBER 2022

The candidate confirms that the work submitted is his own and that appropriate credit has been given where reference has been made to the work of others.

For my wonderful parents; my mother, Joanne, and my late father, Howard.

I dedicate my PhD thesis to you, as a thank you for your considerable personal investment in all aspects of my education, in my lifelong journey from St. Anthony's to BGS to Oxford and finally to Leeds.

Thank you both for your unconditional love and support throughout. I sincerely hope that you are proud of the achievements, for I could not have completed them without you.

Acknowledgements

Many people, both within and external to University of Leeds, have provided enormous sources of support which has been essential in enabling me to complete my PhD. Some have given assistance with regards to completion of the research, others have supported me personally or in other ways. A few have helped in both areas. I would now like to offer my acknowledgements and express my gratitude to those who have provided help and support.

Firstly, I would like to express my sincere gratitude to my academic supervisors, Professor Martin Tillotson (School of Civil Engineering) and Dr. Timothy Hunter (School of Chemical and Process Engineering (SCaPE)), for their ongoing support and supervision with regards to all aspects of my research. Their help and contributions have encouraged me to think critically about my own research and constantly be looking for ways to improve and develop my project. These are undoubtedly skills that I will need in my scientific career beyond my PhD: as such I am very grateful for the lessons learned and time they have invested in getting to know me and work alongside me on this fantastic journey. These have been extremely challenging times in which to undertake such an enormous body of research, against the backdrop of unprecedented times during the COVID-19 global pandemic. There have been times when we all have had to dig deep in order to continually develop this research, despite ongoing external challenges over which we have no control. Martin and Tim have ridden the highs and lows of this with me, and I will always be grateful for their support through these challenging times.

I would like to thank Dr. Tom Pugh (Evove Limited), for providing industrial support, being my industrial supervisor and main point of contact with the company since starting his role. I would like to sincerely thank

Tom for his help and ideas, these have been invaluable in helping me to develop the research. By benchmarking my research against progress in the water industry, he has challenged me to improve as a researcher, for this I am very grateful for the assistance Tom has provided.

I would also like to thank other members of Evove Limited, some of whom have now moved on. Dr. David Pears and Dr. Kangsheng Liu were instrumental in helping me to define and shape my scope of research in the earlier stages of my PhD. In addition, Mr. Daniel Clow and Dr. Ola Karczmarczyk helped so much with my initial lab work at the company site and provided me with a platform from which to grow my own research.

Within University of Leeds, I would like to thank my friends and colleagues across the Water, Public Health and Environmental Engineering, water@leeds and Colloids and Polymer Engineering group networks, many of whom I have had the great pleasure of getting to know over the course of my research. In particular, I would like to mention my colleagues from Public Health laboratories, with whom I have whiled away a substantial number of research hours, including Mr. Isah Saidu, Mr. Saleh Al Haddad and Ms. Fika Nikendary. They have all been wonderful friends and a fantastic support network, I would like to wish each of them the best of luck for years to come. In particular, my close friendships with Mr. Jianting Feng and Mr. Heng Song, and our weekly trips to the local snooker club to pot some balls, in attempt to be like Ronnie, have helped me get through the mammoth task of writing a thesis. For this, Jianting and Heng are owed a special thanks. I would also like to thank Ms. Qian Ye for her friendship and wish her the best of luck with completing her research.

In addition, I would like to especially thank the Public Health Laboratory Technicians in School of Civil Engineering, who have provided invaluable technical assistance and a good measure of *moral support*! Ms. Karen Stevens, Ms. Emma Tidswell and Mr. Morgan McGowan have helped with all aspects of laboratory work and to them I am indebted. Dr. David Elliott has helped enormously with the setup of dead end cell and is owed a special thanks. Ms Lucy Leonard and Ms. Victoria Leadley have helped

with training and use of FTIR and Thermal analysis equipment: they are owed a special thanks also.

I would also like to thank the following, who have helped greatly with separate aspects of my research:-

- Dr. Andrew Britton (SCaPE), for his help with XPS analysis, and the Henry Royce Institute for making the analysis possible.
- Dr. Ben Douglas (SCaPE), for training and help with particle sizing equipment, Water Contact Angle measurement, zeta potential measurement and BET analysis.
- Dr. Faye Esat (SCaPE), for her help with XRD.
- Dr. Alexander Kulak (School of Chemistry), for his help with Raman Spectroscopy.
- LEMAS and in particular, Mr Stuart Mickelthwaite, for help with SEMEDX and FIBSEM.

Last but not least, I would of course like to thank my family. For my amazing girlfriend Xin, thank you for all your love and for being there for me always, in reaching this point. We have supported each other in getting through the PhD and can now look ahead to building our lives together. My mother Joanne and sister Kate, through their love and support, have provided a great source of motivation and inspiration and carried me through my PhD studies.

For financial support, I would like to express my gratitude to Evove Limited and Engineering and Physical Sciences Research Council, for funding the research and making it possible.

Abstract

This research investigates the utility of two commercial graphene oxide (GO) materials in treatment of cationic Methylene Blue (MB) and anionic Methyl Orange (MO) dyes and salt-contaminated waters, as a means to provide a scalable solution to address the challenges faced by the global water industry. The crucial feature of the GO materials was realised in terms of their disparity in flake size, a key parameter in terms of the interactions of GO with contaminant species.

To elucidate the flake sizes, a unique approach, using laser diffraction and dynamic light scattering, was applied to characterise the GO flake sizes. This showed that the materials were clearly of different size order, thus they were termed Smaller flake (SFGO) and larger flake GO (LFGO), respectively. Brunauer-Emmett-Teller analysis was conducted on both GO's, demonstrating that SFGO possessed higher surface area and total pore volume. Electrokinetic properties were investigated by measurement of zeta potential; confirming the electronegative character of the GO flakes in pH range 3.50 - 10. In particular, the negativity of SFGO was very prominent. Fourier Transform Infrared and X-Ray Photoelectron spectroscopic techniques were employed to characterise the GO chemistry, revealing that the functional group presence was highly similar for both GOs.

Treatment of dye-contaminated waters was investigated by application of commercial GO's as adsorbents and as polymeric membrane coatings. Both GO's were demonstrated as having high capacity to adsorb MB, due to electrostatic attraction between the flakes and cationic dye. In particular, SFGO was an effective adsorbent of MB, owed to its high zeta potential, small flake size and greater pore volume. In contrast, electrostatic repulsion

hindered the adsorption of MO, though both GO systems achieved promising levels of MO sorption. In membrane filtration of dyes, SFGO coatings were found to reject both dyes effectively; the mechanism for MB filtration was likely based on charge-mediated adsorption, while for MO, repulsion ensured that levels of MO rejection were particularly high. LFGO demonstrated effective operation at lower GO coating concentration, a feature that is potentially attractive for industrial usage.

Application of the materials was extended to consider the impact of salt upon dye adsorption and filtration, and the desalination capacity of GO membranes in sodium chloride, sodium sulphate, magnesium sulphate and ammonium heptamolybdate salt solutions. In desalination, the Donnan Effect, relating to electrostatic properties of the system, was considered the most important mechanism for rejection of salts, as demonstrated by the respective ordering of the rejections. Rejection capacities decreased with increasing ratio of valencies (Z^+/Z^-) and increasing charge cationic charge density. In dye adsorption studies, addition of magnesium sulphate and sodium sulphates to dye solution was demonstrated to have an adverse impact upon the adsorption capacity of both GO's for MB, due to the effects of charge neutralisation. In particular, the Mg^{2+} cations reduced the adsorption of dye significantly; SFGO was strongly affected, due to its high negative charge. Dye-salt fractionation experiments confirmed that the MB rejection capabilities of the GO membranes was impacted greatest by the addition of magnesium sulphate. This feature was attributed to the divalent cation having capability to diminish the electronegativity of the GO surface and thus weaken the Donnan effect of the membranes.

This research contributes to knowledge of GO adsorbent and membrane systems, by application of a unique analytical characterisation system coupled with detailed exploration and analysis of the impact of flake sizes upon performance. From this, it is anticipated that further research into commercial GO's may follow and develop the role of parameters including flake size and oxygen content.

Abbreviations

Listed in alphabetical order

ATR	Attenuated Total Internal Reflectance
BET	Brunauer-Emmett-Teller
DLS	Dynamic Light Scattering
DLVO	Derjaguin - Landau - Verwey - Overbeek (Theory)
FWHM	Full Width at Half Maximum
FIBSEM	Focussed Ion Beam Scanning Electron Microscopy
FTIR	Fourier Transform Infrared
GO	Graphene Oxide
LD	Laser Diffraction
LFGO	Larger Flake Graphene Oxide
MB	Methylene Blue
MF	Microfiltration
MO	Methyl Orange
MOF	Metal Oxide Framework
NF	Nanofiltration
NMR	Nuclear Magnetic Resonance
PA	Polyamide
PES	Polyethersulfone
PFO	Pseudo First Order
PSD	Particle Size Distribution
PSO	Pseudo Second Order
RPM	Revolutions per minute
PVDF	Polyvinylidiene fluoride
RGO	Reduced Graphene Oxide
RhB	Rhodamine B
RO	Reverse Osmosis
SEM	Scanning Electron Microscopy
SFGO	Smaller Flake Graphene Oxide
SSA	Specific Surface Area
TGA	Thermogravimetric Analysis
TPV	Total Pore Volume
UF	Ultrafiltration
UV	Ultraviolet
UV-Vis.	Ultraviolet-Visible
XPS	X-Ray Photoelectron spectroscopy
XRD	X-Ray Diffraction

Contents

List of Figures

List of Tables

Chapter 1

Introduction and Background

1.1 Background and Research Challenge

1.1.1 The water crisis

Water is one of the most precious resources on earth: essential for sustaining life and for usage by a plethora of industries. There is ever-growing worldwide concern, however, regarding the availability of clean water, this is driven by the adverse impacts of factors including climate change [31] and increasing global population [32]. *Water scarcity* is the term given to the situation in which there is inadequate fresh water to meet the standard water demand [33]. Typically, the boundary for water scarcity is considered $<$1000 m^3/person/day of available fresh water [34]. As little as 3% of total water capacity on Earth is fresh water, with virtually all remaining water locked away in salt water in the vast oceans and seas [35].

Alarmingly, water scarcity is an issue which affects nearly 1 billion people and 28 countries across the globe, including some of the poorest worldwide on the African and Asian continents [32]. In addition, the trend for populations in these countries to migrate from rural - urban habitation causes further difficulties including increased difficulty to access water, and this leads to increased levels of freshwater abstraction

[36, 37]. Population growth is a significant factor in the water crisis, as the global population is expected to swell to approximately 9 billion people by 2050 [38]. This will place significant pressure upon those countries currently existing under conditions of water scarcity, as their already stretched water resources will be further pressurised. In addition, the expansion in global population will increase the forecast number of people who will be living under situations of water scarcity to 2.0 billion; close to 95% of this total will be living in the developing world [39].

Different countries are facing unique challenges in terms of their own water scarcity issues. In the Middle East, Yemen is among the most water-starved counties with only 120 m^3/person/day: this is a combination of *physical* scarcity due to droughts, but also accelerated depletion of existing resources due to political issues and years of war [40, 41]. Syria is another country that has suffered similarly and greatly, as severe droughts with total rainfall <8 inches per year and strategic militarised targeting of water facilities during times of conflict have crippled already fragile water resources [42]. Water scarcity in Italy is, however, very different in nature, as Italy has a network of rivers and receives plentiful water supplies from river and rain (combined 300 billion m^3 per year) [43]. Despite this, the geographic situation in Italy, with its mountainous terrain, makes movement of water very challenging, such that only around 58 billion m^3 per year are usable. This situation is made worse by the out-dated existing water transport facilities: Rome, for example, loses in excess of 40% water each year due to leaky, poorly maintained pipes [44]. Thus, the challenges faced by Italy may be due to infrastructural issues resulting in water scarcity, as opposed to physical water scarcity.

1.1.2 Industrial pollution of water: the textile industry

In the context of the water crisis, which was discussed in the previous section, a multitude of issues are rooted in global industrialisation [45, 46]. In total, the UN reports that industrial water usage accounts for as much as 22% of the total global water us-

age [47]. Undoubtedly, the expansion of a number of industries including information and technology, which perhaps barely existed several decades ago, have contributed to industrial demand for water. A grave consequence of industrialisation and water is, however, the accumulation of pollutants in water sources, exacerbated by the fact that as much as 80% of industrial wastewater is discharged back to environment without treatment [48]. Currently, the agricultural industry, which provides food for the planet, is the largest single user of water [49]. In addition to water usage, the global agricultural industry consumes up to 2 million tons of pesticides, often rich in nitrogen and phosphorous, in order to combat insects which are a threat to plants [50]. Pesticide runoff into water sources is a significant cause of water pollution, as the nitrogen and phosphorous rich pesticides lead to eutrophication of rivers and streams, giving rise to algal bloom, thus harming the aquatic life therein [51, 52].

The textile industry is also a major source of global water pollution. The textile industry is a markedly heavy user of water, as nearly all of the requisite textile processing steps require water, meaning that in a fabric production plant, approximately 200 litres of water are required for production of a kilogram of material [53]. The textile industry has, however, played an important role in the growth of economies in developing regions such as China, India and Bangladesh [54]. Western countries began outsourcing textile production to Asia as early as the 1960's, such that at present, almost 80% of the world's clothing and fabrics is produced in Asia [55]. The EU is the world's largest importer of textile materials: as of 2020, the EU imports as much as US$ 87 billion per year [56], thus reflecting the enormity of the textile market.

Synthetic dyes are dominant in the textile industry, as they have excellent colouration properties and remain bound to clothing after repeated wash cycles [57]. By far the largest of industrial dye classes is the azo dye class, occupying in total 70% of the industrial dye market [58]. They have molecular structure R - N = N - R', where the R and R' side groups are typically aryl. The chromophore (responsible for imparting

colouration) is the N = N group. The azo dye class boasts a number of advantages enabling their application in textile dyeing: including vivid colouration and good resistance to oxidation when on fabric [59]. Azo dyes tend, however, to be very stable and resistant to natural degradation: upon discharge into effluent they may exhibit recalcitrance to degradation [60, 61]. In addition, their persistence in the environment is a serious problem owing to their toxicity and carcinogenicity, which may cause health concern for humans and animal species [62]. An example azo dye structure, that of Basic Red 18, is shown in Figure 1.1. The dye clearly possesses characteristic azo group (C - N = N - C linkage) and associated aryl side groups.

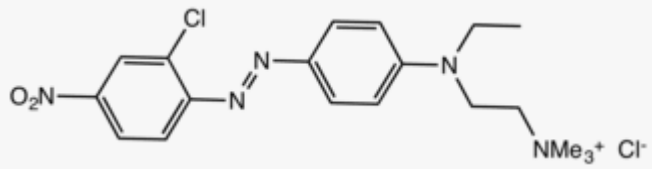

Figure 1.1: Azo dye Basic Red 18, with the characteristic N = N chrompohore. Adapted from [1].

In addition to dye pollution, there is likewise an associated problem with discharge of chemicals which are not dyes but are used to aid the dyeing process. Two such examples are heavy metal ions and salts. Heavy metal cations such as Lead (Pb^{2+}), Chromium(Cr^{6+}), Nickel(Ni^{2+}), Copper(Cu^{2+}), Cadmium(Cd^{2+}), Mercury(Hg^{2+}) are often a significant feature in textile effluent owing to the usage of chemicals containing them during the processing stages [63, 64]. Certain dye classes, known as metal complex dyes, even contain cations within their chemical structure, comprising side groups stabilised around a central metal cation such as Zn^{2+} [65]. Heavy metals cause a myriad of environmental problems, as they are persistent and highly toxic: many are also capable of dissolution in water, thus enabling them to undergo water-borne migration from their initial locality to distant places [63]. Usage of salts, in particular sodium salts such as sodium chloride and sodium sulphate (in textile terms, the decahydrate

form, often known as Glauber's salt, is heavily used) play an important role. Salts are used to aid the adsorption of dye onto fabrics, for example, in dyeing cotton (negatively charged) with anionic reactive dye [66]. Accordingly, salts may act as electrolytes to overcome initial electrostatic repulsion between dye and fabric, and maximise the completeness of the dyeing process, termed *exhaustion* of the dye [67]. High salinity is a further complication which must be addressed during effluent treatment, as the accumulation of excess salt in waterways is responsible for termination of micro-organisms [68].

A country that illustrates both positive and adverse impacts of the textile industry is China. China has economically prospered from textile industry exports: to highlight this, China single-handedly accounts for in excess of 40% of the world's annual clothing exports, this boosts the Chinese economy by bringing in enormous financial gain (in total US$ 270 billion in 2013) [69]. China's contributions to the textile industry are of such magnitude that the second-placed global exporter, Bangladesh, exports less than one-seventh of the amount that China does [70]. The environmental burden placed on on the country by the textile industry is however, grave. In textile dyeing, around 200,000 tons of dye are lost annually, due to inefficiencies in the dyeing process [71]. The lack of strict enforcing local effluent discharge regulation has led to irresponsible discharge of dye-containing effluent into water sources, meaning that in China, over 80% of the rivers are considered to have some degree of dye-related contamination [72]. Perhaps an issue of even greater magnitude is that 74% of these are considered unsafe for human contact [73]. Exacerbating the situation further is the fact that as many as 30 of the toxic components (including those from heavy metal and salt groups) contained within the effluent cannot be removed from water and are as such, discharged into water sources without treatment [74]. The anticipated impact that this may have upon the world's largest national population is alarming: with increased cases in recent years of serious long term health conditions correlating to contaminated water including

impaired cognitive functioning and memory losses [75]. As such, China is among the countries most in need of a means to address the issues brought by textile-related pollution of waterways, otherwise it faces damning consequences for its own ecology and population.

1.1.3 Classical membrane principals and processes

A membrane is a selective barrier, capable of separating fluid streams and restricting the passage of certain components from within a stream, while being permeable to others. It belongs within the group of methods related to physical separation of species.

Fundamentally, membrane based operations have three fluid streams: these are feed (inlet), permeate (flows through the membrane) and retentate (retained by the membrane) [76]. This is represented in Figure 1.2, in which the flow of permeate is in a direction perpendicular to the flow of feed.

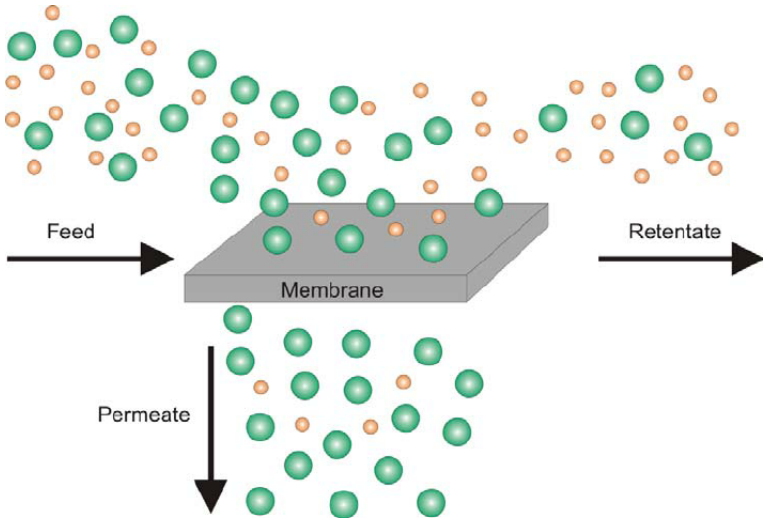

Figure 1.2: Feed, permeate and retentate streams of membrane-based operations. Adapted from [2].

Material selection is an important criteria in the design of membranes. Incumbent materials include a multitude of polymeric materials, boasting a number of advantages

including ease of formulation and handling, modest cost and reasonable levels of contaminant removal [77, 78]. In industrial desalination, for example, polyamide (PA) membranes are the dominant material class, occupying 91% of the market share [79]. These membranes boast high levels of salt removal and are capable of producing membranes having small pore size. Alternative materials include polyethersulfone (PES), which boasts favourable mechanical and thermal properties [80], and polyvinylidiene fluoride (PVDF), which is also very chlorine resistant and mechanically rugged [81]. Ceramic materials, typically metal oxide varieties including aluminium oxide [82], are an alternative to polymers. These are a popular choice given the superior mechanical and thermal performance compared to polymers, in addition to their robustness to harsh environments and chemical cleaning [83].

Despite their proven application in removal of a multitude of contaminants, polymeric membranes suffer a number of disadvantages which provide a practical challenge to their application.

The phenomenon known as *fouling* is a persistent and inevitable challenge to which membranes are prone. During operation, dissolved or particulate species from the feedstream are deposited onto the surface of the membrane, thus blockading the pores and hindering effective passage of cleaned fluid through the membrane [84]. Depending on the nature of the feed, foulant species can be organic [85], inorganic [86] or biological [87] in nature. Halting the filtration process does not enable the foulant to simply vacate the membrane surface freely, as such chemical cleaning is often required to cleanse the surface, often using harsh cleaning agents including hydrochloric acid and concentrated bleach [88]. The requirement of a membrane to undergo periodic cleaning is a serious hindrance in terms of enforced membrane down-time, which in turn has an unfavourable impact on process economics: for example, Jafari *et al.* [89] report that the enforced replacement of RO membrane modules due to fouling is a significant cost (approximately 24%) of the total operating expenditure.

Technological advancements, including installation of energy recovery devices, have enabled membrane systems to operate with lower overall energy footprint, such that overall power demands have reduced twofold over the past two decades [90]. Industrial seawater desalination plants are, however, still considered to be energy-intensive, as there must be a minimum required energy input to provide sufficient pressure on feed side to counteract the osmotic pressure and drive the flux [91]. At present, there are concerns that some membrane systems are approaching this thermodynamic limit of energy input and are thus running as efficiently as possible [92]. Membrane systems also require space for housing physically very large units, which is an issue when the plant is competing with urban space for habitation [93]. Issues of economics and energy of operation have led to a number of the world's most water scarce but also economically disadvantaged countries to steer away from desalination completely: as of 2020, Burundi, Malawi and Uganda had no desalination plants, while Ethiopia had only limited desalination capacity (1720 m^3/day) [94]. In turn, many of the large (10,000 - 50,000 m^3/day) or extra-large (>50,000 m^3/day) plants seem to be concentrated in regions with greater overall space or stronger economies, such as the Middle East [94].

Innovation is essential in overcoming these challenges associated with the use of membranes. Attempts to address issues related to fouling, for example, have led to serious research and investment in anti-fouling membranes [95]. The development of novel 2D materials, such as GO have provided an innovative step in membrane technologies, as they have the potential to offer lucrative advantages including efficient separation of contaminants including salts [96] and dyes [97]. Additionally, they have demonstrated promising anti-fouling capabilities and it is hoped that they will lead to cost-effective operation, thus enabling the downscale of the aforementioned very large desalination plants.

1.1.4 2D materials: Graphene and Graphene Oxide

2D materials are now a cornerstone of modern science, and are finding application in a number of scientific areas. The first of these to be discovered was graphene, by Geim and Novoselov in 2004 at University of Manchester [98]. Graphene possesses a planar hexagonal carbon system, a single atom thick, with carbon bonds making up an sp^2 carbon system [99]. As discussed below, graphene was determined to have remarkable physical and chemical properties, a feature which inspired the search for further materials of this kind. Zeolites are aluminosilicate mineral-based materials, with mineral structure comprising elemental aluminium, oxygen and silicon packed into a three dimensional structure, with high surface area [100]. Metal Oxide Frameworks (MOF's) are another class. Their high surface area structure comprises a heavy metal cation stabilised by coordinate bonds with surrounding chemical ligands known as linkers [101].

Among the expanding class of 2D materials, the unique properties of graphene oxide (GO) are unique and have enabled its application in a myriad of diverse fields including electronics [102], water purification [103], coatings [104] and in printing [105]. GO, unlike the aforementioned graphene, possesses embedded oxygen functionality on its basal plane. The physical properties of pristine graphene have, however, been considered superior to those of GO, owing largely to the strength of the carbon bonding in the sp^2 system and the ordered material planes [106]. Both graphene and GO possess remarkable mechanical properties. The Youngs' Modulus of monolayer GO was shown by Suk *et al.* [107] to be 207.6 GPa, which despite being lower than pristine graphene by an order of magnitude (1.0 TPa) [108], is significantly higher than metals such as copper (115 GPa) [109]. In terms of thermal properties, GO is a an insulator, having demonstrated low overall thermal conductivity (0.5 $W \cdot m^{-1} \cdot K^{-1}$) [110], in comparison to that of graphene (3000 - 5000 $W \cdot m^{-1} \cdot K^{-1}$) [111]. Given its insulating properties, GO may however find usage in improving the flame retardant properties of polymer

composites: for example, Higginbotham *et al.* [112] demonstrated that incorporation of GO into polycarbonate matrix decreased the heat released from the composite, based on calorimetric measurements. GO possesses high electrical resistivity ($1.64 \cdot 10^4$ Ωm), as a result of disruption to conduction of charge carriers in the carbon system brought about by the introduction of oxygenated surface groups [113]. Graphene, on the other hand, has a zero valence gap between conduction and valence bands, resulting in remarkably high conductivities ([114]). Improving the electrical conductivity of GO is possible, however, given the remarkable property of GO to undergo chemical modification (as discussed in subsequent paragraphs) by chemically reducing GO to an alternate form reduced-GO (RGO) [115]. Modification of GO to RGO has enabled the application of the material in nano-electronics, fo example, in energy storage applications [116].

GO is, by nature, amphiphilic, owing to its distinct regions of sp^2 and sp^3 bonding of connected carbon-carbon and carbon-oxygen regions, respectively [117]. GO is able to form stable dispersions in water with ease, as in water the material exfoliates to a series of stabilised GO sheets. Given this ability, it is favourable for GO to undergo reactions in dispersed phase, thus opening the pathway for interaction of species with the oxygenated groups on the exfoliated sheets [118].

Reduction of GO to RGO was mentioned in the previous paragraph. One common reducing agent employed for chemical reduction of GO is hydrazine (N_2H_4), which is suitable given its stability in water [119]. Alternative reducing agents are also utilised, such as sodium borohydride ($NaBH_4$), which is considered less toxic than hydrazine [120]. Chemical reduction of GO is therefore considered simple to perform and is capable of significantly lowering the oxygen content in GO, which may in turn improve the electrical and thermal properties of the material, as highlighted above. A recent article by Liu and Speranza [121] reported that chemical reduction of a GO material, in which oxygen content decreased upon reduction from 33.6% to 10.7%, was capable

of producing low resistance films (92 Ω) of the material.

In addition to chemical reduction of GO, the abundance of oxygen functionality enables GO to react with other materials, thus introducing chemical functionality to the material. By considering the Lerk-Klinowski model, GO possesses carboxylic groups on the edges of its planes and epoxy/hydroxyl groups on the basal planes. These properties enable GO to undergo a fascinating array of chemical reactions: several such examples will be highlighted here, though there are in fact an abundance of possibilities. Liu *et al.* [122] conjugated six-armed polyethylene glycol (PEG) onto the carboxyl groups of a Hummers' Method GO, by sonication with 1-Ethyl-3-(3-dimethylaminopropyl)carbodiimide under basic conditions. The resulting PEGylated GO was utilised as a drug delivery vehicle as it exhibited increased stability in protein serums and saline solutions, relative to GO, in resisting aggregation. The epoxy groups on GO are able to undergo ring opening polymerisation reactions, for example with amine groups in an amine-terminated ionic liquid [123], and may also undergo nucleophilic substitutions with amine-containing groups, both of which may stabilise the material in solution [124].

Among the methods to prepare GO, the *Hummers' Method* (1958) [125] remains a highly prominent means to oxidise multilayered graphite to produce GO on an industrial scale. The method is applicable at low temperature therefore mitigating the risks of explosion. Graphite is an inexpensive starting material and is capable of oxidation to GO by treatment with concentrated sulfuric acid (H_2SO_4), sodium nitrate ($NaNO_3$) and potassium permanganate ($KMnO_3$). The original synthesis was performed by Hummers and Offeman [125] adding H_2SO_4 and $NaNO_3$ to graphite at 66°C, before cooling in an ice bath to 0°C and slow addition of the $KMnO_3$. Interaction of $KMnO_3$ with the acid creates Manganese (VII) Oxide (Mn_2O_7), which is the oxidising agent involved in oxidation of graphite to GO.

A representation of the Hummers' Method is shown in Figure 1.3.

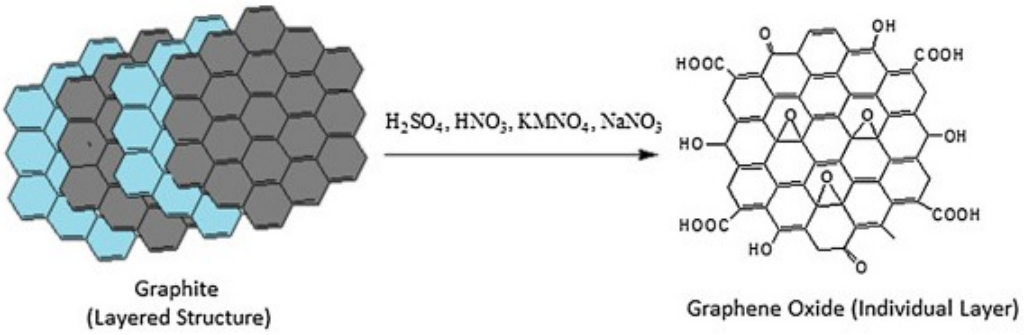

Figure 1.3: Hummers' Method of GO synthesis from graphite. Adapted from [3].

Although many processes are based upon the Hummers' Method, a number of modifications to the original method have been investigated as a means to expedite and improve the production process. In essence, a multitude of these exist, primarily focusing on alternative chemicals to those utilised in Hummers' Method. The utility of $NaNO_3$ in the Hummers' procedure results in the unwanted by-product of sodium ions, which must then be treated [126]. A number of research studies have focused on the exclusion of $NaNO_3$ altogether, for example, Alam *et al.* [127] and Marcano *et al.* [128]. Others have focused on switching or eliminating the use of $KMnO_3$ as the oxidising agent: Peng *et al.* [129] suggests the use of K_2FeO_4, which is a stronger oxidising agent compared to $KMnO_3$, and is reportedly capable of producing exfoliated and completely oxidised GO in less time. Furthermore Yu *et al.* [130] substitute the corrosive H_2SO_4 with hydrogen peroxide (H_2O_2), claiming that their yield was 25% higher compared to the analogous Hummers' Method.

The chemical structure of GO has been been a matter of debate among researchers for some time, and there are a number of proposed models in existence. The Lerf-Klinowski model [131], introduced in 1998 and developed around ^{13}C and ^{1}H Nuclear Magnetic Resonance (NMR) studies of GO, has become a very prominent and widely accepted structural model. In the Lerf-Klinowski model, GO comprises a flat, planar

arrangement of hexagonal carbon atoms, decorated with oxygen functionality around the carbon rings, in such forms as carboxyl (-COOH), ether (-COC-) and hydroxyl (-COH) groups, thus, carbon is present in both sp^2 and sp^3 form [131, 132].

Earlier examples of possible GO structural models include Hofmann-Rudolph (1936) [133], in which the structure of GO comprises graphite layers with randomly introduced expoxy functional groups embedded, but failed to provide information regarding the hydrogen atoms within the material. Another example is the 1946 model by Ruess [134], in which the intercalation of hydroxl groups into the GO basal plane introduces wrinkles into the structure, with carbons present in chair-like cyclohexane configuration. Scholz-Boehm (1969) [135] subsequently improved this by suggesting a more disordered chemical structure containing ketone groups and C = C bonds. Representative examples of the four GO structures discussed in this section are presented in Figure 1.4.

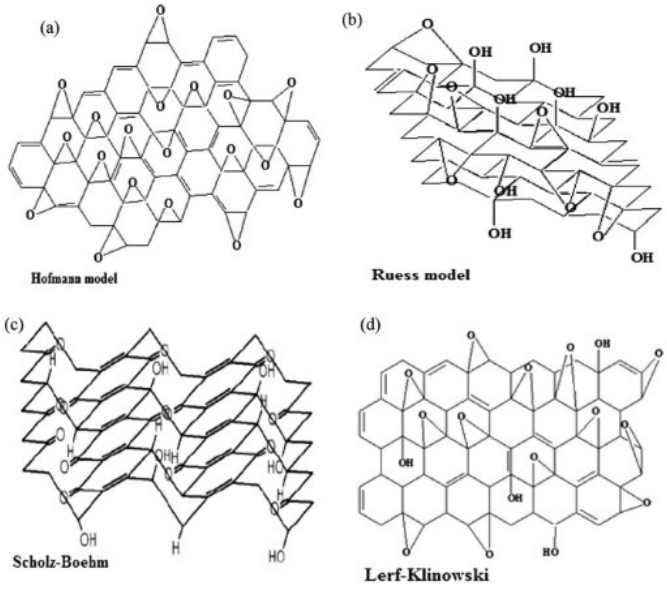

Figure 1.4: Structural models of of graphene oxide (GO), based on (a) Hofmann-Rudolph, (b) Reuss, (c) Scolz-Boehm and (d) Lerf - Klinowski structural models. Adapted from [4].

1.1.5 Emergence of Graphene Oxide within water treatment

In the previous section, the physical and chemical properties of GO were introduced. The unique structure of GO, based on the Lerf-Klinowski model, possesses distinct regions of sp^2 and sp^3 carbon bonding, which enables GO to interact with aqueous-based contaminants including salts and dyes. The principal characteristics of GO have given rise to the emergence of GO and derivative materials in water treatment [136]. Increasingly, GO is utilised primarily in two distinct areas of water treatment, namely in adsorption [137] and in membrane filtration [138]. In this section, the utility of GO in these key areas is briefly introduced, though a more detailed review is provided in the following literature review.

Adsorption of dyes

GO possesses a number of attractive properties that enable its utility as a dye adsorbent. These include very high surface area and ability to interact with dyes via mechanisms including π - π interaction and electrostatic mechanisms [139, 140]. Owing to the presence of negatively charged oxygen-containing groups, GO is electronegative and very hydrophilic [118]. In particular, the property of electronegativity has meant that GO has seen prominent usage for adsorption of cationic dyes, such as Methylene Blue (MB) [141] and Rhodamine B (RhB) [142]. Electrostatic attraction facilitates the contact between adsorbent and adsorbate, and the very high surface area enables the adsorption to be abundant and rapid. In contrast, adsorption of anionic dye such as MO onto GO is less commonly reported, as electrostatic repulsion between the like-charged adsorbent and adsorbate limits the capacity of GO to adsorb MO.

Membrane filtration of dyes

In membrane systems, it is desirable to restrict the motion of contaminants while simultaneously achieving rapid passage of cleaned fluid through the membrane geometry. In terms of dye removal, GO has demonstrated capability in improving the dye removal and permeation rates of cleaned water through polymeric membranes, as such

it has been attracted significant attention in the field of dye removal by membrane filtration [97, 143]. GO in aqueous dispersion may be coated onto the surface of polymer substrates including PES [144], PVDF [145] and PA [146]. When applied as a surface coating, flakes of GO tend to stack onto one another and impart electronegativity onto the polymer surface, thus enabling interaction with charged species such as dyes. A schematic representation of dye filtration using a surface-coated GO membrane is shown in Figure 1.5, showing the retention of dye molecules on the feed (top) and transited water molecules on permeate (bottom) side.

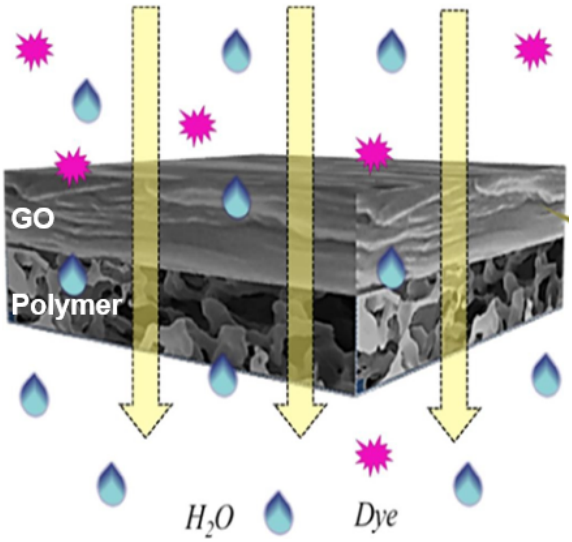

Figure 1.5: Schematic representation showing rejection of dyes by a GO-coated polymer membrane. Adapted from [5].

Membrane filtration of salts

The charged nature of GO has seen the material attract significant research interest with regards to sieving of ionic species from water: thus demonstrating the potential of GO membranes to desalinate seawater [147]. Salts dissociate into their ionic constituents in water: for example, sodium chloride dissociates into Na^+ cations and Cl^- anions. GO-coated membranes offer a means for membranes to interact with these ionic

species, based upon charge interactions [148] and size-based sieving [149]. A schematic representation of the motion of salt ions around stacked layers of GO is depicted in Figure 1.6.

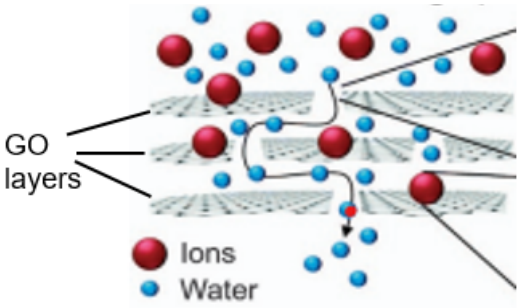

Figure 1.6: Schematic representation showing motion of salt ions around stacked layers of GO. Adapted from [6].

1.2 Research Problem

Since its emergence, GO has been utilised for treatment of a multitude of water-borne contaminants, seeing its rise in applications related to addressing the challenges of the water crisis, including desalination of seawater and cleanup of contaminated water. It has been highlighted that GO is capable of removing contaminants from water based on means including adsorption and membrane filtration. GO has proven an excellent adsorbent of cationic dyes including MB [141], while the efficacy of adsorption of anionic dyes including MO is overall lower [150]. Electrostatic charge and π - π interactions between GO and dye have been attributed as being the prominent features of the adsorption mechanism [139, 140]. The charged nature of GO also enables its application within membrane systems, as it is capable of interaction with charged species such as dyes and ionic species [97, 147]. Given its surface chemistry, including significant oxygen presence (including -COOH, -COC- and -OH groups) on basal plane and sheet edges, GO is capable of undergoing chemical reduction [119, 121] or chemical modifi-

cations to incorporate new functional groups [122, 124]. Production of exfoliated GO at industrial or commercial scale is now possible: based on well-established methods based on oxidation of powdered graphite [111, 114, 151].

A common trend for existing literature studies involves in-house synthesis of GO from graphite powder, based on oxidation techniques such as Hummers' Method, for adsorption of dyes [152, 153] and filtration of dyes [154] and salts [155]. Utilisation of commercially available GO products, including aqueous dispersions of the material that require minimal or no further purification, have been comparatively less well reported. One such example of the utility of commercial GO in water treatment applications was the adsorption study of Zhang *et al.* [150], in which high adsorption capacity for MB (429 mg/g) was achieved using a GO prepared from commercial GO powder by dispersing in water. Commercial GO is considered to have a number of advantages over in-house GO, including reliability of formulation, time-savings, experimental reproducibility and lending of itself to upscale industrial applications. Zhang *et al.* [150] were able to reduce the commercial GO and conduct adsorption studies with the reduced form. As a reflection of its advantages, commercial and industrial organisations may be expected to favour commercial GO over that which is prepared in-house, for reasons such as efficacy of time and scalability. In addition, if the efficacy of commercial GO materials could be demonstrated within membrane fabrications, namely in membrane coatings, then this would have potential to provide cost-effective improvements in membrane performance. Thus, there is significant attractiveness for utility in treatment of contaminated waters.

An essential stage in development of GO technologies within water treatment involves obtaining detailed analytical characterisation. Many studies offer rigorous characterisation approaches [156, 157, 158]. Furthermore, several interesting studies have contextualised the characterisation of multiple materials against one another, including GO with RGO, in order to gain comparative understanding of the respective behaviours

and properties [158, 159]. An important property governing the interaction of GO with contaminants is the flake size of the material. Studies involving characterisation of GO flakes have utilised microscopic imaging techniques including optical microscopy, coupled with analysis on software [160, 161]. Accordingly, a study that explores the property of different material flake sizes and the interaction of GO with contaminant species, coupled with a detailed characterisation methodology would contribute knowledge to the field. Furthermore, this would offer a novel approach to developing GO within water treatment, by providing a unique pathway for GO material and membrane characterisation, coupled with in-depth analysis of the behaviour.

1.3 Aims and Objectives

The aim of this research is to characterise two commercial GO materials, having the crucial property of different flake size. The importance of flake size will be explored by application of the GO materials in water treatment, namely in adsorption and removal of anionic MO and cationic MB dyes and salts from water.

In order to address the aim of this research, the following objectives are set:

1. Analyse the chemical nature of the commercial GO materials. The flake size of each will be characterised using laser diffraction and dynamic light scattering techniques. Develop further characterisations using spectroscopic techniques and microscopy analysis.

2. Investigate the adsorption of cationic MB and anionic MO dyes onto GO surfaces. Explore the importance of flake size on adsorption. Develop mathematical descriptions of of the kinetics and isotherms of adsorption and relate these to the dye adsorption capacities of the materials in equilibrium.

3. Utilise GO as a coating material for fabrication of PES membrane filter materials.

Apply these GO-coated PES membranes to removal of anionic MO and cationic MB dyes from dye-contaminated waters.

4. Utilise GO-coated PES membranes as a means to desalinate water contaminated with salt, such as magnesium sulphate, ammonium heptamolybdate, sodium chloride and sodium sulphate.

5. Investigate the impact of salt addition upon dye adsorption efficacy of GO, within the context of cationic MB adsorption, by dissolving salts magnesium and sodium sulphate into the dye solution prior to insertion of adsorbent. Explore the differences in adsorption by different flake size materials.

6. Investigate the impact of salt addition upon filtration efficacy of GO-coated membranes, by filtration of MB - sodium sulphate and MB - magnesium sulphate solutions.

1.4 Thesis Scope

This thesis comprises in total seven chapters, the contents of which are summarised as follows:

Chapter 1 provides an introduction to the thesis and provides some background information, regarding classical methods of water treatment, including membrane separation systems. The motivation of the research is presented and aims and objectives of research are defined. The scope of the thesis is outlined.

Chapter 2 provides a literature review, focusing on methods of GO membrane preparation, the utility of GO as an adsorbent and as a membrane coating for treatment of dye-contaminated and saline waters.

Chapter 3 discusses the materials and experimental methods necessary for obtaining the results in Chapters 4 - 6. Preparation of materials for characterisation and

requisite analytical methods is discussed. Methods for filtration testing with dyes and salts using uniaxial flow testing is discussed. Experimental procedures and subsequent mathematical modelling of dye adsorption systems is also detailed.

Chapter 4 discusses characterisation of GO materials and GO-coated PES membranes. A number of techniques were employed in order to characterise the materials, namely these are: Fourier Transform Infrared (FTIR), Raman, X-ray photoelectron (XPS) and Ultraviolet-Visible (UV-Vis.) spectroscopic techniques. X-ray diffraction (XRD) was used to characterise the interlayer spacings and scanning electron microscopy (SEM) was utilised to analyse the morphologies. Colloidal stability was investigated by measurement of zeta potential and particle sizing achieved by laser diffraction (LD) and dynamic light scattering (DLS). GO-coated PES membrane analysis was achieved using focused ion beam scanning electron microscopy (FIBSEM), Water Contact Angle measurement, FTIR, XRD and Thermogravimetric Analysis (TGA).

The content of this chapter addresses Objective 1, as listed above.

Chapter 5 discusses utility of GO as a material adsorbent and membrane coating, for treatment of dye-contaminated waters. Kinetics and equilibria of adsorption of cationic MB and anionic MO is discussed and the mathematical models are utilised to reveal that adsorption is governed by pseudo-second order (PSO) kinetics and Langmuir (monolayer) equilibrium. Filtration efficacy of GO-coated PES membranes is investigated subject to the impact of a number of parameters including initial dye concentration, filtration pressure and coating thickness. Proposed mechanisms for the interaction of GO with dyes is also discussed. Aggregation of GO in dye solutions is also investigated by LD and measurement of zeta potential.

The content of this chapter addresses Objectives 2 and 3, as listed above.

Chapter 6 discusses utility of GO-coated PES membranes for desalination of saline waters. Desalination experiments were performed using uniaxial flow testing, involving magnesium sulphate, ammonium heptamolybdate, sodium chloride and sodium sul-

phate salts. The suggested mechanisms of salt rejection were discussed. The impact of salt addition upon MB removal efficacy is discussed, as GO is employed as an adsorbent and as a membrane coating for removal of dyes in a mixed dye-salt system. Proposed mechanisms and discussions are provided.

The content of this chapter addresses Objectives 4, 5 and 6, as listed above.

Chapter 7 summarises and concludes the thesis, and highlights areas for development of the research based upon this thesis.

Chapter 2

Literature Review

2.1 Overview

This literature review provides detailed information regarding the application of GO materials as adsorbents of dyes and in membrane materials, for removal of dyes and salts. In order to maintain focus on areas which are highly salient for the research chapters of this thesis, attention is paid to highlighting studies that concern the employment of GO in its unmodified form, though on several occasions, comparisons with modified GO materials are made. In analysis of these studies, the experimental methods and the membrane fabrication method are elucidated, and the relevance of the results are discussed. Comparison of behaviours or trends with other sources from the literature is made, including signposting the performance of materials other than GO in adsorption and filtration.

The content of this literature review is divided into the following themes:

- GO and other materials as dye adsorbents, considered in Section 2.2.
- Methods for preparation of GO membranes, considered in Section 2.3.
- Removal of dyes using GO and other material membranes, considered in Section 2.4.
- Desalination using GO and other material membranes, considered in Section 2.5.

Conducting a literature review of GO is not straightforward, as the existence of an abundance of information may prove challenging to navigate. In order to facilitate this process, a number of literature databases were employed, including *Web of Science* (Clarivate Plc (UK)), *Science Direct* (Elsevier (Netherlands)) and *GoogleScholar* (Google (USA)). After the above themes were decided, these databases were utilised to explore the field for information. As mentioned above, the primary focus was regarding GO materials that are chemically unmodified, thus enabling the content of the review to be restricted.

2.2 Adsorption of dyes using GO

2.2.1 Adsorption of cationic dyes using GO adsorbents

A dye may be classified as a cationic dye provided that upon ionisation in water, it possesses an overall positive charge. Adsorption of these dyes using GO adsorbents is particularly favourable, owing to the strength of interaction between the deprotonated groups on the GO, and the cationic groups on the dye [118]. The adsorption of cationic dye MB was introduced in Section 1.1.5, in which the high capability of GO to adsorb this dye was highlighted. GO has also found utility as an adsorbent for a multitude of other cationic dyes, including malachite green [162], RhB [142] and Crystal Violet [163]. In each case, GO has been demonstrated to adsorb the dyes with high efficacy.

As discussed in Section 1.1.4, the Lerf-Klinowski model of GO proposes a structure comprising regions of sp^2 carbon bonding, and oxygen-containing groups such as hydroxyl, expoxy and carboxyl. Deprotonation of these groups results in an oxygen group with a vacant lone pair of electrons, which has been exploited for the purposes of cationic dye adsorption. A number of studies have examined the impact of pH on cationic dye performance, concluding that increasing the pH results in stronger adsorption, owing to the greater deprotonating effect of the alkaline solution [164, 165]. The

carboxyl groups tend to deprotonate most easily in solution, as the resulting conjugate base formed by the vacation of hydrogen atom is very stable [166]. Efforts have been made to increase the oxygen content in GO and in particular the carboxyl group presence [167]. Zhao *et al.* [168] fabricated a GO sponge material that contained a high content of carboxyl groups, relative to the GO starting material: it was demonstrated that the sponge's adsorption capacity for MB was very promising relative to the GO (780 vs 446 mg/g).

The mechanism of adsorption of cationic dyes by GO has been attributed to a number of features including electrostatic interactions, π - π interactions and hydrogen bonding [7]. Electrostatic interactions are considered the primary mechanism for adsorption of cationic dyes such as MB [169]. π - π interactions between the benzene rings on GO and the aromatic groups on the cationic dyes are thought to provide an important secondary contribution to the adsorption mechanism [170]. These interactions are not considered to be the major mechanism, however. Yang *et al.* [171] compares MB adsorption on GO and expanded graphite, having similar structure but different oxygen content (GO having considerably higher): it was demonstrated that the adsorption capacity of GO was three orders of magnitude higher for GO than expanded graphite. This suggests that the electrostatic interaction is the dominant mechanism, as the MB is clearly inclined to adsorb on the oxygen groups. Hydrogen bonding has also been suggested as a minor contributor to the adsorption mechanism, through the multitude of alcohol-containing groups in the GO structure [171].

Aggregation of GO in cationic dye is typically a hindrance of the adsorption process. GO tends to form an electrokinetically stable suspension in water, with net negative charge, which facilitates the interaction of GO sheets with cationic dyes. GO has high adsorption capacity for cationic dyes but the undesirable aggregation of sheets has the impact of reducing the dye adsorption capacities, due to the stacking of sheets [172]. The mechanism for aggregation of GO sheets has been attributed to the stability

theory developed by Derjaguin, Landau, Verwey and Overbeek (DLVO) [173]. By DLVO theory, a highly charged species, such as negatively charged GO, is electrically stabilised by a summation of attractive van der Waals' forces and repulsive forces due to likeness in electric charge. Adsorption of species such as salt cations or cationic dyes has the effect of neutralising the effective negative charges on the sheets, resulting in a shrinkage of the electrical double layer surrounding the individual flakes [174]. If the repulsive electrical forces are reduced in magnitude, the cohesive van der Waals' attractive forces between sheets of GO will become the dominant force, thereby resulting in aggregation of the sheets [175].

Aggregation of GO sheets and subsequent sedimentation is an irreversible process, as such, recovery of the GO adsorbent following dye adsorption is a problematic task [172, 176]. Separation of GO from adsorbent using magnetic nanoparticles is currently an active area of research. Junyong *et al.* [177] synthesised a GO with embedded Fe_3O_4 nanoparticles, reporting that this material could be separated from RhB using an applied magnetic field after the adsorption process. An alternative means to prevent sheet aggregation was the research of Jayanthi *et al.* [178], who synthesised a 3D foam architecture that was able to resist aggregation in RhB dye while having comparable equilibrium adsorption to flake GO. Despite efforts being made to overcome the adverse effects of GO sheet aggregation, current investigations in the literature suggest that the aggregation of GO sheets is an enormous practical challenge. A number of such investigations have expressed concern that the aggregation phenomenon may limit the overall applicability of GO as an adsorbent, despite the high adsorption capacities for cationic dyes [175, 178].

2.2.2 Adsorption of anionic dyes using GO adsorbents

Adsorption of anionic dyes by GO is hindered in practical application by the effects of electrostatic repulsion, in which the deprotonated oxygen-containing groups on the GO

repel the anionic dye [179]. The mechanism of adsorption for anionic dyes is therefore different to that of cationic dyes, as governed primarily according to π - π interactions of the aromatic structures on GO and dye, and hydrogen bonding [174]. Considering adsorption of MO as an example, the azo (N = N) group on the dye is capable of hydrogen bonding with a hydroxyl group on the GO [180].

A summary of the mechanisms of MB and MO adsorption, as discussed in these two sections, is provided in Figure 2.1.

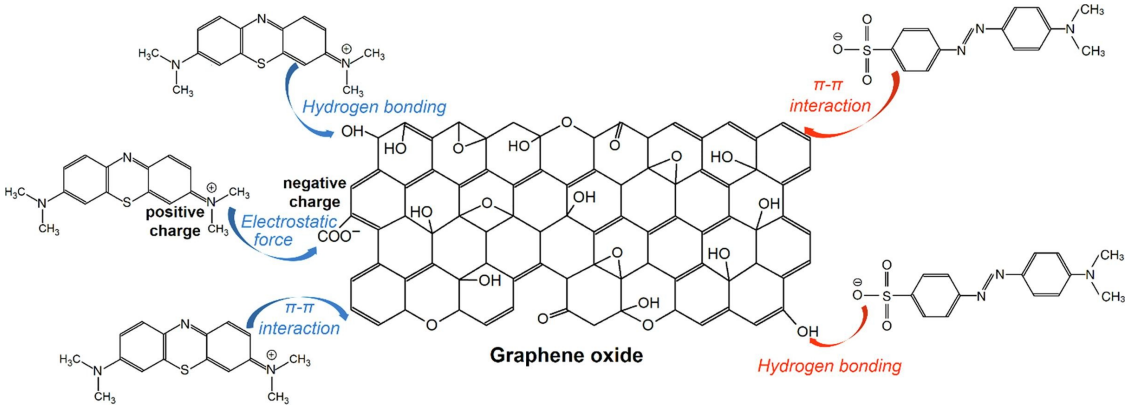

Figure 2.1: Proposed mechanisms of interaction for GO with cationic MB dye (left) and anionic MO (right). GO interacts with MB via electrostatic interaction, π - π interaction and hydrogen bonding. The interaction with MO is considered related to π - π interaction and hydrogen bonding only. Adapted from [7].

As illustrated in a number of comparative dye adsorption studies [169, 179, 181], the adsorption capacity of GO for anionic dyes is reportedly poor relative to the level of adsorption achieved in cationic dye adsorption. In the work of Minitha [179], for example, the adsorption capacity of GO for MB is approximately double that of MO (130 mg/g versus 66 mg/g). This emphasises the significance of electrostatic interactions in the overall dye adsorption mechanism.

Owing to the difficulties in adsorption of anionic dyes using GO, a very popular means of overcoming the electrostatic repulsion involves modifying GO to incorporate

the presence of other species. Crosslinking of GO with chitosan is a very popular means of improving the anionic dye adsorption capacity, as the de-protonated amine groups are a rich source of positivity, capable of promoting electrostatic attraction [182, 183]. Shi *et al.* [184] demonstrated that their GO - chitosan aerogel, with a GO:chitosan blending ratio of 1:2, was able to adsorb MO with roughly five times the capacity of MB. RGO has also been demonstrated a capable adsorbent of anionic dyes: for example, Zhang *et al.* [185] reported that their photo-reduced GO was capable of adsorbing anionic Orange II dye four times more effectively than unmodified GO.

2.2.3 Kinetics of dye adsorption using GO adsorbents

Kinetics of dye adsorption by GO adsorbents is herein considered. Salient models of kinetics are introduced and subsequently contextualised by considering the application of these within existing GO adsorption studies.

Studying the kinetics of dye adsorption involves monitoring the rate at which dye is adsorbed by an adsorbent [186]. The kinetics of the dye adsorption process is dependent upon the characteristics of the adsorbent, in terms of its physical or chemical properties, and the overall mass transport mechanism [187].

A number of computational models have been applied to model the experimental behaviour of a GO adsorbent - dye adsorbate system, the most popular of which are the pseudo first order (PFO) and pseudo second order (PSO) systems [188]. Ho and McKay [189] demonstrated that these models may be linearised, as such their popularity has grown, as they are able to account for the behaviour of most systems [190]. Ho [191] published a subsequent paper that discussed the supposed superiority of the PSO model over the PFO, owing to its potential applicability within a wider range of systems.

The PFO model assumes that the rate of adsorption of solute species is proportional to the difference between equilibrium adsorption and the instantaneous amount of solute adsorbed at a given time instant [192]. PFO model is better suited to the initial stages

of an adsorption process [189]. Additionally, the model assumes that sorption takes place at localised sites only and that a state of maximum adsorption is reached when there are no more available binding sites for occupation [193].

The generalised form of the PFO model is given according to Equation 2.1 [188], where k_1 (min^{-1}) is first order adsorption rate constant, q_t is the amount of adsorption taken place at time t, $q_{e,exp}$ is the *experimental* equilibrium adsorption and $q_{e,cal1}$ is the *calculated* equilibrium adsorption (all having units mg/g).

$$\frac{dq_t}{dt} = k_1 \cdot [q_{e,exp} - q_t] \tag{2.1}$$

Integration subject to the boundary conditions $q_t = 0$ at time $t = 0$ and $q_t = q_t$ at time $t = t$ yield the following exponential form:

$$q_t = q_{e,exp} \cdot [1 - e^{-k_1 \cdot t}] \tag{2.2}$$

The popularised Ho and McKay [189] linearisation of Equation 2.2 is provided by Equation 2.3:

$$ln(q_{e,exp} - q_t) = -k_1 \cdot t + ln(q_{e,cal1}) \tag{2.3}$$

Provided that the relationship between $ln(q_{e,exp1} - q_t)$ and t is linear, the adsorbent - adsorbate system may be assumed to follow PFO kinetics and the values of k_1 and $q_{e,cal1}$ may be yielded, from the slope and vertical intercept of the plot, respectively.

In the PSO model, the rate-limiting step is chemical sorption, that is, a chemical reaction involving transfer of electrons between the adsorbent and adsorbate species [194]. The kinetics of reaction is found to be proportional to the number of active sites which are available on the adsorbent [195]. The curvilinear definition of the PSO model is defined by Equation 2.4 [189], where k_2 ($\text{g} \cdot min^{-1} \cdot mg^{-1}$) is the second order rate constant.

$$\frac{dq_t}{dt} = k_2 \cdot [q_{e,exp} - q_t]^2 \tag{2.4}$$

Ho and McKay [189] proposed in total four linearised forms of the PSO equation. Of these linearised forms, the most widely used, owing to its perceived advantages with regards to fitting properties [186], is given by Equation 2.5:

$$\frac{t}{q_t} = \frac{t}{q_{e,cal2}} + \frac{1}{k_2 \cdot q_{e,cal2}} \tag{2.5}$$

where $q_{e,cal2}$ is the second order *calculated* equilibrium adsorption, in mg/g.

Thus, a plot of $\frac{t}{q_t}$ versus t should yield a linear line, with slope equal to the inverse of $q_{e,cal2}$ and the value of k_2 may be extracted from algebraic manipulation of the vertical intercept.

In GO - dye adsorption systems, a multitude of studies have shown preference for the PSO model over PFO. In the following paragraphs, the kinetics of dye adsorption by GO is considered, using examples from the literature. The comment must be made however, that comparison of kinetic model parameters across multiple sources is often not straightforward. In practice, a number of the calculated and experimental model parameters may vary significantly from one another, according to the features of the adsorbate itself, including particle size [196] and surface area [197]. As such, it is important to consider that the GO morphology between two systems may not be comparable, thus impacting the adsorption.

Peng *et al.* [198] performed adsorption studies using 0.50 g/l MB with 0.6 g/l GO prepared by Hummers' Method, and demonstrated better statistical fit for PSO (R^2 = 0.997) over PFO (R^2 = 0.832). The value of $q_{e,exp}$ was remarkably high, at 2255.35 mg/g, while the values of $q_{e,cal1}$ and $q_{e,cal2}$ were 369.46 mg/g and 2302.1 mg/g, respectively. As such, the higher value of statistical R^2 coupled with the closer fit of the $q_{e,cal2}$ value indicates that the PSO has overall much better fit to the experimental

data compared to the PFO model.

Utilising kinetic models to represent experimental data enables the efficacy of adsorption for multiple materials to be compared within the same study. This has been demonstrated powerfully on a number of studies in the literature, several of which are highlighted here. Li *et al.* [199] compare the adsorption kinetics of MB onto three materials: activated carbon, carbon nanotubes and GO. It was shown that the PSO model provided a better account of the behaviour relative to the PFO model, with R^2 values ranging 0.981 - 0.992. The resulting k_2 values were higher for GO ($90.6 \cdot 10^{-6}$ g $\cdot min^{-1}$ $\cdot mg^{-1}$) compared to the other materials. Minitha *et al.* [179] compared the adsorption kinetics of MB for GO versus a synthesised RGO, reporting near-perfect fitting of the PSO model ($R^2 > 0.999$) for GO - MB and RGO - MB adsorption. This study reveals that the values of k_2 for GO are an order of magnitude larger for GO (0.151 g $\cdot min^{-1}$ $\cdot mg^{-1}$) compared with RGO (0.061 g $\cdot min^{-1}$ $\cdot mg^{-1}$), despite the analogous $q_{e,exp}$ and $q_{e,cal2}$ values being slightly higher for RGO compared to GO. The recent comparative study of Abouzeid *et al.* [200] discusses adsorption of MB onto GO and a GO modified with silica, revealing that the k_2 values for the composite ($9.8 \cdot 10^{-6}$ g $\cdot min^{-1}$ $\cdot mg^{-1}$) are higher than the unmodified GO ($9.3 \cdot 10^{-6}$ g $\cdot min^{-1}$ $\cdot mg^{-1}$).

The comparative element within studies is also employed for internal comparison of adsorption of different dyes by the same adsorbent species, often by means of comparing the efficacy of dyes with contrasting molecular charges. Sabna *et al.* [167] compared the adsorption of crystal violet onto GO, with MO. By PSO, it was demonstrated that the adsorption of the cationic crystal violet was more effective than MO ($q_{e,exp} = 250$ versus 38.3 mg/g). Kim *et al.* [8] compared MB adsorption with anionic Acid Red 1 dye, likewise showing by PSO that the cationic MB was adsorbed more effectively ($q_{e,exp} = 301.2$ versus 52 mg/g) and faster than Acid Red 1 ($k_2 = 0.0050$ versus 0.0004 g $\cdot min^{-1}$ $\cdot mg^{-1}$). Plots of the linear PFO and PSO kinetics models, for MB and Acid Red 1 adsorption, are shown in Figure 2.2.

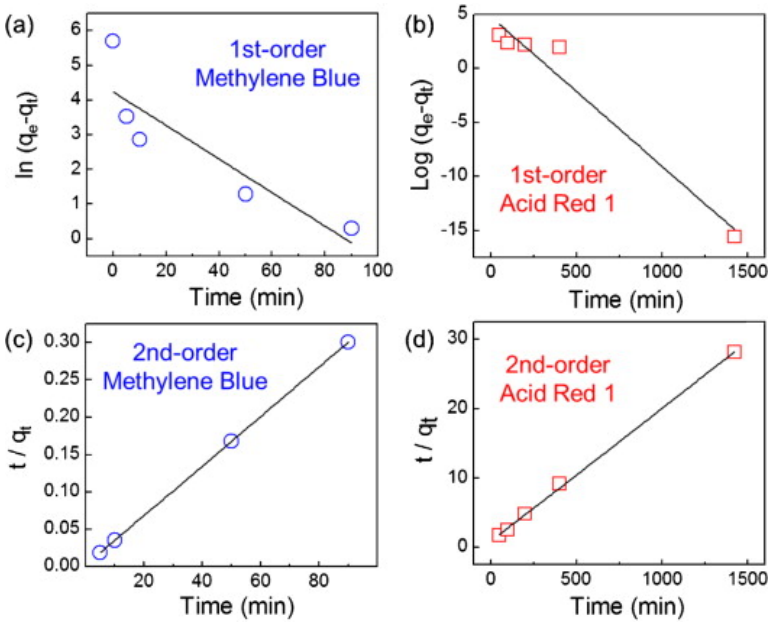

Figure 2.2: Pseudo First Order (PFO) and Pseudo Second Order (PSO) kinetics of adsorption of MB and Acid Red 1 by Reduced GO. PFO plots are shown in (a) for MB and (b) for Acid Red 1. PSO plots are shown in (c) for MB and (d) for Acid Red 1. Adapted from [8].

It is clear by inspection of the plots that the respective PSO fits are better than the corresponding PFO fits, as the data has evidently lower spread about the kinetics lines.

Alternative kinetic models have been suggested alternatives to PFO and PSO. The intraparticle diffusion model, first proposed by Weber and Morris [201], suggests that adsorption happens via a two-stage mechanism, involving the transfer of adsorbate onto adsorbent surface and subsequent penetration of adsorbate into adsorbent pores. The penetration stage is the rate-limiting step. Chia *et al.* [202] demonstrate that their GO - MB system fits the PSO and intraparticle diffusion model simiarly well (for PSO, R^2 = 0.999 - 1.000, for intraparticle diffusion R^2 = 0.997 - 0.999), leading them to conclude that the PSO is the dominant mechanism, but external mass transfer due to intraparticle diffusion is also a fundamental aspect.

Isolated examples from the literature do not actually employ a kinetics model for analysis of their dye adsorption data. Zhang *et al.* [203] prefer to monitor $q_{e,exp}$ at set time intervals, subject to controlled temperature (293 K) and at pH 7, and plot the values of $q_{e,exp}$ versus t. It is acknowledged, however, that the lack of mechanistic model hinders the comparison of this work with other sources from the literature, accordingly, the impact of such a study may be limited.

This section has introduced the key models for predicting the kinetics of adsorption of GO systems, namely, the PFO and especially PSO models. Studies from the literature were brought in to contextualise the utility of these models and demonstrate the power of applying them in linear form. This has provided motivation for later kinetics studies, which will consider the application of these models in GO adsorption systems.

2.2.4 Equilibrium of dye adsorption using GO adsorbents

In this section, equilibria of dye adsorption by GO adsorbents is evaluated. Several key isotherms are introduced, including mathematical definitions, and these are contextualised by considering the application of these within existing GO literature.

The adsorption of adsorbate onto adsorbent is a dynamic process, and if the interaction proceeds for sufficient length of time, an equilibrium will be established between the amount of adsorbate in solution and the amount that is adsorbed onto the adsorbent [204]. An adsorption isotherm is an empirical means of relating the concentration of adsorbate on the surface of an adsorbent to the concentration of that species in solution, at a given temperature [205].

Langmuir [206] and Freundlich [207] isotherms are perhaps the two most commonly studied isotherms, used to define the behaviour of GO - dye systems.

Langmuir adsorption is characterised by the assumption that the adsorbent species is of physically homogeneous configuration [206]. Theoretically, all binding sites on the adsorbent are identical with equivalent binding energies [208]. Langmuir also predicts

that the adsorbent has only limited capacity for adsorption, as such, a saturation value is established that represents a complete monolayer of surface adsorption, where each binding site holds one adsorbate molecule [209]. The linearised Langmuir relationship is expressed by Equation 2.6:

$$\frac{C_e}{q_e} = \frac{1}{K_L \cdot q_{max}} + \frac{C_e}{q_{max}} \tag{2.6}$$

where K_L is the Langmuir constant (l/g), q_{max} (mg/g) is the maximum adsorption capacity, q_e (mg/g) is equilibrium dye adsorption and C_e (mg/l) is equilibrium dye concentration remaining in solution.

For Langmuir isotherm to be obeyed, a plot of C_e/q_e versus C_e ought to be linear with slope equal to the inverse of q_{max} and vertical intercept equal to $1/(K_L \cdot q_{max})$, thus enabling calculation of parameters q_{max} and K_L from intercept and slope, respectively.

Freundlich isotherm is an empirical relationship concerning the non-ideal adsorption of sorbate onto an adsorbent with heterogeneous surface energy [205]. Freundlich predicts that the overall amount of adsorption onto an adsorbent surface will increase provided that the concentration of adsorbate in the solution phase increases [207]. The isotherm is, however, limited in applicability to cases in which the concentration of adsorbate in solution is low and it is optimised for only a narrow range of adsorbate concentrations [210]. The governing linearised equation is given by Equation 2.7:

$$ln(q_e) = \frac{1}{n} \cdot ln(C_e) + ln(K_F) \tag{2.7}$$

where K_F ($\mathrm{mg}^{(1-1/n)} \cdot l^{1/n} \cdot g^{-1}$) is the Freundlich constant, related to the adsorption capacity, and parameter n represents adsorption intensity. A plot of $ln(q_e)$ versus $ln(C_e)$ will be linear if Freundlich model is obeyed, with slope equal to the reciprocal value of n and intercept equal to $ln(K_F)$.

Adsorption studies involving the adsorption of dyes onto GO tend to combine anal-

ysis of kinetics and equilibria within a single study. Konicki *et al.* [211] performed kinetics and equilibrium studies under the same experimental conditions, by taking the equilibrium concentrations to be the values at the end of the kinetics studies. They demonstrated that the adsorption of cationic dyes Basic Yellow 28 and Basic Red 46 was attributed to PSO kinetics and Langmuir adsorption. GO had higher equilibrium adsorption capacity for Basic Red 46 (by Langmuir, q_{max} = 76.9 versus 68.5 mg/g), which was consistent with the calculated q_e values in PSO kinetics. Gong *et al.* [212] likewise combined kinetics and adsorption studies, in a study in which MO was utilised to probe the π - π stacking mechanisms of GO at pH 2, 7 and 10. The kinetics experiments were performed for a total 150 minutes, the equilibria concentrations were measured at time 180 minutes after the commencement (*i.e.* 30 minutes after kinetics experiment ceased). The GO - MO system also behaved according to Langmuir equilibrium and PSO kinetics.

The general trend in GO - dye adsorption studies appears to favour the Langmuir isotherm, but a number of studies have seen favourability of the Freundlich isotherm. Bankole *et al.* [213] studied the adsorption of cationic RhB onto GO nanosheets, finding that the adsorption is governed by PSO kinetics and Freundlich isotherm. In this study, the equilibrium experiments were performed at low RhB concentration (highest 30 mg/l): as such, this may account for the preference towards Freundlich. The calculated Freundlich parameters K_F (46.36 $\text{mg}^{(1-1/n)} \cdot l^{1/n} \cdot g^{-1}$) and n (1.24) suggest favourability of the isotherm, as the K_F value is high and the low value of n suggests that the adsorption is intense. Gan *et al.* [214] use their composite glucomannan/GO hydrogel material for adsorption of MO and MB. They report that higher initial dye concentrations were used for the equilibrium studies compared to the kinetics, and that the preferred isotherm was that of Freundlich. In this study, the material is demonstrated to have higher tendency to adsorb MB, as a study of q_e as a function of pH showed that the adsorption of MB is higher than MO across the full pH range. The

Freundlich model used, however, shows the K_F value to be higher for MO (3.71 versus 2.68 $mg^{(1-1/n)} \cdot l^{1/n} \cdot g^{-1}$), indicating stronger adsorption, and the analogous n is higher for MO, suggesting the adsorption is less intense (1.50 versus 1.36).

The Sips isotherm [215] is an alternative to those of Langmuir and Freundlich, often regarded as a combination of the two. It was previously discussed that the Freundlich isotherm predicts that the surface adsorption will increase provided that the concentration of dye in solution increases, thus predicting theoretically infinite adsorption. Sips isotherm maintains the Freundlich prediction of heterogeneity of adsorption, but introduces a finite limit for dyes at high concentration [216]. A number of GO or modified GO - dye adsorption studies have employed Sips isotherm, as a means of comparison with Freundlich or Langmuir [163, 217, 218]. Other isotherms are also uncommonly used to model the equilibria of GO - dye adsorption: these include Dubinin-Raduskevich [219] and Temkin [220].

This section has introduced adsorption isotherms for modelling the equilibria of dye adsorption for GO - dye systems. The literature has shown that the foremost isotherms are those of Langmuir and Freundlich, both of which are expressible in linear form. The dominance of the former is interesting, especially given the complex aggregate microstructure of GO flake systems.

2.2.5 Impact of ions on dye adsorption

Textile industry effluent is a complex mixture of different chemical species, the composition of which may vary depending upon the location and application [221]. The species contained within the effluent are not necessarily ionic; these species may also significantly impact the adsorption process. As such, it is important to establish a baseline for characterisation of the typical ranges of species present in textile effluent, which may be utilised as a reference point for determining the necessary concentrations in experimental studies. Table 2.1 details a typical effluent composition, taken from

Dos Santos *et al.* [27] and Pal [28]. By inspection, this depicts that the variety of species within effluent is staggering. Also shown in the table is the permissible levels of a number of these species within surface water, in India [29]. Given the tight limits of a number of these, this places significant demand upon the adsorbent species, which must therefore be capable of operation in a variety of chemical environments.

Table 2.1: Textile industry effluent sample composition and permissible limits of species in India [27, 28, 29].

Textile effluent Parameter	Quantity in effluent	Permissible limit
pH	9.69 - 10	6.5
Alkalinity (mg/l)	498.2	20 - 200
Apparent colour (Pt Co)	3280	20
Turbidity (FTU)	183	5
Chemical Oxygen Demand (mg/l)	1395	550
Total Dissolved Solids (mg/l)	3120	2000
Oils and grease (mg/l)	126	0.20
Aluminium (mg/l)	0.24	
Ammonium (mg/l)	17	
Cadmium (mg/l)	0.001	
Calcium (mg/l)	43	
Chloride (mg/l)	2581	600
Chromium (mg/l)	0.69	
Magnesium (mg/l)	4	
Mercury (mg/l)	0.002	
Sulphate (mg/l)	1400	250
Sodium (mg/l)	2900	200
Tin (mg/l)	0.20	

The high degree of alkalinity and associated high pH of the effluent presents a problem for adsorbent species including GO. Given the greater tendency of hydrogen atoms

to deprotonate at high pH, the adoption of greater negative surface potential diminishes the adsorption of anionic dyes due to greater repulsive effects [222, 223]. Given the tendency for textile effluents to be a mixture of dyes, it is difficult to determine the concentration in typical units; as such, the colour is characterised by platinum - cobalt (Pt Co) units. Effluent water is thus highly coloured, which presents problems for aquatic life and for the aesthetics of natural water sources [224]. Similar problems are raised by water which is highly turbid [225]. Total dissolved solids (including ionic species) present another problem, as these can be toxic [226]. Non-ionic species including fats, oils and grease are present in effluent as a natural impurity washed off the fibre during dyeing [227]. They are however capable of interacting with GO adsorbents via hydrogen bonding, thus hindering the process of adsorption [228].

As evidenced, there is also a significant heavy metal presence within effluent. Heavy metals present a serious environmental problem, owing to their accumulation, recalcitrance to degradation and toxicity [229]. In particular, there is a high quantity of ionic species including sodium, sulphates, chlorides and magnesium, necessary for the processing stages of textile dyeing and production [230].

An important consideration is that the presence of ions may have an impact upon the electrokinetic properties and stability of GO adsorbents. This is particularly important given the presence of high valency cations including aluminium (3+) and chromium (3+) within effluent. Although GO tends to form a well dispersed and stable dispersion in water due to repulsion of the negative charges, the addition of ions has the effect of screening the electronegativity, ultimately leading to aggregation of the GO sheets [231]. The electrokinetic stability of GO, subject to the addition of ions, has been studied by Wang *et al.* [9], who obtained zeta potential measurements of GO across a range of salt concentrations 0 - 91 mM, using monovalent sodium chloride, divalent magnesium chloride and trivalent aluminium chloride. It was demonstrated that the impact upon zeta potential increased with increasing cationic valency, such that for ad-

dition of aluminium chloride at sufficiently high salt concentration, the zeta potential was high enough to suggest positively charged colloidal stability (>30 mV). It was proposed that the higher charge and smaller diameter of the Al^{3+} cations enables the ion to bind strongly to GO and that the positivity is a result of excess cations remaining in solution. Figure 2.3 shows the obtained zeta potential, as a function of salt concentration. A similar trend was observed by Baskoro *et al.* [232], who compared the impact of magnesium sulphate and sodium sulphate concentration upon zeta potential (0 - 1.0 M), revealing that the divalent magnesium salt had a significantly greater impact on the stability of GO.

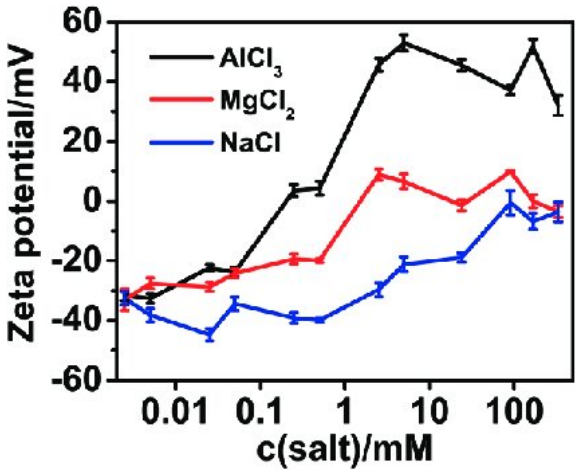

Figure 2.3: Zeta potential of GO-in-water dispersions, subject to variation in salt concentration in the range 0 - 91 mM NaCl, $MgCl_2$ and $AlCl_3$. Adapted from [9].

For low valency sodium salts, the interaction mechanism of GO with Na^+ cations is considered to follow the DLVO theory of aggregation (introduced in Section 2.2.1, in the context of GO aggregation in cationic dye solution) [233]. Sodium cations have no specific adsorption capacity for the functional groups on GO, as such they do not adsorb, though may accumulate in the vicinity of the flakes and have a slight impact upon the electrical double layer in the vicinity [234]. The interaction of GO with higher valency cations such as Mg^{2+} ions is far stronger, as the higher valency on the ion leads

to cation bridging and adsorption [235]. These stronger interactions result in a greater tendency of GO to aggregate in the presence of high valency cations, as the higher valency cations are capable of forming crosslinks between GO sheets [233].

The addition of cations to a GO - dye adsorption system may therefore have a significant adverse impact upon the adsorption capacity of the GO. Survey of the literature reveals that there have been some highly interesting behaviours associated with the adsorption of dyes by GO, subject to the presence of dissolved salts. Nuengmatcha *et al.* [236] demonstrated that the adsorption of cationic malachite green by GO was adversely impacted by the presence of sodium chloride, with q_e values decreasing from around 340 mg/g to 300 mg/g when salt concentration was 0.10 M. Similarly, Travlou *et al.* [217] found that the adsorption of anionic Reactive Black 5 dye onto GO is hindered by sodium chloride addition, with addition of 0.10 M decreasing the q_e values from around 190 to 110 mg/g. Other sources have, however, reported that the addition of cationic species has minimal or no impact upon the adsorption of dyes. Zhang *et al.* [203], for example, reported that addition of monovalent potassium chloride, up to 0.05 M in MB, did not have any significant impact upon the q_e values. Remarkably, the work of Sharma *et al.* [237] reveals that loading MB with salt actually *improves* the MB adsorption capacity of the GO adsorbent. They report that the addition of salt, which introduces anions as well as cations, has the impact of increasing the dispersibility of the GO, contributing to the electrostatic repulsion of the GO in aqueous media. Furthermore, the impact of anion valency also has a positive relationship with MB adsorption: with sulphate (SO_4^{2-}) ions resulting in greater adsorption capacities than chloride (Cl^-) ions, owing to the greater polarisability of the more highly charged anions.

By considering the impact of ions on dye adsorption, this section has introduced a key question in the application of GO adsorbents; that is, how might the performance be hindered in real effluent conditions. Introduction of ions into the dye brings an

element of non-ideality to the system, and the literature has shown that this adversely impacts adsorption. This is a key indicator with regards to industrial application in which the effluent composition, as shown, is highly non-ideal.

2.2.6 Performance of alternative industrial adsorbents in dye adsorption

In this section, the performance of alternative industrial adsorbents will be considered, so as to compare with the performance of GO systems.

Activated carbon is typically a powdered adsorbent, with high carbon content and microporous structure [238]. The process known as *activation* involves introducing porous features into the carbonaceous surface by processing [239]. Like GO, activated carbon has negative surface charge and high specific surface area [240]. Activated carbon has been utilised in adsorption of dyes including MB. In the research of Sharma and Uma [241], an activated carbon synthesised from rice husk adsorbed MB with overall $q_{max} = 14.3$ mg·g^{-1}. Benhachem *et al.* [242] performed kinetics and equilibrium studies, determining that the Langmuir $q_{max} = 38.3$ mg·g^{-1} and PSO $q_e = 43.9$ mg·g^{-1}. Studies have reported on the functionalisation of activated carbon with gold nanoparticles, in order to modify the surface charge and promote adsorption of MO. Ghaedi *et al.* [243] report one such fabrication, achieving by PSO kinetics $q_e = 151.5$ mg·g^{-1}.

Zeolites, highlighted in the previous chapter, are an alternative adsorbent material for dyes. Akgul *et al.* [244] reported on the performance of an alkaline-modified clinoptilolite material, which adsorbed MB with overall PSO $q_e = 47.3$ mg·g^{-1}. Adsorption of anionic dyes using zeolites has also been studied; for example, Alver and Metin [245] modified a silicon-dioxide dominated zeolite with hexamethylenediamine, adsorbing anionic Reactive Blue 250 dye with $q_{max} = 58.5$ mg·g^{-1} by Langmuir model.

This section has highlighted the performance of GO competitor adsorbent materials including activated carbon and zeolites. Adsorption of dyes by a number of these

adsorbents has been shown to follow PSO kinetics and Langmuir adsorption isotherms, much like the previously discussed studies on GO. The performance of the competitor systems does, however, appear significantly lower than GO, likely a feature of the remarkably high surface area and relatively small flakes of GO. Perhaps an advantage of competitors over GO, however, is lower cost [246], also the possibility of natural-based synthetic pathways, using for example rice husks [247] and lignin [248].

2.3 Methods for fabrication of GO membranes: an introduction

2.3.1 Vacuum deposition

Vacuum deposition is an extremely popular method of preparing GO-coated membranes, in which a GO suspension is continuously filtered through a porous substrate under applied vacuum conditions [174, 249]. Given their lateral sizes are larger than the substrate pores, the layers of GO flakes accumulate and stack atop one another on the membrane top surface, resulting in formation of a deposited GO coating layer [250]. The technique is simple to implement, and provided that the concentration of GO is varied, can lead to GO coatings of varying thickness, ranging from single nm [251] to tens of microns [252]. Vacuum deposition is however, currently a small-scale technique, limited to membranes which are only a few cm in size [253]. Another limitation of the technique is the potential for uneven stacking of GO layers [10]. As more GO is deposited, caking of the surface leads to a decrease in vacuum pressure over time, resulting in a coating structure in which the top layers are more loosely packed than those nearer the substrate itself. The layering of GO under vacuum deposition is shown in Figure 2.4, in which *loosely* stacked GO is deposited on more ordered layers of GO.

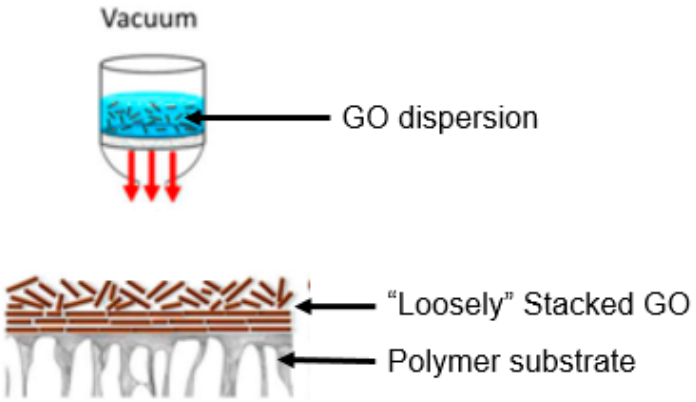

Figure 2.4: Fabrication of GO-coated membrane by vacuum deposition technique. Under the applied vacuum, the GO stacks more densely closer to the substrate and more loosely with increasing distance away from the surface. Adapted from [10].

2.3.2 Layer-by-layer assembly

Layer-by-layer (LbL) assembly of GO membranes involves stacking layers of GO onto a substrate, employing chemical reagents as supporting materials to ensure bonding between GO layers. The bonding materials enhance the coating's internal bonding strength by promoting favourable electrostatic interactions [254] or covalent crosslinking layers of GO [255]. LbL assembly of GO-coated membranes is capable of overcoming some of the previously highlighted limitations of the vacuum deposition technique, in which the GO layers are unsupported and thus the internal bonding is relatively weak [256].

In the case of electrostatic interaction, the support material is typically a polyelectrolyte that possesses opposite electrical charge to the GO [257, 258]. Hu and Mi [259] prepared a GO membrane by LbL approach, using cationic poly(allylamine hydrochloride). The layering was established by immersing a polyacrylontirile membrane in the poly(allylamine hydrochloride) for 30 minutes and subsequently immersing in a prepared GO dispersion. A combined crosslinking-electrostatic interaction approach

was employed by Kandjou *et al.* [260], in which a GO coating was prepared on a glass slide by first soaking the slide in poly(ethylene imine) to initiate the positively charged layer and subsequently immersing in GO. Following rinsing, the slide was soaked in p-phenylenediamine crosslinking agent and again in GO. Alternating cycles of p-phenylenediamine - poly(ethylene imine) soaking were performed to yield the LbL GO membrane, having combined electrostatic - covalent support.

2.3.3 Spin coating

Spin coating involves dropwise addition of GO suspension onto a substrate surface that is rotating rapidly, and subsequently dried by evaporation, resulting in formation of a GO coating that is uniformly deposited [253]. The substrate must, however, be very flat and of a consistent morphology, otherwise the coating integrity and uniformity may be sacrificed.

Spin coated membranes are most popular in separation of gaseous phases, for example hydrogen:carbon dioxide [261]. Several examples have also applied spin coated membranes to separation of liquid phases. Kim *et al.* [262] demonstrated spin coating for sodium chloride rejection, by spinning GO suspension onto a nylon substrate rotating at 1000 revolutions per minute (RPM) for 30 seconds. Abdelkader *et al.* [263] also used spin coating for GO/polyacrylamide membrane with PES support, which was used in desalination. A 47 mm diameter PES membrane was spin coated with 1 ml polyacrylamide at 3000 RPM for 6 minutes prior to undergoing an analogous spinning procedure with 1 ml GO suspension, prior to drying, yielding the final composite membrane.

2.3.4 Bar coating

Bar coating enables coating of substrates to be achieved on a larger scale than is possible using the previously discussed fabrication techniques [253]. Provided that

the concentration of GO in a dispersion is sufficiently high, the viscoelasticity of the material enables a GO laminate to be coated onto substrate if subjected to an imposed shear force [264]. This may be achieved by stroking the surface at constant velocity, using a rigid rod, or doctor blade, resulting in a uniformly deposited GO coating. A schematic depiction of the bar coating process is provided in Figure 2.5, in which a doctor blade is shown traversing the surface of a fixed substrate, layering GO sheets which were formerly in colloidal nematic phase.

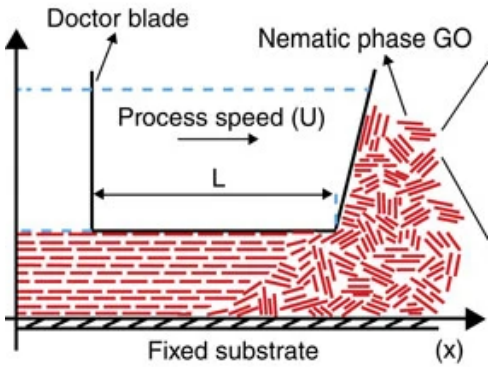

Figure 2.5: Coating of GO onto substrate by bar coating using a rigid rod or doctor blade, resulting in uniformly deposited GO laminates. Adapted from [11].

Akbari *et al.* [11] discuss bar coating of a nylon substrate with dimensions 13 cm X 14 cm. The role of GO coating concentration was investigated using coatings with concentration 0.10 mg/ml - 60 mg/ml, revealing both by visual inspection and electron microscopic imaging that >40 mg/ml was needed for optimised coating uniformity. Interestingly, Wang *et al.* [265] were able to utilise a far lower concentration of GO (<2.5 mg/ml), driven by a doctor blade at 150 mm$\cdot s^{-1}$. By this approach, it was possible to coat very large sheets of poly(ethylene terephthalate), having dimensions 20 cm X 47 cm.

2.4 Filtration of dyes using GO membranes

In Section 2.2, the adsorption of dyes by GO adsorbents was considered in terms of the affinity of GO towards classes of dye, considering mechanisms including electrostatic interactions and π - π interactions. Incorporation of GO into membrane fabrications has proven capability in increasing the performance of a filtration system in removing dyes from a feedstream [266]. In classical membranes, the performance criteria are a high *flux* and high *rejection*: in essence there appears a tradeoff between achievement of both aspects simultaneously [267, 268]. Applications of GO membranes have demonstrated capability in improving the retention of dye species compared to pristine polymer membranes: Kadhim *et al.* [269], for example, showed this in a GO/PES membrane, prepared by drop casting. It was demonstrated that a GO loading of 0.50% resulted in a remarkable ten-fold increase in flux of Acid Black 210 dye, while the corresponding dye rejection increased from 88% to 99%. An inspection of the literature therefore has demonstrated that the incorporation of GO into a membrane offers the advantages of improved flux and rejection, as such, it has become highly popular for membrane-based treatment techniques, particularly within research applications.

2.4.1 Mechanism of dye rejection by GO membranes

The property of GO that enables high permeation rates of water is related to the structure of the material. Its unique chemical structure, comprising distinct sp^2 and sp^3 regions, corresponding to carbon bonding and carbon - oxygen bonding, respectively, enables unique behaviour and interaction with water molecules [270]. The hydrophobic sp^2 regions of GO ensure rapid permeation rates of water, as water transits special hydrophobic nanochannels [271, 272]. The behaviour of water within the unique structure of GO has been considered by Wang *et al.* [12], who propose that the GO structure possesses these hydrophobic channels in the sp^2 regions, meanwhile the sp^3 regions act as hydrophilic *gates*, allowing accumulation and ultimately, passage of water. When

water passes through the hydrophilic gates, it may enter the hydrophobic channels and slide through with high velocity, owing to the very low friction between water and hydrophobic channel caused by drag-reducing effects [273, 274]. A representation of the channeling of water through hydrophilic gates and hydrophobic channels is provided in Figure 2.6.

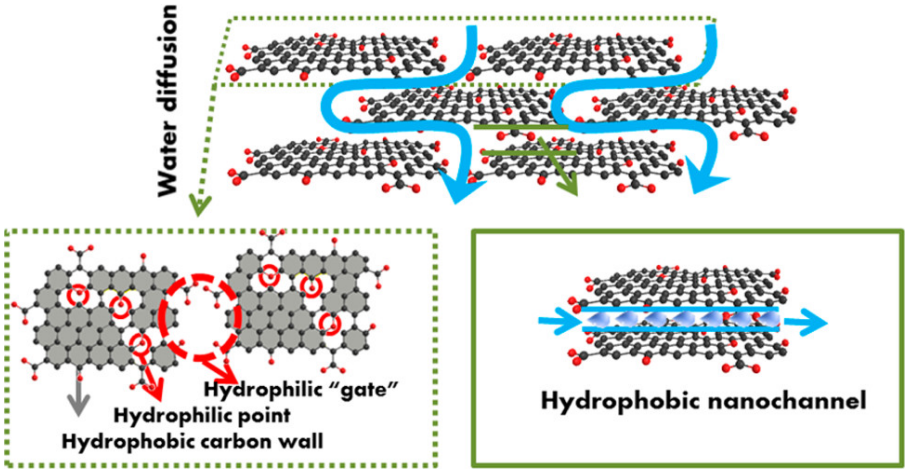

Figure 2.6: Permeation of water through GO. GO is accumulated in the hydrophilic regions, and the high flux of water is generated by the low frictional flow inside hydrophobic nanochannels. Adapted from [12].

The chemistry of GO also enables the material to interact with dyes in a number of unique manners and is an important aspect of the mechanism of dye rejection. The adsorption of cationic and anionic dyes onto GO was considered in Sections 2.2.1 and 2.2.2. A number of important features related to GO - dye interactions were highlighted in these sections, including electrostatic interactions (both attractive and repulsive forces) and π - π stacking.

In filtration of cationic dyes by GO membranes, adsorption is a very prominent feature, as the cationic components can become adsorbed onto the GO surfaces during operation of the filter [275, 276]. In many cases, GO membranes have exhibited very high removal rates for cationic dyes: for example, Jee *et al.* [275] - 92.8% MB, and

Chen *et al.* [277] - 96.29 % MB. In spite of this, there is concern regarding the impact of dye adsorption upon the reusability and longevity of the membrane in operation. An *et al.* [278] discuss that for negatively charged membrane surfaces, contact with cationic species leads to adsorption, and this is an unwanted feature associated with membrane fouling, as the functional groups are dissociated, in time, this leads to flux decline of the membrane. The removal mechanism of cationic dyes by GO membranes was considered by Mahmoudian and Kochameshki [279], who proposed a two stage mechanism. In the first stage, cationic dyes are electrostatically attracted to GO and adsorb onto the surfaces, and in the second stage, they undergo interactions with the membrane geometry in order to remain on the membrane. Khansanami and Esfandiar [280] suggest that van der Waals' forces are principally responsible for the adsorption of cationic dyes onto GO membranes. It seems therefore that electrostatic charge interactions are an important governing characteristic in the adsorption of cationic dyes.

In filtration of anionic dyes, GO membranes exhibit strong electrostatic repulsion to the negative charged dyes, resulting in many cases very high removal rates of dye [179, 281]. Adsorption of anionic dye onto GO is not a prominent feature of anionic dye rejection. Ghaffar *et al.* [282] demonstrated the adsorption capacity of GO/-polyvinylidene fluoride membrane, using four cationic dyes and anionic MO. The q_e value of the membrane was greatest for cationic MB (96.5 mg/g), while for anionic MO, it was very low (1.56 mg/g). As such, it is considered that electrostatic repulsion is the dominant characteristic for rejection of anionic dyes including MO.

Steric effects also play a significant role in the rejection of dyes by GO membranes, these relate the geometry of the dye molecules to the sizes of the membrane pores and interlayer spacing [283]. Additionally, it has been reported that dyes of high molecular weight are removed from water with greater effect compared to smaller molecular weight dyes [284]. Molecular weight is generally related to physical size, as higher molecular

weight typically corresponds to larger size, as such, the contribution to rejection by steric effects is greatest for large molecules [285]. The size or molecular weight of dyes has been shown to have an impact upon the filtration performance of GO membranes. The rejection characteristics of a series of cationic dyes, in the work of Mahmoudian and Kochameshki [279], demonstrated the impact of molecular weight/size on efficacy of removal. For cationic MB (319.85 g/mol) and Crystal Violet (407.99 g/mol), removal of the latter was found to be approximately 5% higher, this was attributed to the combined impacts of increased surface adsorption and steric effects. Similarly, Khadim *et al.* [269] were able to demonstrate comparable behaviour with two anionic dyes, of similar molecular weight: Rose Bengal (973 g/mol) and Acid Black 210 (938 g/mol) were rejected with $> 99\%$ removal rate.

2.4.2 Factors impacting removal of dyes by filtration in GO membrane systems

The separation performance of a membrane system is influenced by a number of factors; these include both intrinsic properties of the membrane itself and also the external properties of the feed. The literature has demonstrated that variation in such external properties including initial dye concentration and filtration pressure and membrane properties including GO content in the membrane provides interesting insight into the behaviour of the membrane system. In this section, the impact of these parameters is considered with attention to the literature.

Increasing the transmembrane pressure (differential in pressure between each side of the membrane) generally correlates to an increase in permeate flux through the membrane. This relationship is however not simple to predict and models have predicted the existence of a critical flux, beyond which flux does not proportionally increase with an increase in transmembranme pressure [286, 287, 288]. Increasing or decreasing the pressure in dye filtration will have an impact upon the flux and rejection characteristics of a GO membrane. In polymeric membranes, the increase in flux with transmembrane

pressure is linear to a point, beyond which the profile flattens [289]. The relationship between flux and pressure in a GO membrane system was explored by Medina *et al.* [290], who fabricated a GO-coated membrane using vacuum deposition technique. Increasing the filtration pressure from 137.8 to 413.4 kPa resulted in an increase in flux from approximately 0.10 to 0.60 $l \cdot m^{-2} \cdot h^{-1}$. The effect of increasing the pressure on dye removal does not appear to have been considered, however. The impact of filtration pressure on the performance of a GO-embedded membrane was investigated by Abdelhamid *et al.* [13], who compared the results of filtration of anionic Congo Red with cationic MB. When the pressure was increased from 3 - 7 bar, the flux increased from approximately 4 to 10 $l \cdot m^{-2} \cdot h^{-1}$ for both dyes, meanwhile the rejection declined in both cases, though the decline was more marked for MB. It was discussed that the increase in pressure is responsible for overcoming the membrane resistance, such that at 7 bar, the resistance is at its lowest, resulting in high flux and low rejection. The corresponding flux and rejection profiles from the study are provided in Figure 2.7. The relationships between flux and pressure are assumed linear for MB, while curvilinear for Congo Red.

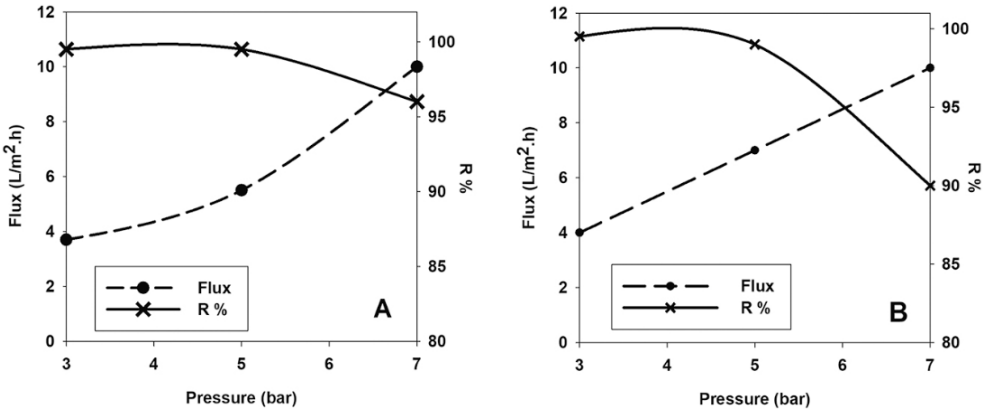

Figure 2.7: Impact of filtration pressure on the performance of GO-embedded polysulfone membrane, in filtration of (A) Congo red or (B) MB dyes. Adapted from [13].

Initial concentration of dye in feedstream impacts membrane performance: this

has been evaluated in NF membrane systems [291]. In general, increasing the initial dye concentration increases the ionic concentration of species in the feed. This has the overall effect of decreasing the permeate flux, as the osmotic pressure in the feed side is increased, resulting in slowing of the water transition across the membrane [292, 293, 294]. Shao *et al.* [295] considered that the effects of increasing dye concentration on filtration performance, including reduced permeation and dye rejection, are accounted for owing to two main reasons. Firstly, increasing concentration results in increased concentration polarisation of dye in the vicinity of the membrane surface, resulting in formation and deposition of a cake layer of dye. Secondly, an increased mass of dye molecules become adsorbed onto the surface due to the higher initial content of dye in the feed. The impact of increasing dye concentration on the filtration performance of GO membranes has also been considered. Homem *et al.* [296] varied the concentration of dye from 10 to 40 mg/l in their GO/PES membrane system, prepared by vacuum filtration methods. It was reported that the increase in concentration resulted in a decrease in both permeate flux (17.2 to 11.4 $l \cdot m^{-2} \cdot h^{-1}$) and dye rejection (96.1% to 91.4%) capabilities of the membrane, tested in dead end configuration at pH 10. Xing *et al.* [297] likewise report that increasing Congo Red concentration from 0 - 1000 mg/l in their vacuum-prepared GO/polyacrylonitrile membrane has effect of significantly decreasing permeate flux, from around 4000 to 500 $l \cdot m^{-2} \cdot h^{-1}$, meanwhile the impact upon rejection is less significant, with decline only around 5%. Other studies have demonstrated only very moderate sensitivity to the effects of increasing dye concentration. One such example is the work of Chen *et al.* [298], whose LbL GO intercalated with titanium dioxide nanoparticles achieving rejections of MB (92.64%) and MO (99.57%) when concentration was 100 mg/l and very similar MB (92.05%) and MO (99.37%) when concentration was 10 mg/l. As such, the dye concentration has been demonstrated to impact membrane performance, however, the mechanism of dye-membrane interaction in relation to the particular dyes and membranes is also

important.

The loading of, or concentration of GO in a membrane is also an important factor in determining the performance. Zhong *et al.* [299] demonstrated that increasing the concentration of GO from 10 - 200 μg/ml, in their GO/cellulose vacuum deposition membrane had the effect of significantly decreasing the flux of MB from >30 to <10 $l \cdot m^{-2} \cdot h^{-1}$. The rejection profile also showed an overall increase with increasing concentration, but the relationship flattened for GO concentrations beyond 25 μg/ml. It has been considered that the increase in concentration results in a thicker coating layer of GO, thus increasing the resistance to mass transfer of species across the membrane and likewise the tortuosity and longer the path length for transport of water molecules [300]. Several studies considered in this literature review have demonstrated that the relationship between GO content and dye removal increases to a maximal value, before following a decline subject to further increase in GO content. Abdelhamid *et al.* [13] show that increasing GO content from 0 - 2 wt% in their phase inversion membrane increases flux of MB due to the hydrophilicity of the GO, but as loading is increased from 2 - 4 wt%, the flux declines due to blockages of membrane pores by GO. Similarly, the membrane of Khadhim *et al.* [269], that was prepared by casting, demonstrates an increase in permeate flux and rejection when GO content is increased from 0 - 0.50 wt%, before declining when GO concentration is increased beyond this level. It was discussed that the increase of GO content results in an increasingly viscous casting solution, thus resulting in poorer filtration performance. The increase of GO content therefore correlates to improvements in membrane properties; if, however, the content is increased too greatly, then the interactions of GO with membrane surface act as a hindrance to the performance.

2.4.3 Comparative filtration of anionic and cationic dyes using GO membranes

The impact of dye electrical charge, in relation to the interaction of dye with membrane, was considered in Section 2.4.1 to play an important role in the overall mechanism. Comparative studies open the pathway to analysis in which it is possible to explore the impacts of charge on filtration performance. A number of these select studies are considered here, to explore the comparative elements of filtration performance in existing literature.

The impact of electrical charge has been studied by a number of authors. Thebo *et al.* [301] report that their vacuum filtration-prepared GO membranes exhibit high rejection capabilities towards two cationic (MB and RhB) dyes and two anionic dyes (Evans Blue and Methyl Blue), with the more significant difference in performance being related to flux. It was found that the anionic dyes were filtered with much lower fluxes (12 and 14 $l \cdot m^{-2} \cdot h^{-1}$, for Methyl Blue and Evans Blue, respectively), compared to cationic dyes (21 and 25 $l \cdot m^{-2} \cdot h^{-1}$, for RhB and MB, respectively). Huang *et al.* [302] prepared a RGO membrane using vacuum filtration technique. This membrane was excellent in rejection of anionic Brilliant Yellow (99.2%) and Evans Blue (100%) dyes, but extremely poor in rejection of cationic MB (12.6%). It was discussed that this was related to the adsorption of cationic dyes on the surface, relative to the repulsion of anionic dyes from the electronegative membrane.

Comparative filtration performance between multiple cationic and anionic dyes has also been used as a means to elucidate the overall mechanism of separation. Chen *et al.* [281] achieved 99.9% and 96.3% rejections of MO and MB, respectively, citing electrostatic repulsion as the predominant reason for the higher overall rejection. Further adsorption studies (the type of which were discussed in Section 2.2) were used to demonstrate that the membrane had adsorption capacity 250 mg/g for MB and only 38 mg/g for MO, thus proving that the adsorption of MO was less significant in the

overall filtration mechanism compared to that of MB. Mahmoudian and Kochameshki [279] likewise achieved higher rejection overall for anionic dyes, citing electrostatic repulsion as being the dominating factor. They gained insight into the mechanism by measuring zeta potential of the membrane coating before filtration (-17 mV) and after, with a series of dyes, including cationic MB (-10 mV) and anionic MO (-18 mV). This suggests that increased levels of adsorption of dye onto the GO during filtration of the cationic dye has the effect of neutralising the negativity of charge, thus being reflective of the poorer performance of the membrane in cationic dye removal.

2.4.4 Performance of alternative membrane materials in removal of dyes

This section presents the removal of dye molecules using competitor membrane materials, alternative to GO-based ones. As discussed in the previous chapter, polymeric membranes are one option, using macro-molecular polysulfones, polypropylene, polytetrafluorethylene and polyethylene materials, among others [303]. As discussed, in industrial operation, these membranes are limited due to their proclivity to foul due to excessive caking of the filter [304]. Efforts to improve the performance and longevity of polymer membranes include modification of the surface using polymeric materials. Chitosan is an example of a natural polymer that is capable of modifying the surface and improving anti-fouling characteristics and mechanical strength [305].

A number of polymer-modified membranes have achieved high performance in removal of dyes. Fradj *et al.* [306] synthesised a chitosan-modified cellulose membrane, that was able to remove approximately 89% of 15 mg/l MO at flux rate 38 $l \cdot m^{-2} \cdot h^{-1}$ at 4 bar. Another example of a biopolymer-based membrane is the chitosan/alginate composite membrane of Mokhena and Luyt [307], showing promising rejection in excess of 95% of anionic congo red. The nitrogen-doped multilayer molybdenum carbide and molybdenum oxide nanosheet membrane of Iqbal *et al.* [308] interestingly operates under zero applied filtration pressure; accordingly, it is termed a gravity-filtration system.

This membrane did achieve promising flux (53.4 $l \cdot m^{-2} \cdot h^{-1}$) and rejection (84.8%) of 100 mg/l MB dye. It is however uncertain whether such a membrane would be useful for industrial application, as performance under pressure is an important factor in membrane design.

This section has demonstrated that alternative materials can be utilised to fabricate membrane structures with promising performance in dye removal. These membranes may also offer advantages including biodegradability and biocompatibility [309]. Possible disadvantages of these systems however include limited industrial relevance; that is, improbability of achieving scalability on an industrial scale.

2.5 Desalination using GO membranes

The utility of membranes in desalination was introduced in Section 1.1.3, in which it was discussed that osmosis-driven filtration is currently the dominant means of separating ions from water. In order to provide sufficient driving force to overcome the effects of osmotic pressure in reverse osmosis (RO) systems, the filtration pressure must be very high: typically of the order 80 bar for seawater desalination [310]. The unique interactions of GO with water molecules, including nanochanneling of water through the hydrophobic sp^2 basal plane regions, is an attractive feature that has seen the rise of GO membranes in desalination [311]. The expectation is that the water-channeling feature of GO will have the capability to reduce the associated energy cost of membrane-based operations [96, 147].

2.5.1 Mechanism of salt separation using GO membranes

The behaviour of ions in the vicinity of a membrane surface are related to the electrical properties of the surface itself. Accordingly, electrostatic interactions of species with GO coating have been considered a salient feature of the overall mechanism of desalination. The governing principal of electrostatic interactions are considered in

terms of the *Gibbs-Donnan Effect* [312, 313], often shortened to the *Donnan Effect*. This model is an electrochemical principle, driven by discrepancies in charge that occur when ions present in solution do not distribute evenly across the membrane feed and permeate sides. When salts dissolve in solvent, the cations and anions disassociate, as such they are free to act as independent, charged electrolytes [314]. With respect to GO membranes, anionic species are termed *co-ions*, as they share the negative charge characteristic of the GO, meanwhile cationic species, with opposite charge, are termed *counter-ions*. Due to effects of electrostatic repulsion effects, the GO surface repels co-ions, thus maintaining their presence in the feed side [315]. If co-ions are retained, then by conservation of electrical charge neutrality on the feed side, counter-ions must be simultaneously retained, to satisfy the requirement that charge is conserved [316]. This implies that for any given salt, the greater number of cations per anion leads to higher rejections of the ions; as for every permeating anion, more cations must transit the membrane, to maintain charge neutrality.

In order to highlight its importance in GO membrane systems, a number of studies have suggested that the Donnan Effect is the predominant mechanism of separation [317, 318]. An illustrated example is the work of Liu *et al.* [319], who prepared a GO membrane by vacuum filtration and tested using dead end filtration with a series of sodium salts: sodium chloride, sulphate, and phosphate. The ordering of salt rejections decreased according to that expected by Gibbs-Donnan (phosphate (PO_4^{3-}), sulphate (SO_4^{2-}), chloride (Cl^-)), leading to the conclusion that this was the dominant mechanism.

2.5.2 Current challenges in GO membrane-based desalination

The hydrophilic character of GO is a feature of its oxygenated regions, dominated by the epoxy, alcohol and carboxylic regions on the edges of the planes [320]. These regions enable the interaction of GO with water, as discussed in Section 2.4.1, facilitating rapid

permeation of water through stacked layers of GO. The negative charge characteristic of GO layers culminates in electrostatic repulsion between layers [174]. Electrostatic repulsion is the cause of intra-layer repulsion in a stacked layer, while the forces holding the stack together are mainly weak van der Waals' attractive forces and hydrogen bonds [321]. In dry state, the combination of electrostatic repulsion and van der Waals' forces results in typical interlayer spacings of the order 0.80 nm ± 0.10 nm [155, 321]. The hydrophilic nature of GO enables the material to uptake water when the membrane is in hydrated state, resulting in a phenomenon known as *swelling*, in which the uptake of water results in expansion of the interlayer distancing [155, 322]. Interlayer spacings of GO layers in hydrated state of up to 1.3 nm have been reported [323]. A schematic representation of swelling in hydrated state, increasing the interlayer spacing of a dry state GO stack, is shown in Figure 2.8.

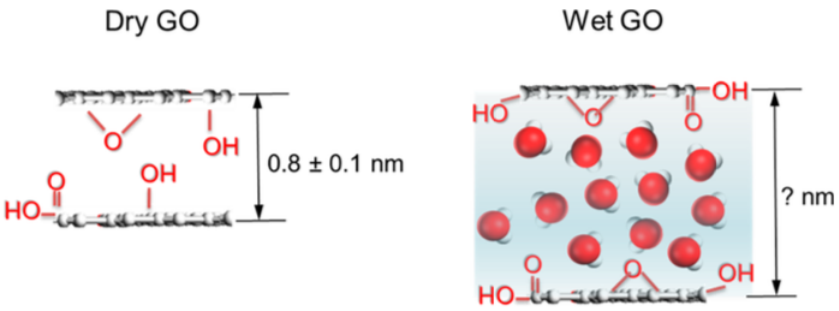

Figure 2.8: Swelling of a GO layer, having initial interlayer spacing 0.80 nm in dry state to an undefined but greater distance in hydrated state. Adapted from [14].

Ionic species are very small, the hydrated diameters of some common ions are as follows: Na^+ - 0.72 nm, Mg^{2+} - 0.86 nm, Cl^- - 0.66 nm, SO_4^{2-} - 0.76 nm [324]. As such, if GO layers are swollen to interlayer spacings exceeding 1 nm, then the ionic species may permeate the gaps with relative ease, as such, size exclusion is no longer a prominent feature of the rejection mechanism. In addition, the layers of GO may regress from an ordered laminate in dry state, to a state of relative disorder when hydrated

[325]. As such, the swelling of GO membranes has a severely degrading impact upon the long-term desalting capability, with studies reporting that in free-standing structures, the rejection inevitably tends towards zero throughout extended periods of operation [14, 326, 327]. It appears that the swelling behaviour of hydrated GO threatens the stability of the membranes and poses a serious challenge to the long-term operational utility of the membranes [328].

Efforts have been made to overcome the adverse impacts of swelling, which typically aim to improve the aqueous stability of the membrane by controlling the interlayer spacings. The work of Abraham *et al.* [329] discusses the use of cations to physically restrict the movement of a GO coating prepared by vacuum filtration. Incorporating the cations resulted in tighter spacings relative to the uncontrolled GO (0.64 nm compared to 0.98 nm). The modified membrane was able to achieve mean rejection of sodium chloride 97%, at low permeate flux ($0.50\ l \cdot m^{-2} \cdot h^{-1}$). Owing to the tunability of GO, it has in fact been possible to modify the structure in attempt to produce composite materials with reduced interlayer spacings relative to unconfined GO. Among the possibilities are nanoparticles, such as zeolites [330], chemical crosslinkers such as dopamine [323] and dicarboxylic acids [331].

2.5.3 Factors affecting desalination in GO membranes

In this section, the impact of a number of parameters on desalination by GO membranes is considered, these include: pressure, initial salt concentration and GO content in the membrane.

Polymer membranes are highly elastic and undergo microstructural compression when exposed to high levels of external pressure [332, 333]. The relationship between applied pressure and flux through a GO membrane on a microstructural level is, however, not always simple to comprehend. A study by Chong *et al.* [15] examined the behaviour of a GO membrane subject to an applied external pressure. Interestingly, it

was observed that in GO coatings prepared by uncontrolled stacking techniques, layers of GO tended to compact and densify subject to an increase in filtration pressure from 1 - 10 bar. The microstructure became more ordered and the pressure-scaled flux of pure water decreased with an increase in filtration pressure. It was deduced that this observation was due to a decrease interlayer spacing and compression of the cavities in GO laminae, resulting from the increase in pressure. A schematic representation of the compaction phenomenon is shown in Figure 2.9.

Figure 2.9: Conversion of a GO membrane from an originally non-ordered state to an ordered state due to the compressing effects of applied pressure. Adapted from [15].

Computational analysis of salt movement in GO membranes has demonstrated that increasing filtration pressure promotes passage of ions by increasing their energy, enabling a greater number of ions to reach the minimum required energy barrier for permeation across a membrane. This results in lower salt rejection subject to increasing pressure [334, 335]. At higher filtration pressure, the interlayer channels that facilitate the rapid permeation rate of water may collapse, resulting in an increase in the difficulty of ions and water to permeate the stacked layers [336]. The compaction process does, however, lead to increased electrostatic repulsion between layers of GO that are brought closer, owing to the densification process [337]. As such, the literature has suggested that increasing pressure both densifies the coating, while resulting in an enhancement of the repulsive forces. The effect of filtration pressure on desalting ability of a GO membrane is highly interesting, as reflected in a number of experimental studies that show an increase in salt rejection subject to increasing filtration pressure, thus contesting the aforementioned computational studies highlighted earlier. Wei *et al.*

[16] investigated the attenuation of flux in a vacuum-prepared GO membrane system, revealing that in water, membrane compaction resulted in a greater degree of attenuation, as at 0.25 MPa, the flux declined by 36% over 5 hours filtration, meanwhile at higher pressure 1.0 MPa the flux declined by 75%. The impact on salt rejection by this membrane was also marked: at 0.25 MPa, sodium sulphate (2000 mg/l) rejection was <22%, meanwhile at 1.0 MPa, rejection was 85.8%. Similarly, Li *et al.* [338] demonstrated that increasing pressure from 2 - 6 MPa decreased the pressure-scaled flux, while had the effect of enhancing the salt rejection of potassium chloride, sodium chloride and calcium chloride. A schematic representation of the effects of membrane compaction resulting in an increase in salt rejection is provided in Figure 2.10.

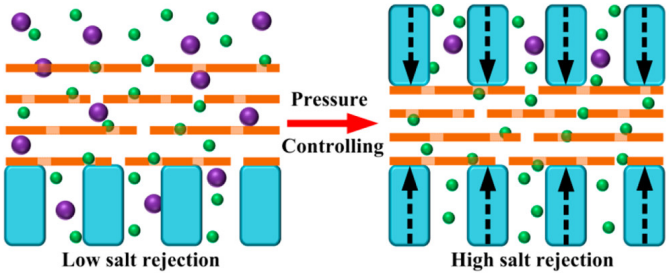

Figure 2.10: Compression of GO coatings layers subject to high pressure, resulting in high salt rejection capabilities of the membrane under increased pressure. Adapted from [16].

The impact of salt concentration has been shown to have a detrimental effect on desalination capabilities of GO membranes. Huang *et al.* [337] determined that increasing the initial feed concentration of sodium chloride from 0 - 100 mmol/l had the impact of reducing the permeability of salt through a GO membrane, due to increased screening of the electrical double layers resulting in tightening of the pores. Similar behaviour was observed by Li *et al.* [339], who reported a drop in sodium chloride rejection from approximately 100% to around 95%, when the initial concentration of salt was increased from 10 - 30 mM. Another interesting recent result was reported

by Wang *et al.* [340], who studied vacuum filtered GO membranes, in desalination of sodium chloride and sodium sulphate feeds at 1000 and 2000 mg/l. It was found that the higher concentration of both salts led to a lower overall permeate flux through the membrane, but the salt rejection behaviour was less typical. Increasing sodium chloride concentration led to decline in rejection, as expected, but for sodium sulphate, it led to an increase in rejection. A detailed mechanism or discussion has not been provided in the article, and similar trends do not appear to have been reported elsewhere. A number of experimental studies have explored the impact of initial salt concentration using dead end filtration as the mode of testing [255, 317, 341]. In these studies, the effects of concentration polarisation are increased in the vicinity of the membrane surface, and the impact on filtration performance is enhanced when the salt concentration is increased. Morelos-Gomez *et al.* [342] demonstrated that utilising cross flow filtration for high salinity feeds is an effective means of overcoming the high concentration polarisation phenomenon in dead end cell systems, as the shearing action mitigates this. As such, the employment of cross flow systems may be utilised for optimisation of desalination experiments.

The impact of GO concentration or loading in membrane fabrications has also been investigated. Li *et al.* [343] studied the effects of GO loading by preparing a series of GO membranes with loadings in the range 0.0025 - 0.0200 wt%, using an immersing technique in which the GO was deposited onto a polyethersulfone base. Desalination experiments were performed with 1.0 M sodium chloride. The results showed an interesting trend, in that an increase in flux was exhibited for increasing GO loading from 0.0025 - 0.0100 wt%, by up to 57%. It was suggested that the increase in hydrophilicity brought by the usage of higher concentration of GO promoted the high flux of water. Further increasing the loading from 0.01 - 0.02 wt% had the effect of reducing the water flux, however, as this increase in GO concentration led to thicker layers of GO on substrate (169.6 - 228.2 nm). Liang *et al.* [344] also studied the

impact of GO coating concentration on permeate flux of salt solution through their GO/polyacrylonitrile membrane, in the range 1.8 - 115.9 $\mu g/cm^2$. It was determined that the lowest GO concentration gave the highest corresponding permeate flux, but in analogy to Li *et al.*, suggested that there was a limiting range of effectiveness, as for GO concentrations up to 5 $\mu g/cm^2$, the drop in flux was more minimal, but more substantial for loadings beyond this. The membrane did, however, exhibit high levels of salt rejection, maintaining >97% across the range. It was concluded that increasing GO loading led to an increased resistance to mass transfer, that inhibited the passage of water, but maintained a stable microstructure to promote rejection at higher concentrations. Qian *et al.* [345] likewise achieved interesting behaviour with loading of GO in a mixed casting membrane comprising GO with chitosan, noting that increasing loading from 0 - 1.0 wt% increased the hydrophilicity and corresponding flux of 10% sodium chloride from 10.5 to 16 $l \cdot m^{-2} \cdot h^{-1}$. Increasing the GO content beyond 1.0 wt% decreased the flux to around 12.5 $l \cdot m^{-2} \cdot h^{-1}$, due to the overlap of GO and chitosan polymeric chains, an effect which hindered the motion of water through the membrane.

2.5.4 Performance of alternative membrane materials in desalination

This section discusses the desalination of saline feeds using alternative membranes.

As highlighted in the previous chapter, polyamides are the dominant polymer for commercial RO membrane fabrication. Thin film composite membranes are typically fabricated by interfacial polymerisation reactions. A polysulfone membrane is typically soaked in a diamine solution, before it is dried and reacted with an acyl chloride [346, 347]. The performance of these membranes has now far surpassed the cellulose-based membranes introduced in the 1950's [348]. One such example of a polyamide is the fabrication of Zhan *et al.* [349], who recorded a permeate flux of 79.2 $l \cdot m^{-2} \cdot h^{-1}$ and 97% rejection of sodium sulphate at 5 bar. The difficulty associated with the interfa-

cial polymerisation process lies in the rapid but uncontrolled reaction at the polymeric interface, resulting in structures with unpredictable morphologies and transport properties [350]. Wen *et al.* [351] attempted to control the reaction by modifying with a metal oxide framework. This membrane achieved relatively low permeate flux with metal oxide loading of 0.20 wt% (4 $l \cdot m^{-2} \cdot h^{-1}$), but a very high rejection (99.1%) of 1.0 g/l sodium chloride solution.

Metal oxide frameworks are another emerging class of material that are being targeted with respect to desalination. It has been suggested that this class of membranes may offer improved resistance to fouling during operation compared to polymeric membrane alternatives [352]. Khadom *et al.* [353] fabricated a metal oxide framework membrane supported on polysulfone; this membrane achieved flux 79.4 $l \cdot m^{-2} \cdot h^{-1}$) and 2.0 g/l sodium chloride rejection approximately 99%. Xu *et al.* [354] fabricated a thin film composite membrane modified with chromium-based MIL-101 nanoparticles. When MIL-101 wt% was 0.10%, the flux was around 48 $l \cdot m^{-2} \cdot h^{-1}$ and rejection 93% at 16 bars pressure.

Carbon nanotube membranes are a further class of exciting developmental membrane for desalination. Owing to the tubular carbon design, they may achieve frictionless passage of water (therefore high permeability) [355]. The carbon nanotube modified polyamide membrane of Chan *et al.* [356] filtered 1.0 g/l sodium chloride solution at 28.5 $l \cdot m^{-2} \cdot h^{-1}$ with rejection 98.6% when the nanotube loading was 20 wt%. Both flux and rejection were greater than the unmodified polyamide membrane, which achieved flux 6.8 $l \cdot m^{-2} \cdot h^{-1}$ and rejection 97.6%.

This section has demonstrated the efficacy of alternative membrane materials in desalination applications. As the dominant class of membrane material for desalination, polyamide thin film composites are highly effective in separation of ions from water. Embedding of novel materials including metal oxide frameworks and carbon nanotubes has been demonstrated to be effective in improving the longevity and fouling resistance

of this class of membranes.

2.6 Summary

In this literature review, the utility of GO within water treatment was explored, by considering the removal of dyes by adsorption and filtration.

The adsorption of dyes by GO adsorbents was first considered. Adsorption of cationic dyes is a significant field, with many studies reporting high adsorption capacities, owing to favourable electrostatic and π - π interactions. Adsorption of anionic dyes is comparatively less well-reported, with the overall interactions of adsorbent and dye typically less favourable than cationic dyes, due to electrostatic repulsion. Kinetics and equilibria of adsorption were also reviewed and a number of salient models were identified for each, including the pseudo first and second order systems (PFO and PSO, respectively) for kinetics, and Langmuir and Freundlich isotherms for equilibria. The impact of ionic species upon adsorption of dyes was also considered, highlighting the effect that cationic presence may have upon the electrokinetic properties of the GO, thus potentially limiting the efficacy of adsorption. The reduction in GO adsorption performance is correlated to increasing cationic valency.

Techniques for preparation of GO membranes were reviewed, including vacuum deposition, layer-by-layer assembly, spin coating and bar coating. Among these, for small scale membrane productions, vacuum deposition was indicated to be a simple yet effective method to produce coatings of fairly uniform consistency, with potentially scalable coating thickness.

Removal of dyes by GO-coated membranes was introduced by considering the mechanism of interaction between GO and dye within a GO membrane system. In analogy to the adsorption of dyes, electrostatic effects were considered important for removal of anionic and cationic dyes, separately. In addition, steric effects, due to the relatively

large sizes of the dyes were considered an important contributor. The impacts of a number of experimental factors were then evaluated, including filtration pressure, GO loading in membrane and dye concentration. Furthermore, a select number of studies were introduced that focus upon the comparative removal of anionic and cationic dyes, as these provide insight into the removal mechanism by exploring the differences in charge.

Desalination of saline feeds by GO-coated membranes was introduced by considering the significance of electrostatic charge by the Gibbs-Donnan Effect. Existing challenges in desalination using GO-coated membranes were also discussed; these include swelling of the layers due to intercalation of water molecules within the hydrophilic regions of the GO. This effect was highlighted as particularly prominent in membrane systems in which the GO layers are unrestricted. In analogy to the removal of dyes by filtration, the impacts of a number of factors on desalting performance were considered, including filtration pressure and GO content in membrane.

It is clear that GO materials have widespread and well-established utility in water treatment, within research applications. The breadth of research in the field is already highly significant, with a multitude of studies providing templates regarding chemical or analytical characterisation, dye adsorption and removal of contaminants by filtration. It is considered that at present, despite such a substantial knowledge basis from research, the commercialisation of GO within membrane treatment systems, is however, not apparent, within published literature, or within widespread searches. Such a system may be considered an essential next step in developing the technologies as the market continues to expand and mature. As an essential feature of this, a comparative study that highlights the utility of commercial GO sources within water treatment applications would provide a salient stepping-stone from which the commercialisation of the technologies may be achieved. At present, this appears to be an omission in terms of achieving the next phase of the development of the technologies and is thus the focal

point of this research.

Chapter 3

Analytical methods and techniques for characterisation of GO materials and membranes

3.1 Overview

The purpose of this section is to introduce the analytical tools and methods pivotal to characterisation of GO materials and membranes. Within this chapter, background information is provided regarding the analytical techniques and their operation; in addition specific experimental methods utilised in characterisation of GO materials or membranes are discussed. In essence, this chapter provides the basis of Chapter 4, which focuses on the results of characterising GO materials and GO-coated membranes, using the analytical characterisation techniques presented in this chapter. The techniques included are as follows: Fourier Transform Infrared spectroscopy (FTIR), Raman spectroscopy, X-ray photoelectron spectroscopy (XPS), Brunauer-Emmett-Teller (BET), Dynamic Light Scattering (DLS), Laser Diffraction (LD), X-ray Diffraction (XRD), zeta potential, Scanning Electron Microscopy (SEM), Focused Ion Beam Scanning Electron Microscopy (FIBSEM), Thermogravimetric Analysis (TGA), Water Contact Angle.

A summary of the analytical techniques utilised in characterisation of the GO materials and GO-coated PES membranes is provided in Table 3.1. This indicates whether

the technique is used for characterisation of GO or GO-coated membranes, provides an overview of the expected information to be obtained from the analysis, and signposts the relevant section of this chapter in which a description of the technique and experimental methods may be found.

Table 3.1: Analytical techniques utilised in characterisation of GO materials and GO-coated PES membranes.

Technique	GO/GO membrane	Section	Expected information
FTIR	GO	3.4	Chemical bonding
Raman spectroscopy	GO	3.5	Defect ratio
XPS	GO	3.6	Chemical Bonding; Elemental analysis
BET	GO	3.7	Specific Surface Area; Total Pore Volume
DLS	GO	3.8	Particle/flake sizing
LD	GO	3.8	Particle/flake sizing
XRD	GO	3.11	Crystalline nature; Interlayer spacing
Zeta potential	GO	3.9	Electrokinetic stability
SEM	GO	3.12	Imaging dried dispersions
FTIR	GO Membrane	3.4	Chemical bonding; Differences pre-/post-coating
FIBSEM	GO Membrane	3.13	Morphological/cross-sectional imaging; GO layer thickness
TGA	GO Membrane	3.10	Thermal stability
XRD	GO Membrane	3.11	Interlayer spacing pre-/post-hydration
Water Contact Angle	GO Membrane	3.14	Hydrophilicity/-phobicity

3.2 Materials

Commercial GO's were obtained from suppliers at 1.0 wt% in aqueous dispersion. Due to commercially sensitive matters, the supplying companies for these GO products are not disclosed. PES filters (pore size 0.20 μm, diameter 47 mm) were obtained from (Sterlitech Corporation (USA)). Aqueous dyes Methyl Orange (0.10 wt%) and Methylene Blue (0.50 wt%) dyes, and sodium chloride, sodium sulphate, magnesium sulphate and ammonium heptamolybdate salts were obtained from (Merck (Germany)). All chemical reagents and solvents were used without further purification or modification.

3.3 Preparation of GO-coated PES membranes

GO-coated PES membranes were prepared via vacuum deposition technique. A labelled picture of the vacuum deposition experimental setup is shown in Figure 3.1.

Figure 3.1: Labelled vacuum deposition experimental setup, showing the vacuum pump connected to a vacuum flask via tubing. GO dispersion is pipetted onto a secured PES membrane, and the liquid phase is pulled through the membrane pores, meanwhile a GO coating remains on the polymer surface.

The GO dispersions were diluted in distilled water down to concentrations 0.01 mg/ml and 0.10 mg/ml and subsequently sonicated in an ultrasound bath for 10 minutes. A clean, dry PES membrane was carefully rinsed in distilled water, mounted on top of a vacuum flask, and sealed in position by clamping inside a containing vessel. Coated membranes were prepared by transferring 7.6 ml of GO at concentration 0.01 mg/ml or 0.10 mg/ml using a pipette onto the top surface of the PES substrate. The vacuum pump was switched on and through the suction action of the vacuum, a GO-coating was deposited on the membrane surface. The water was deposited into the vacuum flask. From switching the vacuum pump on, the process typically required

approximately 15 minutes to fully deposit the GO. Following vacuum deposition, the coated but wet membrane was removed very carefully from the top of the flask using tweezers and dried overnight in a covered petri dish, at room temperature.

In Section 4.3.1, flake sizes of the two GO materials, using DLS and LD particle sizing techniques, will be presented. This analysis will reveal that one GO is of nominally smaller flake size compared to the other; as such, the former will henceforth be referred to as smaller flake GO (SFGO), while the latter will be larger flake GO (LFGO).

A sample of the four GO-coated PES membranes, corresponding to SFGO and LFGO at each respective coating concentration, are shown in Figure 3.2.

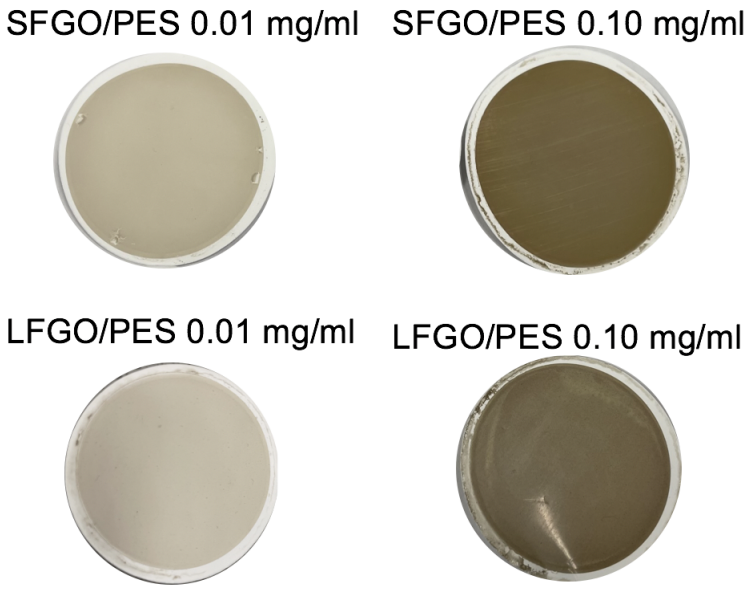

Figure 3.2: SFGO- and LFGO-coated PES membranes. *Top Row:* SFGO coated PES, 0.01 mg/ml SFGO (Left) and 0.10 mg/ml SFGO (Right). *Bottom Row:* LFGO coated PES, 0.01 mg/ml LFGO (Left) and 0.10 mg/ml LFGO (Right).

3.4 Technique: Fourier Transform Infrared spectroscopy

The Infrared (IR) region of the electromagnetic spectrum covers the broad wavelength range of approximately 760 nm - 100,000 nm [357]. Analysis of solid, liquid or gas samples by FTIR spectroscopy is typically conducted in the wavelength region 2.5 - 25 μm (having respective wavenumbers 4000 - 400 cm^{-1}), the region known as the mid-infrared region [358]. In this region of the IR spectrum, chemical bonds within a sample become excited and undergo characteristic molecular vibrations, which determine the rotational-vibrational nature of the sample [359]. Fundamentally, chemical bonds absorb IR radiation at a certain frequency, the resonant frequency of molecular vibration of the particular bond in question. Modern FTIR analysis is conducted by directing a beam of IR at a crystal which is in contact with the sample: resulting in generation of an evanescent wave, which undergoes multiple total internal reflections, passing through the sample material at least one time [360]. The resulting data is Fourier Transformed, giving the FTIR spectrum. The correct name for FTIR systems operating in this manner is Attenuated Total Internal Reflectance (ATR) - FTIR. Analysis of samples by ATR-FTIR enables a multitude of samples to be analysed with no further preparation, thus the technique is simple.

3.4.1 Experimental Methods: FTIR

FTIR analysis of GO materials

Samples of GO at undiluted concentration 1.0 wt% were dried overnight onto glass slides using a (Genlab Prime Oven (UK)) oven at 50°C. The GO was then extracted from the surface by scraping using clean tweezers and ground down using a mortar and pestle.

FTIR spectra of dried GO samples were obtained using a (Thermo Fisher Scientific Nicolet iS10 (USA)) spectrophotometer. For each sample, 5 mg of the dried GO powder

was mixed with 300 mg laboratory grade potassium bromide (KBr) pellets in a ceramic crucible. The GO-KBr powdery mixture was further ground into a fine powder using a pestle, and subsequently compacted into a thin 10 mm diameter disk using a (Specac (UK)) mechanical hydraulic press. Following compaction, FTIR analysis was carried out on the disk in transmission mode, wavenumber interval 4000 - 400 cm^{-1}, using 32 scans at resolution 4 cm^{-1}, with an applied background correction to account for analysis conducted in atmospheric air.

FTIR analysis of GO membranes

FTIR analysis of dry membranes was performed using a (Perkin Elmer (USA)) spectrophotometer. Samples were mounted onto the ATR crystal and the IR beam source directed at the sample. As above, spectra were recorded in transmission mode in wavenumber interval 4000 - 400 cm^{-1}, completed with 32 scans at resolution 4 cm^{-1}, using background correction for air.

3.5 Technique: Raman spectroscopy

Raman spectroscopy is a means of structural fingerprinting that provides information regarding the vibrational modes of molecules within a sample based upon scattering of monochromatic light (often from a visible light source) [361]. When electrons within molecular bonds are excited by incident photons, they temporarily enter a state of higher energy. When the electron returns to its fundamental energy state, a photon is emitted. If this photon is of the same energy as the incident photons from the source, the scattering is termed *elastic*: this phenomenon is known as the Rayleigh Effect [362]. If the energy of the scattered photon is lower than the incoming photons, the scattering is *inelastic*, referred to as Stokes-Raman Scattering [363]. Stokes-Raman scattering is a very weak effect, occurring in approximately one in every 10^8 transitions [364]. The relative energetic levels of the transitions in both Rayleigh and Stokes-Raman

transitions are shown in Figure 3.3. For Stokes-Raman scattering, the electrons are shown returning to a higher energy level relative to their initial state, following decay from a virtual state.

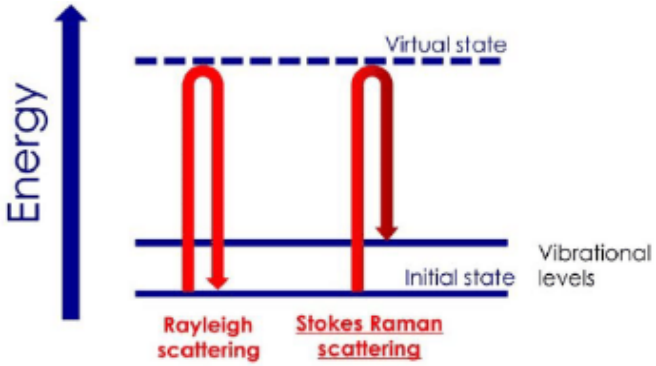

Figure 3.3: Atomic scale electronic energetic transitions in Rayleigh scattering (left) and Stokes-Raman scattering (right). Adapted from [17].

Raman spectra reflect the intensity of photon emission at different wavenumbers of light. Typically, the spectrum is shown in terms of the difference or shift in energy between incident and scattered photons, termed *Raman shift*, in order to represent the inelastic scattering effects [365]. Raman Shift is defined by Equation 3.1 [364]:

$$\Delta\nu = \left(\frac{1}{\lambda_{Incident}} - \frac{1}{\lambda_{Shifted}}\right) \tag{3.1}$$

where $\Delta\nu$ represents the Raman Shift, having units equal to inverse wavelength. $\lambda_{Incident}$ and $\lambda_{Shifted}$ represent the wavelengths of photon from the incident and shifted beams, respectively. For a given material, the Raman Shift is unique to that particular material, as such, Raman spectroscopy enables material fingerprinting, thus enabling identification of a material based on the obtained Raman spectrum [366].

3.5.1 Experimental Methods: Raman Spectroscopy

Raman spectra of dried GO samples were recorded using a (Horiba XploRA PLUS (Japan)) spectrometer. Samples of GO at undiluted concentration 1.0 wt% were dried overnight in an oven onto a glass slide. Raman analysis of the sample was performed by irradiating the GO with green laser light (λ = 532 nm), with output power 1.2 mW. Imaging and positioning of the sample was achieved using a light microscope with 100X magnification. Spectral data was acquired using one measurement spot per sample. Intensity of shift values were recorded for Raman shifts in the wavenumber interval 0 - 3500 cm^{-1}.

Raw Raman data was obtained with a non-zero background. Background correction algorithm was applied to the obtained raw data using *OriginPro* (OriginLab Corporation (USA)). Correction of the background was completed with spline point-to-point interpolation and 16 connection points per each fitted interpolation.

3.6 Technique: X-ray Photoelectron Spectroscopy

XPS is a surface analytical technique, capable of providing detailed information regarding the chemistry of the top 10 nm of a sample [367]. In XPS analysis, the sample surface is irradiated with an X-ray beam, which excites the atoms in the sample, resulting in photoelectric emission of electrons from the surface. In XPS, the mono-energetic X-ray beam is typically generated by an aluminium K_α source inside an X-ray tube, producing photons of wavelength 0.834 nm (1486.7 eV) [368]. The energies of the emitted electrons are analysed in an energy analyser, a hemispherical lid, which forces the electrons to undergo an arc of circular motion [367]. The distance travelled by a given photoelectron is related to its entry speed and therefore initial kinetic energy, as the more initial energy, the greater the arc of travel. A schematic representation of the motion of photoelectrons inside the hemispherical energy analyser is shown in Figure 3.4.

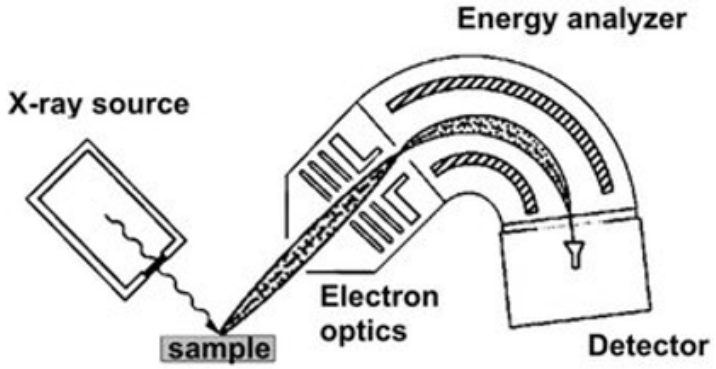

Figure 3.4: The major components of X-ray Photoelectron Spectroscopy (XPS) instrumentation, showing the X-ray source and beam being directed at a sample. The emitted photoelectrons are directed into a hemishperical analyser and their kinetic energies measured by a detector. Adapted from [18].

The electron binding energy ($E_{Binding}$) is the minimum amount of energy required to remove an electron by photoelectric emission. $E_{Binding}$ is related to the kinetic energy of emitted electron ($E_{Kinetic}$) by the Einstein photoelectric relationship [369], which also involves the energy of X-ray photon (E_{Photon}) and the work function (ϕ_{Work}):

$$E_{Binding} = E_{Photon} - (E_{Kinetic} + \phi_{work}) \tag{3.2}$$

The kinetic energies of emitted electrons are measured experimentally, as discussed, such that the corresponding values of $E_{Binding}$ may be calculated using this relationship, with the values of E_{Photon} and ϕ_{Work} also known. The essence of XPS analysis involves obtaining a spectrum that considers the intensity of photoelectric emission, as a function of $E_{Binding}$.

Atomic electrons are arranged in orbital shells (*e.g.* $1s$, $2s$, $2p$), each having different energies depending upon the particular element. As such, the intensity of photoelectric emission at characteristic binding energies is indicative of the elements present. This is in essence a form of fingerprinting by which XPS enables the presence and electronic

state of an atomic element to be identified, as the energies of emitted photoelectrons are corresponding to those within the electron configuration of the element. The intensity of binding energy signal is proportional to the number of photoelectrons emitted: as such, the atomic species may not only be identified but the atomic percentage may be quantified [367].

In XPS spectra, the intensity of photoelectron signal is plotted as a function of binding energy. Spectra are collected via two acquisition modes, these are *i*. survey spectra and *ii*. high resolution spectra. Survey spectra, collected over a broad range of binding energies, for example the range 1100 - 0 eV, are used for identification of atomic species present within a sample [370].

High resolution spectra are focused on a more narrow range of binding energies, typically within regions defined by the the peaks identified during the survey scan [371]. High resolution spectra are used to identify the chemical state and bonding of select elements within the sample [372]. For example, a high resolution spectra collected in the interval around binding energies 284.6 eV reveals the chemical bonding of all carbon $1s$ bonds in the sample. The high resolution spectra tend to be a complex composite profile, however, which must be separated into its constituent peaks (peak fitting) to give information regarding the chemical bonding [367]. Such a process is termed *deconvolution*: this is no easy task, but has been made simpler in modern day by the development of commercial software packages such as *CASAXPS* (CASA Software Limited (UK)).

A sample high resolution spectrum of the C1s region is given in Figure 3.5, with the associated binding energy interval 292 - 282 eV. The raw XPS signal data is represented by the black line, with a smoothing function overlaid onto this data, represented by the red line. The smoothed data has been deconvoluted to five peaks, numbered 1 - 5 on the plot.

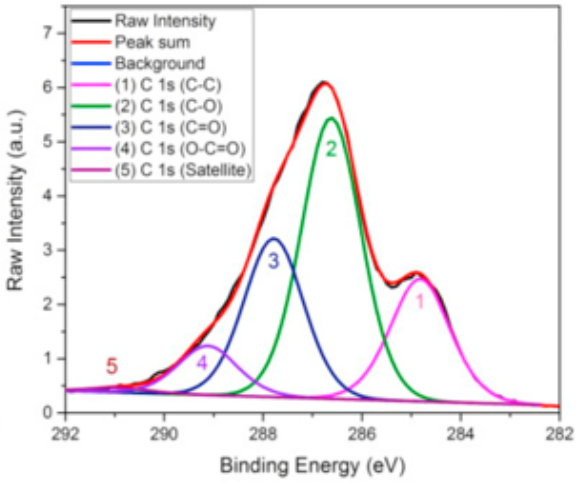

Figure 3.5: High resolution XPS analysis of the C1s region of a GO material. Adapted from [19].

The labelled peaks, with associated functional group identity and concentration are tabluated below:

Table 3.2: Summary of deconvoluted peaks, from high resolution XPS analysis of a GO material, from Figure 3.5.

Peak Number	Binding Energy (eV)	Functional group	Atomic %
1	284.6	C - C	13.06
2	286.6	C - O	29.46
3	287.8	C = O	16.63
4	289.1	O - C = O	5.21
5	290.9	$\pi - \pi^*$ satellite	35.64

During the experimental analysis of a sample by XPS, it is common for an insulating material to become charged [373]. This phenomenon results in unwanted shifting of the observed binding energy peaks to misleadingly high binding energies. As such, this may result in the high resolution spectra giving misrepresentative information regarding the position of the peaks and therefore nature of the chemical bonding within the sample

[374]. In order to compensate for the effects of charging, it is possible, using specialist XPS software packages, to mark a select peak of know position as a reference peak. The raw data will be subsequently translated towards the reference peak, For GO materials, the C - C peak (labelled as Peak 1, on Figure 3.5 and in Table 3.2), positioned at 284.6 eV, referred to as the adventitious carbon peak, is typically used as the reference, and any remaining spectral peaks may be fitted accordingly, their position having been corrected by adventitious carbon [373, 375].

This example has illustrated the qualitative and quantitative uses of XPS, in identifying elements and functional groups and also estimating the amount of select elements and bonds present. XPS has become a very popular means of analysing GO materials, as its power is realised when utilised in conjunction with the other spectroscopic techniques such as FTIR and Raman spectroscopy.

3.6.1 Experimental Methods: XPS

XPS survey and high resolution O1s and C1s analysis was carried out using a (Thermo Fisher Scientific Escalab 250Xi (USA)) ultrahigh vacuum XPS instrument. GO powder was produced as per the method outlined in Section 3.4. Samples were secured on a sample mount using conducting carbon tape and loaded inside the vacuum chamber. Pressure inside the chamber during operation was maintained at $2{\cdot}10^{-11}$ mbar. The X-ray source was AlK_{α}, producing X-rays with energy 1486.7 eV. Photoelectron pass energy (minimum energy with which photoelectrons must have before being allowed to contact the detectors) for survey spectra was 40 eV and for high-resolution C1s and O1s spectra it was 20 eV. The dwell time (duration of each analysis step) was 20 ms for the survey spectra and 100 ms for high resolution analysis. Data was collected at one measurement spot per sample, at room temperature.

XPS data was processed using *CASAXPS*. Analysis of survey data was conducted by ascribing the two obtained peaks as carbon (286 eV) and oxygen (532 eV). Back-

ground correction was not applied to the survey spectra. Quantification of the relative percentages of carbon and oxygen was achieved using the inbuilt quantification tool of *CASAXPS*. Analysis of high resolution O1s and C1s was carried out using adventitious carbon (284.6 eV) as the reference peak. Smoothing of raw experimental data was achieved using the software's quadratic smoothing tool. Background correction was achieved using a Shirley background function, applied to the spectra prior to deconvolution. Deconvolution of spectra was performed using peak fitting with Gaussian shapes. For each C1s spectra, the smoothed data was deconvoluted to five spectral peaks in total, while the O1s were deconvoluted to four.

3.7 Technique: Brunauer-Emmett-Teller Analysis

Brunauer-Emmett-Teller (BET) theory accounts for the adsorption of gas molecules onto the outer surface of a solid-phase adsorbent. Provided that the gas contacts the adsorbent surface at temperature below its critical temperature, then weak solid - gas interactions enable the gas to physically adsorb onto solid by van der Waals' interactions [376]. In order to avoid unwanted chemical interactions of adsorbent with gas, it is important to select an inert adsorbing gas: as such, Nitrogen is most popular, with analysis conducted at the boiling point (77 K) [377]. Detectable levels of gas adsorption are quantifiable if the adsorbent is cooled to cryogenic temperatures.

BET theory predicts that gas molecules adsorb via Langmuir adsorption mechanism (as introduced in Section 2.2), forming a single monolayer of adsorbed molecules [378]. As the sample has been cryogenically cooled and analysis is conducted under isothermal conditions, increasing the quantity of adsorbing gas increases the amount of gas adsorbed [379]. The amount of gas adsorbed is strongly correlated with the surface area of the adsorbent [380]. Conversely, decreasing the quantity of gas (reducing pressure) leads to desorption of gas molecules from adsorption surface. Almost all adsorbents are

porous, to some degree, as such, adsorption may occur inside the pores as well as on the surface. An isotherm is established between the adsorption and desorption quantities of gas, which are visualised as a plot showing quantity of gas adsorbed as a function of relative pressure [381].

The adsorption-desorption isotherms involve strictly non-linear relationships between adsorption and relative pressure. These relationships may be linearised by application of the BET equation [382]. In multi-point BET analysis, adsorption data are collected at five data points in the relative pressure interval 0.025 - 0.30, and manipulation of the obtained relationships enables the calculation of two parameters: *i.* Specific Surface Area (SSA) and *ii.* Total pore volume (TPV) [383]. SSA and TPV are commonly reported parameters used to describe a sample according to BET analysis.

3.7.1 Experimental Methods: BET

GO powder was produced as per the method outlined in Section 3.4. BET surface analysis was carried out using a (Micrometrics Tristar 3000 (USA)). The mass of powdered GO used for testing was recorded as 10 mg. Degassing of samples was achieved by transferring the powders into a round-bottomed flask and purging with Nitrogen in a (Micrometrics FlowPrep (USA)), at 60°C, for 10 hours in total. The samples in flasks were then attached to the surface area analyser, and liquid nitrogen at 77K was decanted into the Dewar flask prior to lowering of the samples.

3.8 Technique: Laser diffraction and dynamic light scattering

LD and DLS are used for characterisation of particle sizes of a material in suspended state. Both techniques are fundamentally based upon scattering of light by particles [384, 385]. It is possible, using the techniques, to generate a particle size distribution (PSD) to describe the array of sizes present within the sample, but not obtain

information regarding the particle shape.

LD is a particle sizing technique that produces a particle size distribution (PSD) of particles that are suspended in liquid medium. Laser light is directed at the suspended particles, which may be assumed to have a varying distribution of sizes: these diffract the light to different extents. The laser source in LD systems is often a red helium-neon, or a blue light emitting diode [386]. The scattering of light by particles is, in modern LD systems, assumed to follow the Mie Theory of scattering, a complete theory and solution to the scattering of waves by a spherical object based on Maxwell's equations [387]. Mie Theory is optimised for particles having geometric dimension greater than the wavelength of the light source, which is typically >350 nm [388]. Diffraction of light is assumed to take place around the edges of the spherical particle, resulting in a diffraction pattern. The diffraction pattern is dependent upon particle size: the smaller a given particle, the greater the extent to which it scatters light, resulting in a larger scattering angle [389]. The diffracted light is detected by a series of detectors which transmit the signal to a computerised system for obtaining the PSD. The intensity of the light signal is proportional to the volume of particles: hence the obtained PSD is said to be volume weighted. For comparison of the PSD obtained for different samples, it is common to utilise statistical values including median diameter (d(50)), and 10^{th} (d(10)) and 90^{th} (d(90)) percentile values of diameter [390].

DLS also sizes particles by analysing the light scattering properties of particles suspended in media. DLS, in contrast to LD, is used for analysis of particles which have lateral sizes significantly less than the wavelength of incident monochromatic light [385]. Particles suspended in medium undergo temporal perturbations about their equilibrium position, due to a phenomenon known as Brownian Motion, in which particles undergo random motions, subject to continual collisions with molecules of solvent [391]. This effect results in randomised movement of particles in suspension. The rapidity of Brownian Motion is inversely proportional to particle size: as small particles will undergo

more rapid perturbations than large particles, owing to the smaller forces required to displace them [392]. DLS measures the time-dependent fluctuations in scattered signal intensity due to Brownian Motion of particles in medium: for smaller particles, this signal intensity is found to vary more rapidly than for large particles. A representation of the signal intensity fluctuation due to Brownian Motion of small and large particles is shown by Figure 3.6, demonstrating that the small particles produce a more rapid fluctuation.

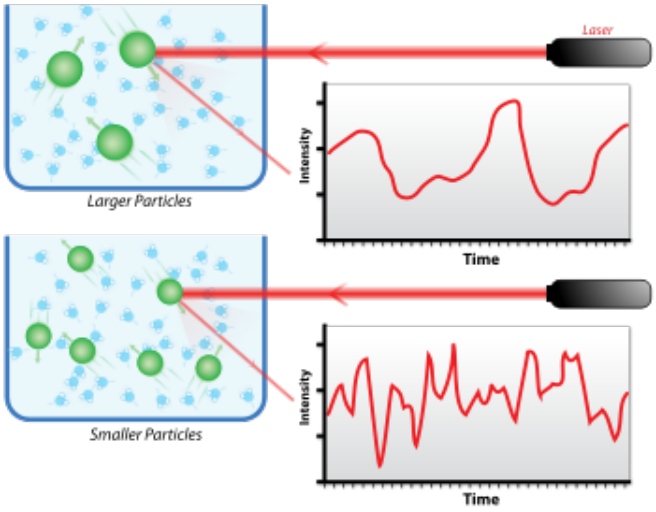

Figure 3.6: Intensity of signals measured by Brownian Motion of small and large particles by dynamic light scattering (DLS). Adapted from [20].

The signal intensity exhibits variation as a function of time. Particle sizing is related to the signal intensity by means of the autocorrelation function of the signal, by decomposing the signal at very small intervals of time and using a correlating device to calculate the autocorrelation (self-similarity) of the signal [393]. This results in the calculation of a mathematical function related to the autocorrelation (termed the autocorrelation function): this function decays in time, as the self-similarity of the signal tends to zero [394]. The rate of decay is proportional to particle size, as small particles decay to zero rapidly. Calculation of particle sizes in DLS is enabled through use of

the Cumulant's Method: this involves fitting an exponential profile to the autocorrelation function in order to obtain the Z-Mean particle size [395]. In DLS, the Z-Mean is considered a mathematically stable parameter and is very commonly used to represent the distribution [394, 395].

3.8.1 Experimental Methods: DLS and LD

Particle size analysis of GO was achieved using both LD and DLS. For both techniques, GO was diluted in distilled water down to 0.01 mg/ml.

DLS was undertaken using a (Malvern Zetasizer Nano ZS (UK)). Dilute GO was transferred by pipette into a 0.75 ml disposable folding capillary cuvette. Data was acquired using the accompanying *Zetasizer* (Malvern (UK)) software. The solvent was set as water at 25 °C, and the refractive index of GO was set as 1.96 [396]. Size measurements were made using an equilibration time of 90 seconds per sample, with three size measurements being taken per sample.

LD was performed using a (Malvern Mastersizer 3000 (UK)). Approximately 20 ml of each dilute sample was transferred into the wet sample chamber. The solvent and material refractive indices were set according to the above. The obscuration limit (percentage of laser signal attenuation by the sample) was set to 5%. Three PSD's were obtained per sample.

3.9 Technique: Zeta potential

Ionisation or dispersion of a species in media results in separation of the charges. In the immediate vicinity of the suspended charged particle, counterions are attracted to the surface. Surrounding this layer of counterions resides the Diffuse layer, which is a loose arrangement of free ions moving under the influence of electrostatic attraction. The narrow region separating the counterions and the Diffuse layer is the Stern layer [397],

while the interface between diffuse layer and bulk media is known as the Slipping plane [398]. Electric potential at the Stern layer is known as the Stern Potential. The zeta potential is the potential at the interface between the slipping plane and an arbitrary, distant location away from the particle in bulk dispersant [399]. A representation of the accumulation of charges, leading to the formation of an electrical double layer in the vicinity of the charged particle, is shown in Figure 3.7, showing also graphical potentials at surface, Stern layer and Slipping planes.

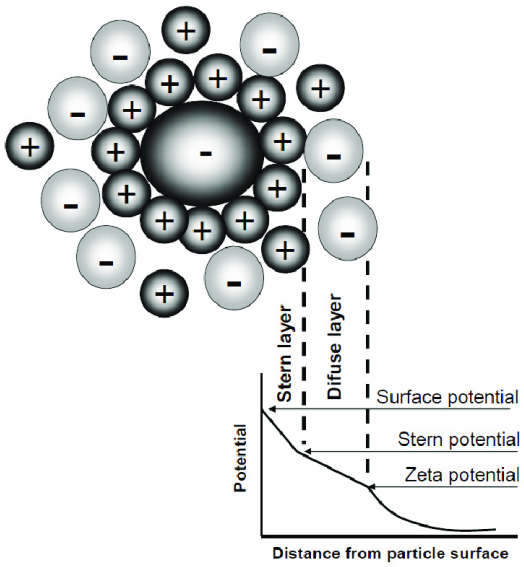

Figure 3.7: Accumulation of charges in the vicinity of an electronegative species. The Stern Layer is adjacent to the charged surface, the diffuse layer surrounds the Stern layer. Zeta potential is measured at the outer diffuse layer (slipping plane). The arbitrary potential at each point is represented graphically. Adapted from [21].

Zeta potential is an important parameter in colloid science, used to indicate the stability of a formulation. Experimental determination of zeta potential is achieved by electrophoresis, in which the sample is placed in a cuvette between a pair of electrodes [400]. Application of a potential difference forces charged particles to motion towards the opposite electrical polarity. The electrophoretic mobility parameter (U_E)

is related to the velocity of the moving charges per unit electric field strength [401]. The relationship between U_E and zeta potential (ζ) is expressed by the Henry Equation [402]:

$$U_E = \frac{2 \cdot \epsilon \cdot F(\kappa\alpha)}{3 \cdot \eta} \cdot \zeta \tag{3.3}$$

where ϵ is the dielectric constant of dispersant (for water, ϵ is approximately equal to 80 at 25°C), κ is the inverse of the Debye Length, and α is the particle radius: the term $F(\kappa\alpha)$ is the Henry Function. The Smoluchowski approximation [403] enables simplification of the Henry Function, taking the value of $F(\kappa\alpha)$ to equal 1.50. It is generally accepted that the Smoluchowski approximation is applicable for particles suspended in aqueous dispersant [404]. As such, the zeta potential may be extracted from the measured electrophoretic mobility ranges of the particles suspended in media.

Like charges in suspension will repel one another by electrostatic repulsion: this behaviour is highly significant for the stability of colloidal suspensions. The higher the magnitude of the zeta potential correlates to higher stability of particles in dispersant [405]. The magnitude of the zeta potential has been related to the degree of stability of particles in media, these have been reported as follows:

Table 3.3: Colloidal stability, as indicated by zeta potential. Adapted from [30].

Zeta Potential (mV)	Stability Indication
0 - ±5	Rapid coagulation/flocculation
±10 – ±30	Delicate stability
±30 – ±40	Moderate stability
±40 – ±60	Good stability
>±60	Excellent stability

Colloidal stability is intrinsically linked by a combination of zeta potential and the DLVO theory of particulate interaction (first introduced in Section 2.2.5). By inspection of Table 3.3, it is clear that the lower the magnitude of the Zeta Potential, the greater

the tendency of the charged species therein to aggregate by van der Waals' interactions, as predicted by DLVO [406]. Conversely, the higher the magnitude of zeta potential, the greater the degree of stabilising electrostatic repulsion, leading to stability.

3.9.1 Experimental Methods: Zeta potential

Zeta potential of aqueous GO dispersions was measured using a (Malvern Zetasizer (UK)). The dispersions were diluted in distilled water to 0.01 and 0.10 mg/ml. pH was measured for each sample, using a (Hach HQ11D Digital pH meter (USA)), but was not adjusted. Data was processed using the accompanying *Zetasizer* software, with measurement of zeta potential made using the instrument setting for Smoluchowski approximation. Three separate measurements were made for each sample, in a folded 0.75 ml capillary cell (as per DLS), at room temperature, and the average value reported.

Determination of the colloidal stability of GO materials subject to a variation in pH, 10 ml samples of 0.01 mg/ml SFGO and LFGO were prepared in distilled water and divided into separate vials, their pH measured in analogy to above. The pH of the respective aliquots were then adjusted to 3.5, 4.0, 5.0, 6.0, 7.0, 8.0, 9.0 and 10.0, under slow and constant agitation, using a magnetic stirrer with speed setting 3 on the instrument, using dilute sodium hydroxide solution as base (0.10 mol/l). Transfer of base was carried out in a dropwise manner close to the end of the adjustment. Measurement of zeta potential was carried out immediately following adjustment of pH, at room temperature. In analogy to above, three separate measurements were made per sample, using Smoluchowski approximation.

Measurement of zeta potential was utilised as a means to determine the stability of GO-salt colloids, with salts sodium chloride, sodium sulphate, ammonium heptamolybdate and magnesium sulphate. Samples of 0.01 mg/ml SFGO and LFGO were prepared in distilled water in 10 ml quantities and divided into separate vials, in analogy to the above. The pH was likewise measured but not adjusted. Under constant

stirring at room temperature (as above), the salts were dissolved in the GO dispersion, so as to achieve respective salt loadings in the GO dispersion 0, 1, 2, 4, 6, 8 and 10 g/l. Measurement of zeta potential was carried out as above, using Smoluchowski approximation.

3.10 Technique: Thermogravimetric Analysis

TGA involves the heating of a sample and monitoring the mass as a function of temperature. As the temperature increases, a range of chemical and physical changes may occur, including dehydration, vaporisation, sublimation and sample degradation [407]. Changes such as these will be accompanied by resulting mass loss of the sample: for example, vaporisation and subsequent evacuation of volatile gases including carbon dioxide and methane result in the mass of the sample decaying with an increase in temperature [408]. The predominant use of TGA is to ascertain the thermal stability of a sample subject to a controlled temperature program: if for example, the mass is unchanged in a defined temperature interval then the material can be assumed to be thermally stable within such a range [409]. In order to ensure that the sample does not suffer side reactions with species in air, the heating takes place in an inert atmosphere, using a steady flow of gases such as nitrogen. In general terms, mass loss from a sample may occur at one major stage only or at a series of smaller stages, corresponding to different phase transitions [410]. TGA is highly popular for the analysis of materials including membranes, as it may be important depending on the intended application to comprehend the thermal stability across a defined temperature range [411, 412]. TGA experimental equipment comprises: a furnace, including temperature controller, an electric balance, the temperature and connection to computerised data acquisition system. The mass sample is measured throughout the analysis on the electric balance.

3.10.1 Experimental Methods: TGA

TGA analysis of membranes was achieved using (Netzsch STA 449 (Germany)) instrumentation. GO-coated membranes were prepared as discussed in Section 3.3. Initial 47 mm diameter membrane samples were cut down to round sections having mass 10 mg, using a scalpel. The masses of cut membrane were recorded using a 5 decimal place balance. TGA thermograms were recorded by heating these 10 mg samples from 30°C - 900°C, in a ceramic heating crucible, at heating rate 10°C/minute. Nitrogen was used as the purge gas for the analysis, at purging rate 50 ml/minute. The analysis was carried out using three separately-prepared membranes per respective sample.

3.11 Technique: X-ray diffraction

XRD is used for analysis of predominantly crystalline structures, as a means to characterise features on an atomic or molecular scale. As X-rays are a form of electromagnetic radiation, they may undergo diffraction around encountered obstacles, provided that they are of comparable size order to the obstacle [413]. Typically, X-rays have wavelength of the order nm, making the technique ideal for analysis of nanostructured materials including GO. In practice, the analysis of materials using XRD is optimised for fine powdered samples that have particle size less than 10 μm [23].

Assuming that a sample is an ordered, crystalline structure, having consistent interplanar spaces between its atoms, then if an an X-ray beam is directed at such a sample, the waves will be diffracted around the atoms. Atomic electrons are particularly strong scatterers of X-ray beams [414]. This X-ray scattering effect occurs elastically and at characteristic scattering angles, the spherical diffraction pattern will be maximised, due to constructive interference of waves. Bragg's Law [415] has become ubiquitous in analysis of materials using XRD, as it enables the interplanar atomic distance, or layer distance (d) to be calculated using the diffraction pattern. Bragg's Law is defined

by Equation 3.4, where n_{Bragg} is a material index integer, λ_{X-ray} is the wavelength of X-ray source and Θ is the angle of incidence of incoming waves. The component of the equation $2d_{spacing} \cdot Sin(\Theta)$ is known as the path length: constructive interference occurs at wavelengths having value equal to integer multiples of the path length.

$$n_{Bragg} \cdot \lambda_{X-ray} = 2d_{spacing} \cdot Sin(\Theta) \tag{3.4}$$

A pictorial representation of Bragg's Law is provided in Figure 3.8, showing the respective inbound and outbound diffracted X-rays, their angle Θ, and the interplanar spacing d.

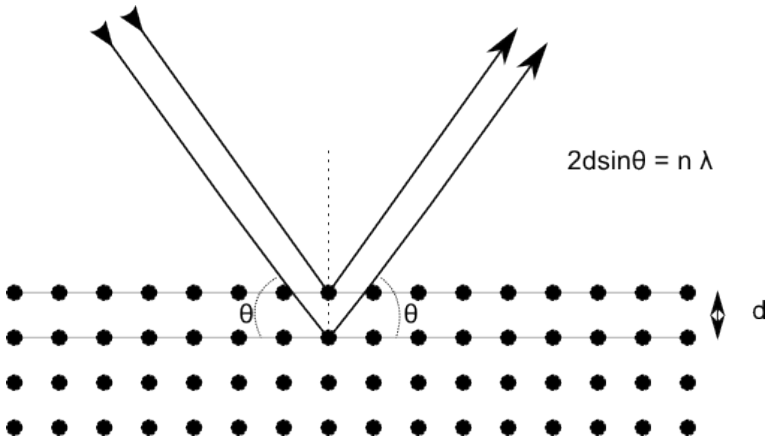

Figure 3.8: Diffraction of X-rays, on atomic scale in an arbitrary sample material. The angle of incidence and diffracted angle are both equal to Θ. Adapted from [22].

In an XRD system, X-rays are generated using an X-ray tube, in which a tungsten filament block is heated, and a potential difference applied across the filament. This results in thermionic emission of electrons from the metal. Inside the evacuated tube, the generated electrons are attracted towards a second metal block, which serves as the anode [416]. The bombardment of electrons results in elastic emission of X-rays from the anode. If the anode is copper metal, then the X-rays will have characteristic energy 8.04 keV and wavelength 0.15406 nm: such an X-ray source of this nature is

termed a CuK_α beam, which is conventionally used in XRD X-ray generation tubes [417]. The X-ray detector is typically a silicon-based transducer that produces a signal upon sensing radiation, where the property of high signal-to-noise ratio is paramount [418].

XRD analysis of a powdered material yields information in the form of a diffraction pattern, wherein the intensity of X-ray detector signal at certain angles is plotted as a function of 2Θ. This has become convention, as the X-ray beam source incidence angle is Θ, while the detector is located at angle 2Θ from the straight line path of the X-ray beam source. The diffraction pattern of the material is obtained by increasing the incident angle Θ, while the detector is simultaneously adjusted such that it always remains 2Θ from the incident beam. This configuration is shown in Figure 3.9.

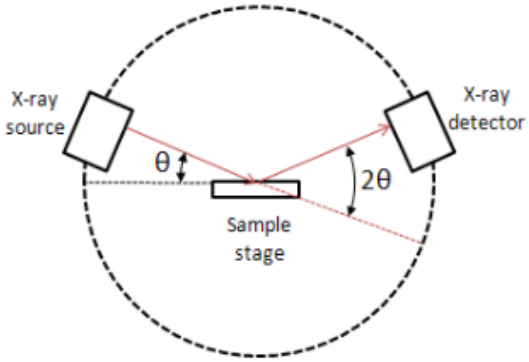

Figure 3.9: X-ray source and detectors, positioned apart by angle 2Θ. During X-ray diffraction (XRD) analysis, the angle Θ is gradually increased and the detector position adjusted so as to maintain the 2Θ spacing. Adapted from [23].

3.11.1 Experimental Methods: XRD

XRD analysis of GO materials

XRD analysis of GO powders was performed using a (Bruker D8 (USA)) diffractometer. GO powder was produced as per the method outlined in Section 3.4. Powdered GO samples were analysed in the scan range $5° < 2\Theta° < 50°$, with angular step size

0.016 degrees/minute, at 0.40 seconds per step, with 0.20 mm wide slits. The X-Ray beam source was CuK$_\alpha$, generating X-rays with wavelength 0.154 nm, at 40 keV, 30 mA current. A single crystal of each sample was chosen for analysis, and placed inside a silicon single crystal sample holder, with zero background. The total scan time for each sample was 30 minutes. For both powders, the $d_{spacing}$ was calculated by Bragg's Law (Equation 3.4), taking the value of n_{Bragg} to equal unity and λ_{X-ray} as 0.154 nm.

XRD analysis of GO membranes

XRD analysis of GO-coated membranes was performed using a (Malvern Empyrean (UK)) diffractometer. GO-coated membranes were prepared as discussed in Section 3.3. Membrane samples were analysed in the scan range $5° < 2\Theta° < 40°$, with angular step size 0.02 degrees/minute. The X-ray beam source was again CuK$_\alpha$, with wavelength 0.154 nm, and beam power 30 keV, 10 mA current. 47 mm membranes were cut using a scalpel down to round shapes of 20 mm in diameter and mounted onto a copper sample support. The total scan time for each sample was 30 minutes. For all membranes, the $d_{spacing}$ was calculated in analogy to the above description of the technique for powders.

3.12 Microscopic analysis of GO

SEM is a powerful imaging technique that scans the surface of a sample in a raster pattern, with a focused electron beam comprising electrons of low energy. As the beam is directed at the sample, the electrons collide with atoms in the sample, resulting in electronic emission via a number of pathways, which, if detected by a solid state detector, may reveal information about the topography of the sample [419]. SEM analysis must be conducted with the sample under a high vacuum, so as to avoid unwanted collisions of the electron beam with particles such as dust within the air [420]. In addition, the sample must be electrically conductive: for non-conductive samples it is common practice to apply a gold coating of the order 50 nm to the surface, so as to

increase the conductivity [421].

In SEM, electrons are emitted from a sample as either secondary electrons or backscattered electrons [420]. Secondary electrons, emitted as ionisation products, have low kinetic energy and low mean free path and as such, may only be detected from the top several nm of sample [422]. This has advantages, as it enables very small features to be analysed: as such, secondary electron detection is the predominant means of imaging in SEM systems. This is also the reason why SEM is considered a surface characterisation technique. Backscattered electrons are reflected by the sample and have much greater kinetic energy and mean free path: as such they may emerge from much greater depths within the sample. Backscattered electron imaging enables depth imaging of samples as atoms below the topmost layers are detectable, albeit that the resolution is lower than secondary electron mode [423]. In addition to electrons, X-rays may be emitted as a result of high energy electrons undergoing inelastic transitioning to a lower energy level, to fill a gap vacated by emitted secondary electrons. The energy of the emitted X-ray is characteristic of the atomic species from which it emerged. As such, this opens the door to analytical characterisation of the composition of a sample, in a method known as Energy-dispersive X-ray (EDX) spectroscopy [424]. SEM/EDX analysis enables the analyst to generate elemental composition maps of a sample surface: it is now commonplace for a false colour representation of each atomic species such as carbon, oxygen, nitrogen *etc.* to be overlaid onto the sample, for differentiation of surface elements. Point spectroscopic analysis is also possible, enabling the composition to be quantified.

A schematic representation of SEM/EDX is shown in Figure 3.10. The electron beam is directed at the sample and accelerated by an anode. Focusing of the electron beam is achieved by condenser and objective lenses. Upon contact of beam electrons with sample, a series of X-rays, secondary and backscattered electrons are emitted from the sample and these are picked up by a relevant detector. As shown, the backscattered

electron detector is positioned directly in-line with the sample and inbound electron beam, such that any emitted backscattered electrons are detected, while the X-ray and secondary electron detectors are situated closer and oriented around the sample [425]. The signals picked up by the detector are subsequently amplified and passed to a data processing computer stage, where ultimately the analyst may visualise the obtained results in real-time [426].

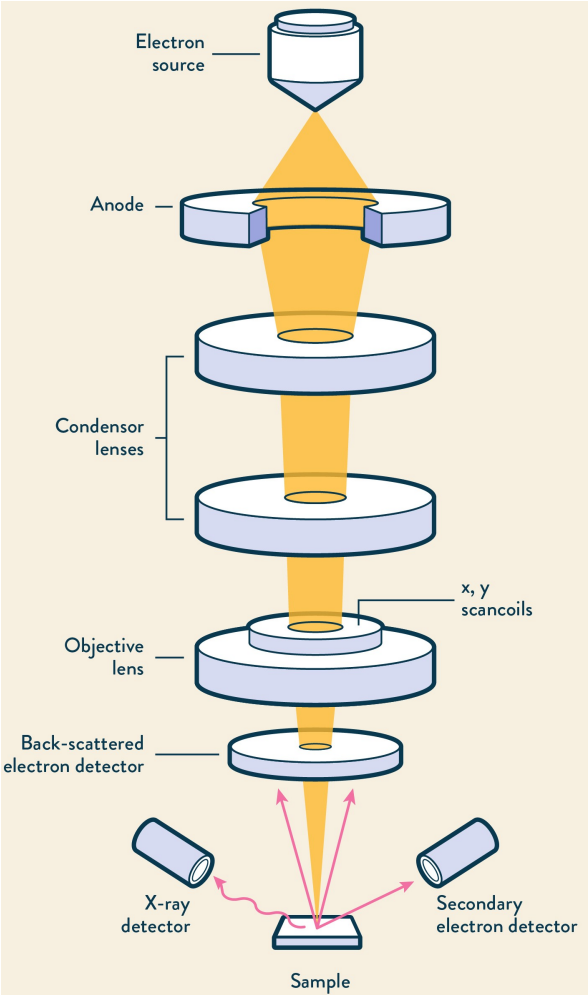

Figure 3.10: Scanning electron microscopy (SEM)/Energy Dispersive X-ray (EDX) (SEM/EDX) spectroscopy. Adapted from [24].

Careful imaging of the GO samples can generate images with high resolution and an excellent level of detail. Modern SEM systems can provide up to 100,000X magnification factor, compared with light microscopy, which is of the much lower order 2000X [422]. The imaging capability and quality of SEM is unparalleled, enabling even the smallest features including wrinkles and pores to be identified and characterised. If combined with EDX, compositional analysis of sample is possible, which may be compared with other spectroscopic techniques including XPS (discussed in Section 3.6). Given the unique and powerful combination of imaging and spectroscopy, SEM and SEM/EDX are foremost methods of GO analysis.

3.12.1 Experimental Methods: SEM

GO was diluted to 0.01 mg/ml concentration in distilled water and sonicated in an ultrasound bath for 15 minutes. A 1 ml volume of the GO dispersion was transferred onto an aluminium stub using a pipette, and placed inside an oven at 50°C for overnight drying. SEM imaging of the GO morphology was performed in a (Hitachi SU8230-CFE-SEM (Japan)), with electron beam accelerating voltage 30 keV and magnification factor 10 - 100,000X. Sample stubs were placed inside the sample chamber, which was subsequently evacuated to 10^{-4}Pa. Images were recorded by varying the magnification and beam powers to optimise the image output. It was found by experiment that imaging at magnification 50,000X, with beam accelerating voltage 2.0 kV and working distance (distance between objective lens and sample) approximately 3 mm resulted in images with good detail.

EDX spectral information was collected using point spectra on a randomly chosen section of the sample. Data was collected at one measurement spot per sample.

3.13 Microscopic analysis of GO membranes

In the previous section, SEM was introduced as a means of producing 2D images of GO flakes. It was discussed that SEM images are generated by directing an electron beam at the surface of a sample. It is possible also to generate a beam of ions and direct this at a sample for imaging purposes. Ionic species, such as heavy metal cations, are much larger and heavier than electrons, as such, contacting of the ion beam with a sample has an inherently destructive impact, as it sputters material from the sample surface [427]. Owing to the damage caused by the sputtering action of the focused ion beam (FIB), it is possible to carve a trench in the sample and even ablate sections of material altogether, provided the power of the ion beam is sufficient to achieve this [428]. During the process, heavy metal ions themselves inherently become stuck in the sample, as they are physically larger than electrons and therefore more prone to surface adherence [429]. Secondary electrons are generated in the process, in analogy to the mechanism for action using an electron beam, and may be subsequently picked up by a solid state detector.

Combination of the milling action of the FIB (typically the ion is Ga^+) with an electron beam enables the FIB-etched surface to be imaged, appearing as a 2D cross-sectional image of the sample surface [430]. This combined FIB-etching with SEM imaging is ubiquitously termed FIBSEM. It has been found that the optimum angle for FIBSEM sample imaging (called the tilt angle) is 52°: that is, the electron beam should contact the FIB at this angle, relative to the direction of the inbound FIB [431]. An experimental setup showing the respective ion and electron beams and the corresponding tilt angle, is shown in Figure 3.11.

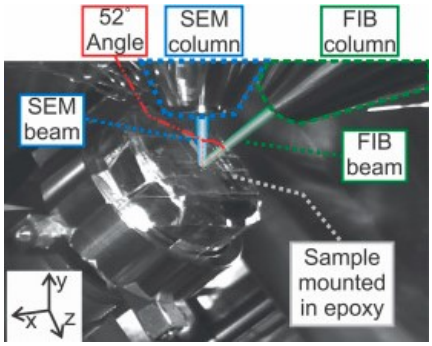

Figure 3.11: Focused ion beam scanning electron microscopy (FIBSEM) sample preparation chamber. The SEM is positioned at angle 52° relative to the direction of the incoming FIB. Adapted from [25].

Analysis of membrane samples by FIBSEM is capable of generating unparalleled levels of detail in accurately imaging the cross sections, as control of beam energy and positioning is simple, with imaging possible at sub-nanometric scale [432]. FIBSEM has become a very popular method for quantifying the layer thicknesses of material coatings, as the precise etching action of the beam enables imaging of the sliced membrane sections [433, 434]. This is a very powerful means to obtain an image of both the coating and substrate surface.

3.13.1 Experimental Methods: FIBSEM

Cross sectional and morphological FIBSEM imaging of membrane samples was achieved using a (FEI Helios G4 CX DualBeam (USA)). Membranes were prepared as discussed in Section 3.3. Samples were prepared for milling by sputter coating with platinum ions, which coat the material with a thin layer of cations, to protect it from being burnt by the ion beam. Following coating, the sample was secured on a silicon wafer using conductive carbon tape, and placed inside the sample chamber. The chamber was evacuated to 10^{-9} bar. The ion beam used for milling comprised gallium ions, which were directed vertically at the secured sample, with power setting 30 kV, 20 nA. The

beam was steered to mill a trench in the sample of width 150 X 100 μm. Cross-sectional imaging of the milled trench was achieved by directing the electron beam at the trench, at angle 52° relative to the ion beam direction. The electron beam power was 30 kV, 10 nA. Images were processed using *Auto Slice and View* software. GO coating layer thicknesses were estimated using an in-built tool in the software: for each image on which a thickness estimate was made, ideally three or four measurements were made at different positions on the image, and a mean value of thickness was calculated. In some cases, however, this was not possible.

3.14 Technique: Water Contact Angle

When a liquid phase contacts a solid, the intermolecular forces between the phases are responsible for the spreading of liquid phase across the solid. A schematic representation of a hemispherical droplet on a solid substrate, surrounded by vapor (in air).

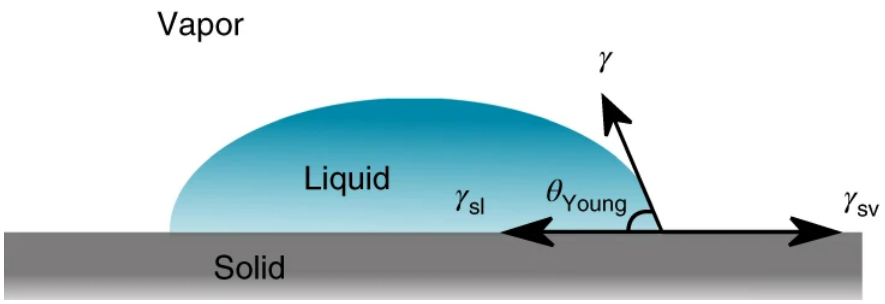

Figure 3.12: Phase equilibrium between solid, liquid and vapour phases, with surface tension (γ) existing at the solid - vapour (γ_{sv}), solid - liquid (γ_{sl}) and liquid - vapour (γ_{lv}) interfaces. The angle Θ_{Young} is the Young's contact angle. Adapted from [26].

Young's Equation [435] is used to define the minimum energetic state of a resting droplet, which forms a hemispherical shape due to the equilibrium established between the three phases. Young's Equation is defined as follows:

$$cos(\Theta) = \frac{\gamma_{sg} - \gamma_{sl}}{\gamma_{lg}} \tag{3.5}$$

The surface tension (γ) between phase interfaces are denoted as follows: solid and vapor (γ_{sv}), liquid and vapor (γ_{lv}) and solid and liquid (γ_{sg}). The angle Θ_{Young} is termed the Young's contact angle; if the liquid phase is water, then it is simply water contact angle [436]. By convention, water contact angle is measured from the liquid side.

Water Contact angle is an indicator of the wettability of a substrate, that is, a measure of how well water spreads over the surface [437]. In general, values of contact angle $0° < \Theta < 90°$ indicate that water spreads well over the surface and the surface energy is high [438]. Values $90° < \Theta < 180°$ are indicative of a poorly wetting substrate, in which the surface free energy is low [438]. Substrates with high wettability are thus termed hydrophilic while those with low wettability are hydrophobic [439].

The sessile drop technique is a popular method for determination of the contact angle, in which the substrate is positioned flatly and a singe water droplet is deposited [440]. Modern sessile drop techniques are computerised such that the droplet can be imaged with a high resolution camera, the combined system is known as a tensiometer. It is also possible using software to fit algorithmic profiles to the droplets to mathematically define their shape, such as the Young-Laplace profile [441], in which the optimised shape is attributed to the droplet and a corresponding water contact angle may be calculated.

3.14.1 Experimental Methods: Water Contact Angle

Water Contact Angle measurements were made using a (Kruss Optronic GmbH (Germany)) contact angle tensiometer. Measurements were made at room temperature, by depositing distilled water onto each substrate, in a dropwise manner, using a syringe

to achieve consistently small droplets. Imaging of the droplet on the substrate was achieved using a digital camera and images were processed using *Attension Theta* software. Measurements of contact angle were made by selecting the Young-Laplace option for droplet shaping. In total three measurements of water contact angle were made per substrate, such that the mean value of Water Contact Angle could be reported.

Chapter 4

Characterisation of GO materials and membranes

4.1 Introduction

Characterisation of materials in any study is a crucial stage of the research development process, as the analysis of materials using characterisation techniques enables one to gather detailed information regarding the chemistry and properties of the material. In the context of this research, analytical information assists in the understanding of a number of aspects of GO characterisation, including material chemistry, charge and flake size, among others. In the previous chapter, a number of such techniques were introduced. This chapter utilises the techniques introduced in the previous, in order to obtain analytical information. Here, the characterisation of two commercially available GO dispersions and GO-coated PES membranes is presented. These materials were selected for characterisation in this study owing to their similarity in chemistry and functional group presence, but more crucially, due to the difference in flake size. Accordingly, the analytical characterisation will be contextualised in later research chapters in which the properties are correlated to performance in contaminant removal. The characterisation is subdivided as follows:

- Characterisation of GO materials, is considered in Section 4.3.

- Characterisation of GO-coated PES membranes, is considered in Section 4.4.

GO materials are characterised using a number of spectroscopic techniques, such as FTIR, Raman, XPS and UV-Visible spectroscopic analysis. Interlayer spacing is analysed using XRD analysis of powdered GO's. Particle sizing of aqueous dispersions is measured using DLS and LD techniques. Colloidal stability of aqueous GO's is investigated subject to variation in pH, by measurement of zeta potential. Detailed imaging of dried GO on a fine scale is achieved using SEM.

GO-coated PES characteristics are also investigated using a number of techniques. Spectroscopic analysis was conducted using FTIR. Thermal stability of membranes was analysed by TGA. Degree of hydrophobicity or -philicity was assessed by measurement of Water Contact Angle. Interlayer spacing of GO coating was analysed using XRD. Detailed images of membrane morphology and cross section were recorded by FIBSEM analysis.

It is true that a vast quantity of research papers have dedicated discussions related to characterisation of GO materials and membranes [252, 442, 443], though the techniques and analysis presented in each is typically unique for the material in question. Establishment of a rigorous analytical pathway for characterising the material properties is of particular significance, given that this research focuses on GO materials with differing flake size, which is demonstrated to be a cornerstone factor. The results of this chapter provide important insights into the particular characteristics of the materials used throughout this research, prominently flake size and chemistry. Additionally, characterisation of the materials assists in elucidating the behaviour of the GO materials, particularly when seeking an explanation for the ways in which GO materials and membranes interact with species such as dyes and salts, in the subsequent chapters of this research.

4.2 Materials and Methods

Materials required for conducting the experiments were detailed in Section 3.2.

Analysis of GO by the following techniques, including analytical methods, was discussed in the given sections of Chapter 3:- FTIR (Section 3.4), Raman spectroscopy (Section 3.5), XPS (Section 3.6), BET (Section 3.7), LD and DLS (Section 3.8), zeta potential (Section 3.9), microscopy, for imaging of dried GO (Section 3.12).

Furthermore, analysis of GO-coated PES was given in the following sections:- FTIR (Section 3.4), TGA (Section 3.10), XRD (Section 3.11), microscopy, including FIBSEM morphological and cross-sectional imaging (Section 3.12) and Water Contact Angle (Section 3.14).

4.3 Results and Discussion: Characterisation of GO materials

4.3.1 Particle Size Analysis

PSD's for 0.01 mg/ml SFGO and LFGO, obtained by DLS, are shown in Figure 4.1; the horizontal axis of the plot is shown with logarithmic index, base 10.

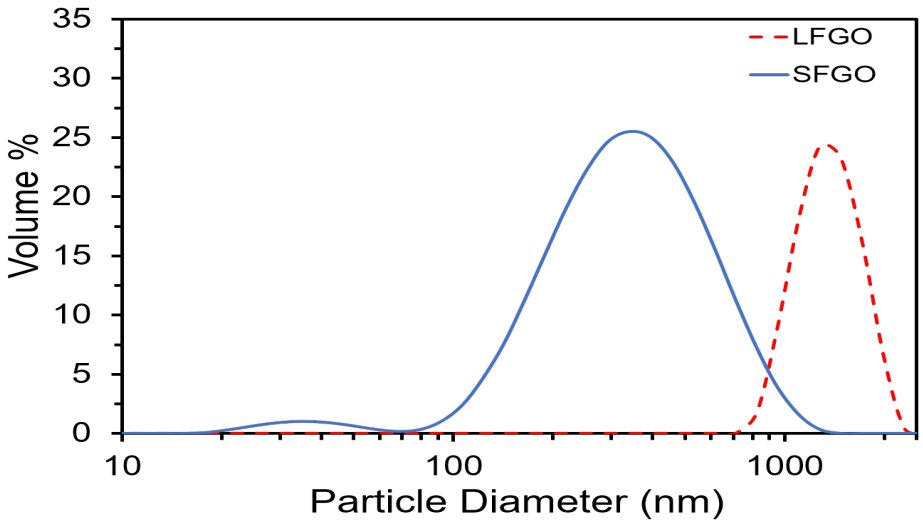

Figure 4.1: Particle size distribution (PSD) of 0.01 mg/ml SFGO and LFGO dispersions, obtained by Dynamic Light Scattering (DLS) analysis. Horizontal axis is shown on a logarithmic scale.

In DLS analysis, parameter Z-Mean particle size is commonly reported as a stable parameter to describe the particle size (as discussed in Section 3.8). Z-Mean sizes, as calculated by the *Zetasizer* software, for SFGO and LFGO are reported in Table 4.1.

Table 4.1: Z-Mean values of particle size in GO dispersions, measured by DLS.

GO	Z-Mean (nm)
SFGO	403
LFGO	1566

Inspection of the size distribution and Z-Mean values reveals that LFGO is indeed larger than SFGO, as the Z-Mean size is an order of magnitude larger, consistent with the shifting of the PSD of LFGO to larger values than SFGO. In addition, the modal peaks for each GO, in terms of Volume percentage, is 342 nm for SFGO and 1480

nm for LFGO, again confirming that by DLS analysis, LFGO is the overall larger. A concern regarding DLS analysis is the relatively limited size range of particles that may be analysed using the technique, as the limits of even a modern DLS system extends no further than approximately 10^0 - 10^1 μm, as DLS is a diffusion-driven technique [444]. It may be seen in particular with the LFGO sample that the Z-Mean size is in excess of 1 μm, thus limiting the potential suitability of the technique.

The anologous PSD's for SFGO and LFGO, obtained by LD, are shown in Figure 4.2. Again the particle diameter axis is shown in logarithmic scale.

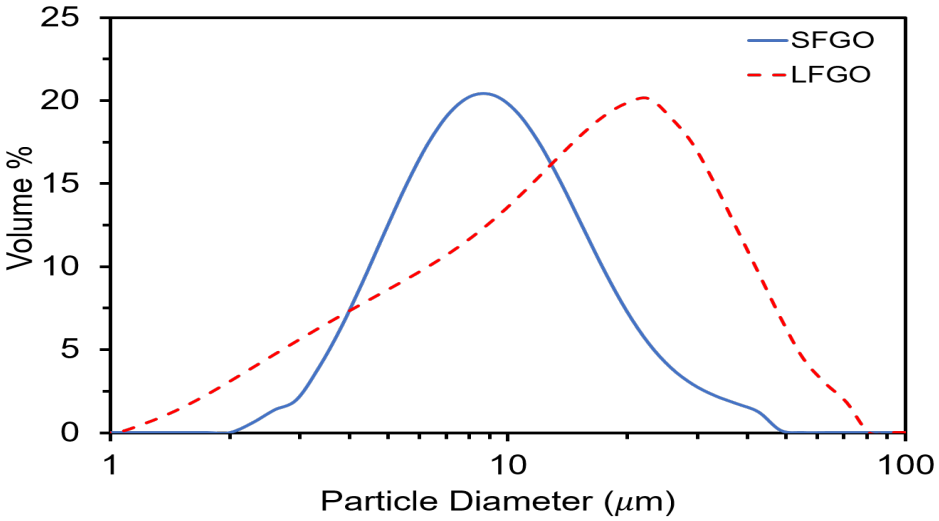

Figure 4.2: PSD of 0.01 mg/ml SFGO and LFGO dispersions, obtained by Laser Diffraction (LD).

In LD, PSD's are described by the percentile particle sizes, d(10), d(50) and d(90) (as discussed in Section 3.8). Percentiles were calculated for both samples by the *Mastersizer* software; these values are tabulated in Table 5.9.

Table 4.2: d(10), d(50) and d(90) values of particle size in GO dispersions, measured by LD technique.

GO	d(10) (μm)	d(50) (μm)	d(90) (μm)
SFGO	4.4	9.0	18.8
LFGO	3.5	13.3	29.6

It is again evident from LD analysis that the size distributions of LFGO are larger relative to SFGO, as the respective median and d(90) size values and the modal peak size are all larger. The size distribution of LFGO is very broad, with some very small flakes of size order 10^0 μm, and some very large clusters of size order 10^2, that are very likely to be aggregated sections of flakes. The LD distributions indicate that the respective particle sizes are of comparable order relative to those reported in the literature for GO dispersions [445]. Compared to DLS, LD has far greater sizing capabilities and may be suitable for analysis of particles up to 10^3 μm in size [446]. Given that the median particle size of both GO's was of the order 9 - 13.3 μm, it is considered that the median set of particles is beyond the limits of DLS, thus implying that LD is the more suitable technique.

Alternate and commonly used sizing techniques involve the use of microscopes such as SEM [447, 448], in order to image the dried material and estimate the lateral sizes. In this study, the use of light scattering techniques LD and DLS was preferred, for two reasons. Firstly, the adsorption studies (in the next chapter) were carried out using aqueous dispersions of GO, it was considered a better approximation to obtain PSD's for the GO in dispersed state. Secondly, when GO is dried for SEM it tends to aggregate as a result of evaporation of water from the sample, even at very low mass concentration, due to the effects of capillary bridging forces, potentially giving misleading information regarding flake sizes [449]. As such, DLS and LD were selected as the chosen methods of particle sizing: recent studies have demonstrated the applicability and suitability of

light-based techniques for GO flake sizing [450].

4.3.2 Brunauer-Emmett-Teller Analysis

BET surface area and pore volume analysis of SFGO and LFGO powders is tabulated in Table 4.3.

Table 4.3: BET analysis of SFGO and LFGO, including both specific surface area and total pore volume, measured during gas adsorption.

GO	BET Surface Area (m^2/g)	Total Pore Volume (cm^3/g)
SFGO	85.7	0.0535
LFGO	22.7	0.0234

BET analysis revealed that the SSA of SFGO relative to LFGO is a factor of four larger, while the TPV was a factor of two larger. Considering that one application of these materials is in dye adsorption (in the next chapter), SFGO therefore has a greater volume of pores and surface area, which may assist in the adsorption process by offering greater adsorption site contact area, per unit mass, compared to LFGO. In Section 4.3.1, DLS and LD analysis confirmed that the particle size of SFGO was an order of magnitude smaller than LFGO. The greater SSA and TPV of the SFGO system is consistent with expectation given the overall smaller flakes [451]. The obtained SSA value for the GO's is consistent with values found in literature [452], thus confirming the validity of measurement.

BET nitrogen isotherm adsorption - desorption plots, for SFGO and LFGO are shown in the Appendix (Figure A.1(a) and (b), respectively). The adsorption/desorption of nitrogen by both GO's is revealed to follow a Type IV isotherm, which suggests the materials are mesoporous (having pore sizes 2 - 50 nm [453]). The gaseous desorption stage demonstrated a hysterisis loop at high values of relative pressure. Examples from literature have also exhibited this adsorption profile [454]. In this isotherm, the surface

mesopores fill with adsorbed nitrogen at low and intermediate gaseous pressure, with multilayer formation onsetting at intermediate pressure, before capillary condensation occurs at higher pressure [455].

4.3.3 FTIR Spectroscopy

FTIR analysis of SFGO and LFGO powders are shown in Figure 4.3, in wavenumber range 4000 - 0 cm^{-1} in signal transmission mode. Salient bonding transmission peaks, with the associated functional groups, are labelled on the spectra for both materials.

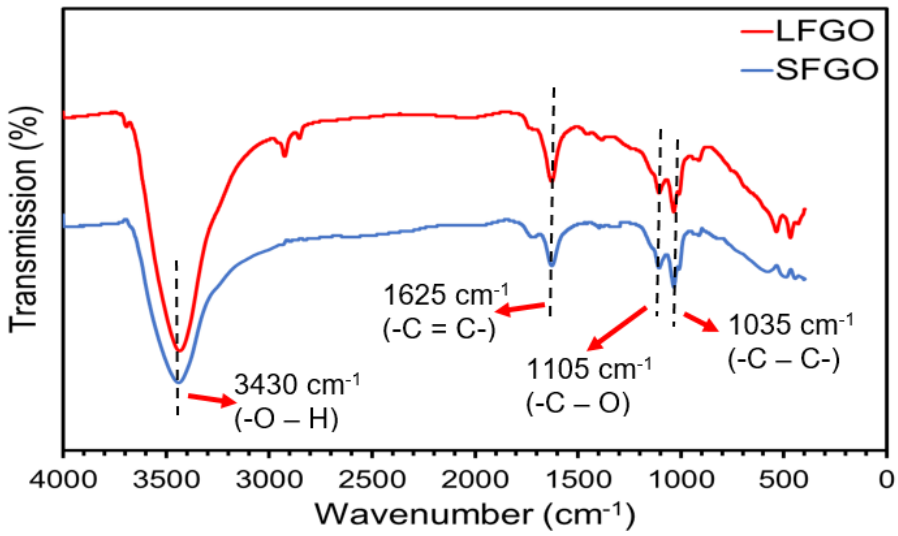

Figure 4.3: Fourier Transform Infrared (FTIR) spectroscopic analysis of commercial GO materials, SFGO and LFGO. Spectra are shown in wavenumber range 4000 - 0 cm^{-1}.

Inspection reveals that the spectra have strong resemblance to one another, suggesting a gross overall similarity in the overall chemistry and functional group presence within the materials. SFGO and LFGO both contain a broad and strong absorbance peak at 3430 cm^{-1}, attributed to an -OH hydroxylic stretch [279]. Bands situated at 1625 cm^{-1} are indicative of - C = C - stretching [456]. Further peaks present in the

materials at 1105 cm^{-1} and 1035 cm^{-1} are indicative of vibrational stretching, of C - O and C - C groups, respectively [457]. The spectra achieved for both GO materials, and corresponding bonding peaks in the samples are similar to a number of similar spectra from the literature: [458, 459]. This was expected given the likely synthetic pathway for manufacture of the GO materials.

4.3.4 Raman Spectroscopy

Raman spectrum of GO is characterised by the presence of two high intensity bands, both of which have Raman Shift values <2000 cm^{-1}, separately referred to as the D and G bands. For GO, the D band is typically observed at approximate Raman Shift 1350 cm^1, while the G peak is observed at approximately 1600 cm^1 [157]. The G peak corresponds to in-plane stretching motion of the E_{2g} phonon in sp^2 C - C bonds [460]. The G peak may be present in all carbon structures [461]. D peak presence is arisen from secondary, out-of-plane vibrations of bonds within the sample, during the breathing mode of aromatic rings [462]. This band is permissbile in structures with inherent defects, as such it is rather typical for GO, as the introduction of oxygen containing groups gives rise to an abundance of aberrations, including edge artefacts, folds and vacancies [463, 464]. These defects have an impact upon the Raman scattering of light properties, resulting in the emergence of the D band.

Raman spectra of SFGO and LFGO are shown in Figure 4.4. The respective D and G bands are labelled on the plots. The peak positions of the bands are taken as the value with highest signal intensity. For SFGO, D and G bands are positioned at 1354 cm^{-1} and 1604 cm^{-1}, respectively, while for LFGO the D and G bands are at 1353 cm^{-1} and 1605 cm^{-1}. In addition, in both spectra, there appears to be non-zero intensities, having significantly lower magnitude than either of the D or G peaks, recorded at higher shift values (*c.a.* 2700 cm^{-1}). This region is denoted the 2D band, and is dependent upon the number of graphitic layers in the sample.

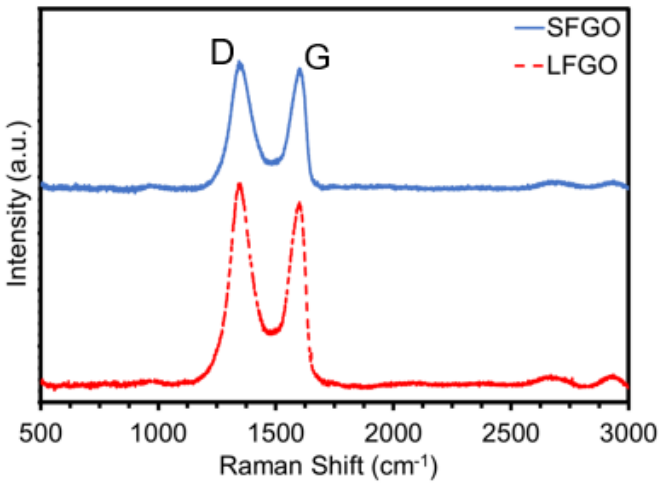

Figure 4.4: Analysis of SFGO and LFGO by Raman Spectroscopy. D and G peak positions are indicated on the spectra.

Magnitude ratio of the D and G peak intensities, denoted $I_D : I_G$ ratio, is a common and popular parameter used to characterise of the level of disorder within a graphitic material structure [465, 466]. There has, however, been conjecture over the stability of this parameter, as it has been argued that the D peak may be deconvoluted to a series of smaller peaks, thus the D peak may not be wholly representative of the defect ratio of the material [157, 462]. Additionally, the ratio is dependent upon the crystalline size; in some cases involving very small (<2 nm) crystals, it has been reported that the $I_D : I_G$ ratio can be high regardless of defect presence [467]. The calculated $I_D : I_G$ ratios for SFGO and LFGO are tabulated in Table 4.4.

Table 4.4: Calculated $I_D : I_G$ ratios of of SFGO and LFGO, obtained from Raman Spectroscopy analysis.

GO	$I_D : I_G$
SFGO	1.08
LFGO	1.10

For GO materials, it is common for the $I_D : I_G$ ratio to be approximately, or even

exceeding unity, thus suggesting the material possesses a high degree of disorder. This feature that results from the breakage of sp^2 carbon - carbon bonds and formation of new sp^3 bonds upon the insertion of oxygen and formation of carbon - oxygen bonds [468]. As such, the values obtained were typical of those in the literature [469, 470].

In the next section (Section 4.3.5, regarding XPS analysis), it is revealed that the oxygen content of both materials is high (>20%). Accordingly, it extends that the introduction of a high degree of oxygenation introduces a large number of structural defects in both GO's, thus accounting for the high I_D : I_G ratios. A further highly important conclusion is drawn from the fact that the defect ratio is shown to be high regardless of flake size. This feature is particularly relevant given the similarity of chemistry but difference in flake size.

4.3.5 XPS

Low resolution survey spectra of SFGO and LFGO are shown in Figure 4.5, across a range of photoelectron binding energies from 600 - 0 eV. The spectra clearly shows the presence of two high intensity peaks at respective binding energies 286 eV and 532 eV, corresponding to carbon and oxygen presence, respectively.

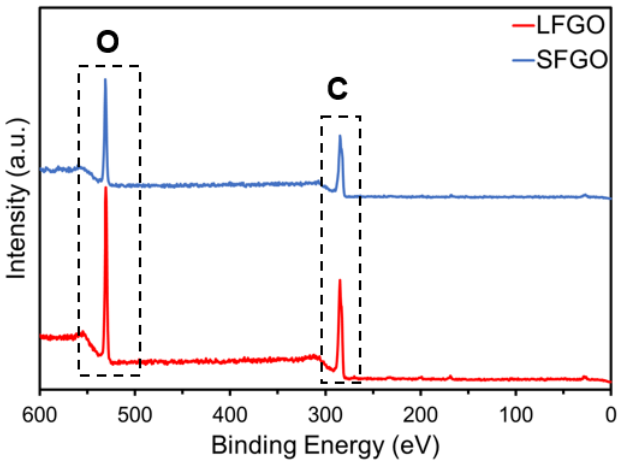

Figure 4.5: Low resolution XPS survey spectra of SFGO and LFGO. Two peaks were identified; positioned at binding energies 286 eV and 532 eV, corresponding to carbon and oxygen, respectively.

The percentage quantities of both species were quantitatively interpreted using *CASAXPS*; these quantitative results are tabulated in Figure 4.5.

Table 4.5: Quantitative analysis of XPS survey spectra of SFGO and LFGO, showing the percentage of elemental carbon and oxygen within the materials.

GO	Elemental C (%)	Elemental O (%)
SFGO	74.4	25.6
LFGO	71.9	28.1

Both materials are therefore shown to contain a high quantity of oxygen, this is typical for commercial GO materials as manufacturing processes typically introduce substantial magnitudes of oxygen functionality into the materials [471]. The oxygen presence in LFGO is demonstrated to be slightly higher compared to SFGO, a characteristic which is also reflective of the higher $I_D : I_G$ ratio obtained in Raman Spectroscopy. [469].

High resolution C1s spectra of SFGO and LFGO is shown in Figure 4.6(a) and (b),

respectively. These spectra reveal the identity of of all bonded C1s atoms within the materials. The profiles are observed to be composite two-peak spectra, each of which was deconvoluted to five peaks. A similar spectral deconvolution, in which GO spectra was deconvoluted to five peaks, was observed in [472]. The deconvolution revealed the presence of the following bonding groups, observed to be present in both samples: C = C (284.4 eV), C - C (284.6 eV), C - O (286.5 eV), C = O (287.5 eV) and COOH (289.3 eV). Functional groups such as these are within expectation for GO materials [19].

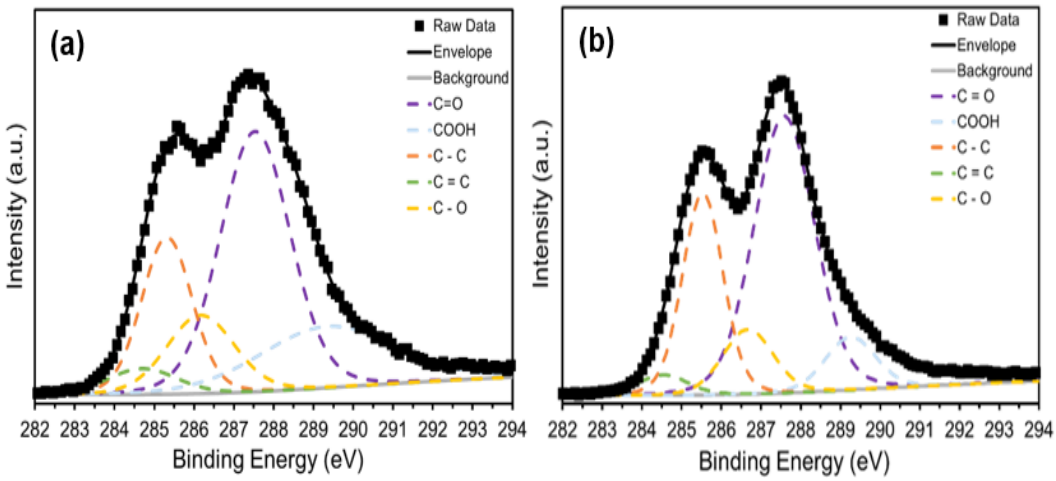

Figure 4.6: High resolution XPS C1s spectra of (a) SFGO and (b) LFGO.

High resolution O1s spectra of SFGO and LFGO is shown in Figure 4.7(a) and (b), respectively. In analogy to the C1s spectra, these reveal the summation of all bonded O1s atoms. The O1s profiles are observed to be composite one-peak spectra, each of which was deconvoluted to four peaks. Another similar O1s deconvolution, in which the spectra was deconvoluted to three peaks, was provided by [473]. The deconvoluted O1s spectra have the following peaks: C = O (530.5 eV), C - O - C (532.0 eV), C - O (533.3 eV) and O - H (535.5 eV). Again, peaks such as these are typical for the oxygen atoms present in a GO material [471].

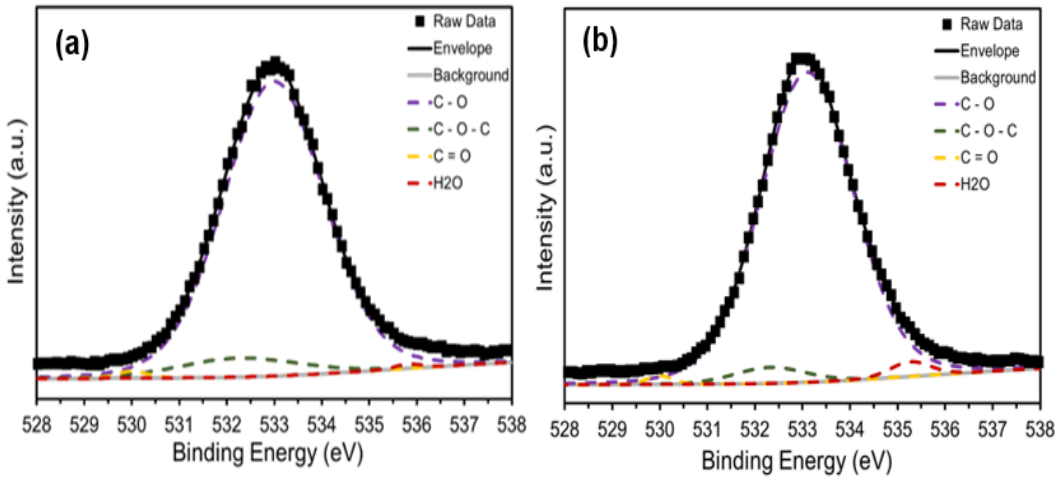

Figure 4.7: High resolution XPS O1s spectra of (a) SFGO and (b) LFGO.

Analysis of GO materials by combination of analytical spectroscopic techniques XPS and FTIR (Section 4.3.3) has therefore demonstrated a very powerful means of identifying atomic elements and functional groups present on the surface of GO materials. A number of the functional groups identified by XPS also had demonstrated their presence in FTIR analysis. The presence of heavily oxygenated groups on the GO surface is an important characteristic related to the adsorption of dyes by GO [474] (considered in the next chapter). Survey XPS analysis indicated that the overall oxygen quantities of both materials was quite considerable. High resolution C1s and O1s spectra revealed the presence of such groups as COOH, which are attractive targets for cationic dye adsorption, in particular, which may bind to the carboxyl-rich edges of the GO [474]. It is considered, then, that the substantial quantity of oxygen present in the GO's may have a significant impact upon their capacity to adsorb species in later parts of this work, and that the overall chemistry is independent of GO flake size.

4.3.6 X-ray Diffraction analysis of GO

XRD diffraction patterns of SFGO and LFGO powders are shown in Figure 4.8(a) and (b), respectively. Diffraction patters for both materials reveals the dominance of two peaks, one of very high intensity (labelled 1) and a second, of much lower intensity (labelled 2).

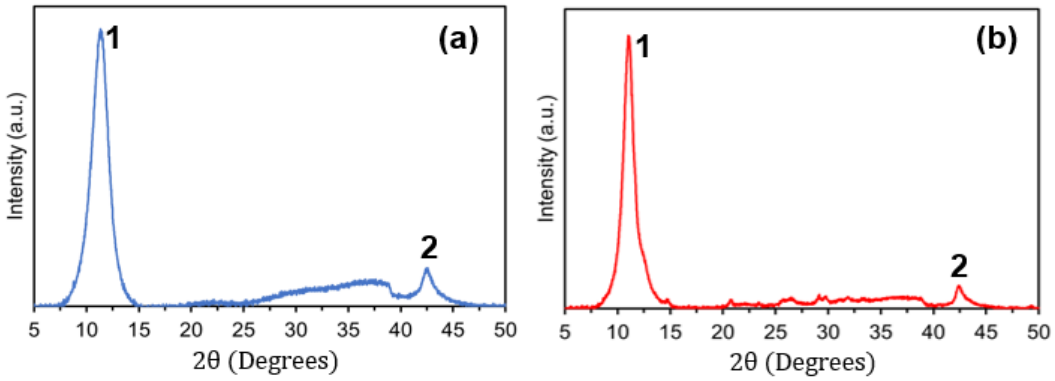

Figure 4.8: XRD patterns obtained for (a) SFGO and (b) LFGO.

Bragg Equation (Equation 3.4) was utilised to compute the d-spacings of both materials, at respective positions 1 and 2. The 2Θ peaks and associated d-spacings are tabulated in Table 4.6. The corresponding full width at half maximum (FWHM) for peak 1 has also been included in the table.

Table 4.6: 2Θ peaks and associated d-spacing of SFGO and LFGO, obtained by X-ray Diffraction analysis.

Peak number	2Θ (Degrees)	d-spacing (nm)	FWHM
SFGO			
1	11.34	0.780	1.61
2	42.5	0.213	
LFGO			
1	11.09	0.798	0.95
2	42.4	0.213	

These peak positions and d-spacings are consistent with those reported elsewhere in the literature as characteristic for GO materials (regardless of flake size) [279, 475]. Even higher d-spacings of GO materials have been found, with one GO having d-spacing 0.963 nm [476]. The interlayer spacings of GO materials measured by XRD are typically larger than those observed in alternative materials such as graphite, owing to the insertion of oxygen functionality at the edges of the sheets thus increasing interlayer electrostatic repulsion and contributing to the separation of layers [477]. The slightly larger d-spacing of LFGO compared with SFGO may be attributed to the particular arrangement of the oxygen-containing functional groups present within the material, and the location of the oxygen atoms that act as spacers [471]. Furthermore, the presence of peak 2 for both materials is indicative of stacking of unexfoliated GO layers [478]. The FWHM describes the width of the peak at intensity equal to half of the peak intensity: it may be seen that SFGO has higher FHWM than LFGO. The flake size of a species has been demonstrated to be inversely related to FHWM, as such, the wider peak of SFGO is consistent with its smaller flake size [479].

4.3.7 Zeta potential

GO-in-water dispersions

In later filtration experiments, SFGO and LFGO were coated onto PES, with GO concentration in coating 0.01 mg/ml or 0.10 mg/ml. In this section, zeta potential and pH of the 0.01 and 0.10 mg/ml samples were measured, as shown in Figure 4.9.

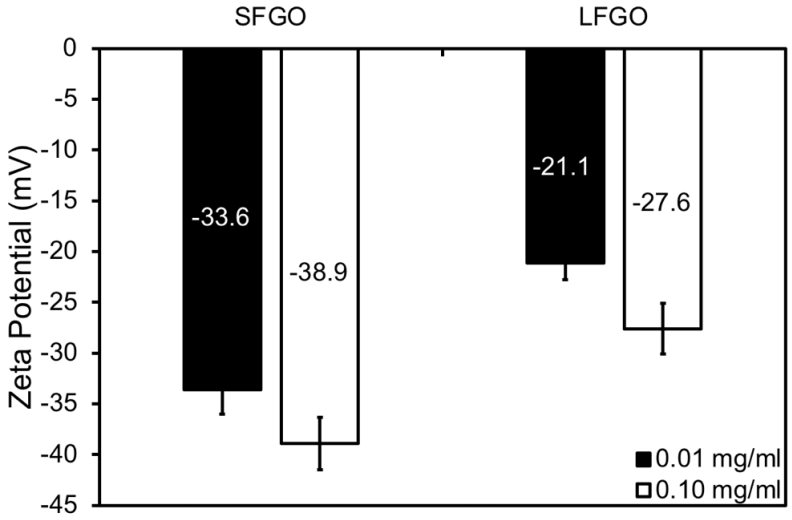

Figure 4.9: Zeta potential of 0.01 and 0.10 mg/ml aliquots of SFGO and LFGO, in distilled water.

The measured pH of each GO dispersion is reported in Table 4.7.

Table 4.7: pH of SFGO and LFGO, at respective concentrations 0.01 and 0.10 mg/ml.

Concentration (mg/ml)	pH SFGO	pH LFGO
0.01	3.48	3.42
0.10	3.35	3.33

It is apparent that the GO-in-water dispersions possess moderately acidic character without deliberate modification of the pH, as the deprotionation of hydrogen-containing

groups increases the hydrogen ion concentration in the water, thus lowering pH [480].

Both materials possess negative surface charge, as indicated by the negative values of zeta potential. Increasing the GO concentration from 0.01 to 0.10 mg/ml led to an increase in the magnitude of the zeta potential, for both GO's. It is considered that this occurs due to the increased electrostatic repulsion caused by the greater concentration of charge negativity in the higher concentration dispersions [481]. As such, coating of PES membranes with GO at respective concentrations 0.01 and 0.10 mg/ml therefore imparts electronegativity onto the surface of the polymer, a feature observed for both despite differences in flake size. This salient feature is a pivotal and governing characteristic of the membranes and will be explored in greater detail in later sections, in which the interaction of GO coating with charged species such as salts and dyes is explored. In addition, the SFGO dispersions are found to possess significantly higher zeta potential compared to LFGO: in accordance with Table 3.3, the SFGO dispersions have moderate - good stability, while LFGO has only incipient stability. It is proposed that the smaller flakes, owing to their greater surface area as demonstrated by BET analysis (Section 4.3.2), possess higher electronegative charge densities in the vicinity of the flakes. This leads to increased levels of electrostatic repulsion between flakes and thus greater overall zeta potential [482].

Impact of pH upon GO-in-water stability

Zeta potential, measured as a function of GO dispersion pH, of 0.01 mg/ml SFGO and LFGO, is shown in Figure 4.10.

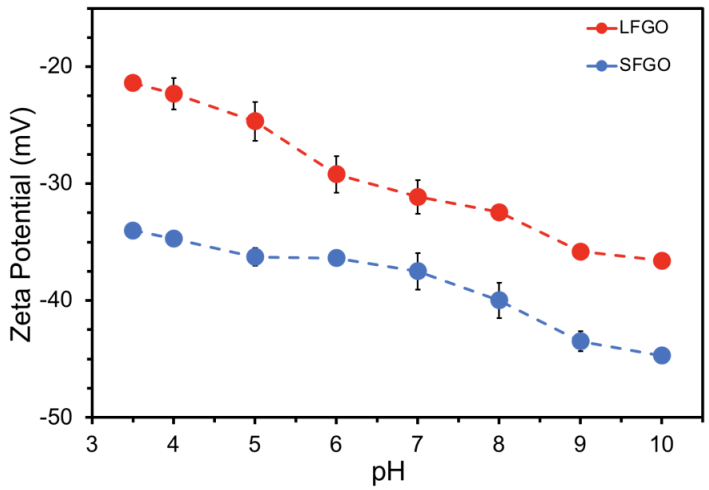

Figure 4.10: Zeta potential of 0.01 mg/ml SFGO and LFGO across a range of pH values from 3.5 - 10.0. pH was adjusted using dilute sodium hydroxide.

Zeta potential response demonstrates that SFGO and LFGO exhibit increasing colloidal stability (indicated by increasing magnitude of zeta potential), subject to increasing pH in the range 3.5 - 10.0. SFGO exhibits the largest peak potential across the complete pH range, and has highest potential of -44.7 mV at pH 10.0, compared to that of LFGO, which had highest potential of -36.6 mV at pH 10.0. As the GO dispersions indicate negative charge overall, at high pH, hydrogen atoms present within the GO structure tend to deprotonate, an effect which becomes increasingly prominent as pH increases [483]. This results in increasing electrostatic repulsion of negatively charged (oxygen-containing) deprotonated functional groups in the GO, therefore increasing stability as pH increases. The high magnitudes of both negative zeta potentials across the complete pH range suggests that the GO's should be electrokinetically stable in water and be capable of resisting aggregation [232]. Zeta potential of SFGO and LFGO was not explored beyond pH 10, as very high pH has been shown to cause contraction of the electrical double layers, therefore potentially limiting the accuracy of zeta potential measurement [484].

Impact of electrolyte presence upon GO-in-water stability

Measurement of zeta potential was used to characterise the impact of electrolyte presence upon the stability of GO, for 0.01 mg/ml GO in distilled water. Zeta potential, measured as a function of electrolyte concentration, across the range of concentrations 0 - 10 g/l, is shown for SFGO and LFGO in Figures 4.11(a) and (b) respectively. The salts used for this investigation were sodium chloride, sodium sulphate, magnesium sulphate and ammonium heptamolybdate.

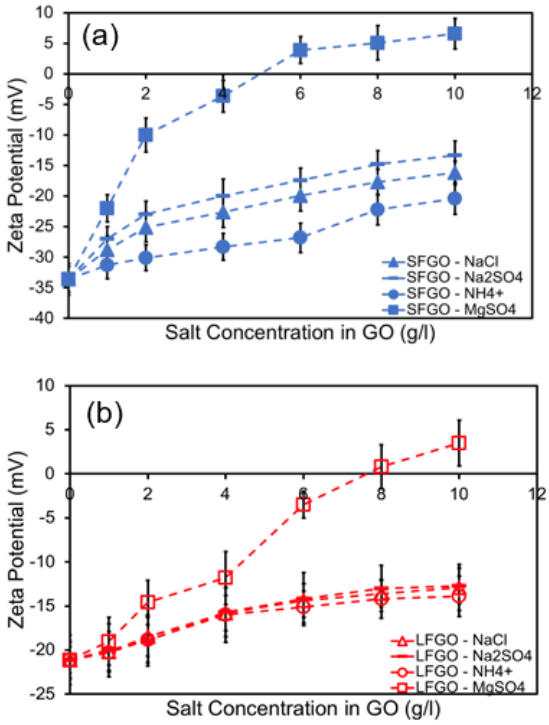

Figure 4.11: Zeta potential of electrolytes dispersed in 0.01 mg/ml (a) SFGO and (b) LFGO aqueous dispersions. Salts sodium chloride, sodium sulphate, magnesium sulphate and ammonium heptamolybdate were used. Electrolyte concentrations were adjusted to 0, 1, 2, 4, 6, 8 or 10 g/l.

The results indicate that there is a general decrease in the magnitude of zeta potential, as electrolyte concentration is increased from 0 - 10 g/l. Increasing the electrolyte

concentration has the effect of increasing the number of cations in the dispersion. The valency of the cations in the respective salts are as follows: sodium sulphate and sodium chloride possess monovalent Na^+ cations and ammonium heptamolybdate possesses monovalent NH_4^+, meanwhile magnesium sulphate has Mg^{2+} cations. For both SFGO and LFGO, addition of magnesium sulphate has significantly greater impact upon the zeta potential compared to the three monovalent cationic salts. At sufficient ionic concentration, addition of divalent magnesium sulphate resulted in charge neutralisation and ultimately, charge reversal, as evidenced by the zeta potential becoming positive, in both GO systems. Addition of cations beyond the point of charge neutralisation results in the overall positive zeta potential. The divalent Mg^{2+} cation has evidently greater destabilising impact upon the electrokinetic properties of the GO dispersion, due to its strong interaction with GO flakes, in particular those of smaller size [232]. The impact of electrolyte presence upon the dye adsorption capabilities of GO is later explored (Section 6.4); the results obtained regarding zeta potential will be revisited in these later discussions.

4.3.8 Scanning Electron Microscopy/Energy Dispersive X-Ray spectroscopy

Images of SFGO and LFGO, captured during SEM analysis of the materials, is depicted in Figure 4.12(a) and (b), respectively.

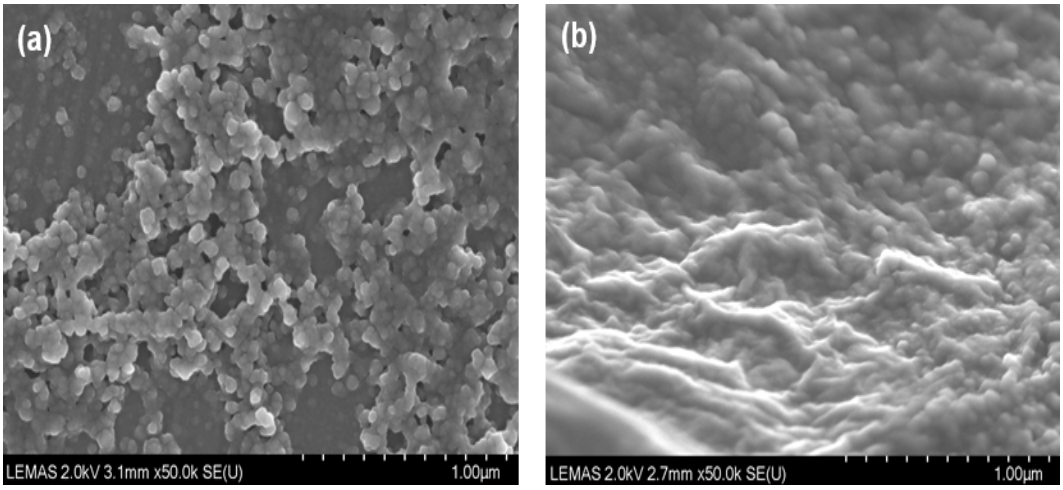

Figure 4.12: SEM image of (a) SFGO and (b) LFGO. Both images captured at 50,000X magnification, with scale bar set at 1.00 μm.

The surface morphologies of both GO's were revealed to be highly disordered, with randomly aggregated sections of stacked and overlapping flakes. LFGO, in particular, was observed to possess a number of surface wrinkles and crumpled sections, which may have resulted from randomly stacked layers of thin nanosheets [476]. Both materials do however possess nanoscale size features, having dimensions significantly less than 1 μm. As discussed in Section 4.3.1, SEM imaging of dispersions is faced by a number of challenges, as the liquid component must be dried prior to contacting the sample with the ultra high vacuum of the SEM, resulting in aggregation of particles within the dispersion as the liquid is removed. As such, the GO aggregation observed was likely an artefact of these effects; even at low concentration, the degree of aggregation within the dispersions appears too high for imaging singular, exfoliated flakes. This feature is observed regardless of flake size, though the aggregation appears to be of greater extent in LFGO systems.

A summary of EDX analysis of both materials is presented in Table 4.8, revealing the contents in terms of atomic percentages of Carbon and Oxygen. The EDX spectra

of SFGO and LFGO is shown in the Appendix (Figure A.2(a) and (b), respectively).

Table 4.8: EDX spectroscopic analysis of SFGO and LFGO, showing the percentage makeup of elemental carbon and oxygen within the materials.

GO	Elemental C (%)	Elemental O (%)
SFGO	72.3	27.7
LFGO	68.9	31.1

EDX analysis determined that carbon was the dominant element in both materials, with a secondary contribution from the oxygen signal. The EDX composition of oxygen in SFGO and LFGO was demonstrated to be consistent with the results achieved in XPS survey spectra (Figure 4.5), with LFGO shown to possess higher overall oxygen content than SFGO.

4.4 Results and Discussion: Characterisation of GO-coated PES membranes

4.4.1 Membrane stability investigations

Stability of GO-coated membranes subject to contact with water was investigated by immersing the membranes in 150 ml distilled water in a glass beaker for a period of 24 hours. Following this, the water was poured out and the appearance of the membranes was visually inspected. Samples of the respective dry and hydrated membranes, with 0.01 mg/ml and 0.10 mg/ml SFGO and LFGO coatings, is shown in Figure 4.13.

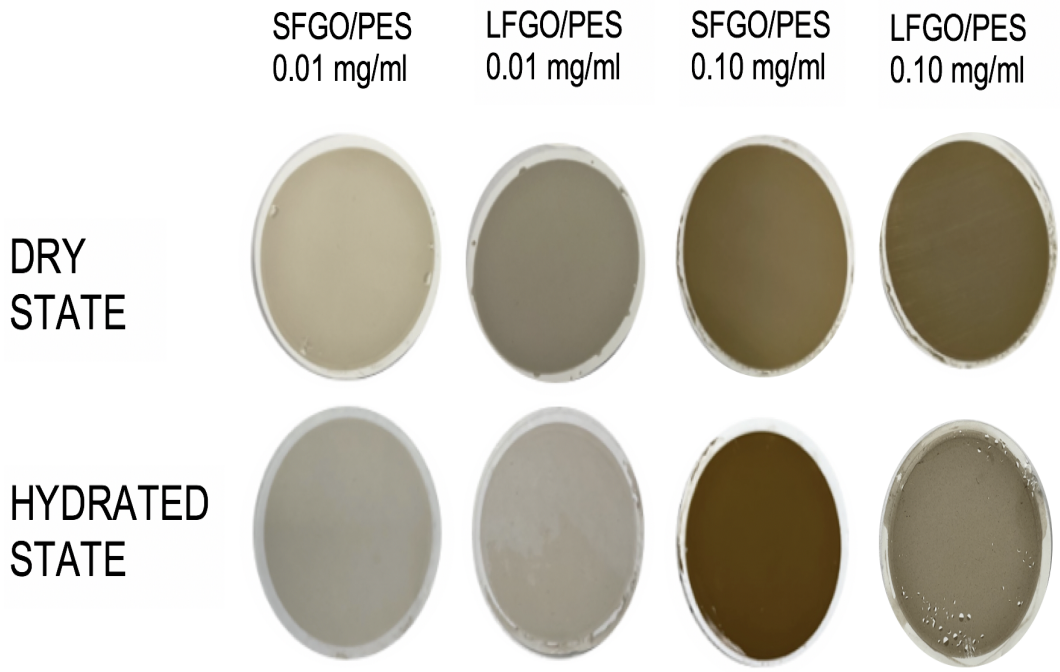

Figure 4.13: Dry (Top row) and hydrated (Bottom row) SFGO- and LFGO-coated membranes. Hydrated state images were taken following 24 hour immersion of the membranes in distilled water.

Inspection of the images for 0.01 mg/ml and 0.10 mg/ml SFGO and 0.01 mg/ml LFGO coatings reveals that these membrane coatings do not appear by eye to show obvious signs of macroscopic damage or delamination subject to an immersion period in water, with no visible differences resulting from the immersion.

The LFGO 0.10 mg/ml coating, however, does clearly exhibit physical changes following immersion in water. It appears that the coating suffers macroscopic damage, as small sections are chipped and cracked, revealing the white coloured polymer substrate below the coating layer. This effect was observed upon immediate immersion of membrane in water. Figure 4.14 shows the LFGO 0.10/PES membrane after in hydrated state, with the damaged section expanded.

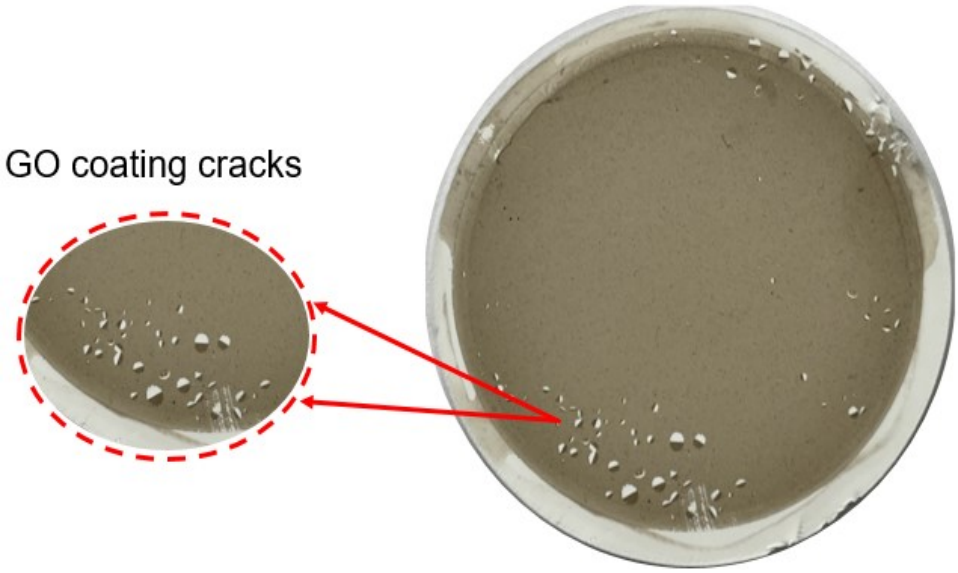

Figure 4.14: Hydrated state LFGO/PES 0.10 mg/ml membrane. Surface cracks appear on the coating following contact with water, these sections are expanded.

Cracking of the coating may certainly not be considered advantageous in terms of promoting performance of the membranes. In fact, in subsequent chapters, this membrane was found to be poorer at rejecting salts and dyes compared to the 0.01 mg/ml coating of LFGO, which does not show visible signs of cracking. Efforts were made to overcome the surface cracking, including rinsing the PES membrane in distilled water prior to coating the GO onto substrate. This was carried out with the intention of washing away any resident particles or contaminants on the surface of the PES, that may have caused damage to the coated surface during wetting. Unfortunately, this proved unsuccessful, as the cracks still persisted. The immersion experiments were carried out with 0.10 mg/ml coatings of LFGO in total ten times, with the PES rinsed in the aforementioned manner each time. All ten coatings were found to crack in a comparable manner as observed in Figure 4.14.

Water uptake capacity of the uncoated PES and GO-coated membranes was inves-

tigated by immersing the membranes in 150 ml distilled water, in analogous fashion to the above. The dry-state mass of the membranes was measured prior to immersing in distilled water. The mean masses and standard deviation (σ) of each membrane is tabulated in Table 4.9.

Table 4.9: Dry state masses of PES, SFGO and LFGO coated membranes. σ represents the standard deviation of masses, measured across three membrane samples.

Membrane	Dry-State mass (mg)	σ
PES	72.30027	0.73
SFGO/PES 0.01 mg/ml	72.30028	0.64
SFGO/PES 0.10 mg/ml	72.30035	0.69
LFGO/PES 0.01 mg/ml	72.30029	0.98
LFGO/PES 0.10 mg/ml	72.30035	1.02

Water uptake percentage ($W(\%)$) is calculated by considering the relative difference in dry state mass (W_{Dry}) and hydrated state mass ($W_{Hydrated}$) of the membranes, utilising Equation 4.1 [485]:

$$W(\%) = \left(\frac{W_{Hydrated} - W_{Dry}}{W_{Dry}}\right) \cdot 100\% \tag{4.1}$$

The calculated values of $W(\%)$ for uncoated PES and GO-coated membranes are depicted in bar chart format, in Figure 4.15.

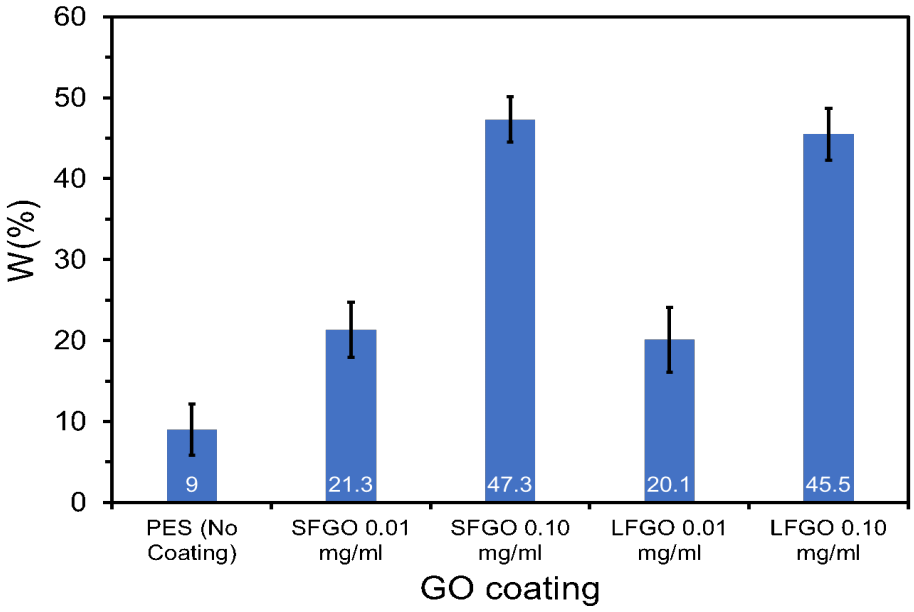

Figure 4.15: Calculated W(%) values of the uncoated PES and 0.01 and 0.10 mg/ml SFGO- and LFGO-coated PES membranes. Error bars represent standard deviation across three different membrane samples.

The uncoated PES achieved the lowest overall water uptake, as the mean mass increase was only 9%. For GO-coated membranes, the value of *W(%)* was found to increase with GO coating concentration: similar behaviour was observed in [486]. Owing to the presence of oxygenated groups, GO possesses hydrophilic characteristics [487, 488]. The parameter *W(%)* is highly sensitive to the hydrophilicity of the membrane and may be increased by providing a greater overall concentration of hydrophilic groups within the membrane fabrication, as these groups have strong tendency to intercalate water molecules [489]. Uncoated PES is assumed to be the least hydrophilic, with a GO content of zero, as such the value of *W(%)* for the unmodified polymer was lowest overall. The value of *W(%)* for the 0.10 mg/ml LFGO coating was 34.7%, which is lower than the *W(%)* for the analogous 0.10 mg/ml SFGO coating (47.3%).

It is considered that this discrepancy is a feature of the cracking of the LFGO coating, which may result in material (and therefore mass) losses of GO coating and impacting the membrane mass in hydrated state. An interesting initial observation is that the SFGO coatings achieved higher values of *W(%)* overall, despite the demonstration of greater oxygen content in the LFGO system, by XPS (Table 4.5) and EDX (Table 4.8). This feature will be furthered as part of a general discussion regarding hydrophilicity of the membranes in Section 4.4.5, regarding Water Contact Angle of membranes.

4.4.2 FTIR analysis of GO-coated PES

The FTIR spectra obtained for commercial, unmodified PES is shown in Figure 4.16. Bonding peaks were found to be present for wavenumbers <2000 cm^{-1}, as such, the spectra is expanded into the wavenumber range 2000 - 400 cm^{-1}. A number of salient bonding peaks, which give insight into the nature of PES, are labelled on the spectra. The full spectra for PES, in wavenumber range 4000 - 0 cm^{-1}, is shown in the Appendix (Figure A.3).

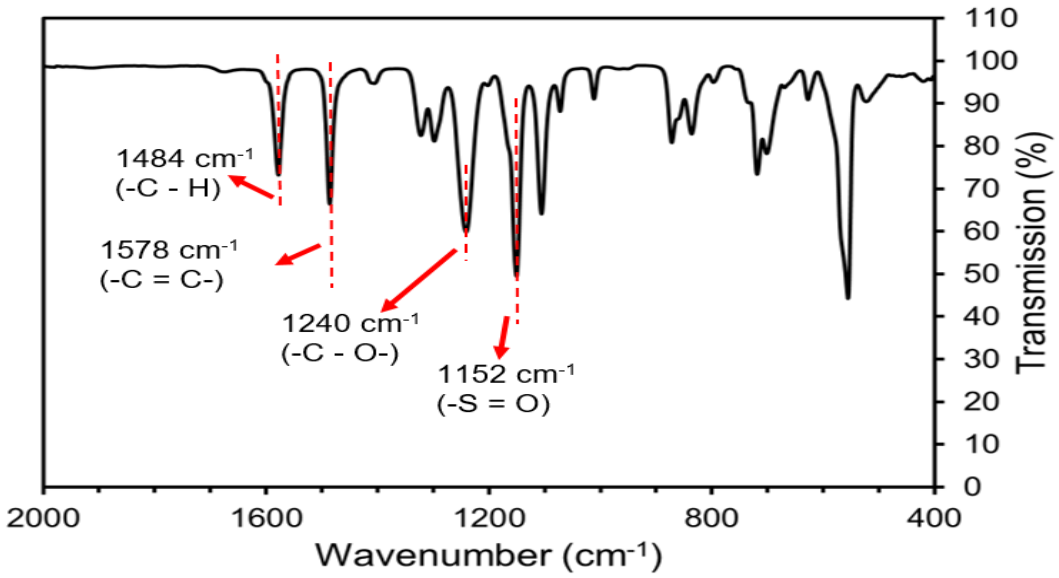

Figure 4.16: FTIR analysis of commercial polyethersulfone (PES) membrane. Spectrum is shown in wavenumber range 2000 - 400 cm^{-1}.

As indicated on the spectrum, the PES peaks are situated at 1578 cm^{-1}, 1484 cm^{-1}, 1240 cm^{-1} and 1152 cm^{-1}, which have been assigned to the following functional groups, respectively: C = C, C - H, C - O and S = O [490].

FTIR spectra were obtained for each of the SFGO- and LFGO-coated PES membranes, with GO coating concentrations 0.01 and 0.10 mg/ml. Spectra of GO-coated PES, and pure (uncoated) PES membrane is presented in Figure 4.17, in the range 2000 - 0 cm^{-1}. The full 4000 - 0 cm^{-1} spectra is shown in the Appendix (Figure A.4).

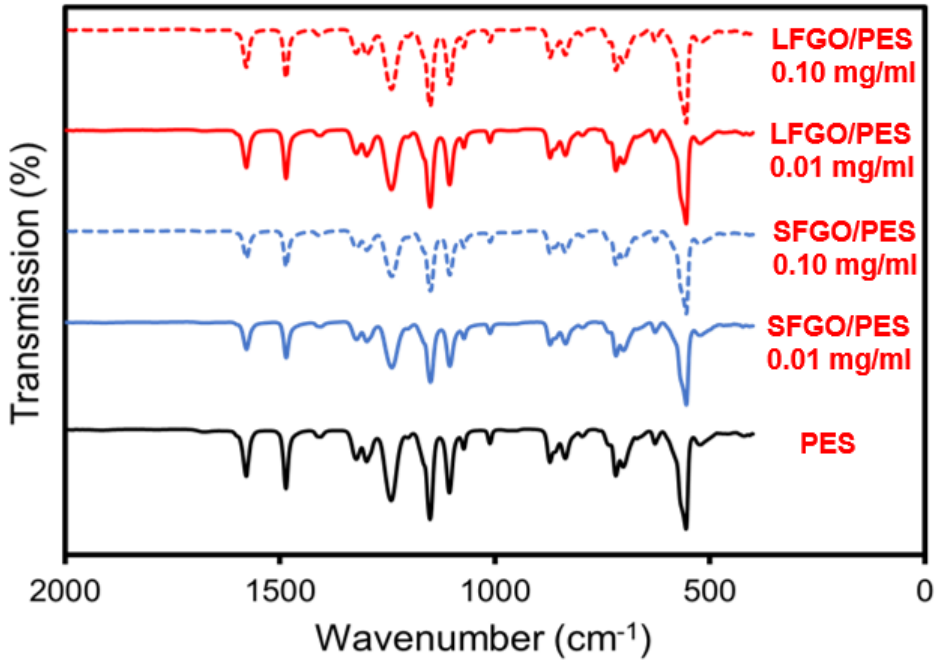

Figure 4.17: FTIR analysis of commercial PES membrane, and SFGO- and LFGO-coated membranes. Spectra are shown in wavenumber range 2000 - 0 cm^{-1}.

FTIR analysis revealed that the traces given by all four of the GO-coated substrates were identical to pure PES: as such, the presence of GO surface coating does not introduce any new bonding peaks. Recorded wavenumber positions for any peaks which were identified for PES are not shifted by GO coating. Furthermore, the magnitude of peak intensities which were recorded for PES are neither diminished nor enhanced by GO coating. In terms of the surface chemistry, the identical nature of the spectra suggests that the application of GO coating does not chemically alter the PES surface. Any interaction between GO and PES, therefore, is not chemical in nature, as there is no modification to the surface chemistry. It may also be concluded that the FTIR spectra (and in turn the chemistry of PES substrate) is unaffected by the concentration of GO used in the coating, as the signals for 0.01 and 0.10 mg/ml coatings are identical to one

another, and to PES. Similar behaviour was noted in [491], in which GO was deemed to act as a filler material in a GO-PES membrane, showing no chemical interaction with the membrane. Different behaviour was, however, observed by [492], in which a new bonding peak at 1480 cm^{-1}, corresponding to incorporation of a benzene ring from GO, was identified following reaction of GO with PES.

4.4.3 X-ray Diffraction analysis of GO-coated PES

XRD analysis of GO coated membranes was utilised as a means to evaluate the inter-layer spacing of the GO coating. XRD diffraction patterns of the SFGO- and LFGO-coated PES membranes, in angular scan range $5° < 2\Theta < 25°$, is shown in Figure 4.18.

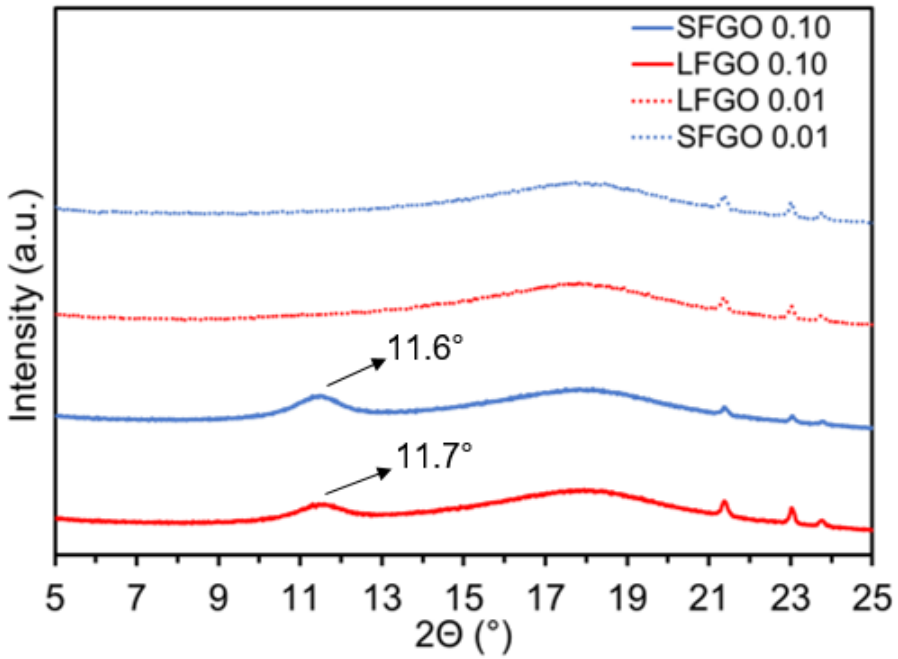

Figure 4.18: XRD analysis of GO-coated PES membranes.

The patterns of all four samples reveal a very broad, hump-like peak centred around

$2\Theta = 18°$. This peak is attributed to the underlying PES substrate, indicating the semi-crystalline nature of the material [15]. Two low intensity peaks are observed at $2\Theta = 21.4°$ and 23.0°, due to the copper sample holder. The diffraction pattern of the sample holder, recorded in the absence of sample, shown in the Appendix (Figure A.5), reveals the two peaks in identical positions, thus confirming their identity.

The two samples with higher concentration of GO (Figure 4.18) display broad peaks around 11°, as indicated on the separate diffraction patterns; these peaks are ascribed to the presence of the GO coating. For the LFGO membrane, the peak is positioned at $2\Theta = 11.7°$; by Bragg Equation (Equation 3.4), this corresponds to a d-spacing of 0.76 nm. Analogously, for SFGO, the peak is relatively low amplitude, positioned at $2\Theta = 11.6°$, corresponding by Bragg's Law to a d-spacing of 0.76 nm. The broad nature of the GO peaks implies that the samples possesses a low degree of crytallinity [493]. Comparison of these d-spacings to the literature reveals that the values for GO/PES membranes are consistent with other studies [493, 494]. In contrast, the two lower concentration GO membranes do not appear to show distinguishable XRD intensity in the identified GO region, as such, an associated diffraction peak is not evident. Similar behaviour was noted by Peng *et al.* [495], who studied 2 and 4 mg loadings of GO into PES membranes and obtained no discernible GO diffraction peak for the lower mass 2 mg sample. It was considered that the lower loading resulted in a structure with overall lower levels of disorder, thereby making the diffraction peak have negligible intensity. A second proposal is that the GO layer is simply too thin to provide substantial diffraction of X-rays in addition to that of the PES [496]. This second proposal is perhaps more intuitive for our GO systems, given that the GO concentration is greater by a factor of ten in higher versus lower concentration coatings, therefore providing greater potential for scattering, regardless of GO flake size.

The phenomenon of GO layer swelling (Section 2.5.2 of the literature review), due to intercalation of water amongst the layers during filtration testing, presents a major

practical challenge for the application of GO membranes in desalination. It was discussed that this effect is particularly prominent for membranes that have no control over layer swelling, such as those prepared by vacuum filtration (also highlighted in literature review Section 2.3.1). In order to investigate the swelling of GO membranes when in hydrated state, the XRD diffraction patterns of membranes that had been dried following overnight immersion in water were obtained. These are shown in Figure 4.19.

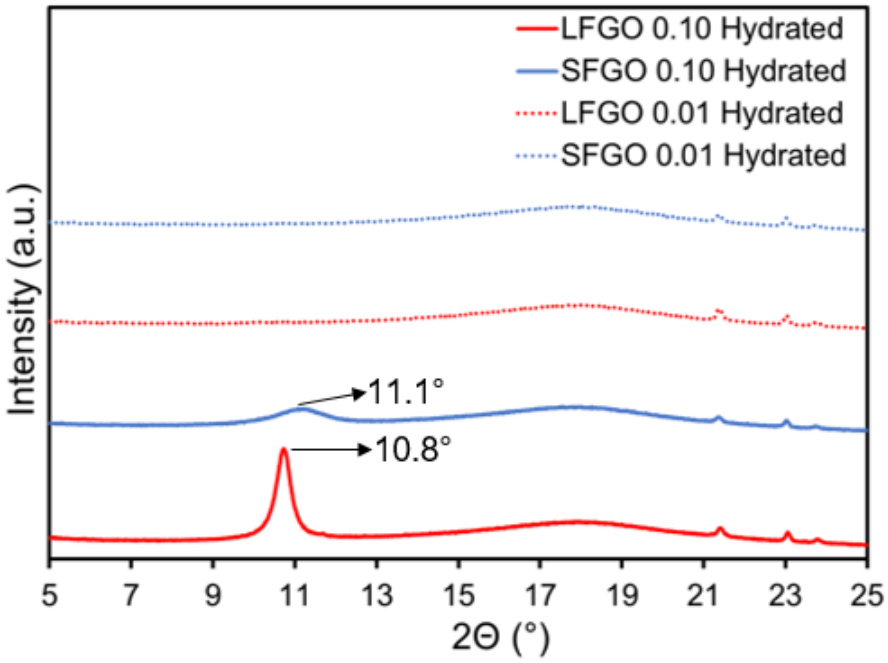

Figure 4.19: XRD analysis of hydrated GO-coated PES membranes, which were dried following overnight immersion in distilled water.

The higher GO concentration membranes show tendency to swell in water, as the diffraction peaks are shifted to lower 2Θ angles following immersion in water, corresponding to an increase in interlayer spacing. The uptake of water by GO-coated membranes was earlier demonstrated (Figure 4.15), as such the changes in diffraction pattern are consistent with this behaviour. For LFGO membranes, the peak shifts to

$2\Theta = 10.8°$, such that the d-spacing is increased to 0.82 nm. Meanwhile, for SFGO, the peak shift was slightly less, to $2\Theta = 11.1°$, such that the d-spacing increased to 0.80 nm, evidencing a slightly greater shift for the larger flake systems. The lower concentration GO membranes again exhibit no distinguishable GO diffraction peak. At this stage, it is considered that these changes to the GO microstructure may have an impact upon the efficacy of the membranes in desalination; this will be revisited in later sections regarding desalination using GO membranes.

4.4.4 Thermal Analysis

A summary of the TGA thermograms, for PES membrane and GO-coated PES membranes, subject to heating the membranes to 900°C, is shown in Figure 4.20. The remaining mass percentage of the membrane sample is plotted as a function of temperature.

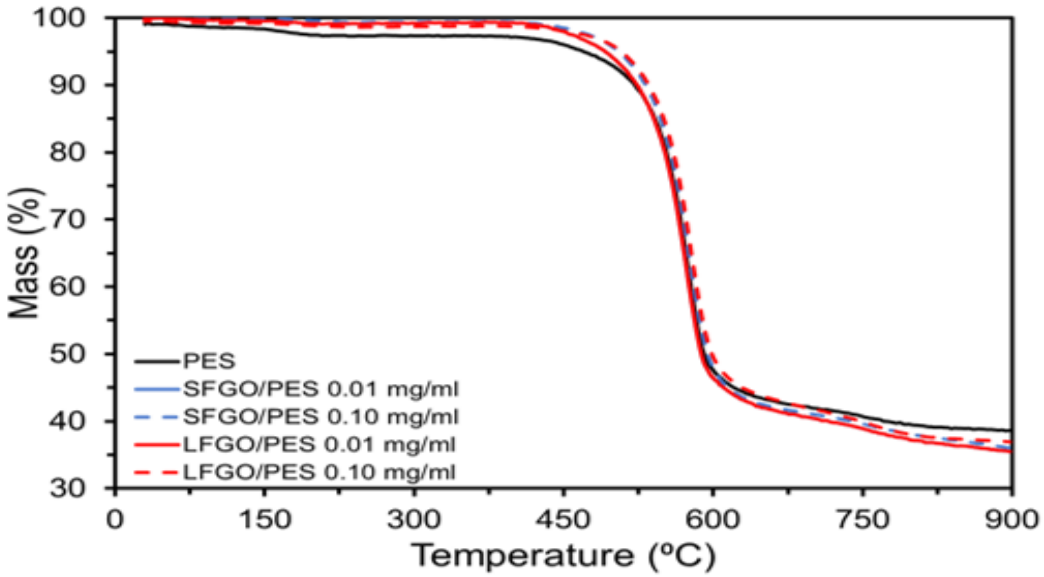

Figure 4.20: Thermogravimetric analysis (TGA) profiles of PES membrane and SFGO- and LFGO-coated PES membranes. Profiles are shown as remaining mass percentage of sample versus temperature.

Thermal response of all materials was demonstrated by TGA to follow a single step degradation profile, in which significant mass loss is observed at one stage only, ultimately leading to sample degradation. Percentages of mass loss were determined to be insignificant (<10%) for all membranes up to approximately 520°C, thus the membranes may be considered thermally stable in this temperature region, which is consistent with thermal response behaviour reported in literature for PES [497]. Slight mass losses in the lower temperature region may however be attributed to residual solvent loss [498]. Significant depletion of mass occurred in the temperature range 520°C - 600°C, due to degradation of the polymer chains that resulted in the release of gases likely including oxides of carbon [499]. Elevation of temperature beyond 600°C resulted in flattening of the degradation profiles and as the temperature reached the upper limit of 900°C, a stable carbonaceous ashen material was left [500].

The temperature at which mass loss from the sample is 3% ($Td_{3\%}$) has been used as a means of characterising the stability of a material and for comparison with others [501]. Figure 4.21 shows the $Td_{3\%}$ and accompanying standard deviation for each membrane.

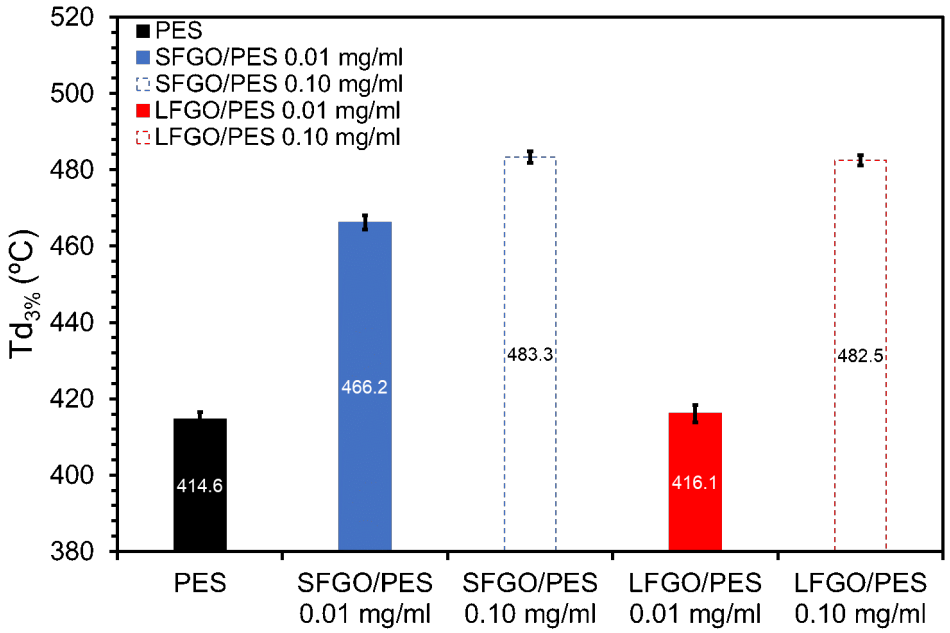

Figure 4.21: The temperature at which mass loss from the sample is 3% ($Td_{3\%}$) of PES membrane and SFGO- and LFGO-coated PES membranes. Vertical error bars represent the standard deviation across three samples.

It appears then that the $Td_{3\%}$ value is inversely related to GO coating concentration: increasing GO loading results in an increase in $Td_{3\%}$, thus confirming that the incorporation of GO in the fabrication improves the thermal stability of the membrane. Comparable behaviour has been reported in the literature, in which it has been shown that increasing the GO loading from 0 - 1.0 wt% resulted in greater thermal stability of GO/PES membranes [502]. The improvement in thermal stability due to incorporation of GO is owed to the strong adhesive forces at the interface between PES and coating GO layer, which enhance the ability to remain intact subject to heating [503]. The exception appears to be the LFGO/PES 0.01 mg/ml sample, in which the $Td_{3\%}$ was only marginally higher than the pristine PES sample, thus indicating that for this membrane there is poorer correlation for $Td_{3\%}$ value. It is speculated that this be-

haviour is a result of poorer interfacial adhesion between GO and PES, though this is indeterminate.

4.4.5 Water Contact Angle

Images of water droplets on the surfaces of uncoated and GO-coated PES substrates depicting the droplet shapes, used for measurement of contact angle, is shown in Figure 4.22.

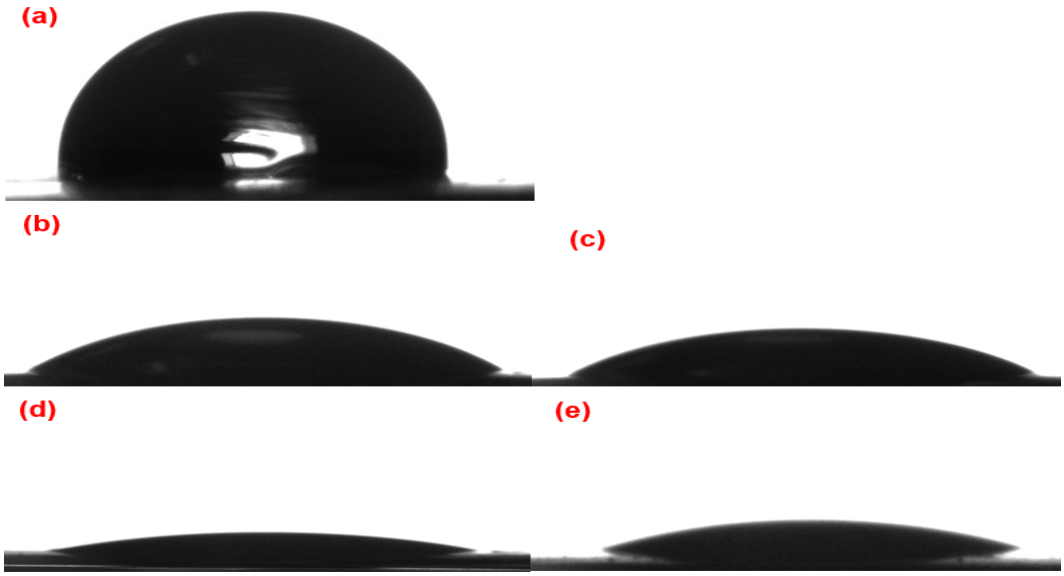

Figure 4.22: Droplet shapes of deposited water droplets, sitting atop (a) PES, (b) SFGO/PES 0.01 mg/ml, (c) LFGO/PES 0.01 mg/ml, (d) SFGO/PES 0.10 mg/ml and (e) LFGO/PES 0.10 mg/ml.

The associated mean values of Water Contact Angle and the standard error, for the five membranes is provided in Table 4.10.

Table 4.10: Water Contact Angle measurements for uncoated PES, 0.01 and 0.10 mg/ml SFGO- and LFGO- coated PES. Corresponding images are shown in Figure 4.22.

Membrane	Corresponding Image	Water Contact Angle (Degrees)	σ
PES	a	95.2	1.7
SFGO/PES 0.01 mg/ml	b	42.2	1.8
SFGO/PES 0.10 mg/ml	d	28.5	2.0
LFGO/PES 0.01 mg/ml	c	45.7	1.5
LFGO/PES 0.10 mg/ml	e	30.3	1.7

Water Contact Angle of uncoated PES indicates that the polymer is hydrophobic in nature, as the contact angle exceeding 90° is a consequence of poor surface wettability (discussed in Section 3.14). This may be further evidenced by inspection of the droplet shape on the surface (Figure 4.22(a)), in which it is apparent that the liquid phase is unable to appreciably wet the surface. The measured Water Contact Angle was even higher (more hydrophobic) than some literature values for PES, in which angles of the order 80° have been reported [504].

Application of a GO coating onto the polymer has the effect of reducing the Water Contact Angle of the membrane. A higher concentration of GO in the coating resulted in overall lower Water Contact Angle, due to the increasing of the interfacial tensions and surface energies resulting from the presence of GO [505]. The low contact angle values of the four GO-coated PES substrates indicate that the membranes are all hydrophilic, as water tends to wet the surfaces readily. As such, it follows that coating the polymer with GO has the effect of increasing the hydrophilicity of the membrane and that increasing GO concentration in the PES surface coating leads to an increase in the hydrophilicity (therefore, lower Water Contact Angle) [506]. Consistent behaviour regarding the impacts of GO content on hydrophilicity and Water Contact Angle have been reported in literature [507, 508]. Given their lower contact angle val-

ues at both concentrations, it may also be concluded that SFGO leads to a slightly more hydrophilic surface compared with LFGO. This appears somewhat inconsistent with the oxygen content measurement by EDX (Table 4.8) and XPS (Table 4.5), in which it was demonstrated that LFGO contained a higher oxygen content than SFGO. It is concluded that overall oxygen content may actually have poor correlation with hydrophilicity, as in these cases, the slightly higher content in LFGO did not result in greater hydrophilicity. A study has however shown that increasing flake size correlates to an increase in contact angle, owing to the more significant increase in surface free energy [509]. This behaviour is in accordance with the results for our systems.

4.4.6 FIBSEM

Analysis of coated membranes by FIBSEM is subdivided into two distinct parts, namely:

- Morphological imaging of coated membranes from a *top down* direction, that is directing the electron beam at the coated surface from above the sample.
- Cross sectional imaging of membrane cross sections, taken from inside the cut membrane trench.

Morphological imaging

Morphologies of the membranes are revealed in Figure 4.23. Image (a) depicts the PES substrate, (b) and (c) show SFGO coatings at 0.01 and 0.10 mg/ml, respectively, (d) and (e) show LFGO coatings at 0.01 and 0.10 mg/ml.

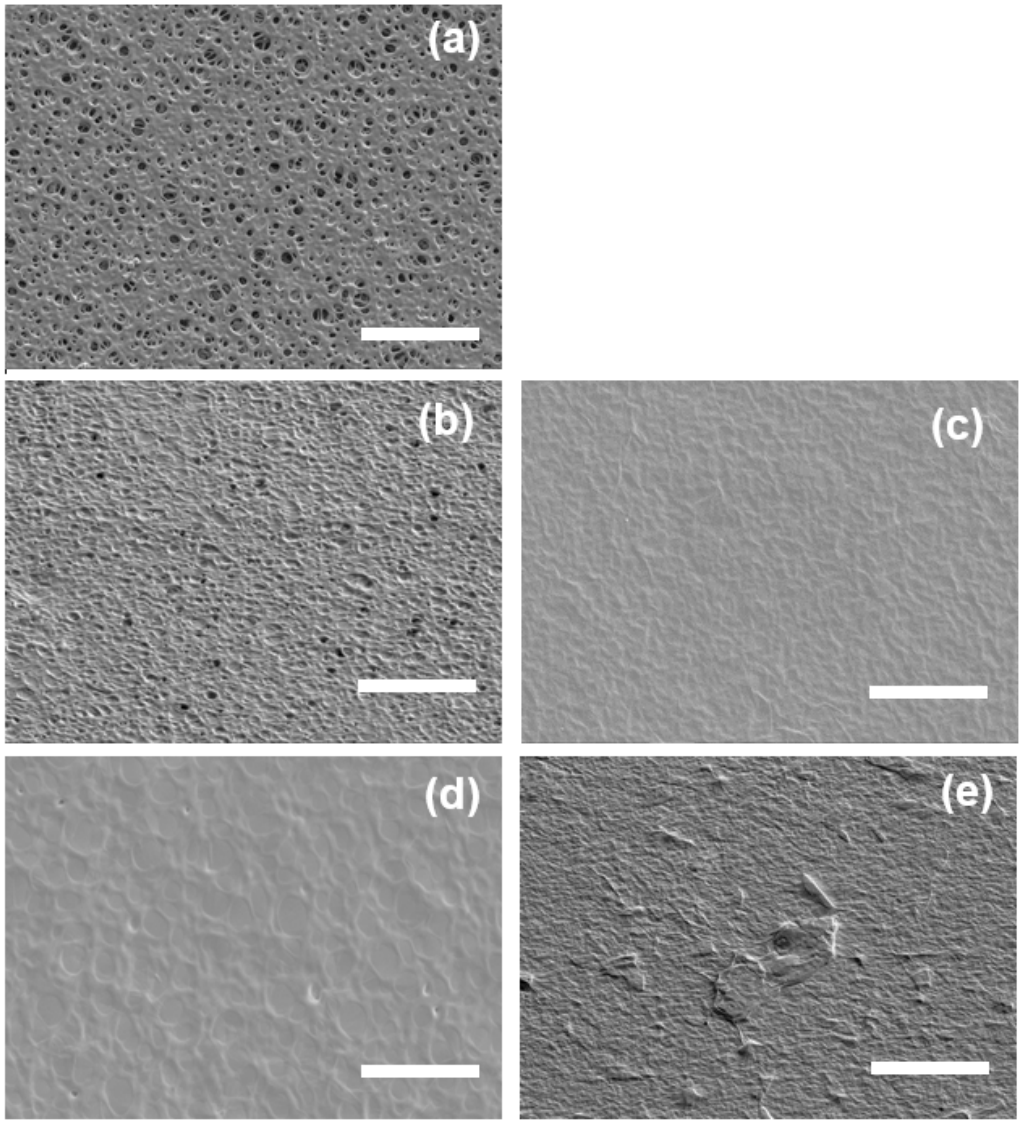

Figure 4.23: Morphological imaging of (a) PES, (b) SFGO/PES 0.01 mg/ml, (c) SFGO/PES 0.10 mg/ml, (d) LFGO/PES 0.01 mg/ml and (e) LFGO/PES 0.10 mg/ml by FIBSEM. Horizontal scale bars represent lateral dimensions 10 μm. Magnification factor 10,000X.

Morphological imaging of uncoated PES surface (Figure 4.23(a)) revealed the highly porous, almost sponge-like nature of the substrate. In Section 4.4.5, Water Contact

Angle measurements of membrane samples revealed that the PES membrane had very high contact angle, higher even than other PES materials from literature. By Cassie-Baxter model of super-hydrophobicity, these pores may entrap air, thus leading to elevated levels of hydrophobicity [510, 511]. PES morphology comprises a multitude of pores (stated pore size from manufacturer was 0.20 μm), of varying lateral dimension, which are visible with the image scale bar set at 10 μm. In Sections 5.5.1 and 6.3.1, the removal of dyes and salts, respectively, using PES membranes will be investigated. The results in these sections will demonstrate that, unsurprisingly, the PES substrate offers almost no rejection of the species, which are significantly smaller than 0.20 μm and are thus able to permeate the pores, regardless of mass transfer resistance of the PES membrane.

Imaging of the GO-coated membranes (Figure 4.23(b) - (e)) revealed that the application of GO coating to PES has a significant impact upon the morphology of the substrate.

Coating of PES with 0.01 mg/ml SFGO (image (b)) appears to offer near complete coverage of PES surface pores, as it seems that the SFGO coating covers the majority of the membrane. There are however, still a number of pores visible, likely corresponding to areas which have not been covered by the SFGO, rendering the porous substrate visible beneath the coating.

Images corresponding to 0.10 mg/ml SFGO and 0.01 mg/ml LFGO (images (c) and (d)), respectively) appear to show that the coverage of substrate by GO is complete, as there are no visible pores. From a morphological perspective, these coatings appear to be uniform, with wrinkled GO coating tightly packed across the surface of the membrane.

Coating with 0.10 mg/ml LFGO (image (e)) also appears to offer complete coverage of PES surface, as there are again no visible pores. The coating does not appear uniform, however, as there are regions on the surface which appear distorted and large

in lateral dimension, visible on a 10 μm scale. It is proposed that these regions result from aggregated layers of GO, which do not deposit flatly onto the PES substrate during vacuum deposition process.

Cross-sectional imaging

Cross-sectional images of the four coated membrane samples are shown in Figure 4.24.

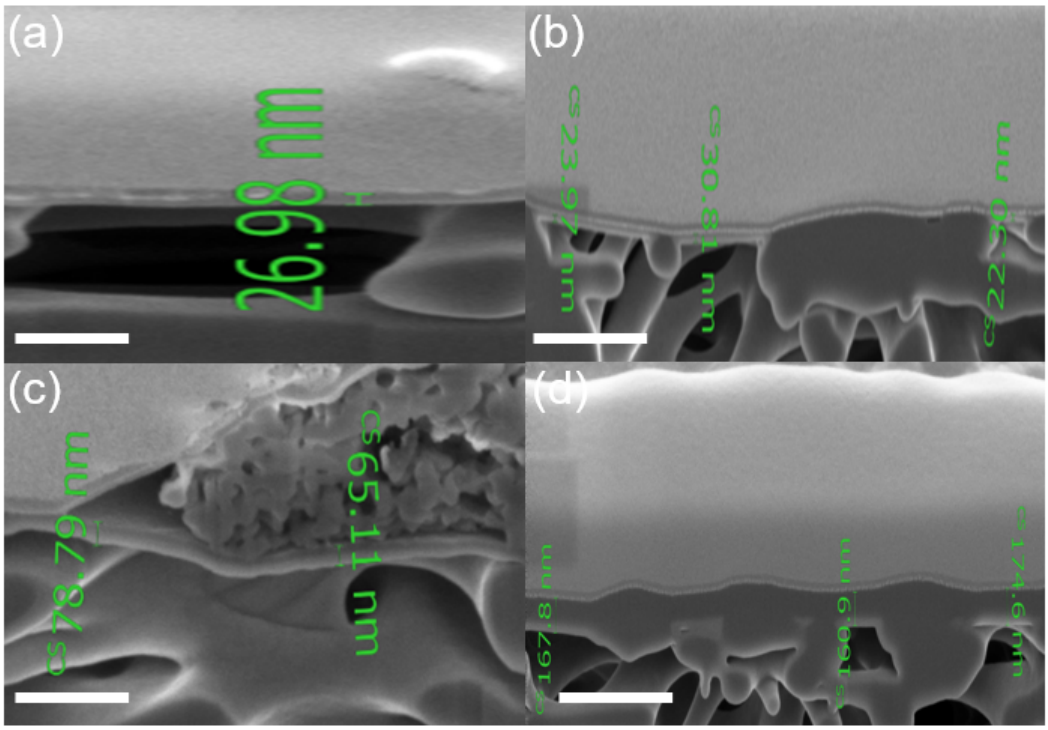

Figure 4.24: Cross sectional images of (a) SFGO/PES 0.01 mg/ml, (b) LFGO/PES 0.01 mg/ml, (c) SFGO/PES 0.10 mg/ml and (d) LFGO/PES 0.10 mg/ml. Horizontal scale bars represent lateral dimensions 500 nm. Magnification factor 100,000X.

Inspection of the images reveals that the GO is layered on top of the PES substrate. The introduction of porous features into the polymeric film is a feature of the membrane manufacturing process, as such, the pores are observable from the side-facing direction in cross-sectional analysis. There appears to be no uniform pathway through which

contaminant species or water may permeate. Similar observations of polymer membranes from literature reveal the randomly configured polymeric structures [512, 513]. The GO coatings themselves are revealed to be ordered and compacted, spreading thoroughly across the PES surface, typically dipping randomly along the path, perhaps as the coating layer encounters a PES pore. It is not evident from the images that GO is penetrating into the substrate pores, as below the coating layer, only the PES lamellae are visible. This is consistent with expectation, given the relatively large size of the GO flakes in relation to the 0.20 μm pores on the PES substrate. The SFGO/PES 0.10 mg/ml sample (Figure 4.24(c)) does however reveal the presence of an agglomerated section of matter; it is considered that this is likely a contaminant species present on the surface of the membrane prior to coating.

The corresponding mean GO layer thicknesses were calculated from the above obtained images; using only the values of thickness recorded on the annotated images in Figure 4.24. The mean thicknesses and standard deviation are reported as follows:

Table 4.11: Mean GO layer thicknesses of the four GO-coated membrane samples. The image column corresponds to the ordering of images in Figure 4.24.

Membrane	Image	Mean GO layer thickness (nm)	σ
SFGO/PES 0.01 mg/ml	a	26.98	0
SFGO/PES 0.10 mg/ml	c	71.95	6.8
LFGO/PES 0.01 mg/ml	b	25.69	3.7
LFGO/PES 0.10 mg/ml	d	167.77	5.6

The GO coatings therefore appeared to deposit flatly onto the substrate, with local variation in layer thickness observed to be of the same order of magnitude. As such, it appears that the GO dispersions are well exfoliated in aqueous suspension prior to preparation of membrane samples. Furthermore, the layer thickness was observed to be positively related to GO concentration in coating, a trend which is consistent with expectation. It is, however, not the case that increasing the concentration by a factor of

ten (from 0.01 mg/ml to 0.10 mg/ml) results in an increase in coating thickness by the same factor: for SFGO, the factor of increase was 2.67, while for LFGO it was 6.53. It is proposed that the increase in GO concentration results in a coating layer that contains a higher density of GO therein [514]. As such, the utilisation of higher concentration GO results in microstructural densification of the coating and this is particularly prominent for smaller flake systems, due to the greater tendency to compact together [15]. As discussed, the pore sizes of the PES substrate are nominally too small in dimension to permit entrapment of the GO flakes, as such, it is not considered that GO losses due to entanglement in the pores is impacting the layer thickness. In one study that compared different flake sizes of GO coating on a nylon substrate, it was found that the smaller flake GO sample was small enough to transit the membrane pores, resulting in thinner than expected coatings [515]. The higher concentration LFGO coating results in significantly thicker GO coating layer compared to the higher concentration of SFGO. XRD analysis of the membranes (Section 4.4.3), however, revealed that the interlayer spacing of the membranes was almost identical, implying that the spacing between GO layers is not a significant contributor. It is proposed, then that the smaller flakes are able to stack more tightly on the substrate, resulting in a thinner but denser coating layer. In the morphological images of the higher concentration LFGO membrane (Figure 4.23(e)), it was discovered that the membrane appeared to contain patches of uneven consistency. This was not, however, revealed to be the case in cross sectional imaging; with coating layers ranging 174.6 nm - 160.9 nm, which is within range of the variation noted in the other images.

4.5 Conclusions

This chapter has presented the results regarding characterisation of commercial GO materials and GO-coated PES membranes. As discussed, the salient feature of these GO

materials that merited their selection was the difference in flake size. Characterisation of materials has been a salient stage in the research process, as it revealed the nature of the GO materials, and characterised the flake size and surface charge. The content of this chapter will be used to assist the understanding of the behaviours of GO in subsequent chapters, regarding application of the GO materials.

Analysis of GO materials was completed by a number of techniques. DLS and LD techniques were used as a novel means to characterise the GO flake sizes. LD was considered the more appropriate technique, demonstrating that LFGO has d(50) size 13.3 μm, whereas SFGO was 9.0 μm. Analysis of the GO chemistry by spectroscopic analysis, using FTIR and XPS techniques, revealed the GO materials to be very similar in terms of their chemistry, with a number of associated functional groups identified including carbonyl, carboxyl and epoxy groups. These pieces of information were crucial in developing the rest of the research, having ascertained that the materials were of similar chemical nature but starkly different flake size. Raman spectroscopy revealed the structural disorder of the materials, with calculated $I_D : I_G$ ratios for both materials exceeding unity. This is also demonstrated to be independent of flake size. Zeta potential was utilised to assess the electrokinetic stability of GO dispersions. Measurement of zeta potential, as a function of dispersion pH in interval 3.50 - 10.0, revealed that both materials are negatively charged across the range, becoming increasingly stable (with lower potential) as pH increases up to pH 10. GO materials were also imaged using SEM, revealingn that upon drying, the materials are highly disordered and randomly aggregated even at low concentration. This confirmed the lack of suitability of the technique for flake sizing. Characterisation of GO materials has been essential in developing understanding of the flake sizing, electrokinetic behaviour and surface area, each of which will be crucial in the subsequent chapters.

Analysis of GO-coated PES membranes was also completed by a number of different techniques. FTIR analysis revealed that the spectra pre- and post-coating were

identical, therefore implying that coating the PES with GO does not lead to a chemical reaction between coating and substrate. Thermal analysis revealed that degradation was via a one-step mechanism and that the impact of coating on thermal properties is very minor, but suggestive of a slight improvement in thermal properties. XRD analysis of membranes in dry and wet state showed that the interlayer spacing of the wet membrane was greater than the dry membrane, suggesting that GO swelled slightly when wet, due to the intercalation of water among the coating layers. Measurement of water contact angle showed that increasing GO concentration in surface coating from zero (pure PES) to 0.10 mg/ml had the effect of reducing the contact angle overall, such that they became more hydrophilic with increasing GO content. The SFGO system was proven more hydrophilic than LFGO, a feature consistent with the smaller flake sizes. Imaging of the GO membrane morphologies by FIBSEM demonstrated that the surfaces were different in appearance and offered a varying degree of surface coverage. Cross-sectional FIBSEM analysis enabled estimations of the GO coating layer thickness to be made, demonstrating that an increase in GO concentration led to denser coatings with increased thickness, in particular for the LFGO systems due to the greater tendency of the smaller flake system to compact.

The findings of this chapter have demonstrated a novel approach to characterisation of GO flake size based on LD technique. Importantly, these materials were demonstrated to have similar material chemistry. The impact of this chapter is to provide a solid foundation from which understanding of each materials interactions with charged species may be understood. Furthermore, this characterisation is essential for understanding the role of GO in adsorbent and membrane formulations. This chapter will contribute knowledge to those seeking a detailed understanding of the power of GO characterisation pathways, in particular with regards to flake size measurement.

Chapter 5

Adsorption and filtration of textile dyes using GO

5.1 Introduction

As highlighted in Section 1.1.5, GO is attracting enormous research attention in removal of dyes by methods including adsorption and filtration. GO boasts a number of significant advantages for use in removal of dyes by filtration and adsorption, such as very high theoretical surface area and favourable surface chemistry [516], which enables the interaction of GO with dye, by charge-mediated adsorption and π - π interactions [179]. Much of the aforementioned literature regarding treatment of dye-contaminated water by GO regards *synthetic GO*, that has been prepared for one-time use in a laboratory, by methods including Hummers' Method [126, 128]. Commercially available GO, that is GO product obtained directly from a supplier, has a number of advantages compared to synthetic GO, including reproducibility and reliability of formulation, ease and time effectiveness. In addition, commercial GO is highly relevant to industrial applications of GO, in adsorption and filtration, in which time and financial implications are often paramount.

In this chapter, two commercially available GO dispersions are employed within dye filtration and adsorption, for treatment of water contaminated by anionic MO

and cationic MB dyes. Characterisation of the GO materials revealed that the flake sizes were starkly different; the impact of this salient property will be explored in this chapter. Selection of the dyes in this chapter is merited by the contrasting molecular charges alone, with comparable molecular weights, as this renders the study highly informative in terms of probing the behaviours of GO. Consideration was also given, however, to the fact that these dyes are a source of considerable environmental burden, as both are toxic and capable of causing vascular diseases in humans [517, 518]. Thus their removal from textile effluent prior to discharge is imperative. As highlighted in the literature review, GO has been employed for removal of MB and MO, by means including adsorption and filtration; as such, it is considered a timely development that a study is introduced which considers removal using GO materials of differing flake size. This is especially relevant, given the expected difference in performance and the impact that flake size may have upon the adsorption and filtration systems. The results of this chapter therefore establish a baseline of removal performance achieved by adsorption and filtration.

Through the results obtained in this chapter, the potency and efficacy of commercial GO materials in dye removal by adsorption and membrane filtration will be demonstrated. The tendency of GO to aggregate in charged media has been presented as a potential hindrance to its application as an adsorbent; though, this feature may actually be beneficial for separation of the GO from dye downstream post-adsorption. The results of this research chapter are broken down into the the following sections:

- Adsorption of dyes using GO adsorbents: Kinetics of dye adsorption (Section 5.3) and Equilibria of dye adsorption (Section 5.4). Aggregation of GO in charged dyes is considered in Section 5.4.3.
- Filtration of dyes using GO-coated membranes, is considered in Section 5.5.

It is expected that the results demonstrated in this chapter will have a significant research impact, with tangibility to those from academia and industry wishing to de-

velop the end uses of commercial GO, especially those having the key difference in terms of flake size.

5.2 Materials and Methods

5.2.1 Dye Adsorption: UV calibration of MB and MO

The position of the UV absorbance peak in MB and MO dyes was established by UV-Vis. Dye solutions of MB and MO were prepared at 5.0 mg/l in distilled water, by diluting down the bulk concentration from supplier. Following dilution, the dye solutions were stirred under constant agitation at stirring speed 3, on the instrument dial, at room temperature for a period of ten minutes, to ensure optimal mixing of dye in water. The UV-Vis. spectra were recorded using a (Agilent Cary 60 (USA)) spectrophotometer, in wavelength region 350 - 800 nm, as shown in Figure 5.1. Absorption maxima of MB and MO were found to be at wavelengths 664 nm and 464 nm, respectively, which is in agreement with literature [519, 520].

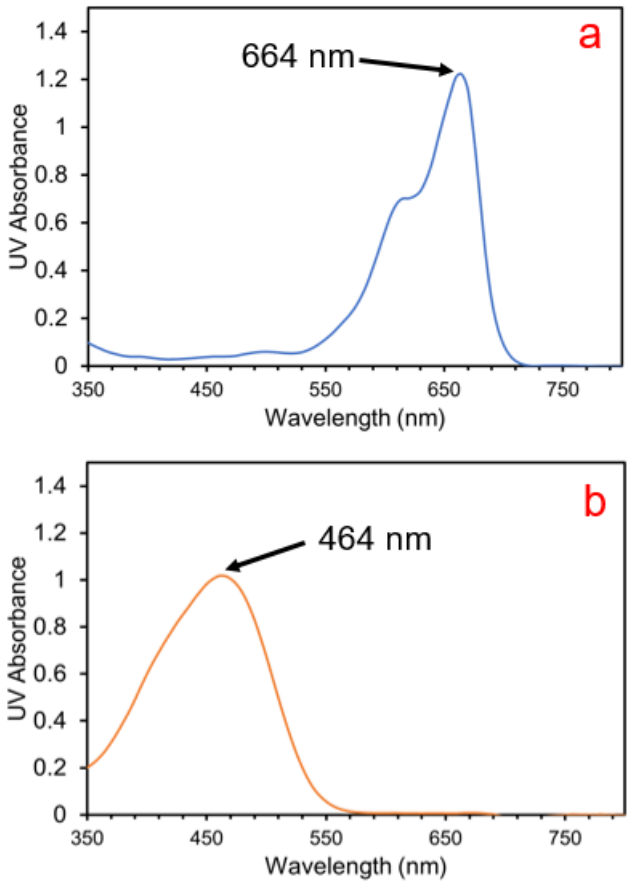

Figure 5.1: UV-Vis spectra of (a) MB and (b) MO dyes, in wavelength range 350 - 800 nm. Solutions of both dyes prepared at 5 mg/l in distilled water. The adsorption maximum of MB was observed at 664 nm, and MO at 464 nm.

In order to calibrate the absorbance of each dye as function of initial dye concentration (C_0), dye solutions of MB and MO were first prepared as above by dilution at 0 (distilled water), 1.25, 2.50, 5.0, 10, 12.5 and 15.0 mg/l.

UV absorbance of MB aliquots were measured at 664 nm, and MO at 464 nm (maxima of absorbance for the respective dyes as per Figure 5.1), using a (Thermo Fisher Scientific Biomate 3 (USA)). The UV cuvette used was a 3 ml plastic standard cuvette. From this point onward, all UV absorbance measurements were made using this instrument, unless otherwise stated. Calibration plots, detailing the UV absorbance

as a function of dye concentration, is shown in Figure 5.2(a) and (b), respectively. The behaviour was observed to be linear in this range, with typical form $Absorbance = Gradient \cdot C_0$.

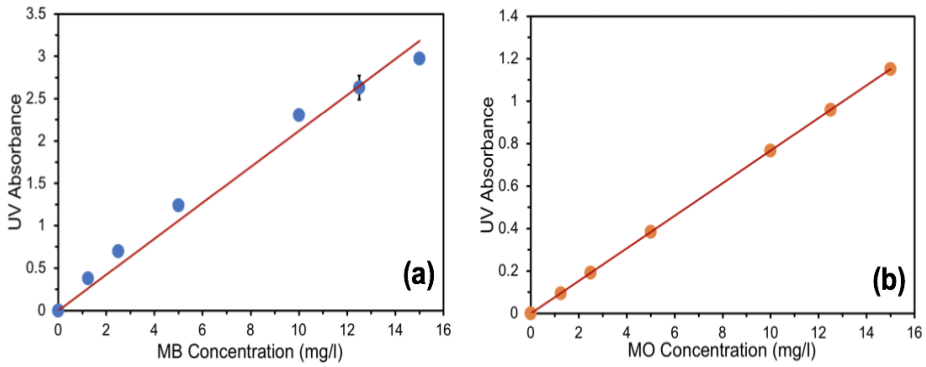

Figure 5.2: UV-Visible spectroscopy calibration of (a) MB and (b) MO dyes. Dyes were calibrated in the range of concentrations 0 - 15 mg/l.

For MB, the calibration was: $Absorbance = 0.2120 \cdot C_0$, with statistical $R^2 = 0.994$.

For MO, the calibration was of the form: $Absorbance = 0.0767 \cdot C_0$, with statistical $R^2 = 1$.

5.2.2 Dye Adsorption: Kinetics of dye adsorption

Kinetics of adsorption of MB and MO dyes onto GO were studied at respective $C_0 =$ 5, 10 and 15 mg/l in distilled water. Dyes were firstly prepared as above and an initial measurement of UV absorbance was made at the corresponding maxima, to ensure correctness of dilution as per the calibration.

For adsorption of MB, 0.50 ml (solid GO mass 5 mg) of GO from the original 1.0 wt% dispersion was transferred by pipette into 100 ml of prepared dye solution, at initial concentration either 5, 10 or 15 mg/l, such that the total volume of GO and dye was 100.5 ml. These concentrations were selected in order to maximise material efficiency

of GO consumption, and achieve a level of dye adsorption <100%. A higher content of GO would be capable of adsorbing a greater number of dye molecules, requiring the use of higher dye concentrations. In order to utilise a minimum but measurable quantity of GO for each experiment, the dye concentrations were varied from 5 - 15 mg/l to investigate the dye removal percentage at these concentrations (later presented in Figure 5.6). After inserting the GO into dye solution, the mass:liquid phase ratio of solid GO:total volume was 0.0497 mg/ml. The GO-MB mixture was constantly agitated during the adsorption procedure using a magnetic stirrer bar, at speed setting 5 on the instrument dial. At times of 10, 20, 30, 40 and 50 minutes after insertion of GO, 5 ml aliquots of the GO-MB suspension were withdrawn from suspension and deposited inside a 50 ml centrifugation tube. The withdrawn aliquot was centrifuged at 4000 revolutions per minute (rpm) using an (Eppendorf Centrifuge 5810 (Germany)) for ten minutes in order to separate the GO from the MB. The supernatant MB was filtered through a (Sartorius Minisart Syringe Filter Plus (Germany)) 0.45 μm cellulose acetate syringe filter. UV absorbance of the MB was recorded at 664 nm. The experiments were conducted entirely at room temperature, with no applied heating effects. pH was not adjusted.

For adsorption of MO, the above method was adjusted owing to the more limited adsorption of MO by the GO's. The dosage of GO was set at 10 mg for each experiment, such that the total volume of GO and dye was 101 ml. Thus, the loading ratio of GO solid:total volume was 0.0990 mg/ml. By experimental observation, the GO was slower at dropping out of the GO-MO suspension and, as such, the centrifugation time was increased from 10 minutes to 25 minutes.

In Section 2.2.4, parameters q_t and $q_{e,exp}$, which are relevant to dye adsorption, were mentioned but not formally defined, as such, they will be given definition here [521]:

$$q_t = (\frac{C_0 - C_t}{m}) \cdot V \tag{5.1}$$

$$q_{e,exp} = (\frac{C_0 - C_e}{m}) \cdot V \tag{5.2}$$

where C_t and C_e are the concentrations of dye at time t and equilibrium stage, respectively, as obtained by experiment. The equilibrium value was taken as the final experimentally measured value, *i.e.* that corresponding to the UV absorbance at time = 50 minutes. V is the total volume of solution and m is the mass of adsorbent. The UV calibration relationships were utilised to allow internal conversion of UV absorbance and concentration.

The parameter *removal percentage*, representing the overall amount of dye adsorbed by the GO adsorbent, was calculated as per Equation 5.3:

$$Removal(\%) = (\frac{C_0 - C_e}{C_0}) \cdot 100\% \tag{5.3}$$

5.2.3 Dye Adsorption: Kinetic models

GO-dye adsorbent systems were modelled by the linear PFO and PSO kinetics models (introduced in Section 2.2.4). Linear PFO model is provided by Equation 2.3, while linear PSO is given by 2.5.

In PFO analysis, the experimental values of q_t and $q_{e,exp}$ were utilised to calculate a value of ($q_{e,exp}$ - q_t), which was plotted logarithmically as a function of time. Three values of initial concentration were utilised in these studies for each GO-dye system, thus three corresponding kinetics profiles were obtained. As such, the PFO model was fitted to each profile separately, and the values of k_1 and $q_{e,cal1}$ were calculated by the gradient and vertical intercept, as discussed in the literature review.

In PSO analysis, the experimental q_t were used in calculation of t/q_t, for each kinetic

profile, as a function of time. Values of k_2 and $q_{e,cal2}$ were calculated by the respective gradient and vertical intercept, as discussed in the literature review.

5.2.4 Dye Adsorption: Equilibrium of dye adsorption

Dye solutions of MB and MO were prepared at initial concentrations 50, 75, 100, 125 and 150 mg/l in distilled water, as illustrated above. These concentrations are of the order 10X higher than the concentrations utilised for the kinetics experiments, as such, the corresponding UV absorbances were of too high magnitude to be recorded by the UV-Vis. A 1 ml portion of the dye was transferred into a beaker and diluted in 9 ml distilled water (total volume 10 ml), with transfer of all liquids done by pipette. UV absorbances of the diluted dyes were measured and converted to concentrations by use of the corresponding calibration profile (Figure 5.2). These initial measurements of absorbance were thus recorded with concentration equal to a tenth of the actual dye concentration. The corresponding *actual* concentrations of dye were calculated by multiplying this reduced concentration by ten. This process was iterated throughout the series of equilibrium studies experiments.

Experiments to determine the equilibria of dye adsorption were carried out using 20 mg GO adsorbent for MB studies and 30 mg GO for MO studies. The adsorbent was dispersed and agitated in 100 ml of dye at each of the respective concentrations 50 - 150 mg/l. The respective ratios of GO solid:total volume were thus 0.0196 mg/ml for MB and 0.0291 mg/ml for MO. These ratios were thus higher than the analogous systems for kinetics experiments, in effort to compensate for the higher concentration of dye used in equilibrium studies. In analogy to the kinetics experiments, 5 ml of the GO-dye suspension was extracted at a time 80 minutes after addition of adsorbent, centrifuged, and the filtered supernatant analysed by UV-Vis, as described earlier. The temporal variation in dye concentration was not measured in intervals as per the kinetics experiments: instead the sole measurement was taken at the aforementioned

80 minutes. Equilibrium UV absorbance was translated into concentration using the calibration relationships and subsequently multiplied by the dilution factor to provide the C_e value for equilibrium. Similarly, values of q_e were calculated by Equation 5.2.

5.2.5 Dye Adsorption: Equilibrium isotherms

Equilibrium studies of dye adsorption were analysed according to linear Langmuir and Freundlich isotherms (introduced in Section 2.2.4). The isotherm equations for Langmuir and Freundlich are given by Equations 2.6 and 2.7, respectively.

In Langmuir analysis, values of C_e/q_e values were plotted against C_e. As there were five initial dye concentrations used, this provided an obtained isotherm with five corresponding points. Values of q_{max} and K_L were calculated from the respective gradient and vertical intercept of the isotherms, as outlined in the literature review.

In Freundlich analysis, logarithmic values of q_e were plotted against logarithmic C_e, again resulting in an isotherm with five points. Values of q_{max} and K_L were calculated from gradient and intercept, as outlined in the literature review. n and K_F values were calculated from the respective slope and vertical intercept of the isotherms, again outlined in the literature.

5.2.6 GO-coated membranes: Filtration testing

This section details the methods used to assess the performance of commercial GO-coated PES membranes, in removal of contaminants from water by filtration.

The concept of *rejection* in membranes was first introduced, but not formally defined, in Section 2.4, in which the rejection of certain contaminants was identified as a key performance parameter. Rejection defines the percentage quantity of contaminant that the membrane is able to remove from a feedstream, relative to the initial amount therein.

Rejection % ($R\%$), is calculated according to Equation 5.4 [275]:

$$R\% = (1 - \frac{C_{permeate}}{C_{feed}}) \cdot 100\% \tag{5.4}$$

where C_{feed} and $C_{permeate}$ (both mg/l) are the concentrations of contaminant in feed and permeate, respectively.

The second parameter used to define the performance of a membrane system is permeate flux, related to the mass transfer of species (including water and unremoved contaminant) through the membrane. Permeate flux (J, in $l \cdot m^{-2} \cdot h^{-1}$), is defined by Equation 5.5 [522].

$$J = \frac{V_{permeate}}{A_{membrane} \cdot t} \tag{5.5}$$

where area $A_{membrane}$ is the membrane cross-sectional area (m^2), $V_{permeate}$ is permeate volume (l), t is time (hours).

Similarly, the parameter permeability (P, in $l \cdot m^{-2} \cdot h^{-1} \cdot bar^{-1}$), is defined as the permeate flux per unit pressure (p, in bar), calculated according to Equation 5.6 [523]:

$$P = \frac{V_{permeate}}{A_{membrane} \cdot t \cdot p} \tag{5.6}$$

5.2.7 GO-coated membranes: Dead end filtration

Filtration testing was performed using dead end filtration mode (introduced in Section 1.1.3). In this section, the experimental method for preparation and loading of the cell with membrane and contaminant is discussed, though the specific tests for different contaminants are discussed in the following sections.

The (Sterlitech HP4750 (USA)) filtration cell was prepared by wetting a porous support disk with distilled water. The membrane was transferred carefully onto the support disk using tweezers, with care taken to position such that the entirety of the membrane covered the disk. For GO-coated membrane samples, the coated side was

positioned facing upwards. The membrane was then placed in the base of the cell reservoir and sealed tightly by screwing inside the cell bottom using a 3-inch lower reservoir clamp. The solution containing contaminant was then decanted into the closed cell, thus directly contacting the membrane surface. A magnetic stir bar assembly was lowered into the solution and the cell positioned on a magnetic stirrer, which was then used to agitate the solution constantly at speed setting 5, on the instrument. An O-ring spacer was placed on top of the loaded cell and the top clamped using a 2-inch upper reservoir clamp. At this stage, the cell was connected to a (BOC 9.8 m^3, 230 bar (UK)) nitrogen gas cylinder via rubber tubing, for pressurisation of the cell during operation. The 2500 psig (≈170 bar) pressure bleed value was then opened, permitting the flow of nitrogen. Gaseous pressure was increased steadily by an external pressure regulator, with 2000 psig (≈138 bar) output, and set at the desired magnitude for the given experiment. A mass balance with 3 decimal places was positioned adjacent to the cell, with the output of the cell positioned such that any permeating solvent may be deposited into the collecting beaker/vial directly.

A labelled diagram of the filtration apparatus, including mass balance, is shown in Figure 5.3.

Figure 5.3: Experimental setup of the (Sterlitech HP4750) dead end filtration cell, used for filtration testing of membranes throughout the filtration experiments.

5.2.8 GO-coated membranes: Filtration of dyes

MB and MO dyes were prepared at concentration 5 or 10 mg/l, using the procedure outlined in Section 5.2.1. The UV absorbance was also measured as outlined, for MB at 664 nm and for MO at 464 nm.

Filtration tests were carried out with an initial volume of 50 ml aqueous dye loaded into the apparatus. The mass balance was zeroed with a beaker in position. Following pressurisation of the cell up to the desired pressure, the mass output was measured as a function of time. Separate series of experiments were conducted at 2 and 4 bars pressure. It was observed that in practice the system required an initialisation period before droplets of liquid began to emerge for collection in the beaker. After several droplets had fallen, the beaker was changed and the mass balance re-zeroed. A timer was started at this point and the time taken for each gram (ml) of permeate recorded. For every 4 grams of dye permeate that was collected, a measurement of UV absorbance

was made at the maximum for the dye being tested. The procedure was iterated in this fashion until 20 ml had permeated through the cell.

Following this, the apparatus was depressurised by reducing the regulator pressure to zero and the pressure bleed valve was opened to vent the nitrogen. The remaining 30 ml of dye solution in the feed was discarded and the remainder of the cell taken apart. All components of the cell that had contacted dye were rinsed with distilled water. To undergo another round of cleaning, the cell was set up again with no membrane loaded, and 100 ml distilled water decanted inside. This was then pressurised, with the rapidly permeating water collected by beaker.

At the completion of a single experiment there were 20 readings of time taken to permeate each ml, and five readings of UV absorbance (one every 4 grams), in addition to the initial absorbance of feed. The volume of permeating fluid was translated into P at each stage by Equation 5.6 and the $R\%$ by Equation 5.4, using the measured UV absorbance of permeate at each permeation stage, and the initial measurement of feed absorbance.

5.3 Results and Discussion: Kinetics of Dye Adsorption

5.3.1 Effects of contact time and initial dye concentration upon kinetics of dye adsorption

The effects of contact time upon the kinetics of dye adsorption were explored by inserting GO adsorbent into dye solution for a period of 50 minutes in total, meanwhile the UV absorbance of the dye was routinely monitored in intervals of 10 minutes. To determine the effects of contact time, values of q_t (calculated by Equation 5.1), were plotted as a function of time in the aforementioned intervals of 10 minutes, as shown in Figure 5.4. Calculated values of q_t for MB adsorption by SFGO and LFGO are shown in Figure 5.4(a), and for MO adsorption in Figure 5.4(b). Each of the kinetics profiles has been fitted with a PSO fitting line.

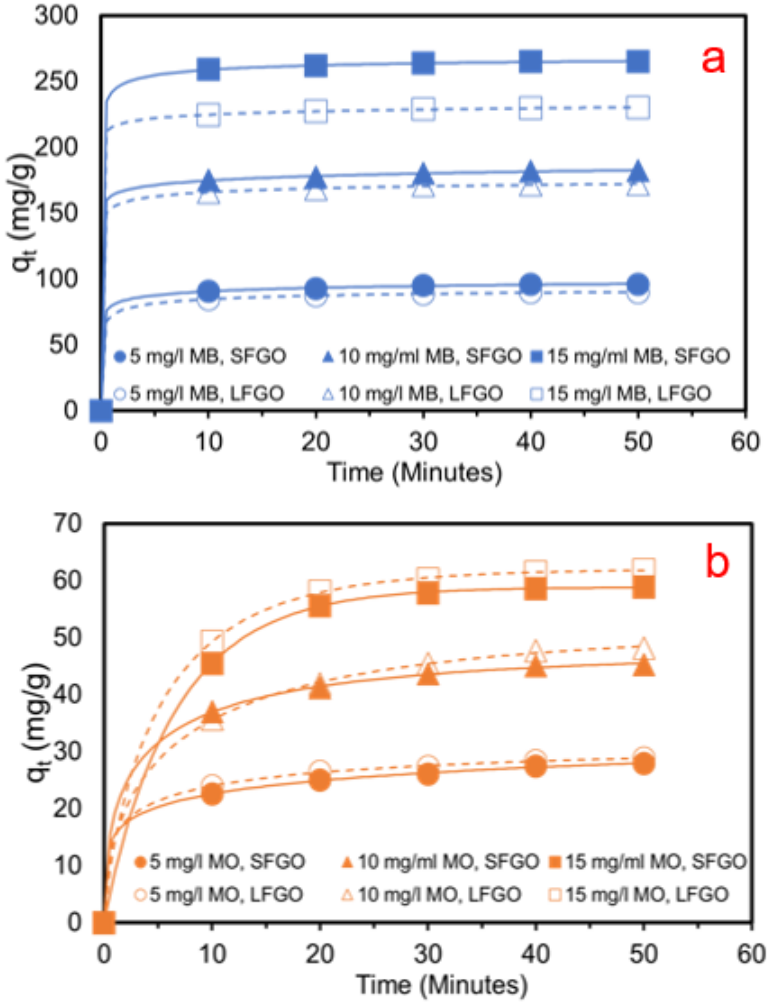

Figure 5.4: Effect of Contact Time upon dye adsorption, using SFGO and LFGO adsorbents. Adsorption of (a) MB and (b) MO, is given as a function of Contact Time, for a 50 minute adsorption cycle.

For both GO adsorbents, the adsorption of MB appeared to take place rapidly with values of q_t reaching equilibrium by the time of the first measurement of absorbance (*i.e.* <10 minutes). The q_t were, however, proportionally higher for the larger surface area and higher zeta potential SFGO, this appears most noticeable at the highest initial dye concentration, in which there is a sizeable discrepancy between the fit line corresponding

to SFGO and that of LFGO. It was, however, not possible to take measurements over finer increments of time to completely confirm the behaviour at small time, as the lengthy time requirement for withdrawal and centrifugation of the samples restricted ability to gain measurements over smaller times. It was found that increasing initial dye concentration from 5 - 15 mg/l had the effect of significantly increasing the values of q_t for both GO-dye systems. This is within expectation for experimental conditions under maximum adsorption, in which the effect of higher initial dye concentrations is to overcome the inherent resistance to mass transfer between liquid:solid phase equilibrium [524, 525]. The difference between the two GO types was also more significant for the higher dye concentration. Adsorption of MO was found to be considerably less favourable than MB, with q_t values of the order one fifth of those for MB, for both SFGO and LFGO. Furthermore, equilibration appears to occur after a significantly longer time span of approximately 30 minutes. Despite its very high capacity to adsorb MB, SFGO was not observed to have increased levels of MO adsorption, as its performance was slightly below that of the LFGO.

Images of the GO-MB and GO-MO dispersions were recorded at Contact Times 0 - 50 minutes, as shown in Figure 5.5. Adsorption of MB by SFGO and LFGO is shown in image (a) and adsorption of MO by SFGO and LFGO is shown in image (b). For the purposes of taking these images, the initial dye concentrations of MB and MO was 10 mg/l. Contact time t=0 is considered the time before the GO is inserted into dye, *i.e.* the image at t=0 is just dye solution. In the case of MB adsorption, it is observed by inspection that the colour of the dye becomes consistently weaker as the adsorption proceeds, and the GO is tending to aggregate in the dye, as large, clustered sections of flake-like matter are clearly visible. For MO adsorption, the orange colouration does appear to weaken throughout the adsorption process, but the agglomeration of GO is not as apparently observable by inspection. The aggregation of GO in MB and MO will be revisited and explored in greater detail in Section 5.4.3.

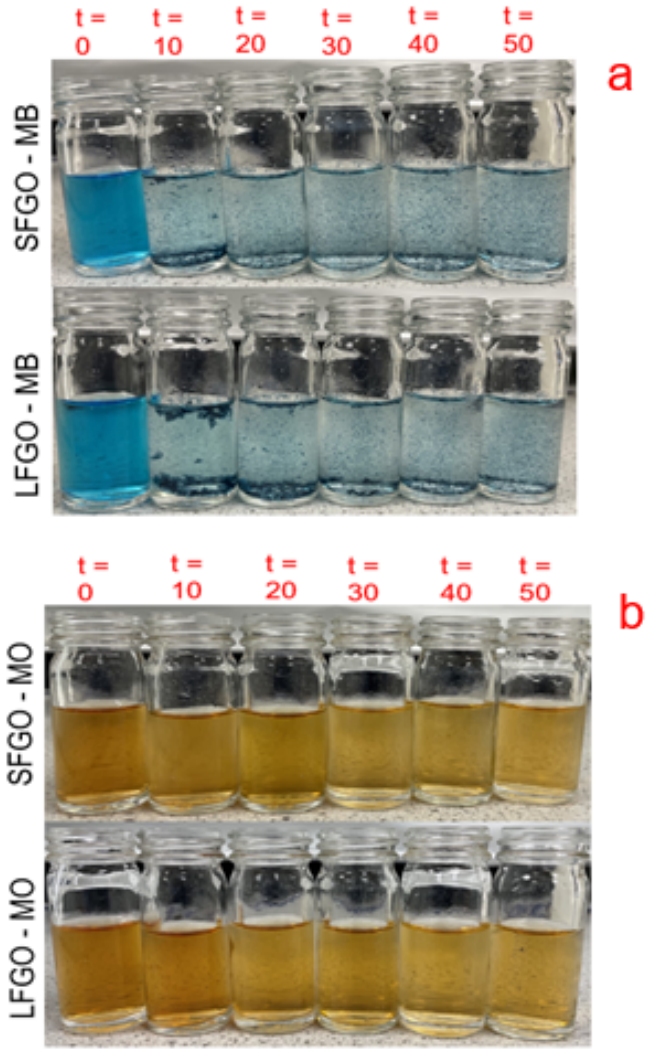

Figure 5.5: Adsorption of (a) MB and (b) MO by SFGO (top row) and LFGO (bottom row). Images captured at contact times t = 0, 10, 20, 30 40, 50 minutes.

The effects of increasing the initial dye concentration in kinetics experiments from 5 - 15 mg/l are revealed by considering the *Dye Removal percentage* (Equation 5.3). Removal percentages were calculated for each GO-dye pairing, after a contact time of 50 minutes, for initial dye concentrations 5, 10 and 15 mg/l. Calculated values of Removal percentage are represented by bars in Figure 5.6, in which the Removal percentages are

shown as a function of initial dye concentration.

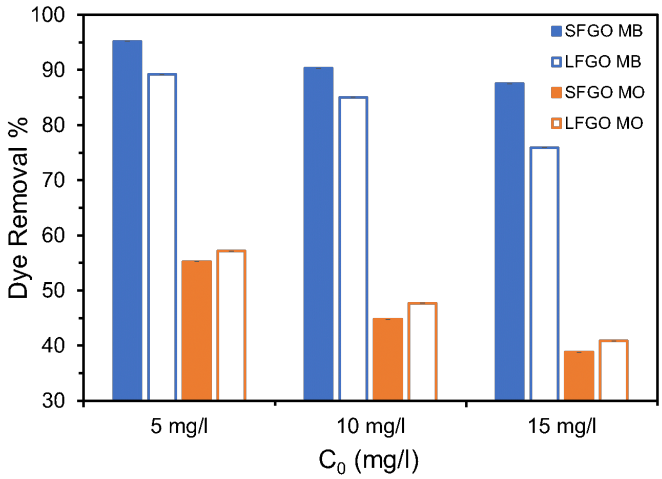

Figure 5.6: Dye Removal percentages of the SFGO and LFGO adsorbents, as a function of initial dye concentration, in removal of 5, 10 and 15 mg/l MB and MO.

Increasing the initial dye concentration from 5 - 15 mg/l has the overall effect of reducing the Dye Removal percentage, for each GO-dye combination. SFGO is again evidenced to offer greater capacity to remove MB compared to LFGO, meanwhile the capacity for adsorption of MO is lower. In the previous discussion, it was noted that increasing the initial dye concentration had the effect of increasing the value of q_t (Figure 5.4), though, it is now observed that the overall Removal percentage decreases at higher concentration. It may be expected that such differences may occur for higher dye concentrations, as the surface binding sites on the adsorbent reach a state of fuller occupancy due to the increased number of adsorbate groups, resulting in a decline in Removal percentage [526]. Comparison of the behaviours between MB and MO systems reveals that similar reductions in Removal percentage are evident, for both MB and MO despite the interaction mechanism being different and the overall level of adsorption being significantly different.

5.3.2 Kinetic Models of dye adsorption *i*: Linear PFO model

Linear PFO model of experimental kinetics data is a logarithmic relationship, that enables values of k_1 and $q_{e,cal1}$ to be calculated from the slope and intercept of the PFO plot, respectively. The governing equation for the linearised PFO model is given by Equation 2.3.

PFO model was fitted to the experimental data obtained for each GO-dye combination, for initial dye concentrations 5, 10 and 15 mg/l. PFO kinetics of 5, 10 and 15 mg/l MB by SFGO and LFGO is shown in Figure 5.7(a) and (b), respectively, while PFO model of 5, 10 and 15 mg/l MO by SFGO and LFGO is shown in (c) and (d). Linear trendlines were fitted to the PFO data and associated linear equations were obtained for each of the series.

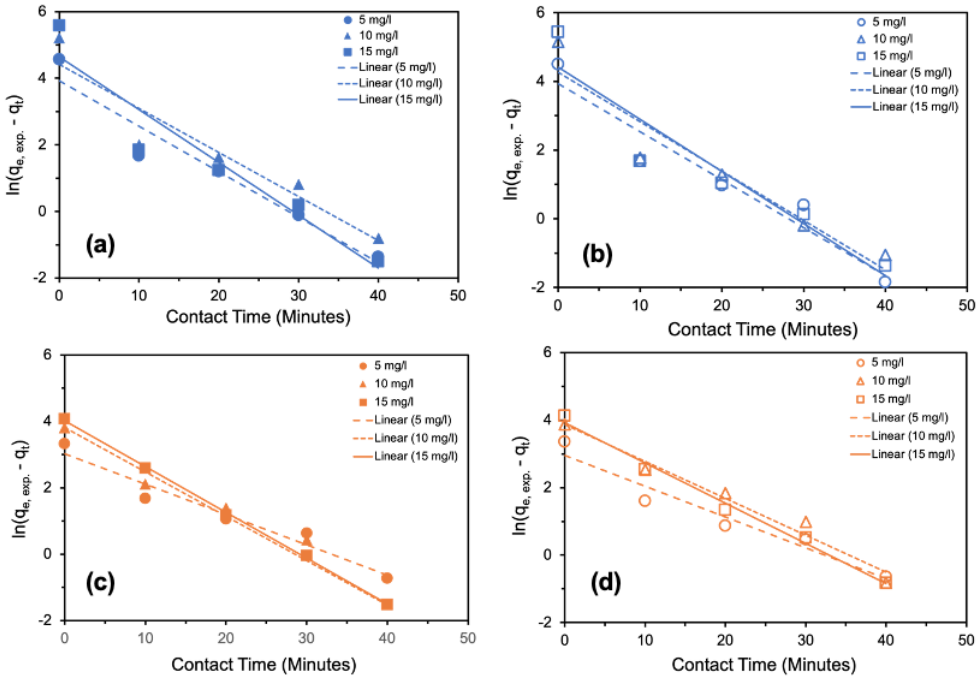

Figure 5.7: PFO kinetics models for adsorption of 5, 10 and 15 mg/l MB by (a) SFGO and (b) LFGO. Similarly, PFO kinetics model for MO adsorption by (c) SFGO and (d) LFGO.

The linear relations obtained from the trendlines of each of these plots are summarised in Table 5.1, for each pairing of GO and dye, with initial dye concentrations 5, 10 and 15 mg/l. Values of q_t were taken from the plots in Figure 5.6 and $q_{e,exp.}$ are taken as the final value of q_t, at time = 50 minutes. All relations are expressed in the familiar linear notation Y = mX + C, where Y represents $ln(q_{e,exp} - q_t)$, X represents contact time, m (slope) represents the negative k_1 and C (vertical intercept) represents $ln(q_{e,cal1})$. The statistical R^2 parameter is also provided in the table for each of the respective PFO relationships, to indicate the appropriateness of fit.

Table 5.1: PFO Kinetics linear models for adsorption of MB and MO.

GO - DYE	*5 mg/l*		*10 mg/l*		*15 mg/l*	
	Y = mX + C	R^2	Y = mX + C	R^2	Y = mX + C	R^2
SFGO - MB	-0.137·X + 3.923	0.939	-0.132·X + 4.412	0.899	-0.158·X + 4.631	0.908
LFGO - MB	-0.140·X + 3.934	0.926	-0.144·X + 4.262	0.907	-0.152·X + 4.414	0.891
SFGO - MO	-0.092·X + 3.027	0.951	-0.134·X + 3.816	0.955	-0.138·X + 4.020	0.999
LFGO - MO	-0.092·X + 2.959	0.944	-0.109·X + 3.867	0.972	-0.119·X + 3.9227	0.990

From the linear relations expressed in Table 5.1, the calculated parameters k_1 and $q_{e,cal1}$ were computed. For each pairing of GO and dye at the respective initial concentrations, these calculated parameters are given in Table 5.2. Experimental values of $q_{e,exp}$ are included in Table 5.2, along with the calculated $q_{e,cal}$ for the purposes of comparison.

Table 5.2: PFO Kinetics parameters k_1 and $q_{e,cal.}$ for adsorption of MB and MO.

GO - DYE	*5 mg/l*			*10 mg/l*			*15 mg/l*		
	$q_{e,exp}$ (mg/g)	$q_{e,cal1}$ (mg/g)	k_1	$q_{e,exp}$ (mg/g)	$q_{e,cal1}$ (mg/g)	k_1	$q_{e,exp}$ (mg/g)	$q_{e,cal1}$(mg/g)	k_1
SFGO - MB	96.0	50.6	0.137	182.4	82.4	0.132	265.2	102.4	0.158
LFGO - MB	89.9	51.1	0.140	171.8	71.0	0.144	230.0	82.6	0.152
SFGO - MO	27.9	20.6	0.092	45.2	45.4	0.134	58.8	55.7	0.138
LFGO - MO	28.9	19.3	0.092	48.2	47.8	0.109	61.9	50.5	0.119

Upon initial inspection of the Tables 5.1 and 5.2, it appears that the PFO model is

an appropriate model for the behaviour of the system, reflected in the fact the R^2 values are all high, ranging from 0.891 - 0.999. This suggests that the obtained experimental data are a good statistical fit for the PFO model. Comparison of the $q_{e,exp}$ and $q_{e,cal1}$ parameters, however, reveals that the differences between experimental and calculated values are in many cases very significant. In particular, the discrepancies appear largest for the adsorption of MB (ranging 75.9 - 178.5% difference), when the adsorption of dye is plentiful, and less so for the adsorption of MO (ranging 0.44 - 22.6 % difference), in which adsorption is more limited. Furthermore, it appears that the respective increases in $q_{e,exp}$ and $q_{e,cal1}$ for all GO-dye pairings increases disproportionately with increasing dye concentration. Again, this discrepancy between experimental and calculated values appears to have greatest error for the MB adsorption systems. In addition, values in PFO model indicate relatively poor correlation to the longer time experimental data. As such, despite the apparent high statistical correlation, the PFO model should be treated with caution when modelling the data obtained in this study.

5.3.3 Kinetic Models of dye adsorption *ii*: PSO model

PSO model of experimental kinetics data enables values of second order rate constant and a calculated model $q_{e,cal2}$ to be obtained from the slope and intercept of the PSO plot, respectively. The governing equation for the PSO model is given by Equation 2.5.

PSO model was fitted to the experimental data obtained for each GO-dye combination, for initial dye concentrations 5, 10 and 15 mg/l, in analogy to the analysis conducted for PFO model, in the previous section. PSO kinetics of 5, 10 and 15 mg/l MB by SFGO and LFGO is shown in Figure 5.8(a) and (b), respectively, while PSO model of 5, 10 and 15 mg/l MO by SFGO and LFGO is shown in (c) and (d). In analogy to the PFO model, q_t were taken from the kinetics plots (Figure 5.6), with $q_{e,exp}$ the final value of q_t, at time = 50 minutes.

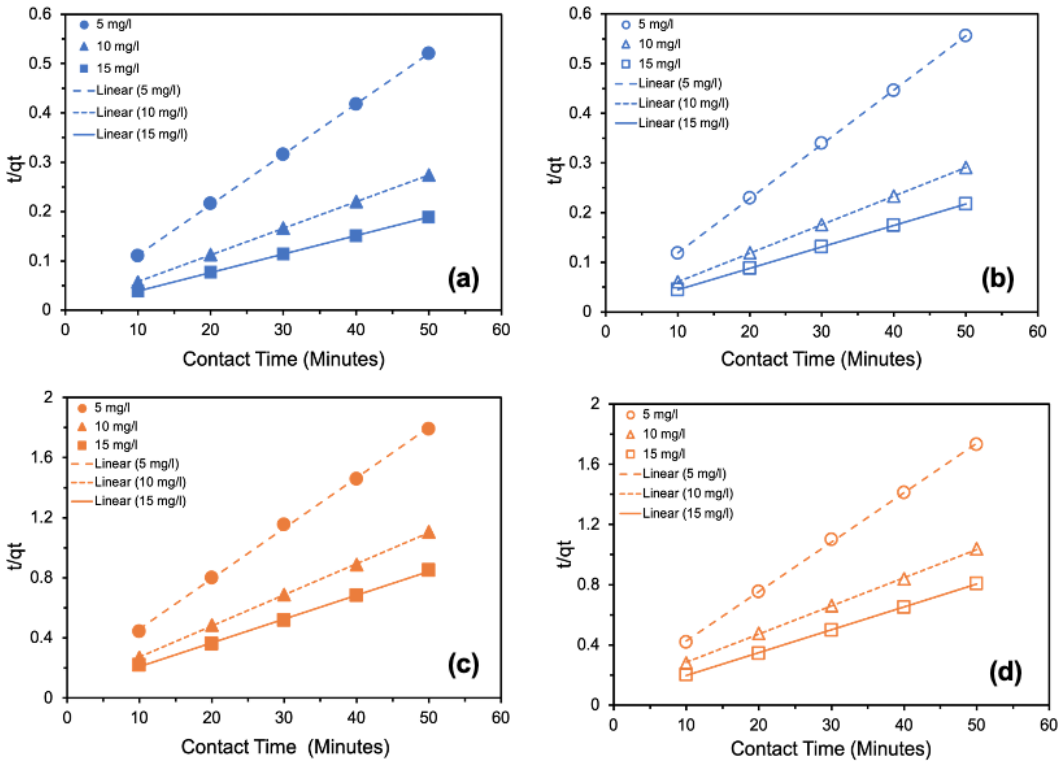

Figure 5.8: PSO kinetics models for adsorption of 5, 10 and 15 mg/l MB by (a) SFGO and (b) LFGO. Similarly, PSO kinetics model for MO adsorption by (c) SFGO and (d) LFGO.

The linear relations obtained from the trendlines of each of these plots are summarised in Table 5.3, for each combination of GO and dye, with initial dye concentrations 5, 10 and 15 mg/l. All relations are expressed in the familiar format Y = mX + C, where Y representing t/q_t, X represents Contact Time, m (slope) represents the inverse value of $q_{e,cal2}$ and C (vertical intercept) represents $1/(k_2 \cdot q_{e,cal2})$. Statistical R^2 parameter is also tabulated.

Table 5.3: PSO Kinetics linear models for adsorption of MB and MO.

GO - DYE	*5 mg/l*		*10 mg/l*		*15 mg/l*	
	Y = mX + C	R^2	Y = mX + C	R^2	Y = mX + C	R^2
SFGO - MB	$0.0102 \cdot X + 0.0091$	1.000	$0.0054 \cdot X + 0.0038$	1.000	$0.0037 \cdot X + 0.0013$	1.000
LFGO - MB	$0.0109 \cdot X + 0.0010$	1.000	$0.0058 \cdot X + 0.0030$	1.000	$0.0043 \cdot X + 0.0015$	1.000
SFGO - MO	$0.0335 \cdot X + 0.1226$	0.999	$0.0207 \cdot X + 0.0656$	1.000	$0.0158 \cdot X + 0.0513$	0.999
LFGO - MO	$0.0328 \cdot X + 0.0978$	1.000	$0.0188 \cdot X + 0.096$	1.000	$0.0152 \cdot X + 0.046$	1.000

Inspection of Table 5.3 reveals that the R^2 values are all very high (>0.999), suggesting immediately that the PSO model is very well suited to the experimental data.

From the linear relations expressed in Table 5.3, the calculated parameters k_2 and $q_{e,cal2}$ were computed, and are presented in Table 5.4, alongside $q_{e,exp}$.

Table 5.4: PSO Kinetics parameters k_2 and $q_{e,cal}$ for adsorption of MB and MO.

GO - DYE	*5 mg/l*			*10 mg/l*			*15 mg/l*		
	$q_{e,exp}$ (mg/g)	$q_{e,cal2}$ (mg/g)	k_2	$q_{e,exp}$ (mg/g)	$q_{e,cal2}$ (mg/g)	k_2	$q_{e,exp}$ (mg/g)	$q_{e,cal2}$ (mg/g)	k_2
SFGO - MB	96.0	98.0	0.0114	182.4	185.2	0.0077	265.2	270.27	0.0105
LFGO - MB	89.9	91.7	0.0119	171.8	172.4	0.0112	230.0	232.6	0.0123
SFGO - MO	27.9	29.9	0.0092	45.2	48.31	0.0065	58.8	63.3	0.0049
LFGO - MO	28.9	30.5	0.0109	48.2	53.19	0.0037	61.9	65.8	0.0050

Comparison of the $q_{e,exp}$ and $q_{e,cal2}$ parameters for the PSO model suggests that the differences between experimental and calculated values are overall less significant than for the PFO model. Discrepancies for MB models ranged between 0.35 - 2.08%, while for MO, the differences were in the range 5.5 - 10.40%. In addition, the increases of $q_{e,exp}$ and $q_{e,cal2}$ subject to increasing dye concentration appear more appropriately proportioned than was the case for the PFO model. The calculated k_2 SFGO and LFGO plots indicated that, in general, the kinetics of adsorption of MB was faster compared to the adsorption of MO, as evidenced by the larger respective PSO rate constants. The values of k_2 for adsorption of MB with SFGO and LFGO did however appear to be somewhat inconsistent, as the values calculated for LFGO were in fact

higher than the SFGO counterparts, albeit that they were the same order of magnitude and very close. Experimental studies suggest that SFGO adsorbs the dye more rapidly and therefore, should have higher k_2 overall, for MB. In addition, SFGO was demonstrated by BET analysis to have significantly higher surface area available for binding of MB molecules (Table 4.3) and greater magnitude zeta potential (Figure 4.10). As such, the counter-intuitive representation of k_2 values obtained suggests that these features are not actually leading to an enhanced rate kinetic of MB sorption. Furthermore, as discussed, the adsorption of MB occurred within the first time-step, meaning there is a greater degree of uncertainty on the k_2 values and their reflection upon our systems. Studies in the literature regarding the impact of flake size upon adsorption efficacy have indicated that smaller flake size adsorbents tend also to have higher rate constants for adsorption [204, 527]. Similar counter-intuitive behaviour with respect to dye adsorption was, however observed in the study of Li *et al.* [199] (highlighted in the literature review (Section 2.2.4)), in which a GO material had higher k_2 than a competitor activated carbon, despite the latter having higher $q_{e,cal2}$.

Application of PSO model appears to be highly reflective of the obtained experimental data, given the high R^2 values of statistical fit and low overall differences between the experimental and calculated $q_{e,exp}$ and $q_{e,cal2}$ parameters. As such, for future dye adsorption studies in the following chapter, the PSO model will be used in preference to the PFO.

Comparing the adsorption performance of the SFGO and LFGO systems with alternative adsorbents is an essential feature for contextualisation of the results. It may be seen that the PSO parameter $q_{e,cal2}$ is for the GO systems high in relation to the analogous values for the activated carbon and zeolite adsorbent systems in Section 2.2.6. This is particularly true for cationic dye adsorption, in which MB was adsorbed with high efficacy by GO adsorbents. For the sample of activated carbon and zeolite studies considered in the literature review section, the $q_{e,cal2}$ values obtained in PSO

analysis was typically <200 mg/g, whereas for GO systems values >200 mg/g were calculated. This suggests that the kinetics if dye adsorption achieved by GO adsorbents out-performs the competitor materials including activated carbon and zeolites; likely a feature of the small flake sizes, high surface charge and surface area of the GO adsorbents.

5.4 Results and Discussion: Equilibrium of Dye Adsorption

5.4.1 Equilibrium of dye adsorption *i*: Freundlich Isotherm

Freundlich isotherm concerns heterogeneous adsorption of adsorbate onto adsorbent surfaces: the isotherm was discussed in Section 5.2.5. The governing linear Freundlich isotherm equation is given by Equation 2.7. Application of Freundlich isotherm to equilibrium data involves the plotting of $ln(q_e)$ as a function of $ln(C_e)$: if the resulting equilibrium line is linear, then the Freundlich model is applicable. The isotherm is used to calculate parameters n and K_F.

Freundlich isotherms of MB adsorption using SFGO and LFGO is shown in Figure 5.9(a), while MO adsorption is shown in (b).

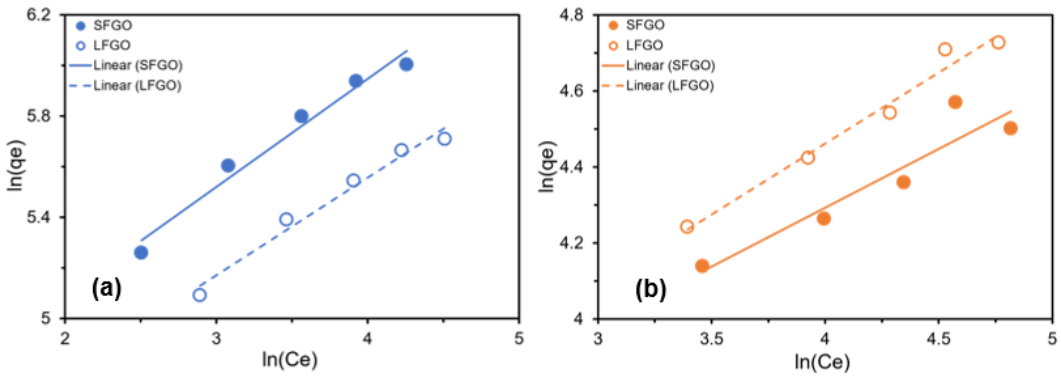

Figure 5.9: Freundlich isotherms for adsorption of 50, 75, 100, 125 and 150 mg/l (a) MB and (b) MO, by SFGO and LFGO.

The obtained linear Freundlich relations are expressed in Table 5.5, in the analogous linear format to kinetics experiments, where vertical axis represents $ln(q_e)$, X represents $ln(C_e)$, slope represents $1/n$ and vertical intercept represents $ln(K_F)$. Statistical R^2 linear parameter is also included.

Table 5.5: Freundlich isotherms for adsorption of MB and MO by SFGO and LFGO.

GO - DYE	*Freundlich isotherm*	
	Y = mX + C	R^2
SFGO - MB	$0.4277 \cdot X + 4.2376$	0.974
LFGO - MB	$0.3852 \cdot X + 4.0161$	0.976
SFGO - MO	$0.3097 \cdot X + 3.0535$	0.881
LFGO - MO	$0.3739 \cdot X + 2.9653$	0.978

The slopes and intercepts of the Freundlich equilibrium lines were used to calculate the parameters n (equal to the inverse of the slope) and K_F (equal to the exponent of the vertical intercept). These parameters are summarised in Table 5.6:

Table 5.6: Freundlich isotherm parameters for adsorption of MB and MO.

GO - DYE	*Isotherm parameters*	
	n	$K_F (mg^{(1-1/n)} \cdot l^{1/n} \cdot g^{-1})$
SFGO - MB	2.34	69.24
LFGO - MB	2.60	55.48
SFGO - MO	3.23	21.19
LFGO - MO	2.67	19.40

Parameter n is used to indicate the intensity of adsorption, where a small value of n is an indicator of greater intensity [528]. It is typical for values of n to exceed unity, where a greater value of the parameter indicates a greater degree of adsorption heterogeneity (and corresponding non-linearity of the isotherm) [529]. It has been suggested, however, that in practice, a value of n exceeding unity suggests favourability of the dye adsorption process [521]. Inspection of Table 5.6 reveals the values of n are lower in each GO system for MB adsorption compared to MO, suggesting that adsorption of

MB is more intense, particularly in the SFGO - MB system, which recorded the lowest n overall. This suggests that this was the most intense and favourable adsorption process and is consistent with the results achieved during kinetics of dye adsorption studies. Conversely, SFGO - MO systems, with the highest corresponding n, was the least intense, which is again consistent with expectation given the kinetics results.

Freundlich parameter K_F is indicative of the overall extent of adsorption and is thus related to the adsorption capacity of the adsorbent [530]. It is therefore expected that a higher numerical value of K_F results from a greater extent of adsorption, thus implying that the adsorption capacity is higher [531]. Values of K_F were observed to decrease according to the order SFGO - MB > LFGO - MB > SFGO - MO > LFGO - MO, which broadly corresponds to the trend observed in practice, perhaps the anomaly is that LFGO - MO has slightly higher adsorption than SFGO - MO, so ought to have higher K_F, though the values are close in magnitude.

Freundlich model appears to be a suitable model for the experimental data, given that values of calculated n and K_F are within expectation, and the R^2 values of all four lines are high (in the range 0.881 - 0.978).

5.4.2 Equilibrium of dye adsorption *ii*: Langmuir Isotherm

Langmuir isotherm, in contrast to Freundlich isotherm, concerns homogeneous adsorption of adsorbate onto adsorbent surfaces. The governing Langmuir isotherm equation is given by Equation 2.6. Langmuir isotherm is applied to equilibrium data by plotting of C_e/q_e as a function of C_e. If the relation is linear, the isotherm is used to calculate parameters q_{max} and K_L, as discussed in Section 5.2.5, in which the fundamental aspects of Langmuir system were also discussed.

Langmuir isotherms of MB adsorption using SFGO and LFGO adsorbents is shown in Figure 5.10(a), while MO adsorption is shown in (b).

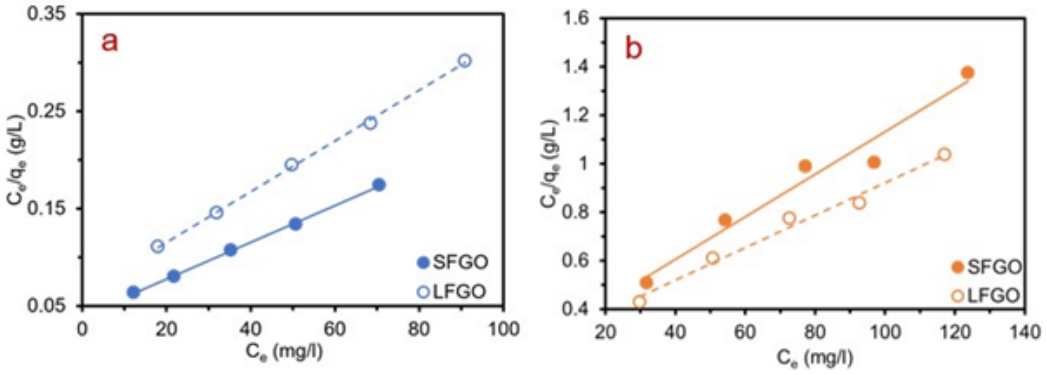

Figure 5.10: Langmuir isotherms for adsorption of 50, 75, 100, 125 and 150 mg/l (a) MB and (b) MO, by SFGO and LFGO.

The linear Langmuir isotherm relations are expressed in Table 5.7, in linear format, where vertical axis represents C_e/q_e, slope represents $1/q_{max}$ and vertical intercept represents $1/(q_{max} \cdot K_L)$.

Table 5.7: Langmuir isotherms for adsorption of MB and MO.

GO - DYE	*Langmuir isotherm*	
	Y = mX + C	R^2
SFGO - MB	$0.0019 \cdot X + 0.0398$	0.999
LFGO - MB	$0.0026 \cdot X + 0.0632$	0.999
SFGO - MO	$0.0088 \cdot X + 0.2543$	0.961
LFGO - MO	$0.0067 \cdot X + 0.2521$	0.984

From these obtained Langmuir equilibrium relations, parameters q_{max} (equal to the inverse of the slope) and K_L were calculated and are summarised in Table 5.8:

Table 5.8: Langmuir isotherm parameters for adsorption of MB and MO.

GO - DYE	*Isotherm parameters*	
	q_{max} (mg/g)	$K_L(l/g)$
SFGO - MB	526.3	0.0477
LFGO - MB	384.6	0.0411
SFGO - MO	113.6	0.0346
LFGO - MO	149.3	0.0266

The ordering of q_{max} values was SFGO - MB > LFGO - MB > LFGO - MO > SFGO - MO. Accordingly, the values of q_{max} reflected the expected trends based on experimental observation. K_L reflects the affinity of adsorption between an adsorbent and adsorbate and is correlated to the surface area and availability of surface pores available for monolayer adsorption [532, 533]. Numerically larger K_L values were found to result from the adsorption of MB, thus inferring greater affinity for MB adsorption than MO.

The dimensionless parameter Langmuir separation factor (R_L) is commonly ascribed to the stability of a Langmuir adsorption system [534]. R_L provides information regarding stability, as the system is considered stable for $0 < R_L < 1$ [237, 535]. The parameter is defined by the following equation:

$$R_L = \frac{1}{1 + (K_L \cdot C_0)} \tag{5.7}$$

The value of R_L is thus inversely proportional to initial dye concentration. As equilibrium adsorption studies were carried out using initial dye concentrations 50, 75, 100, 125 and 150 mg/l, it was possible to calculate a corresponding value of R_L at each concentration, using the associated values of K_L for each GO-dye pairing reported in Table 5.8. R_L values are plotted as a function of initial dye concentration, for each GO-dye pairing, in Figure 5.11. Calculated values of R_L for all systems were observed to lie in the interval 0 - 1, with values of R_L diminishing with increasing dye concentration,

which is suggestive of Langmuir stability, as discussed.

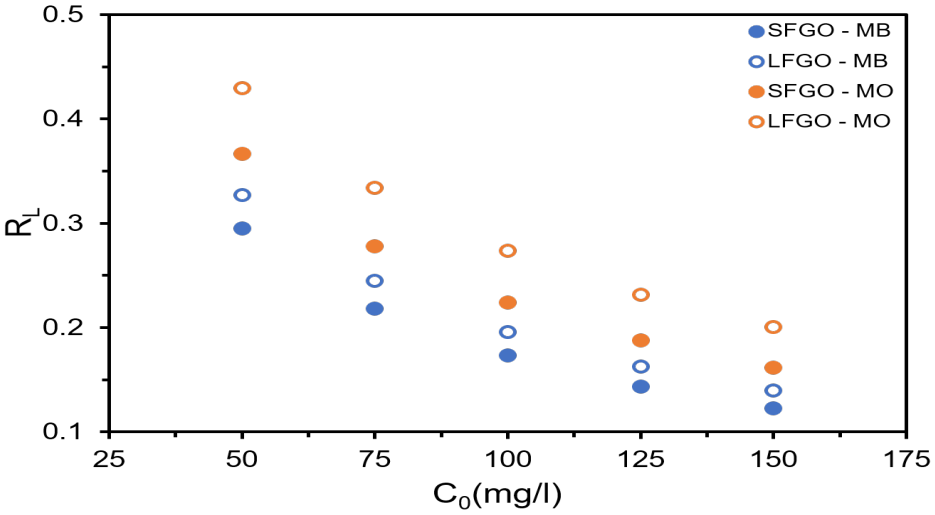

Figure 5.11: R_L plotted as a function of initial dye concentration, for the four GO-dye systems, with initial dye concentrations in the range 50 - 150 mg/l.

Analysis of equilibrium systems by Langmuir and Freundlich isotherms has revealed that both may be suitable models for GO adsorbents, based on their high statistical R^2 coefficients. Langmuir model may be more more appropriate, as respective R^2 values are higher. According to this conclusion, the adsorption of dyes onto GO surfaces assumes a monolayer coverage, and that interaction is governed by dyes binding to a single available adsorbent site on the GO [534]. Freundlich isotherm was however evidenced to be a good fit for the data by the R^2 alone, however this model is ideally suited to experimental systems that have low concentrations of adsorbate, provided also that the concentration range of dyes tested is limited to a strict range [536]. As such, it is considered that the Langmuir model is more appropriate for the GO-dye pairings in these experiments.

Comparison of the calculated Langmuir parameters q_{max} and K_L obtained for MB

and MO adsorption with the sample of literature values suggests that the adsorbents achieve a level of dye adsorption that is consistent with that of competitor GO systems [181, 203]. The performance of the GO systems is however significantly greater than that of competitor adsorbents, considered in Section 2.2.6. For these, the Langmuir isotherm was typically used to describe the equilibrium of adsorption. Across the activated carbon and zeolite systems considered, the calculated q_{max} values were typically low (<100 mg/g), in stark contrast to the high performance of GO systems for cationic dye adsorption in particular. This is suggestive that the GO flakes offer advantages for homogeneous adsorption of dye molecules onto the binding sites, in which the high surface area drives this process.

5.4.3 Aggregation of GO in dyes

Aggregation of GO was introduced in the literature review (Section 2.2.1), in which it was identified as a potential hindrance to the adsorption process. Earlier, in Figure 5.5, it was noted that flocculates of particulate matter were generated and remained clearly visible in the GO - MB suspensions in particular; these were seen to sediment to the base of the container over time. Figure 5.12 shows an enlarged view of the aggregation of GO in 15 mg/l (a) MB and (b) MO. While in the case of MO, aggregation of GO was not strictly observable by inspection with the naked eye, the sedimenting GO material is clearly visible in MB suspensions.

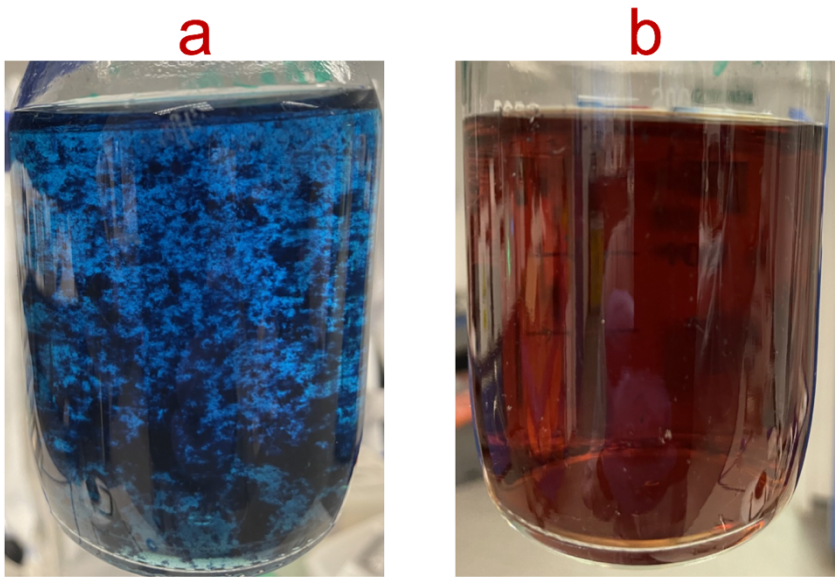

Figure 5.12: Commercial GO dispersed in 15 mg/l (a)MB and (b)MO. Aggregation of GO is particularly evident in the case of MB, as groups of large flakes are visible by the naked eye.

To promote its effectiveness in dye adsorption, GO should ideally exist in exfoliated, homogeneous state, thus maximising adsorption of dye by maximising the contact area availability on the adsorbent surface [178, 537]. One positive aspect is however that such aggregation may lead to easier separation in downstream processes, post adsorption. The substantial electronegative charge characteristic of the GO's was revealed by measurement of zeta potential (Figure 4.10) in pH range 3.50 - 10.0, a feature that should inhibit the aggregation of the flakes suspended in water. As discussed in the literature review, contacting the GO with a charged species, such as salt or dye, which is capable of disrupting the electrokinetic properties of GO in the vicinity of the surface, may result in irreversible aggregation of GO flakes in suspended media [139, 538]. It appears for MB in particular, that neutralisation of the electrostatic charge of GO resulted in high levels of aggregation, to the extent that the generated flocs are clearly visible. Physical changes such as these may limit the recyclability and reusability of

the GO adsorbent to remove these types of dyes in practical application, in which the charge of the dye is having a discernible impact on the stability of the GO [172].

In order to investigate the aggregation of GO in MB and MO, LD was utilised to measure changes in PSD, between the water-dispersed GO and the GO-dye suspensions. Figure 5.13(a) and (b) show the PSD's obtained for SFGO and LFGO, respectively, dispersed in 15 mg/l MB and MO, with the water dispersion indicated by the black lines and the MB and MO suspensions by blue and orange dashed lines, respectively.

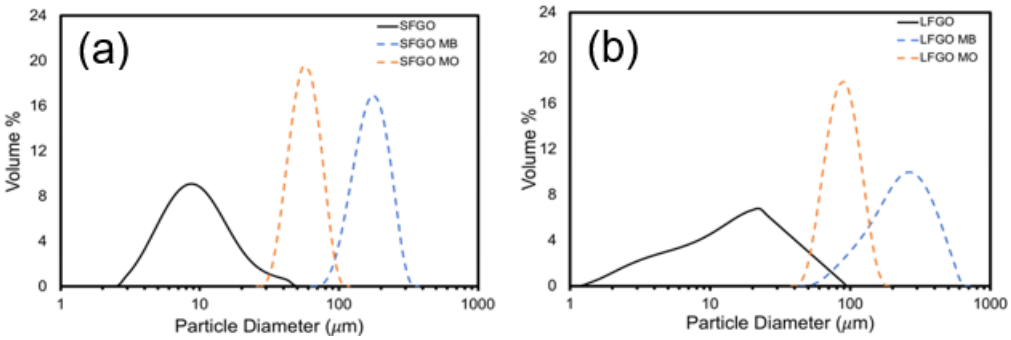

Figure 5.13: Sizing of (a) SFGO and (b) LFGO aggregates in 15 mg/l MB and MO, obtained using LD technique.

Table 5.9: d(10), d(50) and d(90) values, obtained from LD analysis, of SFGO and LFGO dispersed in distilled water at 0.01 mg/ml, and the analogous dispersions of GO in 15 mg/l MB and MO.

GO	d(10) (μm)	d(50) (μm)	d(90) (μm)
SFGO	4.4	9.0	18.9
SFGO - MB	109.1	160.2	225.5
SFGO - MO	38.9	54.2	73.4
LFGO	3.5	13.6	29.7
LFGO - MB	106.3	225.6	404.2
LFGO - MO	59.7	83.2	117.4

Inspection of the respective PSD's and above table of percentiles highlights a number

of prominent features associated with the aggregation. First, it is evident that GO appeared to be aggregate in both MB and MO, and that the PSD's, as a result, shifted towards greater particle sizes on the horizontal axis. Dispersal in MB does, however, result in greater floc sizes than is the case for MO, as indicated by the more significant shifting of the PSD. The tendency of both GO materials to aggregate in MO is very interesting, as this behaviour was less obvious by inspection than was the case for MB. A second feature is that the relative growths of the LFGO aggregates in dyes appear to be of much greater magnitude relative to that of SFGO aggregates. This phenomenon may be explained by the DLVO theory (discussed in Section 2.2.1), that suggests that the aggregation of larger particulates is greater due to the stronger effects of van der Waals' forces [539, 540]. This is also consistent with expectation, given the initially larger nominal flake sizes of the LFGO system, that flocculate to greater size upon aggregation.

Measurement of zeta potential was used to confirm the electrokinetic changes to the GO surface charge, and thus confirm the aggregation of flakes. Figure 5.14(a) and (b) show the zeta potential of SFGO and LFGO dispersed in 5, 10 and 15 mg/l of MB and MO solutions, respectively. The corresponding zeta potential of the GO in distilled water at 0.01 mg/ml (values taken from Figure 4.3.7) is provided in each plot.

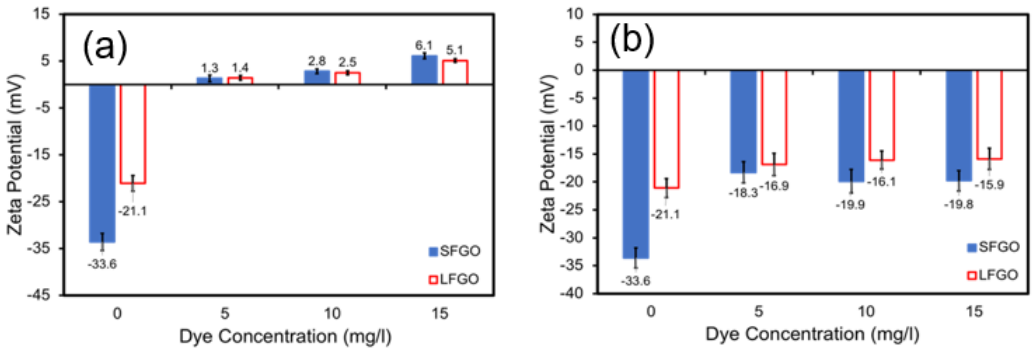

Figure 5.14: Zeta potential of SFGO and LFGO dispersed in 5, 10, 15 mg/l (a) MB and (b) MO. Vertical error bars represent error after three separate measurements, taken from the same sample beaker.

The interaction of GO with dye had a marked effect upon the electrokinetic properties and stability of the GO when dispersed in MB. Dispersal of GO in MB resulted in neutralisation of the surface charge negativity, across the range of MB concentrations. The impact upon zeta potential was so great that the GO even became positively charged, with low magnitude GO - MB potentials ranging approximately +1 - 6 mV. By the earlier discussions regarding zeta potential (Table 3.3), this suggests that the GO - MB colloid is highly unstable, with tendency to rapidly flocculate due to the electrokinetic instability. The magnitude of the impact upon both SFGO and LFGO appears to be similar, suggesting that the interaction of both types is closely related. Neutralisation of charge due to rapid and plentiful adsorption has therefore been demonstrated a salient feature relating to the aggregation of GO flakes in cationic dyes.

Dispersal of GO in anionic MO appeared to have a milder impact upon zeta potential, reducing the potential to magnitudes that is suggestive of incipient GO - MO stability. These changes are likely an effect of double layer contractions from the effective electrolyte addition in the dye solution [541]. This suppression is, however, relatively small in magnitude, and unlikely to be the dominant factor in aggregation,

which is more likely driven through attractive groups on the adsorbed MO. For example, hydrogen bonding or π - π stacking between aromatic groups on adsorbent and adsorbate molecules can lead to strong association [542].

5.4.4 Mechanism of dye adsorption

Sections 5.3 and 5.4 considered respectively kinetics and equilibrium of dye adsorption. In these sections, experimental data was analysed using widely regarded PFO and PSO kinetics models and Langmuir and Freundlich adsorption isotherms. The adsorption of dyes onto both SFGO and LFGO was determined to be governed by PSO kinetics model and Langmuir adsorption isotherm.

Electrostatic interaction is considered to be a significant factor in the adsorption mechanism. Measurement of zeta potential for both SFGO and LFGO (Figure 4.10), revealed that both materials possessed a significant negative surface charge. The zeta potential was lower (more negative) for SFGO compared to LFGO. As discussed in the literature review (Section 2.2.1), this has the bifold effect of enhancing the dispersion of GO in water, but also promoting the electrostatic attraction between negatively charged GO and positively charged MB, due to deprotonation of the hydrogenated groups on the GO [198]. Whereas electrical attraction played a crucial role in attracting MB to GO, it was observed that both GO's were significantly poorer adsorbents of anionic MO compared to cationic MB. Electrostatic repulsion forces, between negatively charged GO and anionic MO, hinder the interaction of the adsorbent and adsorbate groups, due to like-charge repulsion. Despite the effects of repulsion, however, the overall levels of MO sorption were in fact still encouraging, though this is likely due to π - π interactions and hydrogen bonding [139, 140]. In attempt to mitigate the effects of electrostatic repulsion in MO adsorption studies, larger doses of GO were utilised to offer more surface area for binding. Kinetics and equilibrium studies for MO adsorption, however, demonstrated that the addition of more GO surface (in kinetics, GO initial

loading increased from 5 to 10 mg, in equilibrium, 20 to 30 mg), did not significantly promote adsorption to a comparable level to that achieved in MB adsorption, as the calculated adsorption capacities remained significantly lower.

Particle size and surface area are considered to play a further important role in the adsorption process for both dyes. It was found using DLS and LD particle sizing methods (Figures 4.1 and 4.2, respectively) that the LFGO flakes are indeed larger than SFGO. BET surface area (Table 4.3) of SFGO was also revealed to be a factor of four times larger than LFGO and total pore volume was approximately double, implying that the overall surface area available for MB molecule binding is significantly greater. This is perhaps highly significant given that the Langmuir adsorption isotherm was determined to be the governing adsorption process, wherein adsorption of dye molecule to available binding sites is a monolayer coverage of the adsorbent surface.

In addition to charge interactions and GO particle size, surface chemistry interactions also play a significant role. Both GO materials were demonstrated by XPS and FTIR spectroscopic methods to possess a number of reactive oxygen-containing functional groups, including -COOH, -COC and -COO, having tendency to deprotonate. By XPS and EDX analysis, LFGO was determined to have slightly higher oxygen content compared to SFGO: it has been reported that in GO-dye systems, a higher content of oxygen is positively correlated with greater adsorption of cationic dyes, due to the increased number of oxygen-containing binding sites [543]. The higher oxygen content in LFGO, however, does not yield higher MB adsorption, a feature inconsistent with the aforementioned study. This is further highlighted by consideration that LFGO was able to adsorb more MO than SFGO. It is considered thus that the impacts of particle size and surface area are, for our systems, more significant.

In summary, it is proposed that a combination of favourable surface chemistry, smaller flake size and increased binding site surface area coupled with a higher overall negative zeta potential are the dominating factors governing dye adsorption. GO

favours the adsorption of MB over MO, given the electrostatic attraction of GO with MB, that facilitates interaction of MB with binding sites. This explains then the particularly high adsorption capacity associated with SFGO - MB adsorption. For MO adsorption, the particle size and surface area is considered less important, given that electrostatic repulsion is considered to be the driving mechanism. This is further emphasised given that with its smaller particle size and surface area, SFGO achieved in fact slightly lower overall MO adsorption in kinetics and equilibrium compared to LFGO.

5.5 Results and Discussion: Filtration of dyes

In this section, the performance of uncoated and SFGO- and LFGO-coated PES membranes, regarding removal of cationic MB and anionic MO, was assessed by dead end filtration. Performance was quantified by measurement of permeability and dye rejection. Removal of dyes by filtration using GO membranes was evaluated in Section 2.4 of the literature review.

5.5.1 Control experiments: filtration of dyes using uncoated PES

Filtration tests were carried out with uncoated PES membranes, in filtering MB and MO at initial concentrations 5 and 10 mg/l, at pressure 2 bar, in order to serve as a control experiment against which to gauge the performance of the GO-coated membranes. Dye concentrations were selected such that the measured values of absorbance were comfortably within range of the UV-Vis. detector. Mean values of permeability and rejection are reported in Table 5.10.

Table 5.10: Mean Permeability and Mean Rejection of 5, 10 mg/l MB and MO, from dead end filtration using uncoated PES 0.20 μm membranes.

Dye (Concentration, in mg/l)	Mean Permeability ($l \cdot m^{-2} \cdot h^{-1} \cdot bar^{-1}$)	Mean Rejection (%)
MB (5 mg/l)	299.2	0.98
MB (10 mg/l)	292.8	0.48
MO (5 mg/l)	300.9	1.39
MO (10 mg/l)	296.4	0.64

It is apparent that the uncoated PES membrane offers almost no rejection of dyes, as exhibited by the mean rejections, which in all cases were as low as <2%. Permeabilities were very high, further indicating that the uncoated membrane offers essentially no resistance to the permeation of dye molecules, which were able to transit through the membrane practically unhindered. In the literature regarding dye removal using ultrafiltration membranes, several systems have likewise reported very high permeabilities [544, 545]. With respect to the molecular sizes of the dyes, which are of lateral size order <10 nm, it may be considered that the stated membrane pore size of 0.20 μm is very large. Given the size disparity, it is not considered that physical size sieving is likely to be an effective mechanism of exclusion, findings which are consistent with similar dye rejection studies by polymeric filters [546]. Furthermore, uncoated PES membranes are found lacking in the chemical functionality of the GO-coated membranes. GO coating imparts oxygen-based functionality into the surface coating, thereby enabling the membrane to interact with dye species, by means of chemical or charge-based interaction [275, 279]. The lack of these groups therefore is not favourable in terms of promoting dye rejection. Accordingly, very poor levels of rejection are achieved by the PES membranes, a finding that is within expectation.

5.5.2 Impact of initial dye concentration

The impact of initial dye concentration in the feed was explored by preparing solutions of MB or MO, at initial concentration 5 or 10 mg/l, and filtering at 2 bar constant pres-

sure, using SFGO- and LFGO-coated PES membranes. The corresponding literature review is given in Section 2.4.2.

As discussed in the earlier methods section (Section 5.2.8), permeability was measured in 1 ml increments meanwhile rejection every 4 ml. To illustrate the behaviour in removal of 5 and 10 mg/l MB at 2 bar, the 0.01 mg/ml SFGO and LFGO-coated membrane results are provided in Figure 5.15(a) and (b), respectively. The corresponding 0.10 mg/ml coating data for both GO materials is given in the Appendix (Figure A.6).

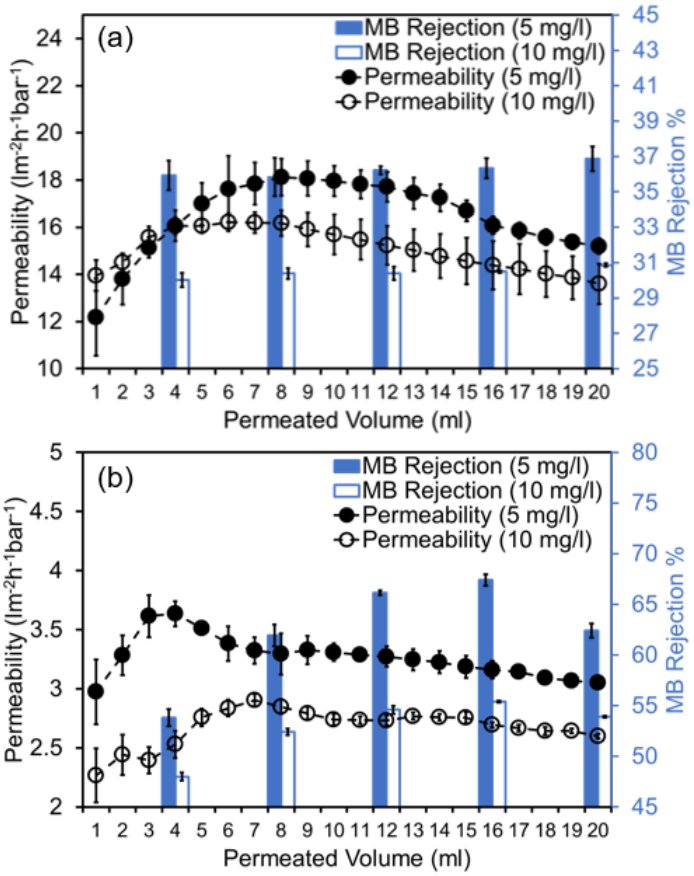

Figure 5.15: Permeability and MB Rejection of (a) 0.01 mg/ml SFGO-coated and (b) 0.01 mg/ml LFGO-coated PES membranes, as a function of permeated volume, with initial dye concentration 5 and 10 mg/l. Filtration pressure 2 bar. Vertical error bars represent standard deviation over three separate runs.

A feature that is evident by inspection of the figures is that the SFGO systems offer significantly higher permeability compared to the analogous LFGO, for example, the permeability of the 0.01 mg/ml coatings are of the order four times higher in SFGO. Smaller flake systems have been demonstrated in several studies to have a positive impact upon solvent permeation [515, 547, 548]. The relatively high permeabilities of the SFGO membranes may be attributed to a number of possible factors, including possession of shorter transport pathways that facilitate the channeling of solvent through the membrane [549].

For all membranes, increasing initial MB concentration in the feed side from 5 to 10 mg/l resulted in a decrease in both overall permeability and dye rejection. The presence of higher initial dye concentration in feed gives rise to a more substantial concentration gradient, as the solute (dye) is initially more concentrated on the feed side. This gives rise to an effect known as *concentration polarisation*, in which solute concentration gradients are responsible for the decline in effective mass transport of solvent across the membrane [13]. Concentration polarisation is caused by the greater osmotic pressure in the higher concentration system [550]. It is considered that concentration polarisation is responsible for the decline in overall permeability and MB rejection of the membranes, as the the higher dye concentration leads to greater amounts of dye being deposited on the surface of the GO membrane [551]. Additionally, operation of a membrane under higher initial concentrations of dye increases the tendency of the membrane to become fouled by the filtration process, thus adversely impacting the efficacy [552]. The SFGO membranes appear to be more sensitive to increase in MB concentration, as evidenced by the seemingly greater drops in permeability for SFGO membranes. For example, the 0.01 mg/ml SFGO coating (Figure 5.15(a)) shows permeability decline of around 18.1 - 15.2 $l \cdot m^{-2} \cdot h^{-1} \cdot bar^{-1}$, from maximum to final permeability, meanwhile for 0.01 mg/ml LFGO the decline is from 3.3 - 3.0 $l \cdot m^{-2} \cdot h^{-1} \cdot bar^{-1}$ (Figure 5.15(b)). It is considered that this behaviour is a result of increased levels of dye adsorption on the membrane

surfaces [553], as SFGO was demonstrated to be a particularly effective adsorbent of MB (Section 5.3). MB rejection is found to generally increase with increasing permeated volume: it is considered that this interesting behaviour is a combination of the accretion of MB onto the membrane coating and possibly physical blockading of the GO porous features, resulting in a lowering of the flux while also contributing to the increase the rejection of MB [5]. The behaviour of the membranes in rejection of MB will be discussed further in the mechanistic discussion section (Section 5.5.5).

The filtration of 5 and 10 mg/l MO, at filtration pressure 2 bar, is shown in Figure 5.16, in which 0.01 mg/ml SFGO and LFGO coating results are provided in (a) and (b), respectively. The corresponding 0.10 mg/ml results for MO are given in the Appendix (Figure A.7).

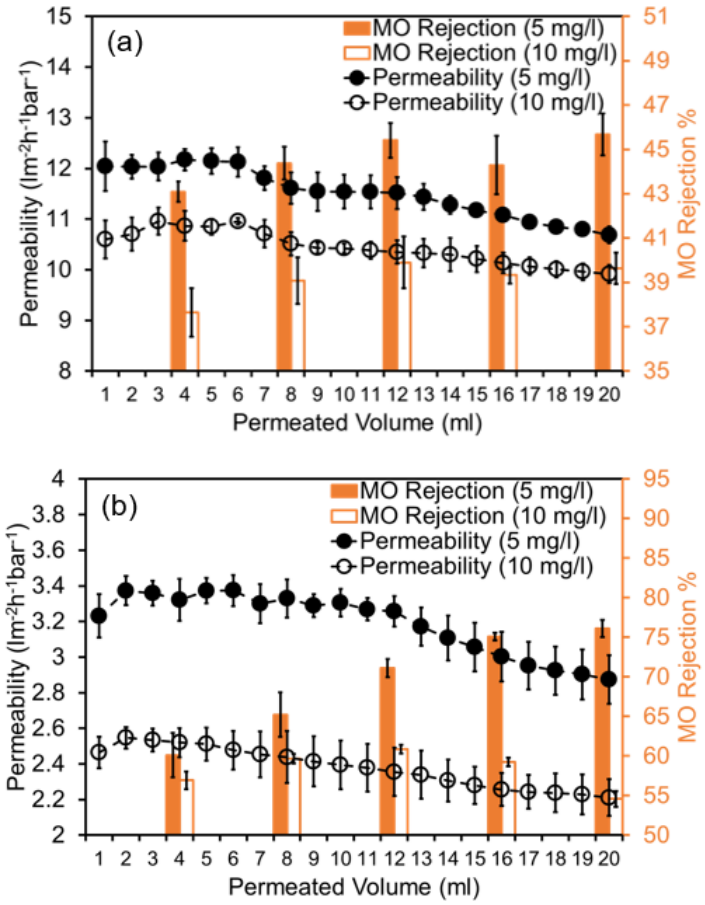

Figure 5.16: Permeability and MO Rejection of (a) 0.01 mg/ml SFGO-coated and (b) 0.01 mg/ml LFGO-coated PES membranes, as a function of permeated volume, with initial dye concentration 5 and 10 mg/l. Vertical error bars represent standard deviation over three separate runs.

In parallel with the results achieved in filtration of MB, it is again observed that increasing the MO feed concentration from 5 to 10 mg/l results in a decline in both mean permeability and MO rejection, for all membranes. In filtration of MO, the anionic dye adsorbs less strongly onto the negatively charged GO surface, compared to MB. By PSO analysis of the GO - dye systems (Section 5.3.3), the obtained $q_{e,cal2}$ values calculated for adsorption of 5 and 10 mg/l MB were an approximate factor 3.5 greater compared

with results achieved in adsorption of MO. Accordingly, the more limited adsorption of MO may suggest that the tendency for this dye to accumulate on the surface due to adsorption is lower overall, compared with MB, and that this may reduce the surface fouling during MO filtration. It was observed that during MO filtration at 5 and 10 mg/l, the permeability of all membranes declined as a function of permeated volume, meanwhile the rejection levels generally increased from the beginning to the end of the process; behaviour consistent with the previously discussed observations for MB filtration. It is very interesting that similar observations are made for the behaviours of both dyes, in terms of their propensity to suffer due to concentration polarisation effects, despite that at this stage, the dye - GO interaction mechanisms are considered to be different. The overall proposed mechanism of filtration of the two oppositely charged dyes will be considered further in Section 5.5.5.

Comparison of the results achieved by commercial GO in these studies with other sources from the literature reveals that the materials are highly competitive. The vacuum deposited commercial GO membrane of Jee *et al.* [275] was reviewed in literature review (Section 2.4.1). Levels of rejection achieved in their studies were slightly improved relative to those in this chapter (MB - 92.8%, MO - 85.4, for 10 mg/l dye), albeit with modest permeability (5.3 $l \cdot m^{-2} \cdot h^{-1} \cdot bar^{-1}$). On the other hand, the electrosprayed GO-coated membrane of Chen *et al.* [554] offered significantly greater rejection of MB(90.1%) and MO (97.4%), with improved permeability (11.1 - 20.3 $l \cdot m^{-2} \cdot h^{-1} \cdot bar^{-1}$).

In summary, it was observed by experiment that increasing the initial concentration of dye in the feed solution was demonstrated to reduce mean permeability and mean dye rejection of GO-coated membranes. The effects of concentration polarisation, when using the higher concentration dye, were considered to be responsible for causing increased deposition of dye on the surface of membranes which in turn, reduces permeability and filtration capabilities of the membranes.

5.5.3 Impact of GO-coating concentration

In this section, the impact of GO coating concentration upon efficacy of dye filtration is considered. Coatings of GO were applied to PES substrate at concentrations 0.01 mg/ml or 0.10 mg/ml. Filtration tests were carried out at 2 bar, using 5 mg/l MB or MO dyes. For clarity, in the previous section regarding the impact of initial dye concentration, the results of filtering dyes with both GO concentrations 0.01 mg/ml and 0.10 mg/ml were included. This section, however, elaborates on the role of coating concentration subject to a single initial dye concentration. As such, a separate series of experiments was not carried out for the purposes of this section.

The impact of coating concentration on permeability is affected by a number of factors. GO concentration has an impact upon the hydrophilicity of the membrane, which may in turn have an effect on the permeation of water [555, 556]. In Section 4.4.5, regarding Water Contact Angle of the GO membranes, it was revealed that increasing the concentration of GO in coating led to a decrease in contact angle, corresponding to an improvement in hydrophilicity with increasing GO content. It has been reported that increasing hydrophilicity has a positive impact upon solvent permeation in membranes [557, 558]. In contrast, however, a number of studies (highlighted in literature review Section 2.4.2) related to GO membranes have suggested that the relationship between GO concentration and permeability reaches a maximum value, before declining with further increase of GO content, due to the excessive blockading of substrate pores at higher loadings [13, 269]. Coating thickness is also an issue of importance, as thicker layers, by solution-diffusion model (also discussed in the literature review) [559], have inherently higher resistance to mass transfer; this may adversely impact the permeation rates of solvent [560]. In Section 4.24, regarding cross sectional FIBSEM analysis, it was revealed that for SFGO and LFGO systems, the increase in GO concentration was correlated to an increase in coating layer thickness, and that the layer thickness of LFGO systems in particular increased substantially.

The case of dye filtration with uncoated PES (which corresponds to a GO coating concentration of zero) was discussed in Section 5.5.1. It was revealed that the uncoated PES offered minimal resistance to the permeation of MB and MO, and mean rejection values were almost zero (<2%, in all cases). Accordingly, the mean permeabilities were very high, of the order *c.a.* 300 $l \cdot m^{-2} \cdot h^{-1} \cdot bar^{-1}$. It was demonstrated therefore that the application of zero GO coating led to very poor dye rejections and high permeability. In principal, this behaviour was attributed to the substantial discrepancy in size between the relatively large membrane pores and the small dyes.

Figure 5.17 shows (a) Mean permeability and (b) Mean rejection of 0.01 and 0.10 mg/ml GO-coated membranes, in filtration of 5 mg/l MB and MO at 2 bar. These plots were generated using the overall mean permeability across the 20 readings, and 5 readings of dye rejection, for Figures 5.15 and 5.16 (0.01 mg/ml) and A.6 and A.7 (0.10 mg/ml). Mean values of permeability and rejection were calculated using these plots, represented as bars in the below figure.

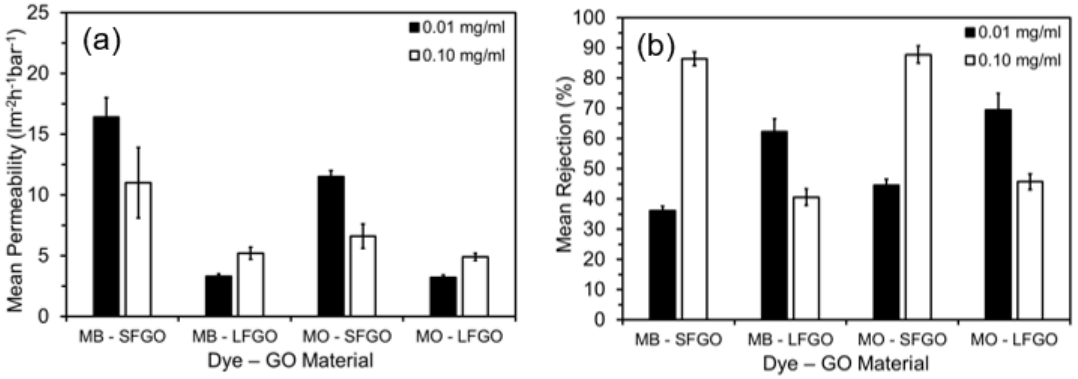

Figure 5.17: (a) Mean permeability and (b) Mean Dye Rejection of SFGO- and LFGO-coated PES membranes, with GO coating concentrations 0.01 and 0.10 mg/ml. Filtration pressure 2 bar. Initial dye concentrations 5 mg/l. Vertical error bars represent standard deviation across three runs.

With reference to the summary charts, it is apparent that the application of GO

coating does have a markedly positive impact upon filtration performance of the membranes. The permeabilities are reduced by an order of magnitude relative to the zero GO case, meanwhile the rejection capabilities of the GO membranes is significantly improved. The behaviour of the separate SFGO and LFGO systems is, in this comparison, very interesting, as the profiles demonstrate conflicting behaviours; in SFGO systems the higher GO concentration leads to lower overall permeability and higher dye rejection, but in LFGO systems, the converse relationship between permeability and rejection is observed. Furthermore, the disparity in permeability, between SFGO and LFGO coatings is again emphasised, as the bars demonstrated that the SFGO coatings invariably lead to higher permeation rates than the LFGO.

For SFGO coatings, it was observed that for both dyes, the dye rejection (R) follows the order: R (0.10mg/ml) > R (0.01mg/ml) > R (Uncoated PES). In turn, the permeability (P) follows the converse order P (Uncoated PES) > P (0.01mg/ml) > P (0.10mg/ml). As such, by the above discussion, it appears that in SFGO systems, the solution-diffusion model of permeation is upheld, as increasing the GO concentration and associated layer thickness is found to result in a higher resistance to mass transport, thereby decreasing the flux while increasing the rejection. It was suggested by [296] that higher concentration may lead to aggregation of the GO, and that the aggregated sections of material further enhance the resistance. It is not certain, however, that this phenomenon is analogous to our systems, as the SFGO sample was demonstrated to be very stable in suspension (Figure 4.9).

For LFGO coatings, there exists a somewhat paradoxical relationship between GO concentration, permeability and dye rejection, in which increasing concentration led to a decline in rejection and an increase in permeability. Based on the above discussion, it is possible that the behaviour is attributed to the increase in hydrophilicity of the membranes: this case is strengthened by considering that the GO layer thickness in the LFGO systems was determined by FIBSEM to increase significantly at the higher load-

ing. A factor of perhaps greater significance, however, was the relatively poor stability of the higher concentration LFGO coating in water. In Section 4.4.1, it was revealed that the thicker LFGO sample was unable to remain macroscopically intact following an immersion period in distilled water, with clear regions of delamination apparent by eye. The regions where the coating was removed revealed the underlying PES, as such dye molecules and solvent were able to permeate through these regions with relative ease, compared to the regions in which the GO remained intact. Accordingly, the resulting permeability of the thicker LFGO coating was thus higher and the rejection of dyes lower, due to the poorer structural stability of the higher concentration coating.

In summary, for SFGO coatings, GO coating concentration was demonstrated to have an expected impact upon permeability and dye rejection of coated membranes, relative to the case for which no GO was applied to the substrate. As coating concentration increases from 0.01 to 0.10 mg/ml, the permeability of both dyes was observed to decline meanwhile the dye rejection increases. For LFGO coatings, the impacts of GO coating concentration was demonstrated to follow a converse trend with regards to the permeability and dye rejection capabilities of the membranes. When coating concentration increased from 0.01 to 0.10 mg/ml, the permeability of both dyes was observed to increase meanwhile the dye rejection decreased.

5.5.4 Impact of filtration pressure

In the previous sections, filtration of MB and MO through GO-coated PES membranes was undertaken at filtration pressure 2 bar, with the pressure being maintained constant throughout the process. In this section, the role of pressure is explored by carrying out analogous filtration experiments with both dyes at 5 mg/l, at constantly-maintained pressure 4 bar.

In Figure 5.18, the results of 5 mg/l MB filtration at 2 and 4 bar are shown for 0.01 mg/ml (a). SFGO and (b). LFGO, meanwhile, filtration of 5 mg/l MO is shown

in (c). SFGO and (d). LFGO. The 2 bar permeability and rejections shown on each separate plot were taken from the 2 bar, 5 mg/l case from the figures discussed in the earlier section (Section 5.5.2) regarding the impact of initial dye concentration. The analogous plots for 0.10 mg/ml coatings are shown in the Appendix (Figure A.8 for MB, and Figure A.9 for MO).

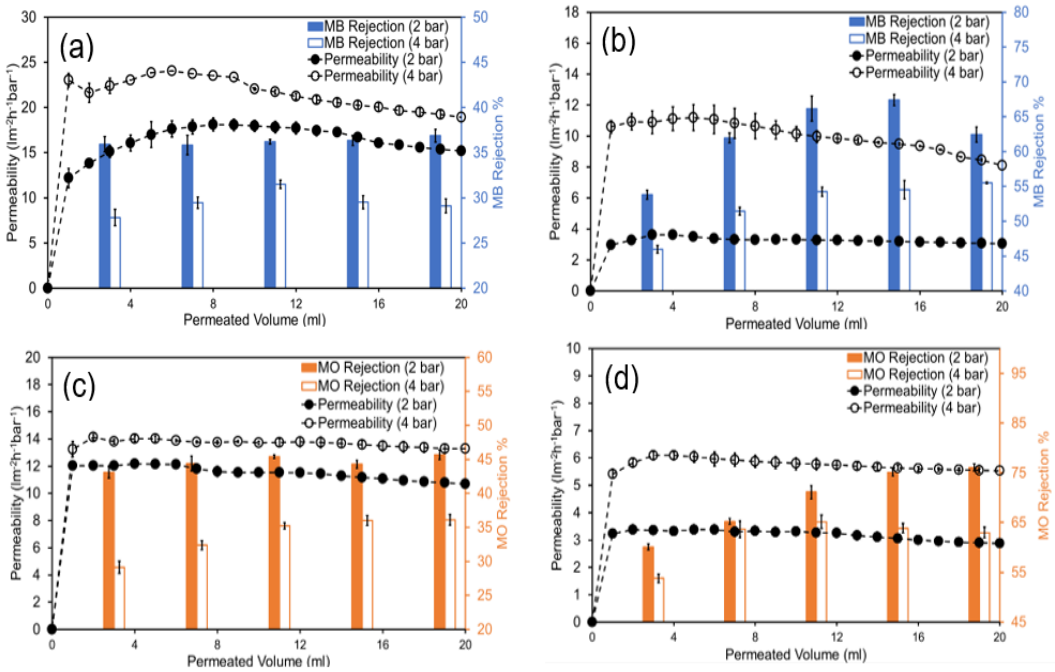

Figure 5.18: Permeability and dye rejection of MB using (a) 0.01 mg/ml SFGO-coated and (b) 0.01 mg/ml LFGO-coated PES membranes, as a function of permeated volume, with initial dye concentration 5 mg/l, at respective pressures 2 and 4 bar. Similarly, permeability and dye rejection of MO using (c) 0.01 mg/ml SFGO-coated and (d) 0.01 mg/ml LFGO-coated PES membranes, under identical pressures and dye concentrations. Vertical error bars represent standard deviation over three separate runs.

Doubling the pressure leads to an increase in flux which is disproportionately greater than a factor of two, and a corresponding step decrease in rejection capabilities. This deviation from linearity in the relations between permeability and pressure gradient is likely due to the presence of mechanical defects in the membrane microstructures. The

presence of defects is particularly prominent in membranes fabricated by vacuum deposition, as GO layers are disordered and randomly stacked on the membrane surface, resulting in significant presence of microstructural defects [561]. At higher operation pressure, the impact of these structural defects is exaggerated, therefore disproportionately increasing the flux and decreasing the dye rejection, of both dye systems [562]. Such behaviour conflicts the study of Li *et al.* [563], who reported that the dye permeability declined with increasing pressure, due to compaction of the membranes under higher pressure. A second study [564] also achieved proportionate scaling of flux with pressure (resulting in a slight decrease in permeability with pressure), while maintaining a steady rejection of MB dye, suggesting the impact of mechanical defects is mitigated.

The presence of defects in dried GO was investigated by Raman spectroscopic analysis of the GO materials (discussed in Section 4.3.4), which demonstrated that both materials contained high levels of structural defects, as exhibited by the high $I_D : I_G$ ratios (Table 4.4). It is straightforward to predict then that these inherent properties are transferred into the membrane coating, particularly given the application of coating by vacuum deposition. It appears that the higher increases in permeability are typically resultant from the LFGO coatings. It may be concluded then that the defects in LFGO coatings lead to more significant deviations from linearity, compared to SFGO.

Comparing the dye removal of these GO membranes with competitor membranes from the literature suggests that the performance is comparable. In Section 2.4.4, several alternative modified polymer materials were considered, including chitosan-based composites, revealing that the dye removal rates of these was typically >90% for dyes including anionic Congo Red. This removal rate therefore out-performs even the best GO candidate considered in this study (SFGO 0.10 mg/ml coating). Perhaps a greater advantage of the GO systems, however, is the high flux of material through the membranes. This is possible owing to the passage of solvent through the relatively small GO flakes and membrane pores. In addition, the amphiphilic nature of the GO

enables a consistently high solvent flux, due to the unique interactions of GO with water and rapid slip-streaming of water molecules through the system. It is for these reasons, including flake size, surface area and charge that the performance of GO membranes is comparable to competitor materials.

In summary, for SFGO and LFGO coatings, filtration pressure was demonstrated to have an impact upon permeability and dye rejection of GO-coated membranes. Increasing filtration pressure from 2 to 4 bar was observed in all cases to increase the permeability of the membranes, while decreasing the dye rejecting capabilities. Inherent structural defects in the GO material coating were suggested as being the main cause of this behaviour.

5.5.5 Mechanism of dye filtration

Section 5.5 has considered removal of MB and MO dyes using GO-coated PES membranes. The effects of a number of experimental parameters and features of the membranes were explored, these include: initial dye concentration in feed, concentration of GO in coating and filtration pressure. In this section, we seek to establish an understanding of the filtration mechanism which governs the permeability and dye rejection performance of the membranes, essential for developing a complete framework for the behaviour of the system.

The role of dye charge is considered to have a significant impact upon the results obtained in filtration studies, and the overall mechanism of dye removal. In the previous discussion section regarding dye adsorption, it was revealed that the electrostatic attraction for cationic dyes and repulsion of anionic dyes was key to the adsorption process. The impact of oppositely charged dyes is considered first. Comparison of the physical sizes of the two dyes suggests that they are of the same order, thus implying that rejection due to steric effects may be comparable in both membrane - dye systems [551].

The removal of cationic dyes by GO membranes (as discussed in the literature review Section 2.4.1) has been proposed to take place in a two-stage mechanism [280]. The first stage consists of cationic dye surface adsorption; the second stage, involves interacts with the surface to remain bound to vacant sites, including π - π interactions. Accordingly, the electronegativity of GO surface is a very important aspect for facilitating the adsorption of dye. The substantial adsorption of MB onto a GO-coated membrane post-filtration of the dye is demonstrated in Figure 5.19 below.

With regards to the MB rejection profiles of the GO-coated membranes, it was found that the level of MB rejection achieved increased overall, with permeated volume, such that the final rejection value was higher than the initial (Figures 5.15 and 5.18(a) and (b)). Interestingly, the interaction of MB with GO membranes, involving both GO types, is analogous to the behaviour during dye adsorption studies, in particular kinetics studies (refer to Section 5.3). In adsorption kinetics studies, the value of q_t increased as a function of time, until the system reached equilibrium. In analogy, in filtration studies, the rejection of the membranes for MB continued to increase as the coated membrane adsorbed MB. In addition, it is considered that the 0.10 mg/ml SFGO coated membrane offered greatest overall MB rejection, as it had greatest surface area and pore volume availability to adsorb MB molecules, coupled with a high capacity for sorption of the dye. It is postulated that beyond the state of maximum dye adsorption, the rejection of the membranes may begin to decline due to the effects of membrane fouling [565]; though for the timescales in this series of experiments, this effect was not routinely observed. Permeabilities were found to be initially high, but reduced with increasing permeated volume; due to the attraction between GO and MB. The permeabilities for SFGO membranes was particularly high due to the rapidity of MB sorption. A secondary interaction is that when MB molecules are adsorbed, they may enter the membrane channels and shield the electronegativity of the GO, meanwhile the presence of interlayer molecules blocks the transit of feed MB molecules to permeate

[5]. This effect may have also contributed to the overall reduction in permeability.

Retention of MO by is governed by electrostatic repulsion mechanism, in which the negative GO surface provides electrostatic repulsion against the transiting MO from feed [507]. By dye adsorption studies, the GO's were shown to be relatively poor adsorbents of MO in comparison to MB, as such the adsorption phase of rejection, as discussed above, is more minimal compared to cationic MB. Interestingly, however, the GO membranes did appear by inspection to adsorb MO, as indicated by the orange colouration on the GO surface coating post-filtration (Figure 5.19). As discussed in Section 2.2.2, adsorption is likely due to π - π interactions between GO and MO [179]. The filtration results in Figures 5.16 and 5.18(c) and (d) also indicated that the permeability tended to diminish as a function of permeated volume, meanwhile the rejection was enhanced. It is considered that the growth of rejection occurs due to the blockading effect of the adsorbed MO molecules. It is thus very interesting that results achieved using oppositely charged dyes have led to comparable behaviours, albeit that the membranes were able to achieve, overall, higher levels of MO rejection. Measurement of zeta potential on a GO - MO mixture (Figure 5.14(b)) revealed that the electronegativity of the GO membrane is not significantly impacted by the MO, such that the GO retains its overall charge negativity. As such, it is considered that during filtration the membrane continues to provide a negatively charged active layer which barriers the permeation of MO. Given the overall higher rejection of MO, this emphasises the importance of charge and zeta potential in the overall rejection mechanism, illustrating the comparison between the two dyes.

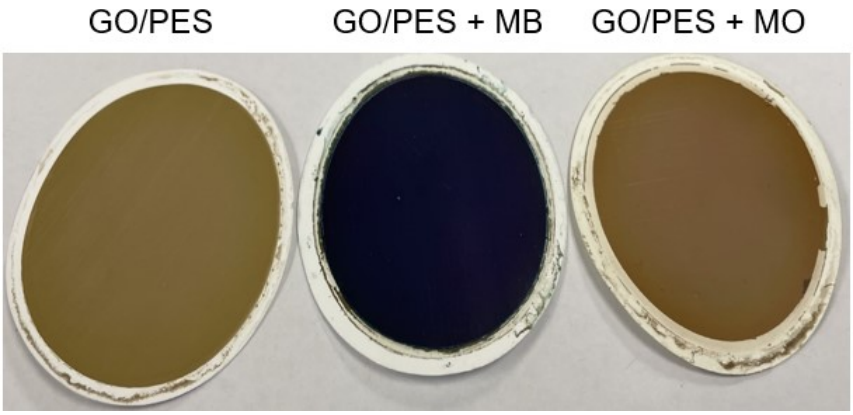

Figure 5.19: Surface adsorption of MB and MO dyes onto GO/PES membranes, images captured following a filtration cycle with each respective dye. Left: GO-coated PES membrane. Middle: GO/PES membrane, post filtration with 10 mg/l MB. Right: GO/PES membrane, post filtration with 10 mg/l MO.

The interaction of GO with PES substrate is also an essential component in relation to the overall rejection mechanism. A number of techniques were used to analyse the coated surface including FTIR (Section 4.4.2), XRD (Section 4.4.3) and morphological FIBSEM (Section 4.4.6). The impact of this analysis is considered here.

FTIR analysis of uncoated and GO-coated PES (Figure 4.17) substrates revealed that GO does not appear to undergo chemical reaction with PES, as no new bonding peaks were exhibited on the membrane surfaces following vacuum deposition of GO. Application of GO does, however, impart GO functionality and surface charge onto the substrate; it has been considered that the dye rejection mechanism is principally governed by the active coating layer, not the substrate [566]. This implies therefore that the features of the GO are responsible for the rejection of dyes, not the PES.

XRD analysis of dry (Figure 4.18) and wet (Figure 4.19) GO-coated membranes revealed that the interlayer spacing of the GO coating did increase as a result of intercalation of water. It is not considered, however, that the increase is sufficient to have an impact upon the mechanism of dye filtration, given the lateral sizes of the

dyes are exceeding 1 nm, whereas even with swelling artefact, the interlayer spacing as calculated by Bragg's Law was below 1 nm. This is clearly insignificant swelling compared to the order of sizing for dye molecules, which are typically several nm [567]. It is considered therefore that size exclusion principle is likely significant for removal of dye molecules. The impact of the GO swelling will however be revisited later, when considering desalination of saline feeds.

Top down SEM imaging of the membrane topological features (Figure 4.23), revealed that the GO coating appeared complete across the membrane surfaces. It is implied, therefore, that GO is adhered physically onto the polymer as a result of hydrogen bonding [568]. Deposition of GO onto the surface thus has the effect of physically blockading the substrate porous features. As such, physical coverage of PES pores due to the presence of coated GO flakes, has the effect of hindering the permeation of dye and water molecules through the membrane. Accordingly, it is considered that physical blocking of pores by GO contributes to the characteristics of the membranes in terms of permeation and rejection. This is further evidenced by comparing the results of uncoated PES membrane with GO-coated membranes, as it was observed that the presence of GO coating significantly improves the rejection of the membranes while reducing the permeability of solvent. Based on the microscopic sections obtained by FIBSEM analysis, it was not possible to calculate the lateral spacing of GO sheets in the membrane coatings, due, in most cases to the near complete surface coverage. If the study were to be extended, the inclusion of a neutrally charged dye could be incorporated, with similar size property to MB and MO. This could ascertain the impact of charge and size effects, and crucially, enable differentiation of one from the other. This would assist with elucidation of the overall interaction mechanism. An example candidate dye is Basic Yellow 51, which is both neutral and of same size order (molecular mass = 430.5 g/mol) [569].

In summary, it is considered that the governing mechanism of dye filtration is di-

vided according to the charge of the dye. Cationic dye rejection is based upon the adsorption of dye by negatively charged GO, while anionic dye is rejected due to repulsion between the like-charged coating and dye. Overall, the best performance was given by the SFGO/PES 0.10 mg/ml coating, as this membrane was found to have a high surface area, thus offering a high volume of pores onto which adsorption may occur, and highly negative zeta potential, in addition to a smoothly-coated morphology. It is worthy of consideration, however, that membranes with high tendency to adsorb contaminants may suffer more greatly due to the adverse impacts of fouling, and may have more limited capacity for operational reusability [570].

5.6 Conclusions

In this chapter, the adsorption and filtration performance of two commercially available GO materials have been compared, for removal of anionic MO and cationic MB dyes from water. The intrinsic properties of GO, including most crucially flake size were essential in the behaviour of GO within these systems.

Kinetics and equilibrium studies of dye adsorption were implemented to analyse the adsorption efficacy and obtain suitable models of the adsorption processes. Kinetics studies demonstrated that the PSO model was more appropriate for the GO-dye systems compared to the PFO model. By PSO model, SFGO was demonstrated to adsorb MB with high efficacy (270 mg/g), compared to LFGO (234 mg/g). This was attributed to the effects of the small flake size coupled with greater negativity in electrical potential. Equilibrium studies showed that Langmuir equilibrium isotherm was more appropriate than the Freundlich isotherm, thus demonstrating that the mechanism of dye adsorption is based upon homogeneous binding. By Langmuir model, adsorption of MB by SFGO was again shown to be more complete (526 mg/g) compared to LFGO systems (384 mg/g). The influence of flake size and charge is thus highly important

in adsorption of cationic dyes, where effects due to the opposite charges dominate. Contrastingly, adsorption of MO was shown to be significantly more limited, an effect attributed to electrostatic repulsion between negatively charged GO and anionic dye acting as a hinderance to the adsorption process. The smaller flake systems were poorer adsorbents of MO due to their greater negativity. Additionally, the tendency of GO to aggregate in both dyes was investigated, by LD particle sizing, and measurement of zeta potential. This demonstrated that the electrokinetic properties of the GO were significantly impacted by the cationic dye, and this was especially prominent for the LFGO systems.

Removal of MB and MO dyes by filtration using GO-coated membranes was also considered in this chapter. SFGO-coated membranes were observed to offer increased levels of dye rejection as GO coating concentration increased from 0.01 mg/ml to 0.10 mg/ml, such that the 0.10 mg/ml coating was most effective in removal of MB (mean removal 82%) and MO (mean removal 86%). Interestingly, it was found that increasing LFGO concentration led to a degradation in performance, due to the poor stability of the higher LFGO concentration dye, leading to macrostructural cracking of the coated LFGO surface. For filtration of MB, the adsorption mechanism is considered to be dominated by **adsorption** and subsequent rejection, aided by the blockading of porous features on the membrane surface. For MO, rejection is dominated by **electrostatic repulsion** of like-charged coating and dye molecules. In the context of commercial application of the GO materials, it is considered highly relevant that LFGO is capable of reasonable levels of dye rejection at lower GO coating concentration. In terms of process economics, each membrane requires a lower quantity of GO to be deposited, as such this may be beneficial in terms of economic favourability and material efficiency.

The results of this chapter contribute novelty to the mechanistic understanding of the interactions of GO with dyes in adsorption and filtration systems. The effects of flake size and surface charge are clearly important factors for determining the behaviour.

This chapter may assist those seeking to enhance their understanding of GO - dye systems. In addition, the research into aggregation of GO flakes in charged media will be invaluable for those seeking to regenerate GO post-adsorption in downstream industrial processes.

Chapter 6

Applications of GO to desalination of saline water and fractionation of dye - salt mixtures

6.1 Introduction

In this chapter, the impact of ionic species upon GO adsorption and filtration systems, having the crucial property of differing flake sizes, is herein considered. With regards to dye adsorption, ions are dispersed in dye solution, and the dye adsorption capacities are characterised in analogy to earlier studies. In filtration studies, the research is subdivided to consider *i.* desalination of aqueous salt solutions, and *ii.* selective filtration of salts and dyes, in a dye-salt system.

Desalination of saline feeds including seawater by GO membranes is a major ambition of the field [147, 148]. With industrial desalination becoming an increasingly important means to extract ionic species from water and provide drinkable water, efforts are being made to reduce the energetic impact of RO membranes, which are currently operating close to their thermodynamic limit [96]. The emergence of GO and its properties such as frictionless flow of water have seen it become a promising candidate for removal of salts [38, 317]. Sodium chloride is the predominant salt in

seawater, making up approximately 3.5% of the total mass [571]. As such, removal of salts such as these is an issue of paramount importance in desalination.

The textile industry utilises salts heavily for a number of processes. It was discussed in Section 2.2.5 that this leads to the output of textile effluents with considerable salinity. As highlighted in Section 1.1.2 and Table 2.1, sodium salts, including sodium chloride and sulphate are among the most commonly used salts in the textile industry: their purpose is to aid the fixation process of dye onto fabric during the dyeing stage [572]. Sodium salt usage is particularly heavy in textile dyeing, as much as 0.8 kg is needed per kilogram of fiber [573]. Furthermore, magnesium salts may be used as a dye enhancer during the dyeing process. Ammonium heptamolybdate is also an industrial salt, with usage in the textile industry in preparation of pigments [574]. The importance of considering a non-ideal system for adsorption or filtration of salt-dye systems is realised in this chapter. In addition, the role of GO flake charge and surface charge are contextualised in these systems, which will contribute knowledge to the importance of these characteristics in conditions resembling simulated effluent.

In the first part of this chapter, we apply commercial GO-coated PES membranes for removal of salts from water by filtration. Given their relevance within seawater desalination and textile or industrial applications, the salts selected for this study were sodium chloride, sodium sulphate, magnesium sulphate and ammonium heptamolybdate. The second aspect of this chapter addresses the performance of commercial GO within multi-component systems, by adsorption of dyes within a dye-salt system and simultaneous removal of salts and dyes from feed. In order to exploit the full potential of the GO adsorption or filtration systems, multi-component systems were investigated using MB dye. As demonstrated in Chapter 5, the electrostatic attraction of GO and MB resulted in high levels of adsorption of this dye onto GO. This was especially prominent for smaller flake systems, with greater capacity for interaction with cationic species. The salts used in these dye-salt studies were sodium sulphate and magnesium

sulphate: these were selected given the different valencies of the cations (divalent Mg^{2+} ion and monovalent Na^{+}). It is expected that the differences in respective valencies will yield interesting behaviour, given the aforementioned differences in flake size and the role this is expected to play in charged media.

The results of this research chapter are divided into the the following sections:

- Desalination of saline feeds using GO-coated membranes, is considered in Section 6.3.
- Impact of salt addition upon dye adsorption, is discussed in Section 6.4.
- Fractionation of dye - salt mixtures, is considered in Section 6.5.

It is anticipated that the results of this chapter will have a significant research impact. This will extend to those from academia, and perhaps more significantly, to industrial practitioners who are seeking to understand the importance of flake size and charge-based interactions of GO in multicomponent systems. This is considered an extension of the previous chapter, with greater emphasis placed on the behaviour of GO systems in non-ideal environments.

6.2 Materials and Methods

6.2.1 Dye adsorption: The impact of salt addition upon dye adsorption

The Impact of salt addition upon dye adsorption was investigated by studies of kinetics and equilibria. Owing to its evidently greater adsorption onto GO, MB was selected as the probe dye for this series of studies. Probe salts selected were sodium sulphate and magnesium sulphate.

For experiments concerning the kinetics of adsorption, MB was prepared at initial concentration 15 mg/l, using the procedure outlined in Section 5.2.2. Sodium sulphate and magnesium sulphate were dispersed separately into 100 ml MB solution, and mixed

by magnetic stirring at speed setting 3 on the instrument for ten minutes to aid dissolution of salt. Salt loadings were selected as 50, 100, 150 or 200 mg, such that the corresponding initial concentrations of salt in the 100 ml MB were 0.50, 1.00, 1.50, 2.00 g/l. These salt concentrations were selected to be consistent with the typical quantity of sodium present within textile effluents, which are of the order 2.0 g/l (Table 2.1). 5 mg GO was loaded into the dye-salt mixture, consistent with above kinetics experiments, such that the loading ratio of GO solid:total volume was maintained at 0.0497 mg/ml. Again, 5 ml aliquots of the suspension were withdrawn at ten minute intervals until 50 minutes had elapsed, centrifuged and syringe filtered. The kinetics of dye adsorption of the experimental data were analysed by PSO model alone, in analogy to the method discussed.

For equilibrium experiments, 100 ml MB was prepared at initial concentration 50, 75, 100, 125 and 150 mg/l, in analogy to the previously outlined equilibrium experiments. 8000 mg sodium or magnesium sulphates were separately loaded into the MB, using the above mixing method, such that the initial salt concentration in MB was 8.0 g/l. GO loading was 20 mg, with GO solid:total volume ratio consistently maintained at 0.0196 mg/ml. Equilibrium of dye adsorption subject to salt addition was modelled by Langmuir isotherms (discussed in Section 5.2.5).

6.2.2 GO-coated membranes: Desalination of saline feeds

Salt solutions of sodium chloride, sodium sulphate, magnesium sulphate and ammonium heptamolybdate were prepared at initial concentration in aqueous solution at 0.50 g/l. Though this ionic concentration is low relative to the typical salt content in seawater (approximately 25 g/l [575]), it is consistent with the overall quantity of ions present within effluent (Table 2.1). The salt solutions were prepared by depositing the solid salt into distilled water at room temperature, using stirrer speed setting 3 to disperse the salt for ten minutes.

In analogy to dye systems in which UV absorbance is used to measure dye rejection, in salt systems, the rejection is calculated by measurement of the electrical conductivity. As such, the initial electrical conductivity of the prepared salt solution was measured using a (Hach HQ1130 portable conductivity meter (UK)). As the analysis was conducted in this manner, the measured conductivity of the salt solutions comprised contributions from both the anions and cations, as such the reported conductivity is the total summation of the two components.

Desalination experiments were conducted in analogy to the method for filtration of dyes, *i.e.* using 50 ml solution, at 2 or 4 bars pressure, with the experiments concluding when 20 ml permeated. Measurements of conductivity were likewise taken for permeation of every 4 ml. Permeability and salt rejection were calculated in analogy to the above system for dye filtration, using Equations 5.6 and 5.4, respectively.

6.2.3 GO-coated membranes: Fractionation of dye-salts

Combined dye-salts were prepared as per the method discussed in Section 6.2.1. MB was selected as the probe dye, at 5 mg/l, and the salts were separately sodium sulphate and magnesium sulphate, at 0.50 g/l. An initial measurement of UV absorbance was made at 664 nm, and likewise an initial reading of electrical conductivity.

The procedure was undertaken in analogy to systems for dye filtration (Section 5.2.8), with 50 ml loading of dye-salt. Filtration experiments were conducted at 2 bar only. For every 4 ml permeated, measurements of conductivity and UV absorbance of the permeate at 664 nm were made. Time measurements were also made in 1 ml increments of permeation.

At the conclusion of the experiment, there had been 20 recordings of permeate collection times and five separate measurements of absorbance and conductivity. Permeability was also calculated as above (Equation 5.6), and also salt and dye rejections, respectively (5.4). Again, the rejection of salt ions is considered in terms of total

rejection of cationic and anionic species.

6.3 Results and Discussion: Desalination of saline feeds

Dead end filtration was used to characterise the performance of uncoated PES and GO-coated PES membranes, in separation of salt from water. The salts selected for use in these studies were sodium chloride, sodium chloride, magnesium chloride and ammonium heptamolybdate. Salt solutions were filtered through the membranes and the performance characteristics realised by calculation of permeability and salt rejection. In particular, performance of GO-coated membranes is characterised subject to varying parameters GO coating concentration and filtration pressure, each of which are considered in this section. Desalination involving the use of GO membranes was discussed in Section 2.5 of the literature review.

6.3.1 Control experiments: desalination of saline feeds using uncoated PES

In analogy to earlier experiments regarding filtration of dye solutions, uncoated PES membranes were used in desalination, in order to establish a baseline of performance against which the filtration of saline feeds using GO-coated PES may be evaluated. Mean values of permeability and salt rejection are reported in Table 6.1.

Table 6.1: Mean Permeability and Mean Rejection of 0.50 g/l salt solutions, from dead end filtration using uncoated PES 0.20 μm membranes. Filtration pressure 2 bar.

Salt	Mean Permeability ($l \cdot m^{-2} \cdot h^{-1} \cdot bar^{-1}$)	Mean Rejection (%)
Sodium chloride	356.7	0.62
Sodium sulphate	343.8	0.83
Magnesium sulphate	351	0.52
Ammonium heptamolybdate	342.1	0.74

As is consistent with the trends observed in dye removal (Section 5.5.1), the polymer exhibits practically no resistance to the permeation of salts across the membrane. Mean

salt rejection values are unsurprisingly very low (<1%, in all cases) and permeabilities are very high, as ions from the salts are able to permeate the membrane with practically no resistance. Again, it is considered that the 0.20 μm pores are simply too large to barrier the permeation of small ionic species. The pore sizes indicate that the PES substrate used in these studies is belonging to the microfiltration class of membranes (Section 1.1.3); the usage of this class is restricted to pretreatment of saline feeds, thus is not intended for effective desalination [576, 577].

6.3.2 Impact of filtration pressure

In this section, the impact of pressure upon desalination efficacy is explored by comparison of permeability and salt rejection achieved in desalination of salts at 0.50 g/l, at respective pressures 2 and 4 bar.

Permeabilities and salt rejections of the 0.01 mg/ml SFGO-coated membranes, at 2 and 4 bar pressures, is shown as a function of permeated volume, in Figure 6.1. On each of the plots the salt is denoted by its chemical nomenclature (sodium chloride - NaCl, sodium sulphate - Na_2SO_4, magnesium sulphate - $MgSO_4$ and ammonium heptamolybdate - NH_4^+), to facilitate reading of the plots. The analogous 0.10 mg/ml SFGO results are provided in the Appendix (Figure A.10).

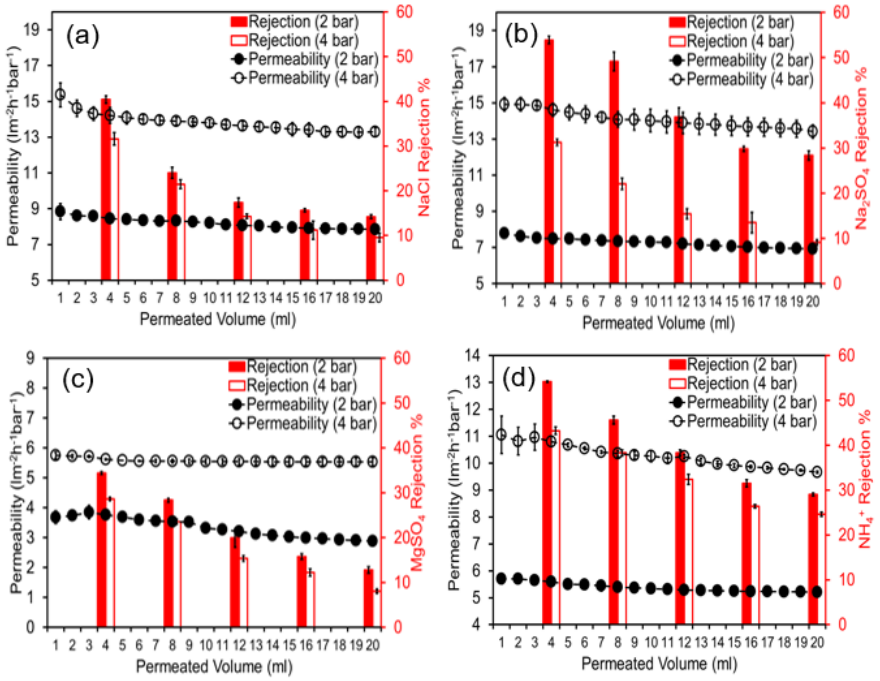

Figure 6.1: Permeability and salt rejection, as a function of permeated volume, in desalination of (a) sodium chloride, (b) sodium sulphate, (c) magnesium sulphate and (d) ammonium heptamolybdate, using 0.01 mg/ml SFGO coating. Salt concentration 0.50 g/l. Filtration pressure 2 and 4 bar. Vertical error bars represents standard deviation across 3 filtration runs.

It is observed that the differences between initial and final permeabilities for SFGO systems exhibit only a mild decrease, in all cases suggesting that the effects of concentration polarisation may be minimal. Although in this series of experiments the impact of varying the initial concentration of salt was not considered, it is proposed that a more significant declension of permeability may have been observed due to concentration polarisation effects at higher salt concentration [317, 337]. A prominent feature of the rejection profile as a function of permeated volume is that the rejection of all salts declined with volume permeated, this characteristic will be considered in the discussion section later (Section 6.3.4). In terms of the impact of pressure, inspection of the plots reveals that for SFGO membranes, an increase in filtration pressure results

in an increase in permeability and associated decline in rejection. With respect to the individual profiles of each salt, the trends in permeability and rejection are internally consistent at 4 bar as at 2 bar, thus implying that the rejection mechanism is upheld at the higher pressure. Furthermore, the utility of 0.10 mg/ml SFGO coating (Figure A.10) results in lower overall permeabilities and higher salt rejections; trends which are consistent with the behaviour of the SFGO systems at 2 bar.

The analogous corresponding permeabilities and salt rejections of the 0.01 mg/ml LFGO-coated membranes, at 2 and 4 bar pressures, is shown as a function of permeated volume, in Figure 6.2. The 0.10 mg/ml LFGO results are provided in the Appendix (Figure A.11).

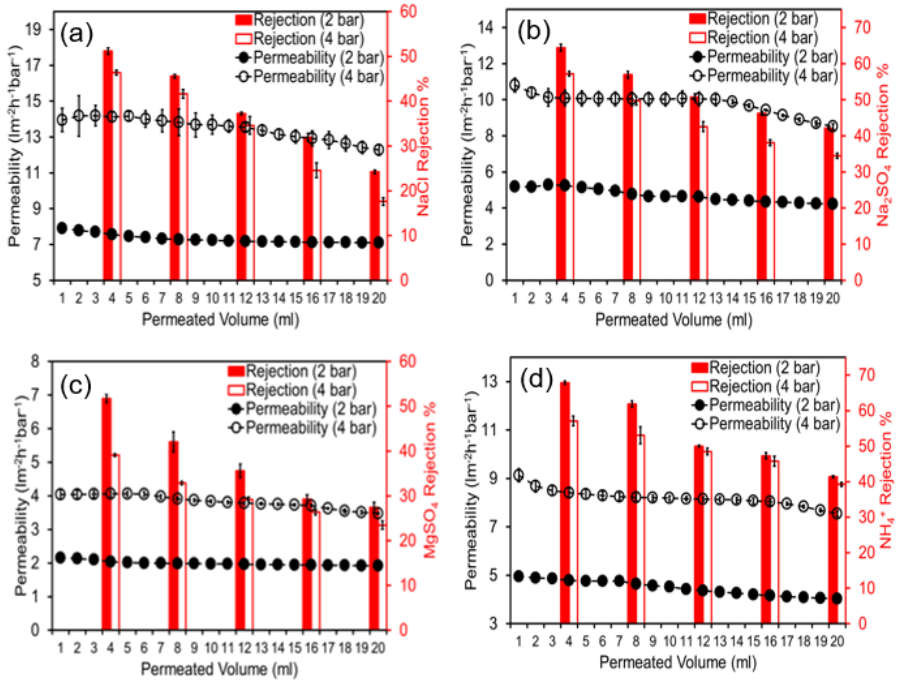

Figure 6.2: Permeability and salt rejection, as a function of permeated volume, in desalination of (a) sodium chloride, (b) sodium sulphate, (c) magnesium sulphate and (d) ammonium heptamolybdate, using 0.01 mg/ml LFGO coating. Salt concentration 0.50 g/l. Filtration pressure 2 and 4 bar. Vertical error bars represents standard deviation across 3 filtration runs.

Inspection of the LFGO membrane profiles reveals consistent behaviour with SFGO systems, in which a step increase in filtration pressure resulted in an increase in permeability and associated decline in salt rejection. In addition, the salt rejection in all cases was found to decrease with permeated volume, while the permeability exhibited a slight decline. The trends in permeability and rejection at 4 bar are also consistent with the results obtained at 2 bar, in terms of GO coating concentration and with respect to the individual salts.

As discussed, the plots of permeability and salt rejection demonstrate that the step increase in filtration pressure results in an increase in permeability and associated decline in rejection, for both GO's. In the earlier section regarding the impact of pressure upon dye removal (Section 5.5.4), it was discussed that the presence of mechanical-type defects in the GO coating results in a similar decline in performance at higher pressure. It is considered that these defects are likely the cause of the behaviour in terms of desalination, with the decline in rejection and increase in permeability a feature of exaggerating the defects at higher operating pressure. As discussed in the literature review (Section 2.5.3), filtration at higher pressure provides the ionic species in feed with increased energy, thereby facilitating their overcoming of inherent resistance to mass transfer from the membrane itself [334]. It appears that this behaviour is consistent with the behaviour of the GO-coated membranes.

Polymer membranes show a tendency to compact when subject to high transmembrane pressure (also discussed in the literature review (Section 2.5.3)). If the membrane is coated with GO, this inevitably leads to the collapse of nanochannels within the structure [15]. The result is that the permeability of membranes may decline at higher pressure, meanwhile the overall rejection capabilities may increase due to this phenomenon [336]. In the case of SFGO and LFGO, however, it was not the case that higher pressure led to lower permeability, in fact, the opposite effect was observed. It may be the case then that the coating compaction artefact is demonstrated to greater

effect at higher filtration pressure, due to the greater compressive forces associated with the higher pressure. The highest pressure used in these experiments was 4 bar, meanwhile the study of Chong *et al.* [15], involving a GO membrane fabricated by vacuum deposition, demonstrated the compaction artefact for filtration pressures as high as 10 bar. A further trend to support this behaviour was evident in the consistent decline in permeabilities and rejection capabilities of all membranes as a function of volume permeated, at pressure 4 bar. As such, this is consistent with expectation that the internal cavities do not collapse under higher pressure, leading to lower overall rejection and higher permeability [578].

It should also be clarified that the results obtained in this section demonstrate the desalination capabilities of the membranes at modest pressure, relative to that of an industrial reverse osmosis (RO) unit. As such, it is speculated that the utility of GO membranes may offer advantages over a competitor RO system, given the encouraging performance at lower operating pressure, which may reduce energetic and financial expenditure on generation of the high pressures.

6.3.3 Impact of GO-coating concentration

In this section, the impact of GO coating concentration, at 0.01 and 0.10 mg/ml, upon desalination performance is evaluated. In order to highlight the impact of GO coating concentration, the results of desalination at 2 bar, using 0.50 g/l salts are summarised. The data corresponds to that taken from Figure 6.1 (0.01 mg/ml SFGO), Figure 6.2 (0.01 mg/ml LFGO), Figure A.10 (0.10 mg/ml SFGO) and Figure A.11 (0.10 mg/ml LFGO). For each of the respective plots, the mean permeabilities and salt rejections were calculated, and are here expressed in bar chart form.

Figure 6.3 shows (a) Mean permeability and (b) Mean salt rejection of 0.01 and 0.10 mg/ml GO-coated membranes. In analogy to the previous section, the salts are denoted on these plots by their respective chemical notation.

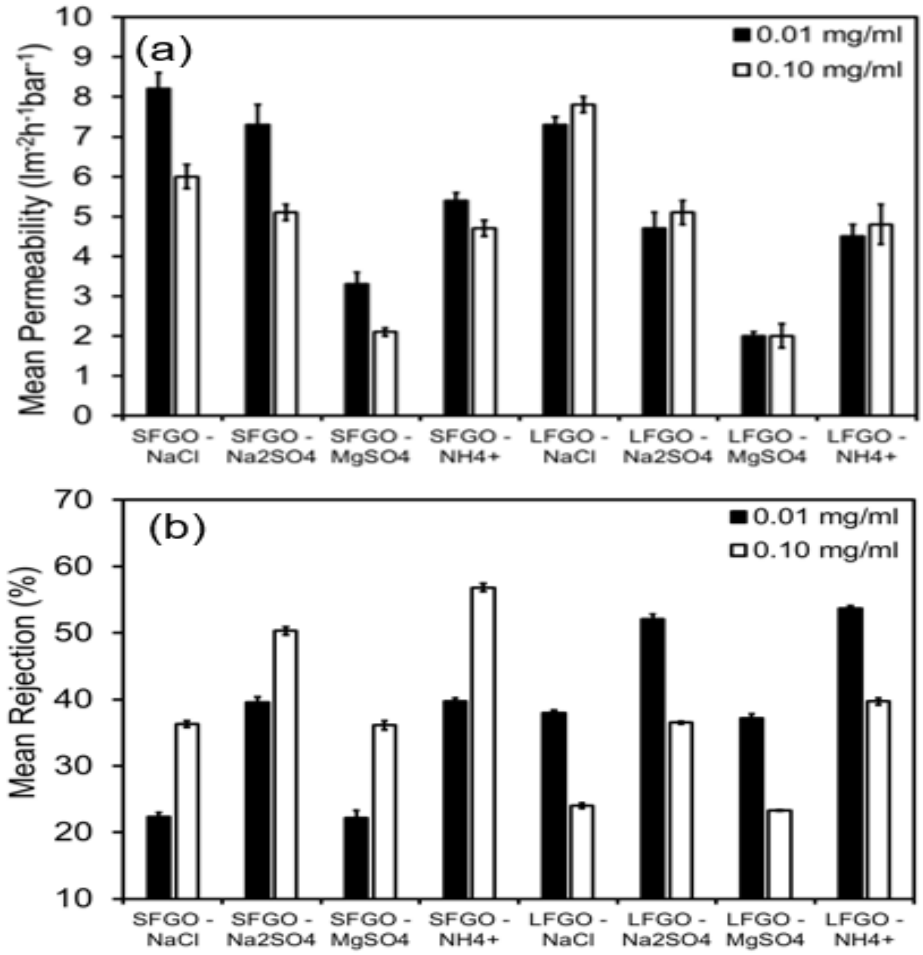

Figure 6.3: Impact of GO coating concentration upon performance. (a) Mean permeability and (b) Mean salt rejection, of SFGO and LFGO coated membranes measured during dead end filtration of 0.50 g/l salt solutions, with GO coating concentrations 0.01 and 0.10 mg/ml. Filtration pressure 2 bar. Vertical error bars represent standard deviation across three runs.

As demonstrated by the permeability and rejection profiles, for SFGO coatings, increasing the GO coating concentration from 0.01 mg/ml to 0.10 mg/ml had the overall effect of reducing the permeability, meanwhile the levels of salt rejection were improved. The overall decrease in permeability is consistent with the work of Liang *et al.* [344] (highlighted in literature review, Section 2.5), who likewise reported a decrease

in permeability, subject to increasing the GO content in a vacuum filtration-prepared membrane. It was considered that the increase in mass transfer resistance gained by using a higher concentration was responsible for the behaviour. Such an explanation is consistent with the trends in these experimental systems.

For LFGO coatings, the relationship between coating concentration and desalination efficacy is contrary to that of SFGO coatings; it was found that increasing the GO coating concentration slightly increases the overall mean permeability, meanwhile decreasing the mean rejection. As such, the trends observed for LFGO coatings mirror those obtained in dye removal experiments. A feature of the mean permeability and rejection trends for both GO's is that the ordering of permeabilities (P (NaCl) > P (Na_2SO_4) > P (NH_4^+) > P ($MgSO_4$)) and rejections (R (NH_4^+) > R (Na_2SO_4) > R (NaCl) > R ($MgSO_4$)) is identical to that for the SFGO coatings. In addition, considering the plots discussed in the previous section, the permeability and salt rejection profiles as a function of permeated volume follow an analogous trend to SFGO membranes, in which both parameters decline with an increase in permeated volume. These are very interesting observations, given that the behaviour subject to changing the coating concentration is otherwise starkly different. Again, this points to the prominence of electrostatic charge-based interactions in desalination with GO-coated membranes and will be addressed in the later discussion section (Section 6.3.4). In both GO systems, the permeability towards the divalent magnesium sulphate was particularly low: this feature will also be considered in the later discussion section.

It was demonstrated by measurement of Water Contact Angle (Section 4.4.5) that the incorporation of a GO coating with higher concentration improves the hydrophilicity of the membrane, which positively correlates to an overall increase in the permeability of membranes [481, 579]. As such, this may be a feature of the LFGO coatings in desalination, though the same trend was not observed in SFGO coatings. As demonstrated by cross-sectional FIBSEM (Section 4.4.6), the higher concentration of LFGO

led to a significantly thicker coating layer; as such, the increase in permeability subject to increasing GO content is inconsistent with the typical behaviour of a thicker coating layer in membrane systems [580]. It has however been suggested that coatings with low overall microstructural density lead to higher permeabilities, due to the ease of transit through the low density coating [496]. It appears for LFGO coatings, however, that increasing the surface area of GO availability does not correlate to increased levels of membrane performance (unlike the trend observed for SFGO); as such, at this stage, it may be speculated that the adsorption of contaminants onto the coated surface is not a prominent feature of the interaction with ions or dyes.

The literature has revealed that there is significant variation in desalination capacity of GO membranes, based on the fabrication and experimental methodology. The vacuum-prepared commercial GO/PES membrane of Hu *et al.* [327] (highlighted in literature review Section 2.5.3) delivered levels of rejection comparable to our systems, with experiments involving sodium sulphate (≈55%), and sodium chloride (≈40%). Chandio *et al.* [581] achieved comparable levels of sodium chloride rejection (≈45%), but with much higher permeability (≈20 $l \cdot m^{-2} \cdot h^{-1} \cdot bar^{-1}$). The performance of GO membranes must also be contextualised against alternative competitor material membranes. In Section 2.5.4, several material classes including metal oxide frameworks, carbon nanotubes and polyamide thin film composites were presented. Many of these materials appear to significantly out-perform GO-polymer composites prepared by vacuum deposition for removal of ions from water. In particular, the removal performance of several polyamide membranes was particularly high, with removal rates >95%. As such there is a gulf between the existing GO-polymer systems from literature and in this study, relative to the current industrial benchmark. It is considered that this may be due to the unpredictability of the pore size distribution brought by the uncontrolled GO layering in vacuum deposition technique.

6.3.4 Mechanism: Desalination

Results achieved in desalination of saline feeds using GO-coated PES membranes were presented in Section 6.3. The effects of a number of factors upon desalination capability have been considered, including concentration of GO in membrane coating and filtration pressure. Understanding the mechanism of desalination, which governs the performance characteristics of the membranes, is the focus of this section. This is an essential stage of developing a complete understanding of the membranes application.

The Donnan Effect, that accounts for electrochemical interactions of GO with ions, was introduced in the literature review (Section 2.5.1). As discussed, a greater number of cations per anion leads to lower rejection of a membrane towards a given salt [582]. With relevance to the studies in this chapter, valencies of the anions and cations present within the four salts are presented in Table 6.2. The impact of valency upon salt rejection is evaluated by introducing the *ratio of valencies* parameter of the cation:anion, denoted Z^+/Z^- *ratio*, where Z^+ and Z^- denote respective valencies of cation and anion [583]. In accordance with the above discussion on the Donnan Effect, a low value of Z^+/Z^- ratio predicts higher overall salt rejection.

Table 6.2: Z^+/Z^- ratio for the salts sodium chloride, sodium sulphate, magnesium sulphate and ammonium heptamolybdate.

Salt	Cation Valency	Anion Valency	Z^+/Z^- Ratio
Sodium Chloride	1	1	1
Sodium Sulphate	1	2	0.50
Magnesium Sulphate	2	2	1
Ammonium Heptamolybdate	1	6	1/6

Figure 6.4 shows the mean salt rejection, achieved for each salt by each GO-coated membrane, as a function of Z^+/Z^- ratio.

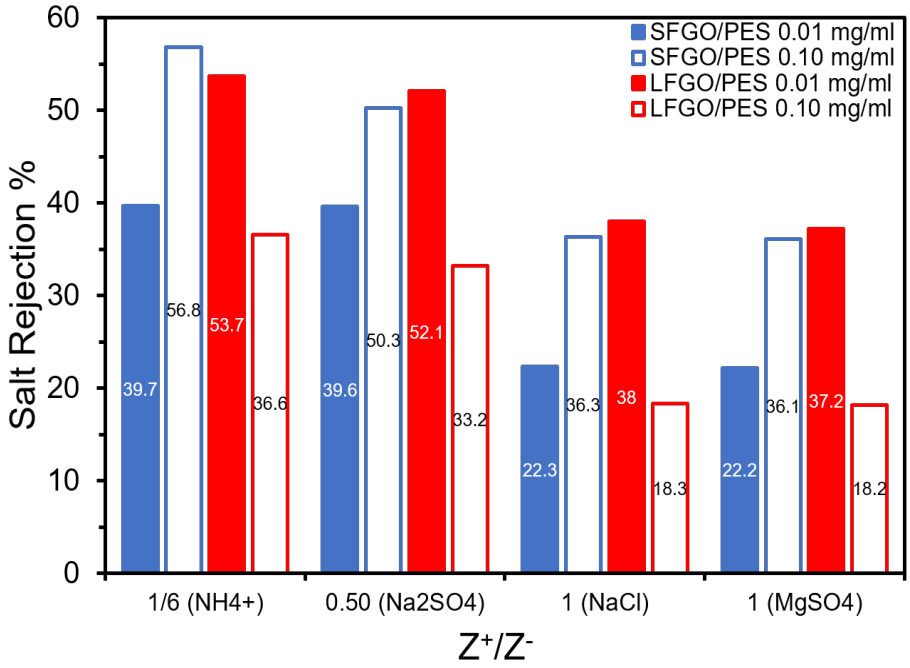

Figure 6.4: Mean salt rejection of the four salts by GO-coated membranes as a function of Z^+/Z^- ratio.

With respect to all GO-coated membranes, it appears that the trend expected by Donnan Effect is upheld, as the experimentally observed ordering of salt rejections (R (NH_4^+) > R (Na_2SO_4) > R (NaCl) ≈ R $(MgSO_4)$) is correlated to the Z^+/Z^- ratio. It is clear from the chart that salts comprising monovalent cations and multi-valent anions led to higher overall rejection. This is exemplified by considering that the overall highest mean rejection achieved was in removal of ammonium heptamolybdate, which is consistent with the expectation that low Z^+/Z^- ratio correlates to high rejection.

The impact of the Donnan Effect is illustrated by comparison of the results for sodium sulphate and magnesium sulphate; as the divalent anions are the same, the significant difference in rejection is attributed to the different valencies of the cations.

Clearly, the divalent Mg^{2+} cation diminishes rejection to a greater extent than Na^{+}, owing to the previously discussed impacts of adsorption, charge neutralisation and ionic valencies that contribute to a weakening of the Donnan Effect [327]. In addition, this is further supported by consideration that two cations are associated with the sodium sulphate, in comparison to the one with magnesium sulphate.

A second interesting comparison is made between the rejection profiles of magnesium sulphate and sodium chloride, both of which have Z^{+}/Z^{-} ratio equal to one. In our systems, the rejection levels of these salts is very close; in several cases, it is marginally higher for sodium chloride. The cations are again Mg^{2+} and Na^{+}. In terms of the anions, the divalent SO_4^{2-} anion (-1.147 C$\cdot mm^{-3}$) has significantly greater negative charge density in comparison to the monovalent Cl^{-} (-0.457 C$\cdot mm^{-3}$) [584]. As such, GO membranes with their initially negative coating repel the sulphate group more strongly than the chloride ion, and are as such better at rejecting the divalent anion. For this comparison of two salts with identical Z^{+}/Z^{-}, there is seemingly an interesting competition established between the balance of attractive and repulsive forces between GO and counter/co-ionic species, that has a very potent impact upon the performance of the systems. Overall, the effects appear to reach a state of parity, resulting in very similar levels of rejection for the two salts.

Another aspect which was mentioned but not discussed in Section 6.3 was that the permeability of the magnesium sulphate systems were in all cases very low; this is also a feature related to the valency of the cation. Divalent cations have higher hydration free energies than monovalent cations, as such, the energetic barrier associated with their motion is greater, resulting in restrictions as they transit through a narrow nanochannel [585]. The electrostatic attraction to the negatively charged functional groups is also stronger [586]. A combination of the restrictions and charge results in overall lower permeability of cations with higher valency.

Membranes also separate components based on physical size effects, an effect known

as steric hindrance. In section 2.5.2 of the literature review, the hydrated diameters of Na^+ (0.72 nm) and Mg^+ (0.86 nm) were given; in addition, the hydrated diameter of NH_4^+ is 0.66 nm [324]. By measurement of d-spacing using XRD (Section 4.4.3), it was demonstrated that the interlayer spacing of the higher concentration coatings for both GO systems in dry state was 0.76 nm. It was further found that the membranes swelled due to intercalation of water molecules; for SFGO to 0.80 nm while for LFGO, to 0.82 nm. Based on argument of steric effects alone, it is thus considered that the membranes would be unable to retain the Na^+ and NH_4^+ cations, as they are smaller than the interlayer spacings, whereas in practice, the rejection of the NH_4^+ salt was highest overall. Similarly, it is hypothesised that the Cl^- (0.66 nm) and SO_4^{2-} ions (0.76 nm) would also be capable of transiting the membrane with minimal or no resistance. By comparison of the results achieved in rejection of sodium chloride and sulphate, it was observed that the rejection of the sulphate salt is significantly higher than the chloride: this feature may be attributed to steric effects and exclusion of the relatively larger SO_4^{2-} anion, in addition to charge-based effects [342]. Based on the above argument in terms of interlayer spacings relative to the sizes of the ions, however, it is considered that size exclusion is not likely to be the dominant mechanism of rejection. Steric effects may however contribute to the decline in salt rejection with permeated volume, a feature that was highlighted in Section 6.3.2: as demonstrated in this section, the GO membranes suffer a continual decline in salt rejection with volume permeated. When the membrane becomes wet, the transport of ions through the swollen structure is facilitated due to the increase in interlayer spacing, thus enabling the permeation of a greater number of ions [327], therefore accounting for the decline in performance.

6.4 Results and Discussion: Impact of salt addition upon Dye Adsorption

6.4.1 Impact of salt addition upon Kinetics of dye adsorption

Exploration of the effects of Contact Time upon adsorption were evaluated by monitoring q_t as a function of time for 50 minutes, in analogy to the analysis which was conducted in GO-dye system (Section 5.3.1). Time-variant values of q_t, subject to sodium sulphate and magnesium sulphate loadings in the range 0 - 200 mg (0 - 2.00 g/l), is shown as a function of contact time for SFGO in Figure 6.5(a) and for LFGO in (b), with PSO curvilinear profiles fitted to the q_t. Note that the values corresponding to salt loading of zero (indicated on the figures as *No Salt*) is simply extracted from the idealised GO-dye system. For brevity in all subsequent figures in this section, sodium sulphate and magnesium sulphate are represented by their cations (Na^+ and Mg^{2+}, respectively).

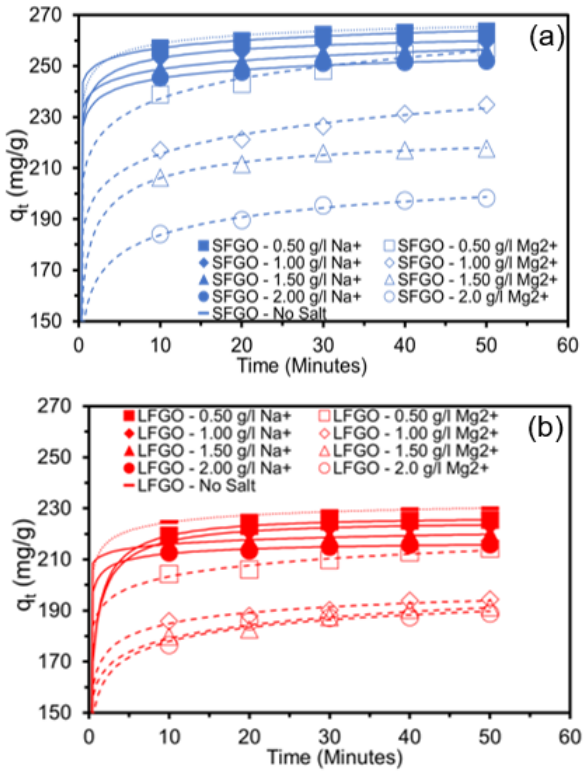

Figure 6.5: Effect of Contact Time upon MB adsorption, subject to magnesium and sodium sulphate loading, for (a) SFGO and (b) LFGO, in which salt concentration varied 0 - 2.00 g/l.

It is observed that the addition of salt ions causes the values of q_t to decline with respect to the case for which no salt is added. Additionally, it is seen that as the the salt concentration in MB is increased from 0.50 - 2.00 g/l, this resulted in a more significant declension in values of q_t. The effect of adding divalent magnesium sulphate to MB appears to be significantly greater than monovalent sodium sulphate, however, as values of q_t were observed for both GO's to decline more significantly with increased loadings of divalent magnesium salt.

The linear PSO model was fitted to the data; for completeness, the PSO plots are provided in the Appendix (Figure A.12), likewise the corresponding linear equations

are given in the Appendix (Table A.1). The PSO model was likewise demonstrated to be appropriate for dye-salt systems, as the R^2 values indicated perfect statistical correlation. In analogous fashion to the case in which no salt was added (Section 5.3.3), the values of $q_{e,cal2}$ were extracted from the linearised systems, for addition of magnesium and sodium sulphate salts, at respective concentrations in the range 0.50 - 2.00 g/l: these are presented in Figure 6.6. The values of $q_{e,cal2}$ obtained for the case in which salt concentration was zero correspond to those discussed in Section 5.3.3. An assumed linear trendline was fitted to the profiles, with the corresponding values of R^2 displayed: the regression coefficients were all >0.85, as such it seems reasonable to assume that the overall response corresponds to a linear decline with increasing salt loading. Again, inspection of Figure 6.6 reveals that addition of divalent magnesium sulphate (dashed lines) caused a more significant declension in $q_{e,cal2}$, as electrolyte concentration increased from 0 – 2.0 g/l.

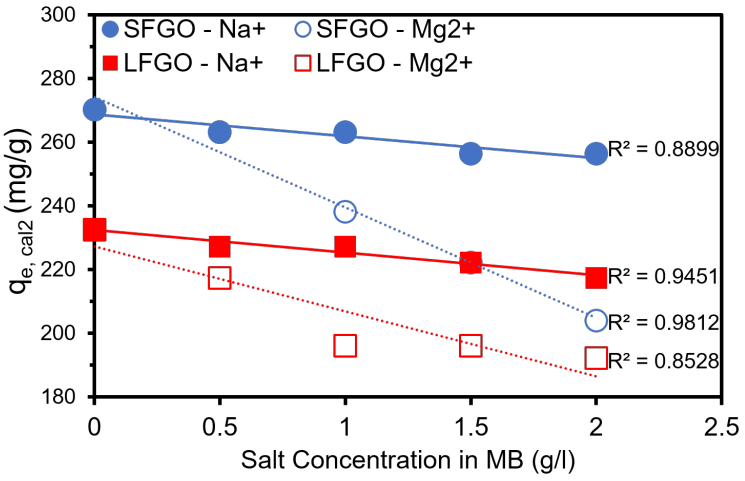

Figure 6.6: PSO $q_{e,cal2}$ values for adsorption of MB, subject to salt loading with sodium sulphate and magnesium sulphate salts. Loadings of salt were 0, 50, 100, 150 and 200 mg, such that salt concentrations in MB were 0.50, 1.00, 1.50 or 2.00 g/l.

As indicated on the plot, for SFGO, $q_{e,cal2}$ declines from 270.27 mg/g when no salt is added, to 256.41 mg/g in the case of sodium sulphate addition and 204.08 mg/g in the case of magnesium sulphate addition, corresponding to a 5.13% and 32.43% reduction, respectively, when salt concentration in MB is 2.00 g/l. For adsorption of MB with LFGO, the effect on $q_{e,cal.}$ values follows a similar trend, declining from 232.56 mg/g when no salt is added to 217.39 mg/g in the case of 2.00 g/l sodium sulphate addition and 192.31 mg/g in the case of magnesium sulphate addition, corresponding to 6.98% and 17.31% reductions, respectively. Importantly, the effective reduction with magnesium sulphate addition with LFGO was approximately half that of the SFGO reduction.

6.4.2 Impact of salt addition upon Equilibria of dye adsorption

The impact of salt addition upon equilibria of dye adsorption was evaluated by Langmuir isotherm. Langmuir plots are included for reference in the Appendix (Figure A.13(a) and (b), respectively). The Langmuir isotherm equations, in the analogous linear format (discussed in Section 5.4.2), are tabulated in the Appendix (Table A.2). Isotherm parameters q_{max} and K_L were calculated from the isotherm plots, in analogous manner to which they were extracted for the case of no salt (Section 5.4.2): these are shown in Table 6.3.

Table 6.3: Langmuir isotherm parameters $q_{max.}$ and K_L, for adsorption of MB using SFGO and LFGO, subject to loading MB with magnesium sulphate or sodium sulphate. Salt concentration in MB was 8.00 g/l.

GO	*No Salt*		*8.00 g/l* Na^+		*8.00 g/l* Mg^{2+}	
	q_{max} (mg/g)	$K_L(l/g)$	q_{max} (mg/g)	$K_L(l/g)$	q_{max} (mg/g)	$K_L(l/g)$
SFGO	526.3	0.0477	500.0	0.0406	333.3	0.0935
LFGO	384.6	0.0411	357.1	0.0290	243.9	0.0065

Consistent with the behaviour observed in kinetics experiments, calculated values of q_{max} are observed to decline with the addition of 8.00 g/l salt. The decline was

more drastic for the addition of magnesium sulphate, again showing consistency with kinetics experiments. The calculated K_L values were found to decline with addition of salt, with greater significance for addition of magnesium sulphate. This suggests that addition of salt reduces the affinity of GO for MB adsorption and that this is particularly pronounced for divalent magnesium sulphate.

One salient consideration, then, was to understand why the impact of magnesium sulphate was more significant overall than sodium sulphate, and why did the influence of magnesium ions seem greater upon SFGO systems compared to LFGO. This, along with other features of the mechanism, will now be considered in greater detail, in the following section.

6.4.3 Mechanism: impact of salt addition upon dye adsorption

In the adsorption systems in Chapter 5 involving binary GO-dye systems, the adsorption of MB by GO was not impeded by the presence of other charged species. Dissolution of electrolytes into MB resulted in the cations competing with MB for occupation of adsorbent binding sites. The impact of electrolyte presence was exhibited clearly by the reduction in $q_{e,cal2}$ values, subject to increased loadings of magnesium sulphate and sodium sulphate (Figure 6.6). A similar trend was observed regarding the equilibria of adsorption (Section 6.4.2). Addition of Mg^{2+} ions had a more severe impact upon the decline in adsorption; as discussed in Section 6.5, the divalent cations are capable of physical adsorption onto GO surface, whereas Na^{+} cations are not. The effect is thus to reduce the electrostatic attraction between the GO and MB, due to charge screening, which is especially prominent for Mg^{2+} addition. Accordingly, with the attraction between adsorbent and adsorbate diminished, the adsorption of MB is lower, due to the presence of cations.

As highlighted in Section 6.4, it is also important to understand why SFGO was more significantly impacted by salt addition than LFGO, as reflected by its greater

depletion in $q_{e,cal2}$ values (Figure 6.6). This was investigated by measurement of zeta potential for salt-in-GO colloids (Section 4.3.7). For SFGO adsorbents charge neutralisation occurs at lower loading of magnesium sulphate; it is considered that the small flakes with high surface area are capable of adsorbing more cations per unit area than LFGO, in addition to having greater initial electrostatic attraction to the dye. As such, the increased tendency to adsorb cations in preference to MB thus accounts for the more significant decline in MB adsorption capacity.

6.5 Results and Discussion: Fractionation of dye and salt mixtures

In this section, the research on membrane filtration is extended to consider fractionation of dye-salt mixed systems. To be consistent with the previous section regarding dye adsorption in a binary dye-salt mixture, sodium and magnesium sulphate salts were dispersed into 5 mg/l MB, and the dye and salt rejections were monitored at periodic intervals. In order to streamline the experimental matrix, only the two most successful membrane candidates were selected for this series of tests: these were the SFGO/PES 0.10 mg/ml coating (higher SFGO concentration) and LFGO/PES 0.01 mg/ml (lower LFGO concentration). For brevity, in this section alone, the SFGO/PES 0.10 mg/ml coating will be referred to as *SFGO*, meanwhile LFGO/PES 0.01 mg/ml will be *LFGO*.

The mean permeability and combined mean MB and salt rejections of the SFGO- and LFGO-coatings, in filtration of MB-sodium sulphate and MB-magnesium sulphate are shown, respectively, in Figure 6.7(a) and (b). The filtration results for removal of MB by the SFGO and LFGO membranes is taken from the earlier dye removal studies (Section 5.5).

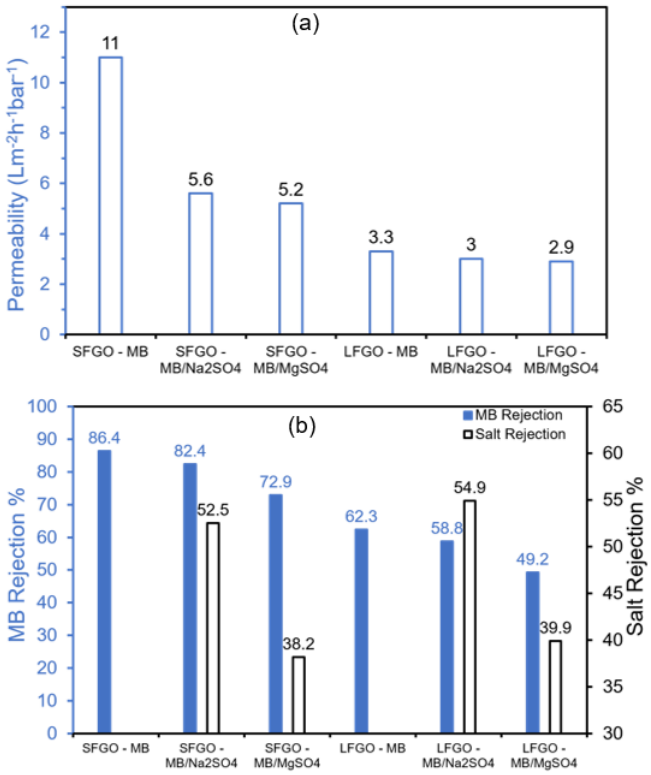

Figure 6.7: (a) Mean permeability and (b) Mean MB and salt rejections of SFGO- and LFGO-coated membranes in fractionation of MB - Na_2SO_4 and MB - $MgSO_4$ dye-salt mixtures.

The presence of electrolytes is demonstrated to have an overall adverse impact upon the permeability for both membrane systems. Introduction of electrolytes into MB increases the ionic concentration in the feed, as such the osmotic pressure increases and permeability is decreased due to the effects of concentration polarisation [587]. The SFGO membranes are significantly more impacted than LFGO; high adsorption capacity and surface area of the SFGO coating for cations is affected more significantly, thus accounting for the greater depletion in permeabilities. Deposition of dyes onto the membrane surfaces due to adsorption causes a reduction in permeation of solvent in dye-salt systems, due to physical pore coverage or blocking [588]. The permeability of

both membrane systems towards MB - $MgSO_4$ was lowest overall, perhaps due to the increased adsorption of the divalent cation onto the membrane surface relative to the monovalent Na^+, which may penetrate the pores and cause shrinkage, thus reducing the permeability [589].

Comparison of the overall mean MB rejections with and without electrolytes reveals that the MB rejection is decreased subject to ionic presence. Adsorption of cations onto the initially electronegative membrane surface disrupts the electrokinetic stability of the surface; the cations are capable of shielding the negative surface potential [590, 591]. The impact of cation adsorption on GO adsorbent surfaces was demonstrated by measurement of zeta potential (Figure 4.11). It was revealed that divalent Mg^{2+} had the greatest impact upon colloidal stability; a feature of the greater charge density of the Mg^{2+} (1.66 $C{\cdot}mm^{-3}$), compared with the Na^+ (0.24 $C{\cdot}mm^{-3}$) [592]. Consistent with the discussion in the literature review (Section 2.2.1), this results in adsorption of Mg^{2+} onto GO membrane surfaces, meanwhile the Na^+ cations accumulate in and compress the electrical double layer of the GO [593, 594]. The overall effect of multi-valent cationic salt addition is thus to cause charge reversal of GO. Such behaviour is consistent with the trends in rejection observed here; as it was found that the incorporation of magnesium sulphate had greater impact than sodium sulphate upon reducing the rejection of MB.

It has also been reported that the presence of low concentrations of salt can assist the dispersion of dyes in solution due to repulsion between dye molecules and cations, an effect that facilitates their transit through the membrane [595]. An interesting observation is that the achieved levels of salt rejection actually very slightly increase when the salts dispersed in MB, compared to the values obtained in desalination experiments (Section 6.3). This observation is due to the increase of thickness that occurs due to the deposition of MB onto the electronegative membrane surface; this has the effect of hindering the passage of ions, thus slightly increasing the resistance to transport across

the membrane [596].

The concept of *selectivity* is a defining parameter in multi-component feeds. Selectivity is an important parameter for assessment of separation quality; achievement of high solvent permeability and high selectivity is a very desirable feature in membrane operations [597]. The selectivity parameter (α), defined in terms of the rejection levels of one species relative to those of another, thus providing assessment of the ability of a membrane to fractionate different species [598]. Given the mixtures in our studies are salts and dyes, the selectivity of salt separation relative to dye ($\alpha_{Salt/Dye}$) is defined by the following relationship [599]:

$$\alpha_{Salt/Dye} = \frac{1 - R(Salt)}{1 - R(Dye)} \tag{6.1}$$

where the values of $R(Salt)$ and $R(Dye)$ are the mean values of the respective salt and dye rejections.

Selectivities of the LFGO/PES 0.01 mg/ml and SFGO/PES 0.10 mg/ml membranes, in fractionation of dye - salt mixtures are reported as follows: for MB - Na_2SO_4, $\alpha_{Salt/Dye} = 2.70 \pm 0.040$ for SFGO and 1.10 ± 0.007 for LFGO, while for MB - $MgSO_4$, $\alpha_{Salt/Dye} = 2.29 \pm 0.015$ for SFGO and 1.18 ± 0.012 for LFGO. The error term in the stated values of $\alpha_{Salt/Dye}$ refers to the standard deviation across three experimental runs.

It is apparent that the SFGO coating offers improved levels of selectivity compared to LFGO, for both MB - Na_2SO_4 and MB - $MgSO_4$ systems. This is considered a feature of the SFGO-coatings retaining high overall levels of MB rejection: as such, the term (1 - $R(Dye)$) in the denominator of Equation 6.1 tends to diminish, meaning that the selectivity parameter is mathematically maximised. It is worth considering, however, that the calculated values of $\alpha_{Salt/Dye}$ are all rather low, relative to a selection of values reported in literature. For example, Kang *et al.* [599] reported a highly selec-

tive magnetite-doped GO membrane that achieved a selectivity of 63.2, when filtering a Congo Red/sodium chloride system. Similarly, Li *et al.* [600] reported a highly selective trimethylamine-doped membrane that achieved a selectivity of 18.3, when separating Congo Red/sodium sulphate system. It is thus considered that the selectivity of membrane systems may be improved by functionalisation of the GO to tailor its properties towards rejection of a certain component.

6.6 Conclusions

This chapter has evaluated the performance of GO materials in ionic environments. The key properties of differing flake sizes was again explored.

GO-coated membranes were demonstrated to have reasonable capacity to desalinate salt solutions, with salt rejection decreasing according to the order: R (NH_4^+) > R (Na_2SO_4) > R (NaCl) ≈ R ($MgSO_4$). The rejection of salts by GO-coated membranes was attributed to the **Donnan Effect**, meaning that electrostatic interactions of GO coating with electrolytes is responsible for the separation performance. A secondary contribution was considered to have been made by the effects of steric hindrance. The highest overall rejections were achieved by the salts having lowest cationic valency and highest anionic valency (ammonium heptamolybdate and sodium sulphate), suggesting that the Donnan Effect is the dominating mechanism. The effects of GO concentration and filtration pressure upon filtration performance were also considered. For SFGO systems, increasing the GO concentration led to an increase in salt rejection but decreased permeability, due to the greater surface area of the coating. For LFGO systems, the increase in GO concentration led to a decrease in sieving performance but an increase in flux; it was considered that this was due to the increase in membrane hydrophilicity. Filtration at higher pressure (4 bar) resulted in an increase in permeability and decline in salt rejection, for all membranes and all salts, due to the inherent microstructural

defects present within the GO coatings.

The impact of salt addition upon dye adsorption capacity of the GO materials for MB dye was assessed by dispersing magnesium sulphate and sodium sulphate into the dye. It was demonstrated, by PSO kinetics and Langmuir isotherm analysis, that the presence of electrolytes had a significant adverse impact upon the dye adsorption performance of the GO adsorbents; this was more pronounced for magnesium sulphate addition compared to sodium sulphate. In addition, the impact of salt presence upon smaller flake systems was particularly prominent, due to the stronger affinity of the ions for the small and highly electronegative flakes. The governing reason for this behaviour is related to the adsorption of high charge density Mg^{2+} counter-ions onto the GO surface, meanwhile Na^{+} ions are not capable of surface adsorption. As such, the Mg^{2+} ions cause charge reversal, eliminating the electronegativity and decreasing the affinity of GO for MB. Accordingly, the SFGO systems suffered a 32.4% reduction in adsorption capacity, meanwhile for LFGO systems the decline was lesser at 17.3%.

GO membranes were also utilised in separation of multi-component feeds comprising MB and sodium sulphate or magnesium sulphate. Fractionation of MB-salt feeds was shown to be moderately successful. It was revealed that the average MB rejection levels decreased compared to that achieved in dye solution, due to the increased ionic concentration in feed causing concentration polarisation. The salt rejection levels were shown to increase due to the deposition of dye molecules onto the surface, resulting in a slight increase in the layer thickness. Both SFGO and LFGO membranes demonstrated a degree of multi-component selectivity; the achieved selectivity was however shown to be low in comparison to selected publications, that typically presented the utility functionalised GO.

The results of this chapter contribute novelty to the mechanistic understanding of the interactions of GO with ionic species, and simulated effluent dye-salt systems. The effects of flake size and surface charge are important factors in governing this

behaviour, in conditions with increased relevant to industrial application. This chapter may assist those seeking to enhance their understanding of the complexities of GO within industrial effluent systems.

Chapter 7

Conclusions and Recommendations for future research

7.1 Conclusions

This research has investigated the importance of flake size, surface area and charge in removal of contaminant species from water. Commercial GO materials were employed for removal of anionic MO and cationic MB dyes and salts from water, by means of adsorption and membrane filtration. The inspiration of this thesis was to conduct a piece of comparative research investigating GO flake size, in order to establish a benchmark for removal of dye and salt contaminated waters by adsorption and filtration studies.

GO's and GO-coated PES membranes were characterised using a number of techniques, in order to establish an understanding of the chemistry and properties of the materials. LD and DLS particle sizing techniques were utilised to gain size distributions of the two GO systems; one of the GO materials was demonstrated as having larger size than the other. In addition, BET analysis confirmed that the surface area and pore volume of the smaller flake GO system were respectively a factor of four and two greater than the larger flake system. Measurement of zeta potential across

pH range 3.50 - 10.0 confirmed that both systems were negatively charged and that the potential for SFGO was more negative than LFGO. These findings from the novel characterisation approach were utilised as the basis for subsequent investigations in the thesis, involving the utility of the GO's in contaminant removal. Investigations into the chemistry of the GO's by FTIR and XPS revealed that the chemical identities of the materials were markedly similar; in terms of functional group presence, both possessed carbonyl, carboxyl and epoxy groups. One difference highlighted by XPS was that the oxygen content of the LFGO sample was slightly higher than SFGO. This feature was supported by EDX analysis, conducted during SEM imaging of the dried flakes. Chemical analysis of the GO-coated PES revealed that the FTIR spectra of pure PES and GO-coated PES were indistinguishable, suggesting that the GO does not modulate the chemistry. XRD analysis of the interlayer spacing of the coating revealed that the d-spacing increased when the membrane was in wet state, due to intercalation of water molecules. Cross-sectional FIBSEM analysis showed that higher GO concentration coatings resulted in membranes with increased thickness, an effect that was particularly marked for the larger flake systems.

Studies of adsorption kinetics and equilibria of dye adsorption exploring the crucial flake size property were implemented to determine the rate and capacities of adsorption, respectively. In respective adsorption studies, PSO and Langmuir isotherms were ascribed to the kinetics and equilibria, respectively. MB adsorption was proven both rapid and plentiful, with both GO systems, though, the rate of adsorption involving small flake GO was particularly effective, due to the interactions of small flakes with high surface area and the cationic dye molecules. Adsorption of MO was comparatively less effective and slower in terms of kinetics than MB, though was still appreciable. Interestingly, the smaller flake system was less effective in adsorption, due to the high negative surface charge. GO's were demonstrated to aggregate in both dyes, in particular MB, due to the strong charge neutralising atmosphere of the opposite charged dye

and GO. It was considered that this feature may offer advantages in terms of downstream separation, despite presenting challenges in practical reusability of the GO.

Based on the results obtained in dye adsorption studies, it is concluded that SFGO is a more effective adsorbent of MB than LFGO, meanwhile LFGO is the better adsorbent of MO. To this end, flake sizes and surface charge were the salient attributes that drove this characteristic behaviour. In order to determine the applicability of the adsorbents over multiple adsorption cycles, the reusability of the materials must be ascertained (refer to next section); in particular given the tendency of GO to aggregate in charged solution. This is considered a salient stage in developing the application of the materials and further develop the understanding of the importance of flake size.

In filtration studies, flake size was also demonstrated to be a crucial feature, as SFGO was shown to have greater capacity for MB and MO rejection when the concentration of GO increased, a feature that is attributed to the greater surface area availability of the smaller flake system. LFGO, on the other hand, showed reduced capacity for filtration at higher GO concentration, due to the instability of the higher LFGO membrane in water. Both GO's exhibited a declension in rejection and increase in permeability subject to pressure increase, due to the presence of mechanical defects in the membrane structures.

GO-coated membranes were used in desalination of saline waters. Of the four salts used for these studies, desalination efficacy of both GO systems declined according to the order: R (NH_4^+) > R (Na_2SO_4) > R (NaCl) ≈ R ($MgSO_4$). It was considered that the Donnan Effect was the dominant mechanism, given the preferential retention of salts with high valency anions and low valency cations. The Z^+/Z^- ratio was used to associate the rejection performance with valencies; a low value of Z^+/Z^- resulted in a higher overall rejection. The dye adsorption studies were extended to consider the impact of salt addition upon adsorption efficacy, in MB-salt systems, with magnesium sulphate and sodium sulphate. Secondly, the effects of ionic presence upon dye adsorp-

tion were explored, where differences in flake size and surface area were anticipated to be significant. It was revealed by PSO kinetics and Langmuir isothermal studies that magnesium sulphate had a greater impact upon adsorption, resulting in significant declines in adsorption efficacy subject to increased loadings of salt. In particular, the impact upon the smaller flake systems was greatest. This behaviour was attributed to charge-based interactions between GO and Mg^{2+} cations; in which physical adsorption of cations onto GO neutralised the charge of the GO, thus reducing the electrostatic attraction between MB and GO. The greater charge and surface area of smaller flake GO offered greater capacity for adsorption of cations in solution. Research into dye-salt systems was also extended by considering multi-component fractionation of MB-sodium sulphate and MB-magnesium sulphate systems. Magnesium sulphate had the greater adverse impact upon MB rejection, due to the ability of the divalent cation to eliminate the negative charge of the membrane and thus weaken the Donnan Effect. The impact upon the smaller flake system was more significant, due to the strong interactions of the small GO flakes with the contaminants.

In membrane treatment of dye- and salt-contaminated waters, it was found that the best overall candidate was the higher GO concentration SFGO membrane. The increase in GO mass or surface area is correlated to the strong interaction of small GO flakes with cationic dyes; considered a function of their ability to adsorb the dye. This adsorption may, however, hinder the reusability of the small flake GO membranes, or limit the applicability of the coating to low concentration feeds, so as not to hinder the performance due to excessive surface adsorption. Of the LFGO coatings, it was found that better performance resulted from a lower concentration GO; despite the performance being overall lower than the higher concentration SFGO competitor. It is considered that the better performance at low LFGO concentration could offer significant advantages in terms of the process economics, due to the fact that lower quantities of GO are required for deposition on each membrane, and more membranes may be

coated per unit volume GO. By extension, this offers potential for cost effectiveness of operation.

Several potential obstacles were identified in relation to the applicability of both GO's in filtration. Firstly, mechanical defects in the GO coatings was identified by increasing pressure from 2 to 4 bar, in desalination and dye filtration experiments. The rejection dropped and permeability increased, suggesting a reduction in performance subject to higher pressure. This behaviour was observed regardless of GO flake size. On one hand, this may be considered a positive outcome, as the membranes are able to desalinate saline feeds at lower pressure; the ultimate ambition of the industry. On the other hand, however, the reduction in performance is a hindrance on industrially-relevant scales, as the operating pressure must be sufficiently high to overcome the osmotic pressure of the feed, in particular for seawater cleanup applications. Coatings resulting from vacuum deposition may increase the tendency of flakes to stack with microstructural defects, due to the uncontrolled layering. This presents a potential means of performance limitation, based on the current GO systems. In addition, the desalting performance of the two GO's declined as a function of permeated volume, attributed to the weakening of the Donnan Effect, a feature particularly related to GO surface charge. This is considered highly disadvantageous for application, given that another cornerstone of industrial application is fabrication of membranes with longevity and stability of performance over extended operation times. This second characteristic flaw in the membranes must essentially be overcome in order for the membranes to be an industrial option.

GO materials have demonstrated highly promising capabilities in terms of contaminated water treatment, by means of adsorption and filtration. The crucial properties including flake size, surface area and charge were explored and investigations launched into the importance of these in application. The studies have provided a full analytic characterisation of flake size GO materials and membranes, and the applications in

dye and salt removal investigated. It is considered that the materials have the potential to provide a scalable solution to meet the needs of the water crisis and achieve their ultimate potential in demonstrating *in situ* applicability, despite, as indicated, the necessity to overcome a number of challenges. It is anticipated that this thesis will contribute to the understanding of flake sizes in GO systems, such that further explorations in contaminant removal may be initiated. From this, GO materials may achieve their full potential of industrial application.

7.2 Recommendations for future research

- Functionalisation of commercial GO materials having different flake size. Perhaps the most significant recommendation is the investment in synthesis of functionalised materials from a commercial GO backbone. The results of this study have provided a substantial knowledge platform, regarding the application of these materials, from which a performance benchmark of GO-functionalised materials may be gained. Functionalisation of GO materials is a promising means of tuning the properties, perhaps leading to favourable interactions with certain components. A serious development of the field as suggested by this research, therefore, is the development of materials that are capable of out-performing the unmodified materials used in these studies. It is anticipated that this development may enhance the already significant utility, enabling them to interact with and therefore remove species from a multitude of industrially relevant environments.

- Restriction of experimental studies to a 2X2 matrix. The studies were constrained to a system comprising two GO materials of different flake size and two dyes having opposing molecular charges. Given time constraints of the project, it was decided to limit the studies as such. In practice, there are a multitude of dyes and GO materials which could have provided interesting comparative results for

use in the studies. A useful development is therefore to increase the array of dyes and GO materials tested. This will establish a broader baseline of performance, from which an understanding of the removal properties of GO may be subdivided according to dye class and properties. In addition, it would also be useful and relevant to seek the optimum GO concentration, that correlates with the peak performance of the materials. This may provide a deeper understanding of the mechanism and behaviour of the systems.

- Dead end cell testing. Filtration testing of GO-coated membranes was carried out using uniaxial flow testing equipment as the lone testing apparatus. Other modes of testing, such as cross-flow filtration, were not utilised in the scope of this research. This was primarily a constraint due to research budget limitations, as the cross flow device has greater associated cost compared to dead end cell. There were also access restrictions, as to the best of our knowledge, there was no availability to carry out this testing in the university. Results of cross-flow filtration would have provided useful results for comparison with those achieved in dead end cell testing. Cross-flow provides high shear flux of contaminants across the membrane surface and is therefore a more realistic means of filtration. It is considered that researchers seeking to expand the utility of GO materials should include cross-flow testing, as this may in turn lead to developments in coating fabrication, so as to withstand the harsher treatment in cross-flow.

- Variation in experimental parameters for adsorption studies. Intentional variation of parameters including solution temperature and pH were not incorporated into adsorption or filtration studies. Deliberate modification of these parameters may have impacted adsorption capacity of the GO materials, as such, exploration of these factors would have been relevant to the studies and should be addressed in future work. In our work, we considered multi-component adsorption and filtra-

tion involving dye-salt systems; these were considered non-ideal systems, as the interactions of GO and dye interaction was impeded by salts. As such, variation in other parameters including temperature and pH would provide interesting results regarding the behaviour of GO materials in a non-idealised setting, such is relevant for their application in industry.

- Long duration filtration stability studies. In order to investigate the stability of the membrane performance over longer periods of operation, it is suggested that stability studies be carried out over extended duration, *i.e.* lasting over several hours to a full day. This would enable the performance (permeability and rejection) of the filter to be monitored over the timescales necessary for industrial operation. Such studies were not possible for the scope of this research, given the restrictions in terms of laboratory access times.

- Reusability of GO materials and membranes. An important stage in the development of GO materials as adsorbents, or for application within membrane filtration, is to consider the resusability of the materials. Recycling of spent adsorbents is a means to improve the process economics, by ensuring that the materials are not a single-use only product. As highlighted in earlier sections, GO tends to aggregate when contacted with charged species, a feature especially relevant for highly charged SFGO systems. It is therefore imperative to assess the potential for separation and re-use of the material. Additionally, within operation of membrane materials, it is important to assess the potential for flux and rejection regeneration properties across multiple filtration cycles, perhaps with an intermittent cleaning cycle. This would enable assessment of the membrane recyclability. Such studies were not incorporated into our research given time constraints.

Appendix A

A.1 Chapter 4

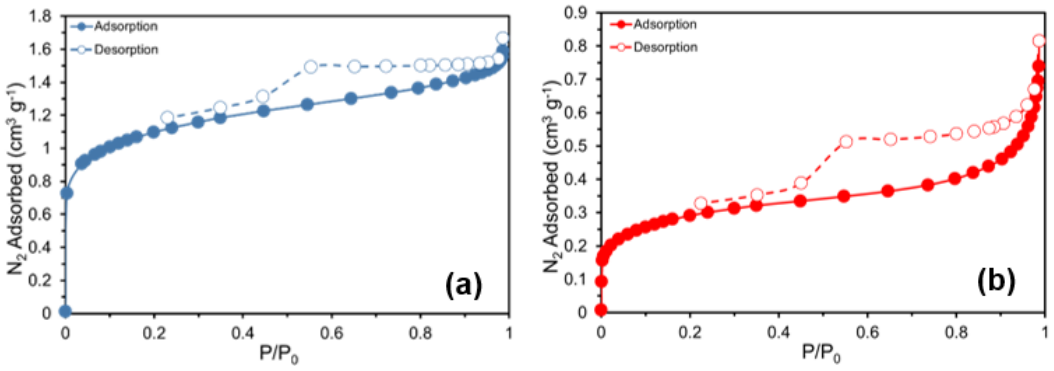

Figure A.1: Nitrogen adsorption isotherms, collected during BET analysis of GO powders at 77K, for (a) SFGO and (b) LFGO.

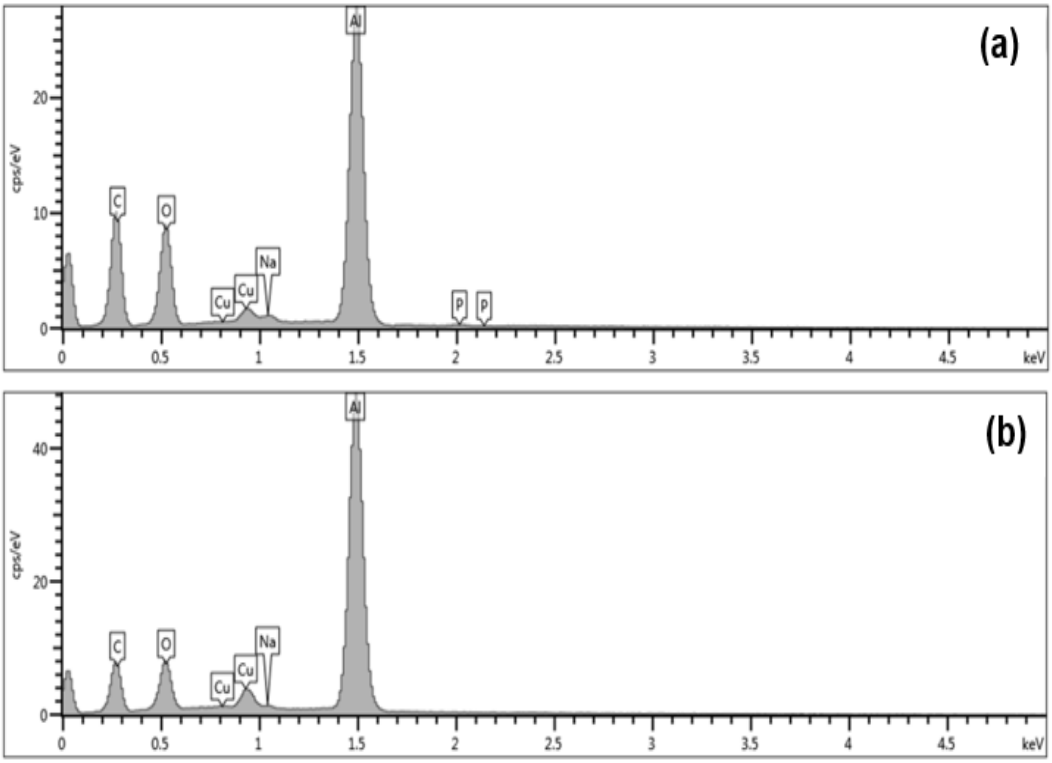

Figure A.2: EDX spectra of (a) SFGO and (b) LFGO, taken from a single spot size on the dried GO materials.

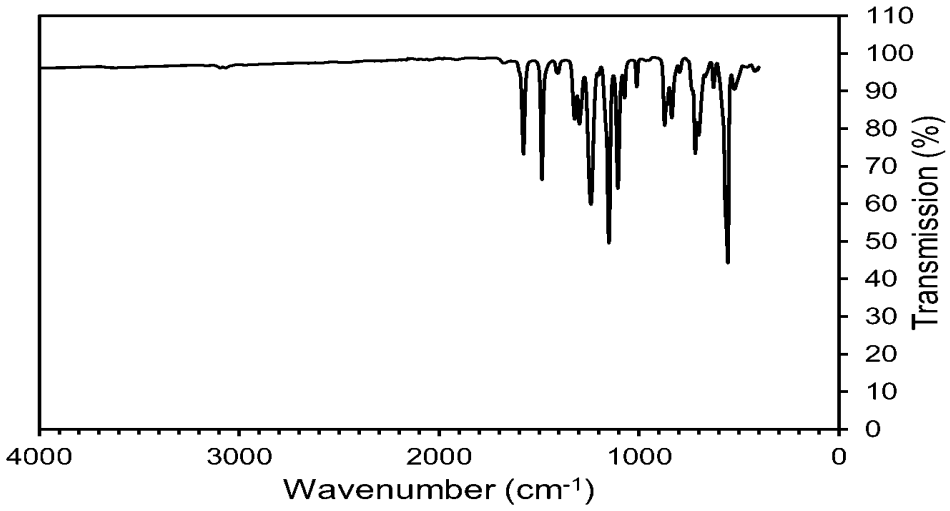

Figure A.3: FTIR spectrum of Sterlitech PES 0.20 μm filter.

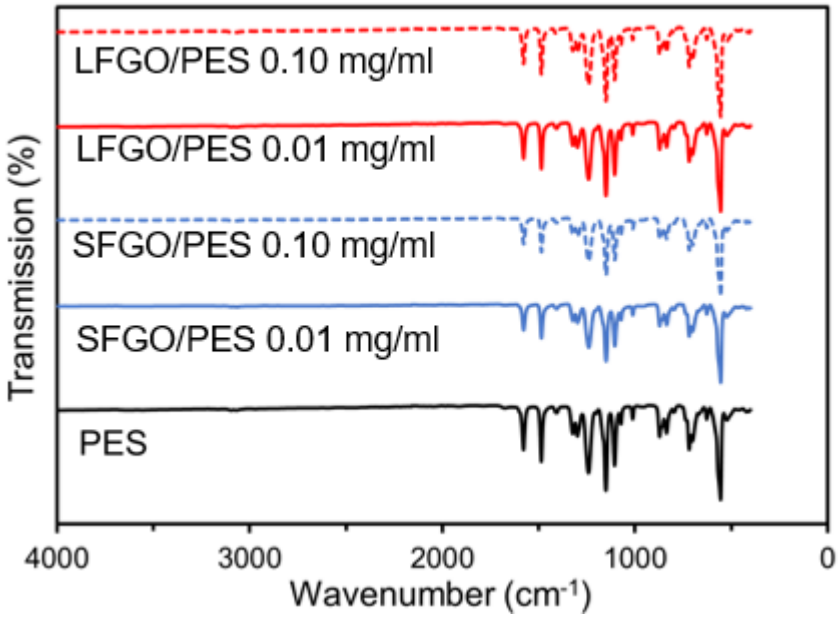

Figure A.4: FTIR analysis of commercial PES membrane, and SFGO- and LFGO-coated membranes. Spectra are shown in wavenumber range 4000 - 0 cm^{-1}.

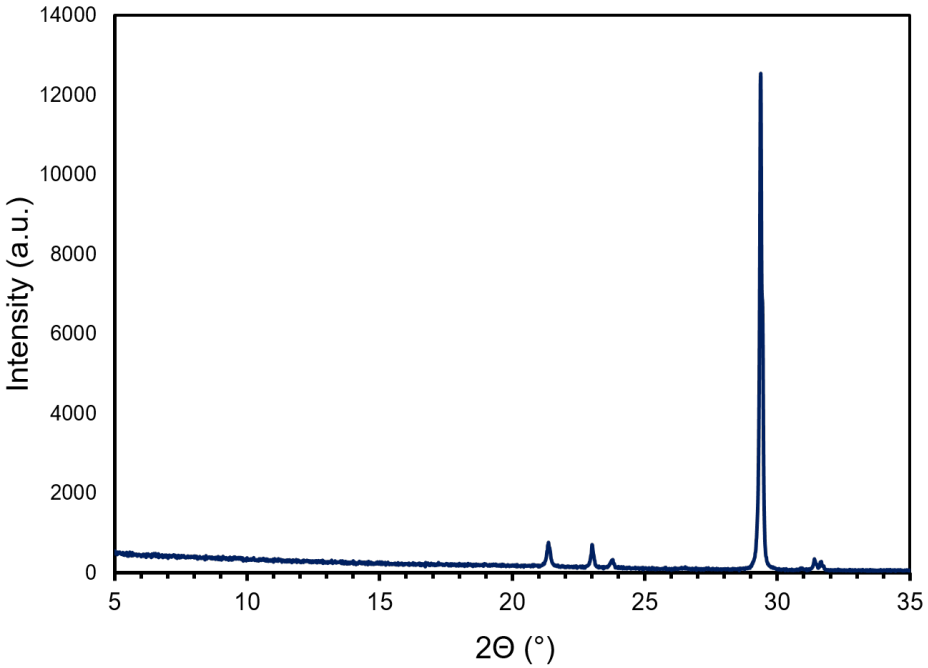

Figure A.5: XRD diffraction pattern of copper sample holder, used during analysis of GO-coated PES membranes.

A.2 Chapter 5

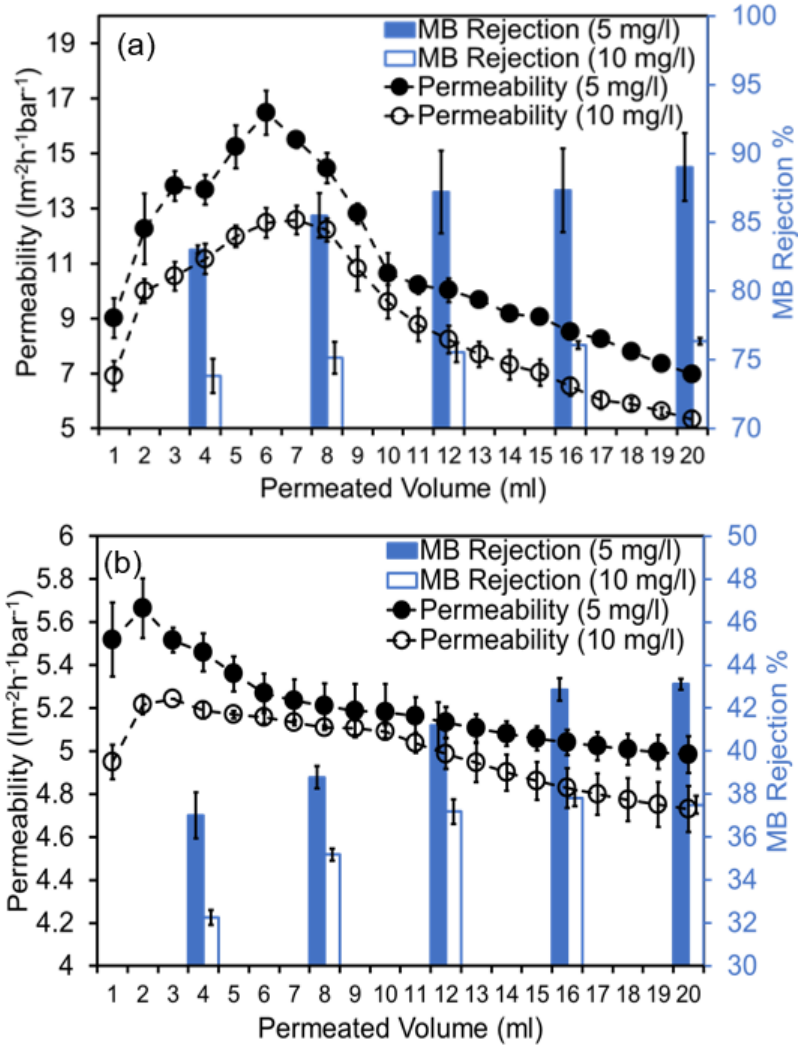

Figure A.6: Permeability and Rejection of 5, 10 mg/l MB using 0.10 mg/ml coatings of (a) SFGO and (b) LFGO. Filtration pressure 2 bar. Vertical error bars represent standard deviation across three separate filtration runs.

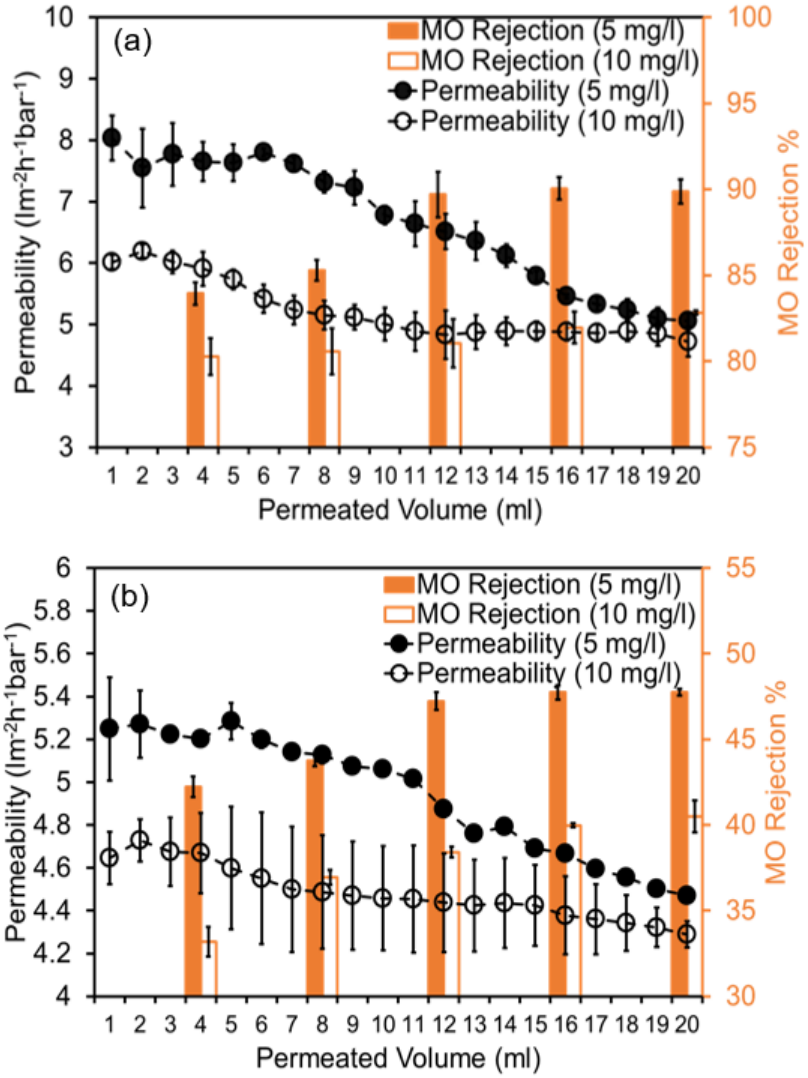

Figure A.7: Permeability and Rejection of 5, 10 mg/l MO using 0.10 mg/ml coatings of (a) SFGO and (b) LFGO. Filtration pressure 2 bar. Vertical error bars represent standard deviation across three separate filtration runs.

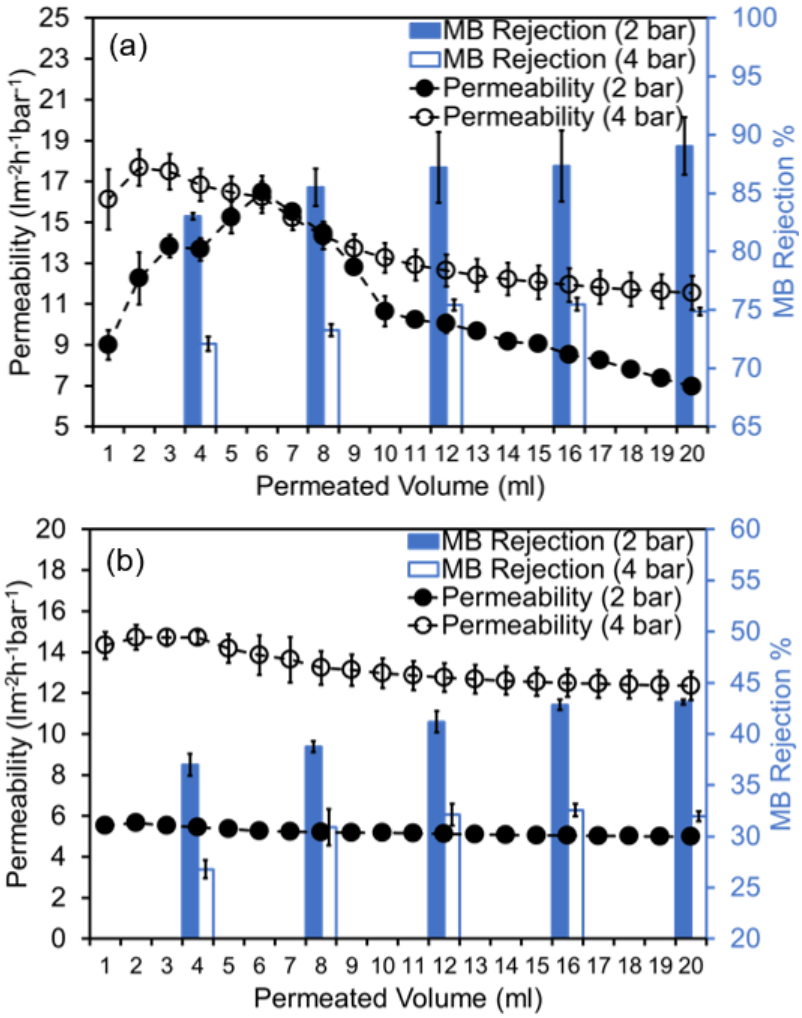

Figure A.8: Permeability and Rejection of 5 mg/l MB using 0.10 mg/ml coatings of (a) SFGO and (b) LFGO. Filtration pressure 2 and 4 bar. Vertical error bars represent standard deviation across three separate filtration runs.

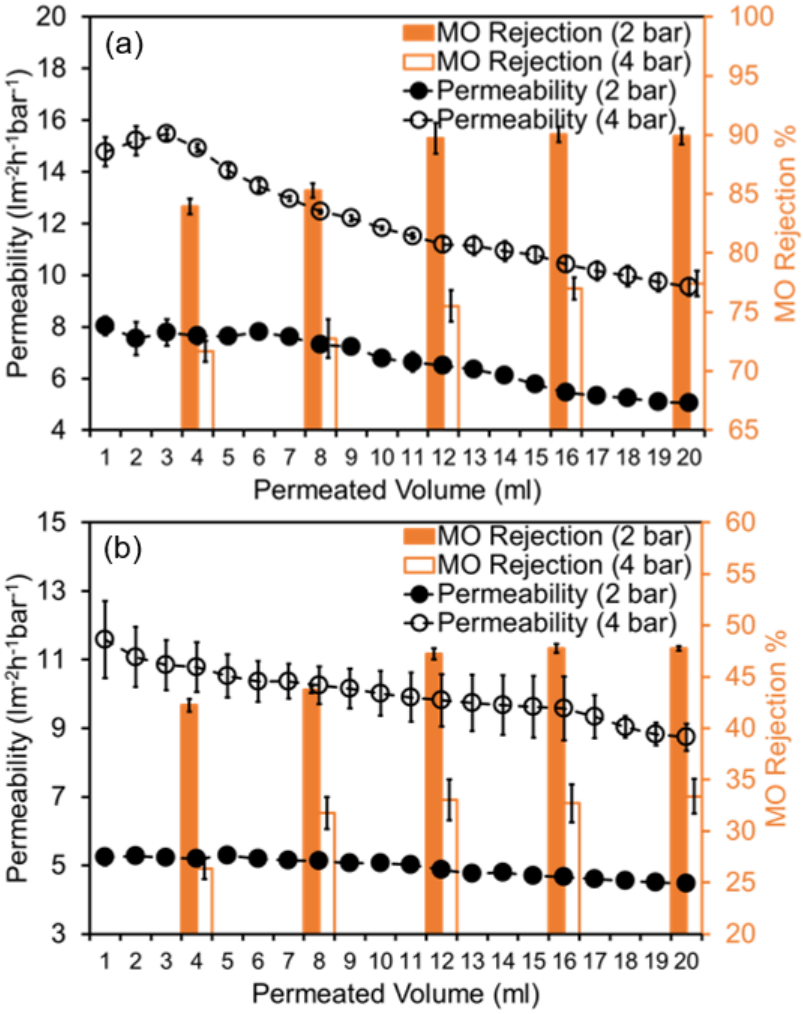

Figure A.9: Permeability and Rejection of 5 mg/l MO using 0.10 mg/ml coatings of (a) SFGO and (b) LFGO. Filtration pressure 2 and 4 bar. Vertical error bars represent standard deviation across three separate filtration runs.

A.3 Chapter 6

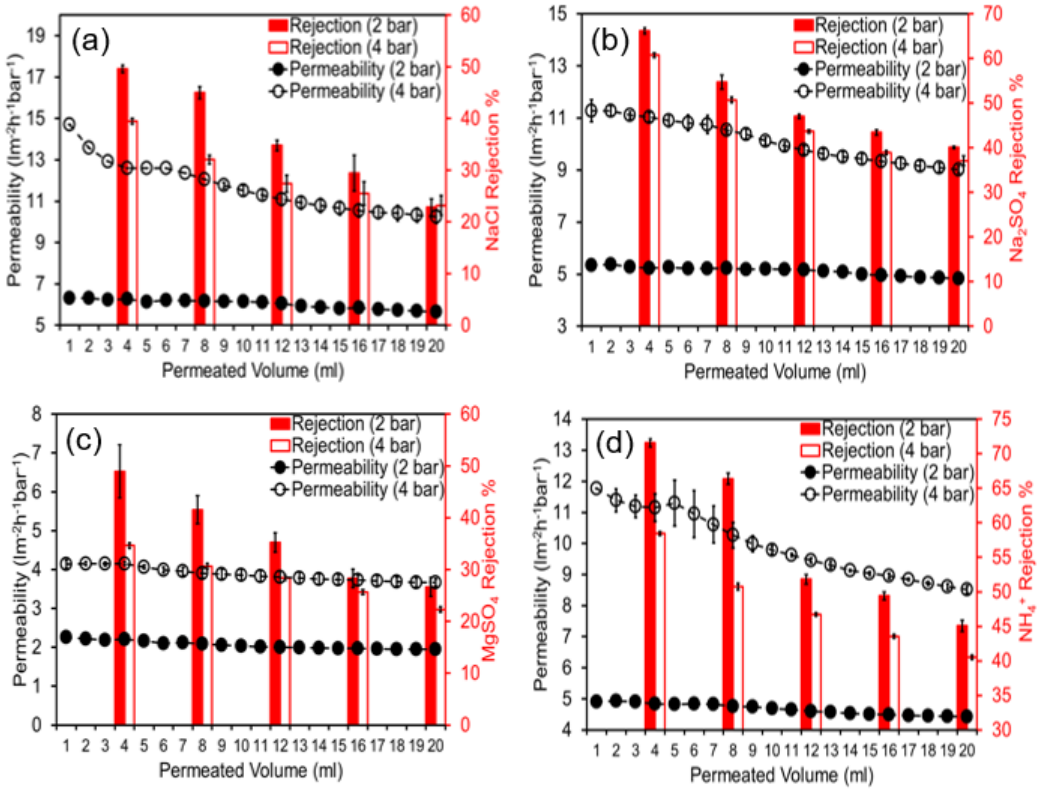

Figure A.10: Permeability and salt rejection, as a function of permeated volume, in desalination of (a) sodium chloride, (b) sodium sulphate, (c) magnesium sulphate and (d) ammonium heptamolybdate, using 0.10 mg/ml SFGO coating. Salt concentration 0.50 mg/ml. Filtration pressure 2 and 4 bar. Vertical error bars represents standard deviation across 3 filtration runs.

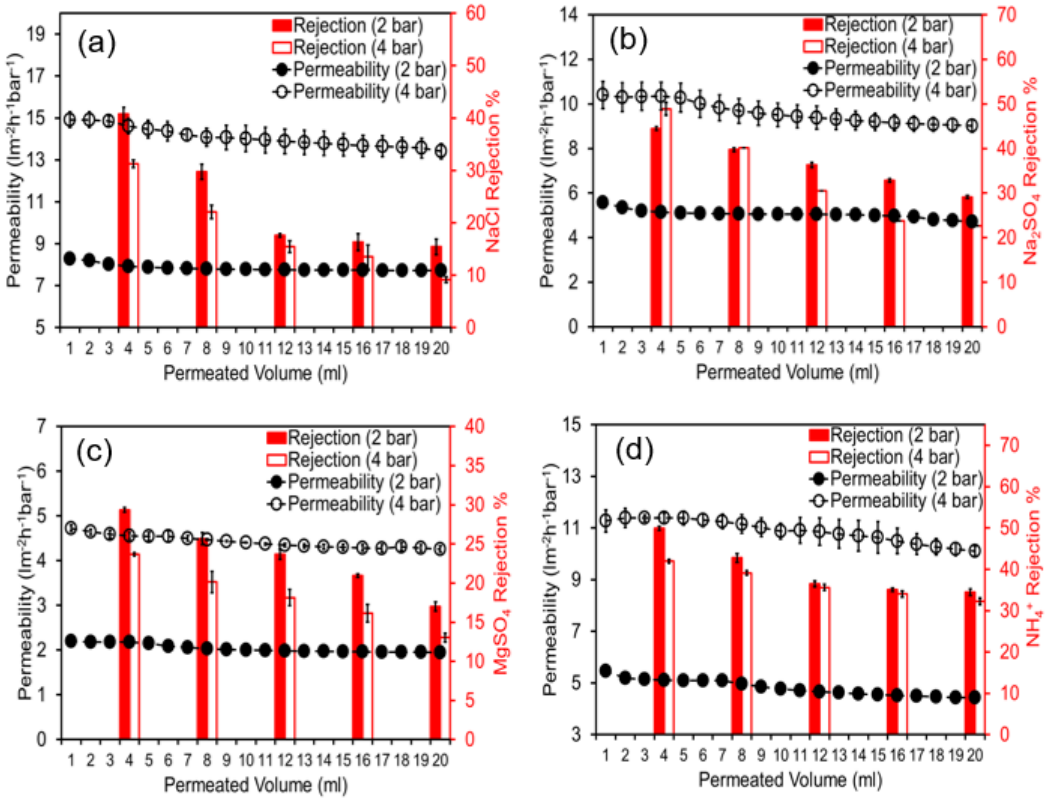

Figure A.11: Permeability and salt rejection, as a function of permeated volume, in desalination of (a) sodium chloride, (b) sodium sulphate, (c) magnesium sulphate and (d) ammonium heptamolybdate, using 0.10 mg/ml LFGO coating. Salt concentration 0.50 mg/ml. Filtration pressure 2 and 4 bar. Vertical error bars represents standard deviation across 3 filtration runs.

Table A.1: PSO kinetics equations for adsorption of MB by SFGO and LFGO, subject to the presence of 0.50 - 2.00 g/l sodium sulphate and magnesium sulphate.

GO - Salt	Y = mX + C	R^2
SFGO - 0.50 g/l Na^+	$0.0038 \cdot X + 0.0014$	1.000
SFGO - 1.0 g/l Na^+	$0.0038 \cdot X + 0.0014$	1.000
SFGO - 1.50 g/l Na^+	$0.0039 \cdot X + 0.0016$	1.000
SFGO - 2.0 g/l Na^+	$0.0039 \cdot X + 0.0016$	1.000
SFGO - 0.50 g/l Mg^{2+}	$0.0038 \cdot X + 0.0053$	1.000
SFGO - 1.0 g/l Mg^{2+}	$0.0042 \cdot X + 0.0062$	1.000
SFGO - 1.50 g/l Mg^{2+}	$0.0045 \cdot X + 0.0035$	1.000
SFGO - 2.0 g/l Mg^{2+}	$0.0049 \cdot X + 0.0058$	1.000
LFGO - 0.50 g/l Na^+	$0.0044 \cdot X + 0.0015$	1.000
LFGO - 1.0 g/l Na^+	$0.0044 \cdot X + 0.0016$	1.000
LFGO - 1.50 g/l Na^+	$0.0045 \cdot X + 0.0013$	1.000
LFGO - 2.0 g/l Na^+	$0.0046 \cdot X + 0.0012$	1.000
LFGO - 0.50 g/l Mg^{2+}	$0.0046 \cdot X + 0.0041$	1.000
LFGO - 1.0 g/l Mg^{2+}	$0.0051 \cdot X + 0.0043$	1.000
LFGO - 1.50 g/l Mg^{2+}	$0.0051 \cdot X + 0.0057$	1.000
LFGO - 2.0 g/l Mg^{2+}	$0.0052 \cdot X + 0.0040$	1.000

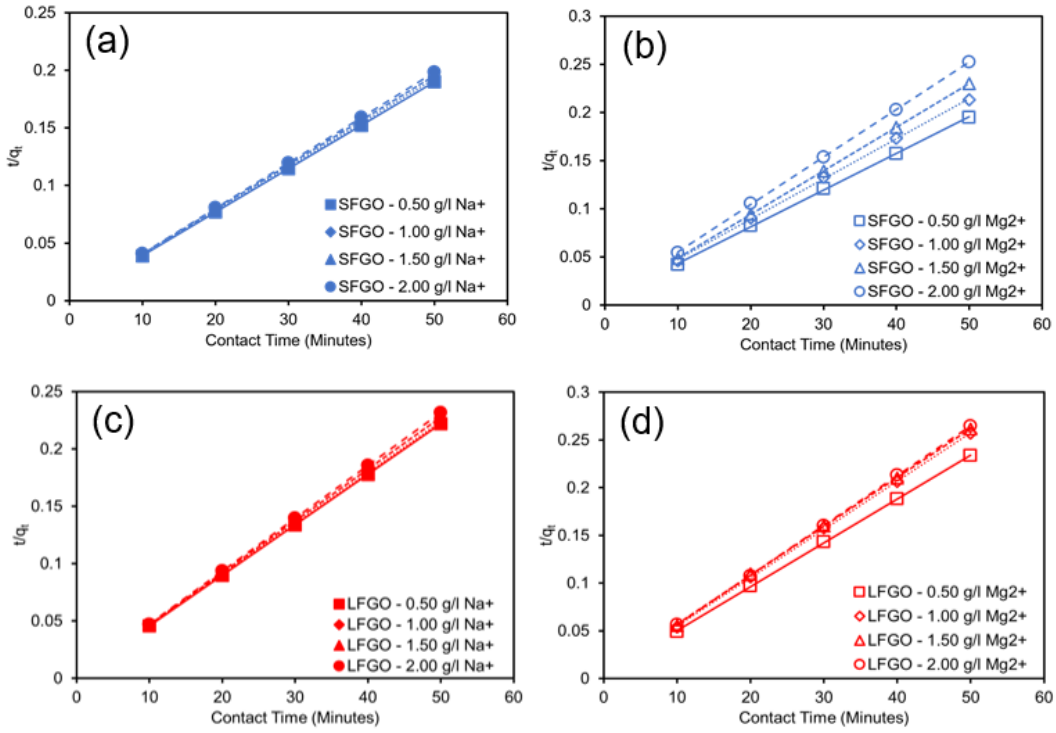

Figure A.12: PSO Kinetics of adsorption for SFGO with (a)MB/sodium sulphate and (b)MB/magnesium sulphate, and LFGO with (c)MB/sodium sulphate and (d)MB/magnesium sulphate

Table A.2: Langmuir isotherms for adsorption of MB, subject to loading the MB with 8.00 g/l sodium sulphate or magnesium sulphate.

GO - Salt	*Langmuir isotherm*	
	Y = mX + C	R^2
SFGO - Na^+	$0.0020 \cdot X + 0.0493$	0.9876
LFGO - Na^+	$0.0028 \cdot X + 0.0964$	0.9956
SFGO - Mg^{2+}	$0.0030 \cdot X + 0.0321$	0.9871
LFGO - Mg^{2+}	$0.0041 \cdot X + 0.0609$	0.9833

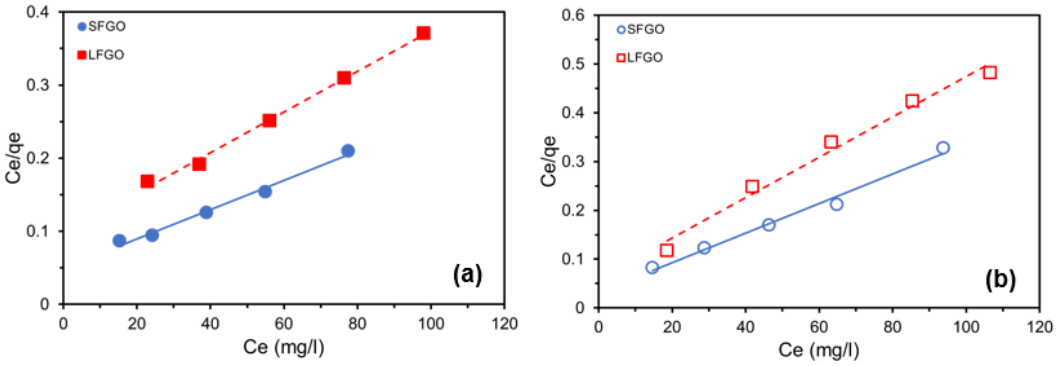

Figure A.13: Langmuir isotherms for adsorption of 50, 75, 100, 125 and 150 mg/l MB using SFGO and LFGO, subject to 8.00 g/l salt loading, for (a) sodium sulphate and (b) magnesium sulphate.

References

[1] Demircivi P. Ercag, A. and J. Hızal. Kinetic, isotherm and pH dependency investigation and environmental application of cationic dye adsorption on montmorillonite . *Desalination and Water Treatment*, 56. xv, 4

[2] Schmeling N. Jeazet H. Janiak C. Staudt C. Hunger, K. and K. Kleinermanns. Investigation of Cross-Linked and Additive Containing Polymer Materials for Membranes with Improved Performance in Pervaporation and Gas Separation . xv, 6

[3] Integrative natural medicine inspired graphene nanovehicle-benzoxazine derivatives as potent therapy for cancer author=Kumar, N., Yadav, N., Amarnath, N. et al. journal= Mol Cell Biochem , volume=454. pages 123 – 138, 2019. xv, 12

[4] Progression from Graphene and Graphene Oxide to High Performance Polymer-Based Nanocomposite: A Review author=Shah, R., Kausar, B., Muhammad, B. and Shah, S. journal= Polymer-Plastics Technology and Engineering, volume=54. pages 173 – 183, 2014. xv, 13

[5] Jingke Hou, Yingbo Chen, Wenxiong Shi, Chenlu Bao, and Xiaoyu Hu. Graphene oxide/methylene blue composite membrane for dyes separation: Formation mechanism and separation performance. *Applied Surface Science*, 505:144145, 2020. xv, 15, 185, 196

[6] François Perreault, Andreia Fonseca De Faria, and Menachem Elimelech. Environmental applications of graphene-based nanomaterials. *Chemical Society Reviews*, 44(16):5861–5896, 2015. xv, 16

[7] Giang TT Le, Narong Chanlek, Jedsada Manyam, Pakorn Opaprakasit, Nurak Grisdanurak, and Paiboon Sreearunothai. Insight into the ultrasonication of graphene oxide with strong changes in its properties and performance for adsorption applications. *Chemical Engineering Journal*, 373:1212–1222, 2019. xv, 24, 26

[8] Han Kim, Sung-Oong Kang, Sungyoul Park, and Ho Seok Park. Adsorption isotherms and kinetics of cationic and anionic dyes on three-dimensional reduced graphene oxide macrostructure. *Journal of Industrial and Engineering Chemistry*, 21:1191–1196, 2015. xv, 30, 31

[9] Meng Wang, Yang Niu, Jihan Zhou, Hao Wen, Zhenyu Zhang, Da Luo, Dongliang Gao, Juan Yang, Dehai Liang, and Yan Li. The dispersion and aggregation of graphene oxide in aqueous media. *Nanoscale*, 8(30):14587–14592, 2016. xv, 37, 38

[10] Chi-Hui Tsou, Quan-Fu An, Shen-Chuan Lo, Manuel De Guzman, Wei-Song Hung, Chien-Chieh Hu, Kueir-Rarn Lee, and Juin-Yih Lai. Effect of microstructure of graphene oxide fabricated through different self-assembly techniques on 1-butanol dehydration. *Journal of Membrane Science*, 477:93–100, 2015. xvi, 41, 42

[11] Abozar Akbari, Phillip Sheath, Samuel T Martin, Dhanraj B Shinde, Mahdokht Shaibani, Parama Chakraborty Banerjee, Rachel Tkacz, Dibakar Bhattacharyya, and Mainak Majumder. Large-area graphene-based nanofiltration membranes by

shear alignment of discotic nematic liquid crystals of graphene oxide. *Nature communications*, 7(1):1–12, 2016. xvi, 44

[12] Jianqiang Wang, Pan Zhang, Bin Liang, Yuxuan Liu, Tao Xu, Lifang Wang, Bing Cao, and Kai Pan. Graphene oxide as an effective barrier on a porous nanofibrous membrane for water treatment. *ACS applied materials & interfaces*, 8(9):6211–6218, 2016. xvi, 45, 46

[13] Ahmed E Abdelhamid, Ahmed A El-Sayed, and Ahmed M Khalil. Polysulfone nanofiltration membranes enriched with functionalized graphene oxide for dye removal from wastewater. *Journal of Polymer Engineering*, 40(10):833–841, 2020. xvi, 49, 51, 184, 188

[14] Sunxiang Zheng, Qingsong Tu, Jeffrey J Urban, Shaofan Li, and Baoxia Mi. Swelling of graphene oxide membranes in aqueous solution: characterization of interlayer spacing and insight into water transport mechanisms. *ACS nano*, 11(6):6440–6450, 2017. xvi, 56, 57

[15] Jeng Yi Chong, Bo Wang, Cecilia Mattevi, and Kang Li. Dynamic microstructure of graphene oxide membranes and the permeation flux. *Journal of membrane science*, 549:385–392, 2018. xvi, 57, 58, 130, 142, 211, 212

[16] Yi Wei, Yushan Zhang, Xueli Gao, Yiqing Yuan, Baowei Su, and Congjie Gao. Declining flux and narrowing nanochannels under wrinkles of compacted graphene oxide nanofiltration membranes. *Carbon*, 108:568–575, 2016. xvi, 59

[17] Stefano Managò, Carmen Valente, Peppino Mirabelli, and Anna Chiara De Luca. Discrimination and classification of acute lymphoblastic leukemia cells by raman spectroscopy. In *Optical Sensors 2015*, volume 9506, page 95060Z. International Society for Optics and Photonics, 2015. xvii, 72

[18] Tomasz Grzela. *Comparative STM-based study of thermal evolution of Co and Ni germanide nanostructures on Ge (001)*. PhD thesis, BTU Cottbus-Senftenberg, 2015. xvii, 74

[19] R Al-Gaashani, A Najjar, Y Zakaria, S Mansour, and MA Atieh. Xps and structural studies of high quality graphene oxide and reduced graphene oxide prepared by different chemical oxidation methods. *Ceramics International*, 45(11):14439–14448, 2019. xvii, 76, 111

[20] Hyun-A Kim, Jung-Kwan Seo, Taksoo Kim, and Byung-Tae Lee. Nanometrology and its perspectives in environmental research. *Environmental health and toxicology*, 29, 2014. xvii, 81

[21] HA Taroco, JAFd Santos, RZ Domingues, and T Matencio. Ceramic materials for solid oxide fuel cells. *Advances in ceramics-Synthesis and Characterization, processing and specific applications*, pages 423–446, 2011. xvii, 83

[22] Yanping Zhu, Tsung-Rong Kuo, Yue-Hua Li, Ming-Yu Qi, Gao Chen, Jiali Wang, Yi-Jun Xu, and Hao Ming Chen. Emerging dynamic structure of electrocatalysts unveiled by in situ x-ray diffraction/absorption spectroscopy. *Energy & Environmental Science*, 14(4):1928–1958, 2021. xvii, 88

[23] Cameron F Holder and Raymond E Schaak. Tutorial on powder x-ray diffraction for characterizing nanoscale materials, 2019. xvii, 87, 89

[24] Mousumi Sen. *Nanotechnology and the Environment*. BoD–Books on Demand, 2020. xvii, 92

[25] José D Arregui-Mena, Cristian I Contescu, Anne A Campbell, Philip D Edmondson, Nidia C Gallego, Quinlan B Smith, Kentaro Takizawa, and Yutai Katoh. Nitrogen adsorption data, fib-sem tomography and tem micrographs of neutron-irradiated superfine grain graphite. *Data in brief*, 21:2643–2650, 2018. xvii, 95

[26] Tommi Huhtamäki, Xuelin Tian, Juuso T Korhonen, and Robin HA Ras. Surface-wetting characterization using contact-angle measurements. *Nature protocols*, 13(7):1521–1538, 2018. xvii, 96

[27] Renan Felinto Dos Santos, Heloisa Ramlow, Neseli Dolzan, Ricardo Antonio Francisco Machado, Catia Rosana Lange de Aguiar, and Cintia Marangoni. Influence of different textile fibers on characterization of dyeing wastewater and final effluent. *Environmental monitoring and assessment*, 190:1–12, 2018. xxv, 36

[28] Parimal Pal. *Industrial water treatment process technology*. Butterworth-Heinemann, 2017. xxv, 36

[29] Chidambaram Thamaraiselvan and Michael Noel. Membrane processes for dye wastewater treatment: recent progress in fouling control. *Critical Reviews in Environmental Science and Technology*, 45(10):1007–1040, 2015. xxv, 36

[30] Mahalingam Arulprakasajothi, Kariappan Elangovan, Udayagiri Chandrasekhar, and Sivan Suresh. Performance study of conical strip inserts in tube heat exchanger using water based titanium oxide nanofluid. *Thermal Science*, 22(1 Part B):477–485, 2018. xxv, 84

[31] Mishra A.K. Wada Y. et al. Konapala, G. Climate change will affect global water availability through compounding changes in seasonal precipitation and evaporation. *Nat. Commun.*, 11. 1

[32] Mishra A.K. Wada Y. et al. Konapala, G. Reassessing the projections of the World Water Development Report. *npj Clean Water*, 2. 1

[33] Solera A. Ferrer J. Estrela T. Pedro-Monzonís, M. and J Paredes-Arquiola. A review of water scarcity and drought indexes in water resources planning and management,. *Journal of Hydrology*, 527. 1

[34] Guillaume J. de Moel H. et al. Kummu, M. The world's road to water scarcity: shortage and stress in the 20th century and pathways towards sustainability. *Sci Rep*, 6. 1

[35] Dong J Yang H Van Zwieten L Lu H Alshameri A Zhan Z Chen X Jiang X Xu W Bao Y Wang H. Zhang Y, Li M. A Critical Review of Methods for Analyzing Freshwater Eutrophication. *Water*, 13. 1

[36] D. Deming. Rural–urban water struggles: urbanizing hydrosocial territories and evolving connections, discourses and identities. *Water International*, 44. 2

[37] Davary K. Kolahi M. Mianabadi, A. and J. Fisher. Water/climate nexus environmental rural-urban migration and coping strategies. *Journal of Environmental Planning and Management*, 65. 2

[38] R. Lee. The outlook for population growth. *Science*, 333. 2, 202

[39] A. Y. Mekonnen, M. M. Hoekstra. Four billion people facing severe water scarcity. *Sci. Adv. 2,*. 2

[40] Roach E. Al-Saidi, M. and Al-Saeedi B. Conflict Resilience of Water and Energy Supply Infrastructure: Insights from Yemen. *Water*, 12. 2

[41] Roach E. Al-Saidi, M. and Al-Saeedi B. Yemen in a Time of Cholera: Current Situation and Challenges. *The American journal of tropical medicine and hygiene*, 98. 2

[42] Roach E. Al-Saidi, M. and Al-Saeedi B. Yemen in a Time of Cholera: Current Situation and Challenges. *Weather, Climate, and Society*, 6. 2

[43] Lompi M Pacetti T Chiarello V Fatichi S. Caporali, E. A review of studies on observed precipitation trends in Italy. *Int. J. Climatol.*, 41. 2

[44] D. Deming. The Aqueducts and Water Supply of Ancient Rome. *Ground Water*, 58. 2

[45] M. Savelyev. Newly Industrialized Countries: Is There an Alternative to the Golden Billion? *IOP Conf. Ser.: Earth Environ. Sci.*, 666. 2

[46] Xue H. Wang H. Zhang, F. and H. Dong. Industrial Growth Path under the Restriction of Water Resources in China. *Procedia Engineering*, 174. 2

[47] UNESCO World Water Assessment Programme. The United Nations World Water Development Report 2022: groundwater: making the invisible visible. 174. 3

[48] Vrishali S. Ganapathy G. David T. Tatjana, S. and P. Rohini. Wastewater Discharge Standards in the Evolving Context of Urban Sustainability–The Case of India . *Frontiers in Environmental Science*, 8. 3

[49] Lannerstad M. Herrero P. Notenbaert M. Hoff H. Heinke, J. and C. Muller. Water Use in Global Livestock Production-Opportunities and Constraints for Increasing Water Productivity . *Water Resources Research*, 56. 3

[50] Alavanja M. Introduction: pesticides use and exposure extensive worldwide . *Reviews on Environmental Health*, 24. 3

[51] Alavanja M. A review on lake eutrophication dynamics and recent developments in lake modeling . *Ecohydrology & Hydrobiology*, 19. 3

[52] Zhang J. Gurkan Z. and Jorgensen S.E. Development of a structurally dynamic model for forecasting the effects of restoration of Lake Fure, Denmark . *Ecological Modelling*, 197. 3

[53] van der Meer Y. Palacios-Mateo, C. and G. Seide. Analysis of the polyester

clothing value chain to identify key intervention points for sustainability . *Environ Sci Eur 33*, 2. 3

[54] Kaur K. Agarwal, V. and D Debdeep. Scenario Analysis of Textile Industry in Asia-Pacific Trade Agreement (APTA) . *Procedia Computer Science*, 122. 3

[55] Maple M. Usher K. et al. Kabir, H. Health vulnerabilities of readymade garment (RMG) workers: a systematic review . *BMC Public Health 19*, 70. 3

[56] Trzepacz S. Löw C. Liu R. Danneck J. Konstantas A. Donatello S. Kohler A., Watson D. and Faraca G. Circular Economy Perspectives in the EU Textile sector, EUR 30734 EN, Publications Office of the European Union . *Publications Office of the European Union*, 70. 3

[57] M'rabet S. Benkhaya S. and A. El Harfi. Classifications, properties, recent synthesis and applications of azo dyes . *Heliyon*, 6. 3

[58] Joglekar A.R. Shankarling G.S., Deshmukh P.P. Process intensification in azo dyes . *J. Environ. Chem. Eng.*, 5. 3

[59] S.-H. Kim and Y.-A. Son. *Near-infrared dyes.* 4

[60] Shaharoona B. Crowley D. Khalid A. Hussain S. Imran, M. and M. Arshad. The stability of textile azo dyes in soil and their impact on microbial phospholipid fatty acid profiles . *Ecotoxicology and Environmental Safety*, 120. 4

[61] Saratale G. D. Chang J. S. Saratale, R. G. and S. P. Govindwar. Bacterial decolorization and degradation of azo dyes: A review . *Journal of the Taiwan Institute of Chemical Engineers*, 42. 4

[62] K. Chung. Azo dyes and human health: A review . *J Environ Sci Health C Environ Carcinog Ecotoxicol Rev.*, 34. 4

[63] Roy A. Sundaram S. Velusamy, S. and T. Mallick. A Review on Heavy Metal Ions and Containing Dyes Removal Through Graphene Oxide-Based Adsorption Strategies for Textile Wastewater Treatment. . *Chem. Rec.*, 21. 4

[64] Roy A. Sundaram S. Velusamy, S. and T. Mallick. Comparison between biosorbents for the removal of metal ions from aqueous solutions . *Water Research*, 32. 4

[65] Liu Y. Chen, X. and Q. et al. Xie. Synthesis and characterization of stable main-chain polymeric metal complex dyes based on phenothiazine or carbazole units for dye-sensitized solar cells . *Polym. J.*, 48. 4

[66] Zhang X. Du H. et al. Sun, D. Application of liquid organic salt to cotton dyeing process with reactive dyes . *Fibers Polym.*, 18. 5

[67] Qian X. Ru, J. and Y. Wang. Low-Salt or Salt-Free Dyeing of Cotton Fibers with Reactive Dyes using Liposomes as Dyeing/Level-Dyeing Promotors . *Sci. Rep. 8*, 13045. 5

[68] Liao C. and L. Shollenberger. Survivability and long-term preservation of bacteria in water and in phosphate-buffered saline . *Lett Appl Microbiol.*, 37. 5

[69] C. Broggi. *Trade and Technology Networks in the Chinese Textile Industry: Opening Up Before the Reform.* 5

[70] TNN. India overtakes Germany and Italy, is new world No. 2 in textile exports . *Times of India.* 5

[71] C. Ogugbue and T. Sawidis. Bioremediation and Detoxification of Synthetic Wastewater Containing Triarylmethane Dyes by Aeromonas hydrophila Isolated from Industrial Effluents . *Biotechnol Res Int.* 5

[72] Guodong C. Qi, F. and M. Masao. Water resources in China: Problems and countermeasures . *Ambio,*, 28. 5

[73] Ministry of Environmental Protection of China. Report on the State of the Environment in China . 5

[74] Ministry of Environmental Protection of China. Hazardous Substance Research Centers/South and Southwest Outreach Program. 5

[75] R. Kant. Textile dyeing industry an environmental hazard . *Natural Science*, 4. 6

[76] S. Judd. *Chapter 2 - Membrane technology.* 6

[77] Chakraborty S. Tow E. Plumlee M. et al. Warsinger, D. A review of polymeric membranes and processes for potable water reuse . 7

[78] X. Tan and D. Rodrigue. A Review on Porous Polymeric Membrane Preparation. Part II: Production Techniques with Polyethylene, Polydimethylsiloxane, Polypropylene, Polyimide, and Polytetrafluoroethylene. 7

[79] J. Bundschuh and B. Tomaszewska. *Geothermal Water Management* . 7

[80] B. Malczewska and A. Zak. Structural Changes and Operational Deterioration of the Uf Polyethersulfone (Pes) Membrane Due to Chemical Cleaning. 7

[81] G.-D. Kang and Y.-M. Cao. Application and modification of poly(vinylidene fluoride) (PVDF) membranes – A review. 7

[82] Yingchao Dong, Hui Wu, Fenglin Yang, and Stephen Gray. Cost and efficiency perspectives of ceramic membranes for water treatment. *Water Research*, page 118629, 2022. 7

[83] M Lee, Z Wu, and K Li. Advances in ceramic membranes for water treatment. In *Advances in membrane technologies for water treatment*, pages 43–82. Elsevier, 2015. 7

[84] Shi Y Du, X. and J. Haq. A Review on the Mechanism, Impacts and Control Methods of Membrane Fouling in MBR System. 7

[85] Giagnorio M. Zodrow K. Ricceri, F. and A. Tiraferri. Organic fouling in forward osmosis: Governing factors and a direct comparison with membrane filtration driven by hydraulic pressure. 7

[86] Pyo M. Shahid, M. and Y. Choi. Inorganic fouling control in reverse osmosis wastewater reclamation by purging carbon dioxide. 7

[87] Roddick F. Nguyen, T. and L. Fan. Biofouling of water treatment membranes: a review of the underlying causes, monitoring techniques and control measures. 7

[88] Q. Li and M. Elimelech. Organic Fouling and Chemical Cleaning of Nanofiltration Membranes: Measurements and Mechanisms. 7

[89] Vanoppen M. van Agtmaal J. Cornelissen E. et al. Jafari, M. Cost of fouling in full-scale reverse osmosis and nanofiltration installations in the Netherlands. 7

[90] N. Voutchkov. Energy use for membrane seawater desalination – current status and trends. 8

[91] Can Large-Scale Offshore Membrane Desalination Cost-Effectively and Ecologically Address Water Scarcity in the Middle East? author=Janowitz, D., Groche, S., Yuce, S., Melin, T. and Wintgens, T. journal= Membranes , volume=12. 2022. 8

[92] The Future of Seawater Desalination: Energy, Technology, and the Environment

author=Elimelech, M. and Phillip, W. journal= Science , volume=431. pages 712 – 717, 2011. 8

[93] Emerging Membrane Technologies for Water and Energy Sustainability: Future Prospects, Constraints and Challenges author=Roy, S. and Ragunath, S. journal= Energies , volume=11. 2018. 8

[94] Is Desalination a Solution to Freshwater Scarcity in Developing Countries? author=Dhakal, N., Salinas-Rodriguez S., Hamdani, J., Abushaban, A., Sawalha, H., Schippers, J. and Kennedy, M. journal= Membranes (Basel) , volume=12. 2018. 8

[95] Antifouling membrane surface construction: Chemistry plays a critical role author=Zhao, X., Zhang, R., Liu, Y., He, M., Su, Y., Gao, C. and Jiang, Z. journal= Journal of Membrane Science, volume=551. pages 145 – 171, 2018. 8

[96] Graphene membranes for water desalination author=Zhao, X., Zhang, R., Liu, Y., He, M., Su, Y., Gao, C. and Jiang, Z. journal= NPG Asia Mater , volume=9. 2017. 8, 54, 202

[97] Advanced graphene oxide-based membranes as a potential alternative for dyes removal: A review author=Januario, E., Vidovix, T., Beluci, N., Paixao, R., Silva L., Homem, N., Bergamasco, R. and Vieira, A. journal= Sci Total Environ. , volume=789. 2021. 8, 15, 16

[98] Kostya S Novoselov, Andre K Geim, Sergei V Morozov, De-eng Jiang, Yanshui Zhang, Sergey V Dubonos, Irina V Grigorieva, and Alexandr A Firsov. Electric field effect in atomically thin carbon films. *science*, 306(5696):666–669, 2004. 9

[99] Jannik C Meyer, Andre K Geim, Mikhail I Katsnelson, Konstantin S Novoselov, Tim J Booth, and Siegmar Roth. The structure of suspended graphene sheets. *Nature*, 446(7131):60–63, 2007. 9

[100] Palomino M. Valencia S. Perez-Botella, E. and F. Rey. *Zeolites and Other Adsorbents*. 9

[101] Kalenak A. Dodson, R. and A. Matzger. Solvent Choice in Metal–Organic Framework Linker Exchange Permits Microstructural Control. 9

[102] A. Dideikin and A. Vul. Graphene oxide and derivatives: the place in graphene family. *Frontiers in Physics*, 6:149, 2019. 9

[103] Y. Liu. *Application of graphene oxide in water treatment*, volume 94. 2017. 9

[104] Wu H. Lin, L., Crompton J. Zhang S. Green, S., and D. Horsell. Formation of tunable graphene oxide coating with high adhesion. *Physical Chemistry Chemical Physics*, 18(7):5086–5090, 2016. 9

[105] C. Qi Y. Qian, Y. Li and J. Zhong. 3d printing of graphene oxide composites with well controlled alignment. *Carbon*, 171:777 – 784, 2021. 9

[106] Andrew T Smith, Anna Marie LaChance, Songshan Zeng, Bin Liu, and Luyi Sun. Synthesis, properties, and applications of graphene oxide/reduced graphene oxide and their nanocomposites. *Nano Materials Science*, 1(1):31–47, 2019. 9

[107] Ji Won Suk, Richard D Piner, Jinho An, and Rodney S Ruoff. Mechanical properties of monolayer graphene oxide. *ACS nano*, 4(11):6557–6564, 2010. 9

[108] Changgu Lee, Xiaoding Wei, Jeffrey W Kysar, and James Hone. Measurement of the elastic properties and intrinsic strength of monolayer graphene. *science*, 321(5887):385–388, 2008. 9

[109] Yong Zhou, Chun-Sheng Yang, Ji-An Chen, Gui-Fu Ding, Wen Ding, Li Wang, Ming-Jun Wang, Ya-Ming Zhang, and Tai-Hua Zhang. Measurement of young's modulus and residual stress of copper film electroplated on silicon wafer. *Thin Solid Films*, 460(1-2):175–180, 2004. 9

[110] Jackie D Renteria, Sylvester Ramirez, Hoda Malekpour, Beatriz Alonso, Alba Centeno, Amaia Zurutuza, Alexandr I Cocemasov, Denis L Nika, and Alexander A Balandin. Strongly anisotropic thermal conductivity of free-standing reduced graphene oxide films annealed at high temperature. *Advanced Functional Materials*, 25(29):4664–4672, 2015. 9

[111] Yanwu Zhu, Shanthi Murali, Weiwei Cai, Xuesong Li, Ji Won Suk, Jeffrey R Potts, and Rodney S Ruoff. Graphene and graphene oxide: synthesis, properties, and applications. *Advanced materials*, 22(35):3906–3924, 2010. 9, 17

[112] Amanda L Higginbotham, Jay R Lomeda, Alexander B Morgan, and James M Tour. Graphite oxide flame-retardant polymer nanocomposites. *ACS applied materials & interfaces*, 1(10):2256–2261, 2009. 10

[113] Zepu Wang, J Keith Nelson, Henrik Hillborg, Su Zhao, and Linda S Schadler. Graphene oxide filled nanocomposite with novel electrical and dielectric properties. *Advanced Materials*, 24(23):3134–3137, 2012. 10

[114] Sungjin Park and Rodney S Ruoff. Chemical methods for the production of graphenes. *Nature nanotechnology*, 4(4):217–224, 2009. 10, 17

[115] Adere Tarekegne Habte and Delele Worku Ayele. Synthesis and characterization of reduced graphene oxide (rgo) started from graphene oxide (go) using the tour method with different parameters. *Advances in Materials Science and Engineering*, 2019, 2019. 10

[116] Harish Kumar, Rahul Sharma, Ankita Yadav, and Rajni Kumari. Recent advancement made in the field of reduced graphene oxide-based nanocomposites used in the energy storage devices: A review. *Journal of Energy Storage*, 33:102032, 2021. 10

[117] Antenor J Paulista Neto and Eudes E Fileti. Elucidating the amphiphilic character of graphene oxide. *Physical Chemistry Chemical Physics*, 20(14):9507–9515, 2018. 10

[118] Rustem R Amirov, Julia Shayimova, Zarina Nasirova, and Ayrat M Dimiev. Chemistry of graphene oxide. reactions with transition metal cations. *Carbon*, 116:356–365, 2017. 10, 14, 23

[119] Sungjin Park, Jinho An, Jeffrey R Potts, Aruna Velamakanni, Shanthi Murali, and Rodney S Ruoff. Hydrazine-reduction of graphite-and graphene oxide. *Carbon*, 49(9):3019–3023, 2011. 10, 16

[120] Chun Kiang Chua and Martin Pumera. Reduction of graphene oxide with substituted borohydrides. *Journal of Materials Chemistry A*, 1(5):1892–1898, 2013. 10

[121] Wei Liu and Giorgio Speranza. Tuning the oxygen content of reduced graphene oxide and effects on its properties. *ACS omega*, 6(9):6195–6205, 2021. 10, 16

[122] Zhuang Liu, Joshua T Robinson, Xiaoming Sun, and Hongjie Dai. Pegylated nanographene oxide for delivery of water-insoluble cancer drugs. *Journal of the American Chemical Society*, 130(33):10876–10877, 2008. 11, 17

[123] Chaoliang Gan, Ting Liang, Wen Li, Xiaoqiang Fan, and Minhao Zhu. Amine-terminated ionic liquid modified graphene oxide/copper nanocomposite toward efficient lubrication. *Applied Surface Science*, 491:105–115, 2019. 11

[124] Isabella A Vacchi, Cinzia Spinato, Jésus Raya, Alberto Bianco, and Cécilia Ménard-Moyon. Chemical reactivity of graphene oxide towards amines elucidated by solid-state nmr. *Nanoscale*, 8(28):13714–13721, 2016. 11, 17

[125] Preparation of Graphitic Oxide author=Hummers, W. Jr. and Offeman, R. journal= J. Am. Chem. Soc. , volume=80. 1958. 11

[126] Efficient synthesis of graphene oxide by Hummers method assisted with an electric field author=Guo, C. et al. journal= Mater. Res. Express , volume=6. 2019. 12, 145

[127] Synthesis of Graphene Oxide (GO) by Modified Hummers Method and Its Thermal Reduction to Obtain Reduced Graphene Oxide (rGO) author=Alam, S. , Sharma, N. and Kumar, L. journal= Graphene , volume=6. pages 1 – 18, 2017. 12

[128] Improved Synthesis of Graphene Oxide author=Marcano, D., Kosynkin, D., Berlin, J., Sinitskii, A. et al. journal= ACS Nano , volume=4. page 4806 – 4814, 2010. 12, 145

[129] Xu Z. Liu Z. et al. Peng, L. An iron-based green approach to 1-h production of single-layer graphene oxide. *Nat Commun 6*, 5716. 12

[130] Facile Access to Graphene Oxide from Ferro-Induced Oxidation author=Yu, C., Wang, C. and Chen, S. journal= Sci Rep , volume=6. 2016. 12

[131] Structure of Graphite Oxide Revisited II author=Lerf, A., He, H., Forster, F. and Klinowski, J. journal= J. Phys. Chem. B , volume=102. page 4477 – 4482, 1998. 12, 13

[132] The edge- and basal-plane-specific electrochemistry of a single-layer graphene sheet author=Yuan, W., Zhou, Y., Li, Y. et al. journal= Sci Rep, volume=3. 2013. 13

[133] Uber die Saurenatur und die Methylierung von Graphitoxyd author=Hofmann,

U. and Holst, R. journal= Ber. dtsch. Chem. Ges., volume=72. page 754 – 771, 1939. 13

[134] Uber das Graphitoxyhydroxyd (Graphitoxyd) author=Ruess, G. journal= Monatshefte fr Chemie, volume=76. page 381 – 417, 1947. 13

[135] Untersuchungen am Graphitoxid VI. Betrachtungen zur Struktur des Graphitoxids author=Scholz, W. and Boehm, H. journal= Z. Anorg. Allg. Chem. , volume=369. page 327 – 340, 1947. 13

[136] Yongchen Liu. Application of graphene oxide in water treatment. In *IOP Conference Series: Earth and Environmental Science*, volume 94, page 012060. IOP Publishing, 2017. 14

[137] Balakrishnan J. Ranjan, P. and A. Thakur. Dye Adsorption Behavior of Graphene Oxide. 14

[138] Rakesh K Joshi, Subbiah Alwarappan, Mashamichi Yoshimura, Veena Sahajwalla, and Yuta Nishina. Graphene oxide: the new membrane material. *Applied Materials Today*, 1(1):1–12, 2015. 14

[139] Shamik Chowdhury and Rajasekhar Balasubramanian. Recent advances in the use of graphene-family nanoadsorbents for removal of toxic pollutants from wastewater. *Advances in colloid and interface science*, 204:35–56, 2014. 14, 16, 175, 179

[140] Jianliang Xiao, Weiyang Lv, Zhou Xie, Yeqiang Tan, Yihu Song, and Qiang Zheng. Environmentally friendly reduced graphene oxide as a broad-spectrum adsorbent for anionic and cationic dyes via π–π interactions. *Journal of Materials Chemistry A*, 4(31):12126–12135, 2016. 14, 16, 179

[141] Weijun Peng, Hongqiang Li, Yanyan Liu, and Shaoxian Song. Adsorption of methylene blue on graphene oxide prepared from amorphous graphite: Effects of ph and foreign ions. *Journal of Molecular Liquids*, 221:82–87, 2016. 14, 16

[142] Minyuan Yin, Yusong Pan, and Chengling Pan. Adsorption properties of graphite oxide for rhodamine b. *Micro & Nano Letters*, 14(11):1192–1197, 2019. 14, 23

[143] Guodong Kong, Jia Pang, Yucheng Tang, Lili Fan, Haixiang Sun, Rongming Wang, Shou Feng, Yang Feng, Weidong Fan, Wenpei Kang, et al. Efficient dye nanofiltration of a graphene oxide membrane via combination with a covalent organic framework by hot pressing. *Journal of Materials Chemistry A*, 7(42):24301–24310, 2019. 15

[144] Azam Marjani, Ali Taghvaie Nakhjiri, Maryam Adimi, Hassan Fathinejad Jirandehi, and Saeed Shirazian. Effect of graphene oxide on modifying polyethersulfone membrane performance and its application in wastewater treatment. *Scientific reports*, 10(1):1–11, 2020. 15

[145] Aygun Cali, Yavuz Yağızatlı, Alpay Sahin, and Irfan Ar. Highly durable phosphonated graphene oxide doped polyvinylidene fluoride (pvdf) composite membranes. *International Journal of Hydrogen Energy*, 45(60):35171–35179, 2020. 15

[146] Saira Bano, Asif Mahmood, Seong-Joong Kim, and Kew-Ho Lee. Graphene oxide modified polyamide nanofiltration membrane with improved flux and antifouling properties. *Journal of Materials Chemistry A*, 3(5):2065–2071, 2015. 15

[147] Albert Boretti, Sarim Al-Zubaidy, Miroslava Vaclavikova, Mohammed Al-Abri, Stefania Castelletto, and Sergey Mikhalovsky. Outlook for graphene-based desalination membranes. *npj Clean Water*, 1(1):1–11, 2018. 15, 16, 54, 202

[148] Liang Chen, Guosheng Shi, Jie Shen, Bingquan Peng, Bowu Zhang, Yuzhu Wang, Fenggang Bian, Jiajun Wang, Deyuan Li, Zhe Qian, et al. Ion sieving

in graphene oxide membranes via cationic control of interlayer spacing. *Nature*, 550(7676):380–383, 2017. 16, 202

[149] Jacob N Israelachvili. *Intermolecular and surface forces*. Academic press, 2011. 16

[150] Xiaorong Zhang, Chengbing Qin, Yani Gong, Yunrui Song, Guofeng Zhang, Ruiyun Chen, Yan Gao, Liantuan Xiao, and Suotang Jia. Co-adsorption of an anionic dye in the presence of a cationic dye and a heavy metal ion by graphene oxide and photoreduced graphene oxide. *RSC advances*, 9(10):5313–5324, 2019. 16, 17

[151] S Ling and F Bunshi. Massive production of graphene oxide from expande d graphite. 2000. 17

[152] Lilian K de Assis, Bárbara S Damasceno, Marilda N Carvalho, Eveline HC Oliveira, and Marcos G Ghislandi. Adsorption capacity comparison between graphene oxide and graphene nanoplatelets for the removal of coloured textile dyes from wastewater. *Environmental technology*, 2019. 17

[153] Caroline Maria Bezerra de Araujo, Gabriel Filipe Oliveira do Nascimento, Gabriel Rodrigues Bezerra da Costa, Karolyne Santos da Silva, Ana Maria Salgueiro Baptisttella, Marcos Gomes Ghislandi, and Maurício Alves da Motta Sobrinho. Adsorptive removal of dye from real textile wastewater using graphene oxide produced via modifications of hummers method. *Chemical Engineering Communications*, 206(11):1375–1387, 2019. 17

[154] Meng Hu and Baoxia Mi. Enabling graphene oxide nanosheets as water separation membranes. *Environmental science & technology*, 47(8):3715–3723, 2013. 17

[155] RK Joshi, Paola Carbone, Feng-Chao Wang, Vasyl G Kravets, Ying Su, Irina V Grigorieva, HA Wu, Andre K Geim, and Rahul Raveendran Nair. Precise

and ultrafast molecular sieving through graphene oxide membranes. *science*, 343(6172):752–754, 2014. 17, 56

[156] B Lesiak, L Stobinski, A Malolepszy, M Mazurkiewicz, L Kövér, and J Tóth. Preparation of graphene oxide and characterisation using electron spectroscopy. *Journal of Electron Spectroscopy and Related Phenomena*, 193:92–99, 2014. 17

[157] Alice AK King, Benjamin R Davies, Nikan Noorbehesht, Peter Newman, Tamara L Church, Andrew T Harris, Joselito M Razal, and Andrew I Minett. A new raman metric for the characterisation of graphene oxide and its derivatives. *Scientific reports*, 6(1):19491, 2016. 17, 107, 108

[158] Peter W Albers, Valeri Leich, Anibal J Ramirez-Cuesta, Yongqiang Cheng, Jonas Hönig, and Stewart F Parker. The characterisation of commercial 2d carbons: graphene, graphene oxide and reduced graphene oxide. *Materials Advances*, 3(6):2810–2826, 2022. 17, 18

[159] MTH Aunkor, IM Mahbubul, R Saidur, and HSC Metselaar. The green reduction of graphene oxide. *Rsc Advances*, 6(33):27807–27828, 2016. 18

[160] Artur Filipe Rodrigues, Leon Newman, Neus Lozano, Sourav P Mukherjee, Bengt Fadeel, Cyrill Bussy, and Kostas Kostarelos. A blueprint for the synthesis and characterisation of thin graphene oxide with controlled lateral dimensions for biomedicine. *2D Materials*, 5(3):035020, 2018. 18

[161] Rabia Ikram, Badrul Mohamed Jan, and Waqas Ahmad. An overview of industrial scalable production of graphene oxide and analytical approaches for synthesis and characterization. *Journal of Materials Research and Technology*, 9(5):11587–11610, 2020. 18

[162] Kanika Gupta and Om P Khatri. Reduced graphene oxide as an effective adsor-

bent for removal of malachite green dye: plausible adsorption pathways. *Journal of colloid and interface science*, 501:11–21, 2017. 23

[163] Huan Wang, Xin Lai, Wei Zhao, Youning Chen, Xiaoling Yang, Xiaohua Meng, and Yuhong Li. Efficient removal of crystal violet dye using edta/graphene oxide functionalized corncob: a novel low cost adsorbent. *RSC advances*, 9(38):21996–22003, 2019. 23, 35

[164] Lavita J Martis, N Parushuram, and Y Sangappa. Preparation, characterization, and methylene blue dye adsorption study of silk fibroin–graphene oxide nanocomposites. *Environmental Science: Advances*, 2022. 23

[165] Mahdi Zarrabi, Mohammad Haghighi, Reza Alizadeh, and Salar Mahboob. Solar-light-driven photodegradation of organic dyes on sono-dispersed zno nanoparticles over graphene oxide: Sono vs. conventional catalyst design. *Separation and Purification Technology*, 211:738–752, 2019. 23

[166] Man Luo, Nicholas A Wauer, Kyle J Angle, Abigail C Dommer, Meishi Song, Christopher M Nowak, Rommie E Amaro, and Vicki H Grassian. Insights into the behavior of nonanoic acid and its conjugate base at the air/water interface through a combined experimental and theoretical approach. *Chemical science*, 11(39):10647–10656, 2020. 24

[167] V Sabna, Santosh G Thampi, and S Chandrakaran. Adsorptive removal of cationic and anionic dyes using graphene oxide. *Water Science and Technology*, 78(4):732–742, 2018. 24, 30

[168] Lianqin Zhao, Sheng-Tao Yang, Shicheng Feng, Qiang Ma, Xiaoling Peng, and Deyi Wu. Preparation and application of carboxylated graphene oxide sponge in dye removal. *International journal of environmental research and public health*, 14(11):1301, 2017. 24

[169] GK Ramesha, A Vijaya Kumara, HB Muralidhara, and S Sampath. Graphene and graphene oxide as effective adsorbents toward anionic and cationic dyes. *Journal of colloid and interface science*, 361(1):270–277, 2011. 24, 26

[170] Mingfei Zhao and Peng Liu. Adsorption of methylene blue from aqueous solutions by modified expanded graphite powder. *Desalination*, 249(1):331–336, 2009. 24

[171] Sheng-Tao Yang, Sheng Chen, Yanli Chang, Aoneng Cao, Yuanfang Liu, and Haifang Wang. Removal of methylene blue from aqueous solution by graphene oxide. *Journal of colloid and interface science*, 359(1):24–29, 2011. 24

[172] Yajun Yue, Zhanfang Cao, Fan Yang, Jing Wang, and Isaac Abrahams. Preparation of an anti-aggregation silica/zinc/graphene oxide nanocomposite with enhanced adsorption capacity. *Chemistry–A European Journal*, 25(71):16340–16349, 2019. 24, 25, 176

[173] B Derjaguin. On the repulsive forces between charged colloid particles and on the theory of slow coagulation and stability of lyophobe sols. *Transactions of the Faraday Society*, 35:203–215, 1940. 25

[174] Dan Li, Marc B Müller, Scott Gilje, Richard B Kaner, and Gordon G Wallace. Processable aqueous dispersions of graphene nanosheets. *Nature nanotechnology*, 3(2):101–105, 2008. 25, 26, 41, 56

[175] Tamas Szabo, Plinio Maroni, and Istvan Szilagyi. Size-dependent aggregation of graphene oxide. *Carbon*, 160:145–155, 2020. 25

[176] Hongmei Sun, Linyuan Cao, and Lehui Lu. Magnetite/reduced graphene oxide nanocomposites: one step solvothermal synthesis and use as a novel platform for removal of dye pollutants. *Nano Research*, 4(6):550–562, 2011. 25

[177] Chen Junyong, Hao Yongmei, Liu Yan, and Gou Jiajia. Magnetic graphene oxides as highly effective adsorbents for rapid removal of a cationic dye rhodamine b from aqueous solutions. *RSC advances*, 3(20):7254–7258, 2013. 25

[178] Swetha Jayanthi, Neerugatti KrishnaRao Eswar, Satyapaul A Singh, Kaushik Chatterjee, Giridhar Madras, and AK Sood. Macroporous three-dimensional graphene oxide foams for dye adsorption and antibacterial applications. *RSC advances*, 6(2):1231–1242, 2016. 25, 175

[179] CR Minitha, M Lalitha, YL Jeyachandran, L Senthilkumar, and Rajendra Kumar RT. Adsorption behaviour of reduced graphene oxide towards cationic and anionic dyes: Co-action of electrostatic and π–π interactions. *Materials chemistry and physics*, 194:243–252, 2017. 26, 30, 47, 145, 196

[180] Mohammad Ilyas Khan, Mohammed Khaloufa Almesfer, Abubakr Elkhaleefa, Ihab Shigidi, Mohammed Zubair Shamim, Ismat H Ali, and Mohammad Rehan. Conductive polymers and their nanocomposites as adsorbents in environmental applications. *Polymers*, 13(21):3810, 2021. 26

[181] D Robati, B Mirza, M Rajabi, O Moradi, I Tyagi, S Agarwal, and VK Gupta. Removal of hazardous dyes-br 12 and methyl orange using graphene oxide as an adsorbent from aqueous phase. *Chemical Engineering Journal*, 284:687–697, 2016. 26, 174

[182] Nirbhai Singh, Sk Riyajuddin, Kaushik Ghosh, Surinder K Mehta, and Abhijit Dan. Chitosan-graphene oxide hydrogels with embedded magnetic iron oxide nanoparticles for dye removal. *ACS Applied Nano Materials*, 2(11):7379–7392, 2019. 27

[183] Delong Kong, Lijuan He, Hansheng Li, Zenghong Song, et al. Preparation and characterization of graphene oxide/chitosan composite aerogel with high adsorp-

tion performance for cr (vi) by a new crosslinking route. *Colloids and Surfaces A: Physicochemical and Engineering Aspects*, 625:126832, 2021. 27

[184] Yawei Shi, Guobin Song, Anqi Li, Jun Wang, Haonan Wang, Ya Sun, and Guanghui Ding. Graphene oxide-chitosan composite aerogel for adsorption of methyl orange and methylene blue: Effect of ph in single and binary systems. *Colloids and Surfaces A: Physicochemical and Engineering Aspects*, 641:128595, 2022. 27

[185] Xiaorong Zhang, Chengbing Qin, Yani Gong, Yunrui Song, Guofeng Zhang, Ruiyun Chen, Yan Gao, Liantuan Xiao, and Suotang Jia. Co-adsorption of an anionic dye in the presence of a cationic dye and a heavy metal ion by graphene oxide and photoreduced graphene oxide. *RSC advances*, 9(10):5313–5324, 2019. 27

[186] G William Kajjumba, Serkan Emik, Atakan Öngen, H Kurtulus Özcan, and Serdar Aydın. Modelling of adsorption kinetic processes—errors, theory and application. *Advanced sorption process applications*, pages 187–206, 2018. 27, 29

[187] Nur Hidayati Othman, Nur Hashimah Alias, Munawar Zaman Shahruddin, Noor Fitrah Abu Bakar, Nik Raikhan Nik Him, and Woei Jye Lau. Adsorption kinetics of methylene blue dyes onto magnetic graphene oxide. *Journal of Environmental Chemical Engineering*, 6(2):2803–2811, 2018. 27

[188] Emmanuel D Revellame, Dhan Lord Fortela, Wayne Sharp, Rafael Hernandez, and Mark E Zappi. Adsorption kinetic modeling using pseudo-first order and pseudo-second order rate laws: A review. *Cleaner Engineering and Technology*, 1:100032, 2020. 27, 28

[189] Yuh-Shan Ho and Gordon McKay. Pseudo-second order model for sorption processes. *Process biochemistry*, 34(5):451–465, 1999. 27, 28, 29

[190] Jean-Pierre Simonin. On the comparison of pseudo-first order and pseudo-second order rate laws in the modeling of adsorption kinetics. *Chemical Engineering Journal*, 300:254–263, 2016. 27

[191] Yuh-Shan Ho. Review of second-order models for adsorption systems. *Journal of hazardous materials*, 136(3):681–689, 2006. 27

[192] Stan Lagergren. Zur theorie der sogenannten adsorption geloster stoffe. *Kungliga svenska vetenskapsakademiens. Handlingar*, 24:1–39, 1898. 27

[193] L Largitte and R Pasquier. A review of the kinetics adsorption models and their application to the adsorption of lead by an activated carbon. *Chemical Engineering Research and Design*, 109:495–504, 2016. 28

[194] Susheel Kalia. *Natural Polymers–Based Green Adsorbents for Water Treatment*. Elsevier, 2021. 28

[195] KL Tan and BH Hameed. Insight into the adsorption kinetics models for the removal of contaminants from aqueous solutions. *Journal of the Taiwan Institute of Chemical Engineers*, 74:25–48, 2017. 28

[196] Maria del Prado Lavin-Lopez, Antonio Patón-Carrero, N Muñoz-Garcia, V Enguilo, Jose Luis Valverde, and A Romero. The influence of graphite particle size on the synthesis of graphene-based materials and their adsorption capacity. *Colloids and Surfaces A: Physicochemical and Engineering Aspects*, 582:123935, 2019. 29

[197] Antonio Paton-Carrero, P Sanchez, Luz Sánchez-Silva, and A Romero. Graphene-based materials behaviour for dyes adsorption. *Materials Today Communications*, 30:103033, 2022. 29

[198] Weijun Peng, Hongqiang Li, Yanyan Liu, and Shaoxian Song. Adsorption of methylene blue on graphene oxide prepared from amorphous graphite: Effects of ph and foreign ions. *Journal of Molecular Liquids*, 221:82–87, 2016. 29, 179

[199] Yanhui Li, Qiuju Du, Tonghao Liu, Xianjia Peng, Junjie Wang, Jiankun Sun, Yonghao Wang, Shaoling Wu, Zonghua Wang, Yanzhi Xia, et al. Comparative study of methylene blue dye adsorption onto activated carbon, graphene oxide, and carbon nanotubes. *Chemical Engineering Research and Design*, 91(2):361–368, 2013. 30, 167

[200] Ragab E Abouzeid, Medhat E Owda, and Sawsan Dacrory. Effective adsorption of cationic methylene blue dye on cellulose nanofiber/graphene oxide/silica nanocomposite: Kinetics and equilibrium. *Journal of Applied Polymer Science*, 139(25):e52377, 2022. 30

[201] Walter J Weber Jr and J Carrell Morris. Kinetics of adsorption on carbon from solution. *Journal of the sanitary engineering division*, 89(2):31–59, 1963. 31

[202] ChinHua Chia, Fazlinda Razali Nur, Shaiful Sajab Mohd, Zakaria Sarani, NayMing Huang, HongNgee Lim, et al. Methylene blue adsorption on graphene oxide. *Sains Malaysiana*, 42(6):819–826, 2013. 31

[203] Wenjie Zhang, Chunjiao Zhou, Weichang Zhou, Aihua Lei, Qinglin Zhang, Qiang Wan, and Bingsuo Zou. Fast and considerable adsorption of methylene blue dye onto graphene oxide. *Bulletin of environmental contamination and toxicology*, 87(1):86–90, 2011. 32, 39, 174

[204] Aseel M Aljeboree, Abbas N Alshirifi, and Ayad F Alkaim. Kinetics and equilibrium study for the adsorption of textile dyes on coconut shell activated carbon. *Arabian journal of chemistry*, 10:S3381–S3393, 2017. 32, 167

[205] M Mourabet, H El Boujaady, A El Rhilassi, H Ramdane, M Bennani-Ziatni, R El Hamri, and A Taitai. Defluoridation of water using brushite: Equilibrium, kinetic and thermodynamic studies. *Desalination*, 278(1-3):1–9, 2011. 32, 33

[206] Irving Langmuir. The adsorption of gases on plane surfaces of glass, mica and platinum. *Journal of the American Chemical society*, 40(9):1361–1403, 1918. 32

[207] Herbert Freundlich. Über die adsorption in lösungen. *Zeitschrift für physikalische Chemie*, 57(1):385–470, 1907. 32, 33

[208] YC Wong, YS Szeto, WH Cheung, and G McKay. Equilibrium studies for acid dye adsorption onto chitosan. *Langmuir*, 19(19):7888–7894, 2003. 32

[209] Pooja Mahajan, Jyotsna Kaushal, Navjeet Kaur, and Rajni Bala. Application of equilibrium and kinetic studies for dye adsorption mechanism. In *AIP Conference Proceedings*, volume 2357, page 030020. AIP Publishing LLC, 2022. 33

[210] Jean-Luc Bersillon, Frederic Villieras, Frederique Bardot, Tatiana Gorner, and Jean-Maurice Cases. Use of the gaussian distribution function as a tool to estimate continuous heterogeneity in adsorbing systems. *Journal of colloid and interface science*, 240(2):400–411, 2001. 33

[211] Wojciech Konicki, Małgorzata Aleksandrzak, and Ewa Mijowska. Equilibrium, kinetic and thermodynamic studies on adsorption of cationic dyes from aqueous solutions using graphene oxide. *Chemical Engineering Research and Design*, 123:35–49, 2017. 34

[212] J Gong, X Gao, M Li, Q Nie, W Pan, and R Liu. Dye adsorption on electrochemical exfoliated graphene oxide nanosheets: ph influence, kinetics and equilibrium in aqueous solution. *International Journal of Environmental Science and Technology*, 14(2):305–314, 2017. 34

[213] Owolabi Mutolib Bankole, Oluwatoba Emmanuel Oyeneyin, Segun Esan Olaseni, Olaniran Kolawole Akeremale, and Pelumi Adanigbo. Kinetics and thermodynamic studies for rhodamine b dye removal onto graphene oxide nanosheets in simulated wastewater. *American Journal of Applied Chemistry*, 7(1):10–24, 2019. 34

[214] Lu Gan, Songmin Shang, Enling Hu, Chun Wah Marcus Yuen, and Shou-xiang Jiang. Konjac glucomannan/graphene oxide hydrogel with enhanced dyes adsorption capability for methyl blue and methyl orange. *Applied Surface Science*, 357:866–872, 2015. 34

[215] Robert Sips. On the structure of a catalyst surface. *The journal of chemical physics*, 16(5):490–495, 1948. 35

[216] Vaneet Kumar et al. Adsorption kinetics and isotherms for the removal of rhodamine b dye and pb+ 2 ions from aqueous solutions by a hybrid ion-exchanger. *Arabian Journal of Chemistry*, 12(3):316–329, 2019. 35

[217] Nikolina A Travlou, George Z Kyzas, Nikolaos K Lazaridis, and Eleni A Deliyanni. Graphite oxide/chitosan composite for reactive dye removal. *Chemical engineering journal*, 217:256–265, 2013. 35, 39

[218] Mina Sabzevari, Duncan E Cree, and Lee D Wilson. Graphene oxide–chitosan composite material for treatment of a model dye effluent. *ACS omega*, 3(10):13045–13054, 2018. 35

[219] MM Dubinin et al. Chemistry and physics of carbon. *v01*, 2:51, 1966. 35

[220] Priya Banerjee, Shubhra Sau, Papita Das, and Aniruddha Mukhopadhayay. Optimization and modelling of synthetic azo dye wastewater treatment using graphene oxide nanoplatelets: characterization toxicity evaluation and optimization us-

ing artificial neural network. *Ecotoxicology and environmental safety*, 119:47–57, 2015. 35

[221] DA Yaseen and M Scholz. Textile dye wastewater characteristics and constituents of synthetic effluents: a critical review. *International journal of environmental science and technology*, 16(2):1193–1226, 2019. 35

[222] Yawei Shi, Guobin Song, Anqi Li, Jun Wang, Haonan Wang, Ya Sun, and Guanghui Ding. Graphene oxide-chitosan composite aerogel for adsorption of methyl orange and methylene blue: Effect of ph in single and binary systems. *Colloids and Surfaces A: Physicochemical and Engineering Aspects*, 641:128595, 2022. 37

[223] Huan Tang, Shuyan Zhang, Tinglin Huang, Fuyi Cui, and Baoshan Xing. ph-dependent adsorption of aromatic compounds on graphene oxide: An experimental, molecular dynamics simulation and density functional theory investigation. *Journal of hazardous materials*, 395:122680, 2020. 37

[224] P Cooper. Removing colour from dyehouse waste waters—a critical review of technology available. *Journal of the Society of Dyers and Colourists*, 109(3):97–100, 1993. 37

[225] Md Asrafuzzaman, ANM Fakhruddin, Md Hossain, et al. Reduction of turbidity of water using locally available natural coagulants. *International Scholarly Research Notices*, 2011, 2011. 37

[226] Phyllis K Weber-Scannell, Lawrence K Duffy, Phyllis K Weber-Scannell, and Lawrence K Duffy. Effects of total dissolved solids on aquatic organisms: A review of literature and recommendation for salmonid species. 2007. 37

[227] Diana Starovoytova Madara and SS Namango. Wool grease recovery from scour-

ing effluent at textile mill. *Journal of Agriculture, Pure and Applied Science and Technology*, 10:1–9, 2014. 37

[228] JM Cases and Frederic Villieras. Thermodynamic model of ionic and nonionic surfactants adsorption-abstraction on heterogeneous surfaces. *Langmuir*, 8(5):1251–1264, 1992. 37

[229] VJ Joshi and DD Santani. Physicochemical characterization and heavy metal concentration in effluent of textile industry. *Universal Journal of environmental research & technology*, 2(2), 2012. 37

[230] RV Khandare, AN Kabra, AV Awate, and SP Govindwar. Synergistic degradation of diazo dye direct red 5b by portulaca grandiflora and pseudomonas putida. *International Journal of Environmental Science and Technology*, 10(5):1039–1050, 2013. 37

[231] Lei Wu, Lin Liu, Bin Gao, Rafael Muñoz-Carpena, Ming Zhang, Hao Chen, Zuhao Zhou, and Hao Wang. Aggregation kinetics of graphene oxides in aqueous solutions: experiments, mechanisms, and modeling. *Langmuir*, 29(49):15174–15181, 2013. 37

[232] Febri Baskoro, Chak-Bor Wong, S Rajesh Kumar, Chia-Wei Chang, Chien-Hao Chen, Dave W Chen, and Shingjiang Jessie Lue. Graphene oxide-cation interaction: Inter-layer spacing and zeta potential changes in response to various salt solutions. *Journal of Membrane Science*, 554:253–263, 2018. 38, 117, 119

[233] Samar Azizighannad and Somenath Mitra. Stepwise reduction of graphene oxide (go) and its effects on chemical and colloidal properties. *Scientific reports*, 8(1):1–8, 2018. 38, 39

[234] Mohsen Moazzami Gudarzi. Colloidal stability of graphene oxide: aggregation in two dimensions. *Langmuir*, 32(20):5058–5068, 2016. 38

[235] Tianjiao Xia, Yu Qi, Jing Liu, Zhichong Qi, Wei Chen, and Mark R Wiesner. Cation-inhibited transport of graphene oxide nanomaterials in saturated porous media: the hofmeister effects. *Environmental science & technology*, 51(2):828–837, 2017. 39

[236] Prawit Nuengmatcha, Ratana Mahachai, and Saksit Chanthai. Thermodynamic and kinetic study of the intrinsic adsorption capacity of graphene oxide for malachite green removal from aqueous solution. *Oriental journal of chemistry*, 30(4):1463, 2014. 39

[237] Ponchami Sharma, Najrul Hussain, Dipankar J Borah, and Manash R Das. Kinetics and adsorption behavior of the methyl blue at the graphene oxide/reduced graphene oxide nanosheet–water interface: a comparative study. *Journal of Chemical & Engineering Data*, 58(12):3477–3488, 2013. 39, 172

[238] Tabbi Wilberforce, AG Olabi, Enas Taha Sayed, Khaled Elsaid, and Mohammad Ali Abdelkareem. Progress in carbon capture technologies. *Science of The Total Environment*, 761:143203, 2021. 40

[239] Yuchoong Soo, Nagaraju Chada, Matthew Beckner, Jimmy Romanos, Jacob Burress, and Peter Pfeifer. Adsorbed methane film properties in nanoporous carbon monoliths. In *APS March Meeting Abstracts*, volume 2013, pages M38–001, 2013. 40

[240] Dingcheng Liang, Fengqin Yu, Keping Zhu, Zhijun Zhang, Jiawei Tang, Qiang Xie, Jinchang Liu, and Fei Xie. Quaternary ammonium salts targeted regulate the surface charge distribution of activated carbon: A study of their binding modes and modification effects. *Environmental Research*, 214:114103, 2022. 40

[241] Yogesh C Sharma. Optimization of parameters for adsorption of methylene

blue on a low-cost activated carbon. *Journal of Chemical & Engineering Data*, 55(1):435–439, 2010. 40

[242] Fatima Zahra Benhachem, Tarik Attar, and Fouzia Bouabdallah. Kinetic study of adsorption methylene blue dye from aqueous solutions using activated carbon. *Chemical Review and Letters*, 2(1):33–39, 2019. 40

[243] M Ghaedi, AM Ghaedi, A Ansari, F Mohammadi, and A Vafaei. Artificial neural network and particle swarm optimization for removal of methyl orange by gold nanoparticles loaded on activated carbon and tamarisk. *Spectrochimica Acta Part A: Molecular and Biomolecular Spectroscopy*, 132:639–654, 2014. 40

[244] Murat Akgül and Abdülkerim Karabakan. Promoted dye adsorption performance over desilicated natural zeolite. *Microporous and Mesoporous Materials*, 145(1-3):157–164, 2011. 40

[245] Erol Alver and Ayşegül Ü Metin. Anionic dye removal from aqueous solutions using modified zeolite: Adsorption kinetics and isotherm studies. *Chemical Engineering Journal*, 200:59–67, 2012. 40

[246] Lijuan Men, Chunyu Chen, An Liu, Jiankang Zhou, Siyang Yu, and Zihan Wei. Activated carbon fiber–loaded single layer graphene oxide–based capacitive deionization electrode materials for water desalination applications. *Ionics*, 28(4):1903–1913, 2022. 41

[247] E Menya, PW Olupot, H Storz, M Lubwama, and Yohannes Kiros. Production and performance of activated carbon from rice husks for removal of natural organic matter from water: a review. *Chemical Engineering Research and Design*, 129:271–296, 2018. 41

[248] PJM Carrott, MML Ribeiro Carrott, et al. Lignin–from natural adsorbent to activated carbon: a review. *Bioresource technology*, 98(12):2301–2312, 2007. 41

[249] J Lyu, X Wen, U Kumar, Y You, V Chen, and RK Joshi. Separation and purification using go and r-go membranes. *RSC advances*, 8(41):23130–23151, 2018. 41

[250] Bo Tang, Lianbin Zhang, Renyuan Li, Jinbo Wu, Mohamed Neijib Hedhili, and Peng Wang. Are vacuum-filtrated reduced graphene oxide membranes symmetric? *Nanoscale*, 8(2):1108–1116, 2016. 41

[251] Goki Eda, Giovanni Fanchini, and Manish Chhowalla. Large-area ultrathin films of reduced graphene oxide as a transparent and flexible electronic material. *Nature nanotechnology*, 3(5):270–274, 2008. 41

[252] Dmitriy A Dikin, Sasha Stankovich, Eric J Zimney, Richard D Piner, Geoffrey HB Dommett, Guennadi Evmenenko, SonBinh T Nguyen, and Rodney S Ruoff. Preparation and characterization of graphene oxide paper. *Nature*, 448(7152):457–460, 2007. 41, 100

[253] Ohchan Kwon, Yunkyu Choi, Eunji Choi, Minsu Kim, Yun Chul Woo, and Dae Woo Kim. Fabrication techniques for graphene oxide-based molecular separation membranes: Towards industrial application. *Nanomaterials*, 11(3):757, 2021. 41, 43

[254] Rathanasamy Rajasekar, Nam Hoon Kim, Daeseung Jung, Tapas Kuila, Jae Kyoo Lim, Min Jeong Park, and Joong Hee Lee. Electrostatically assembled layer-by-layer composites containing graphene oxide for enhanced hydrogen gas barrier application. *Composites Science and Technology*, 89:167–174, 2013. 42

[255] Meng Hu and Baoxia Mi. Enabling graphene oxide nanosheets as water separation membranes. *Environmental science & technology*, 47(8):3715–3723, 2013. 42, 60

[256] Jinxia Ma, Dan Ping, and Xinfa Dong. Recent developments of graphene oxide-based membranes: A review. *Membranes*, 7(3):52, 2017. 42

[257] Hong-Yu Zhang, Ai-Jing Miao, and Min Jiang. Fabrication, characterization and electrochemistry of organic–inorganic multilayer films containing polyoxometalate and polyviologen via layer-by-layer self-assembly. *Materials Chemistry and Physics*, 141(1):482–487, 2013. 42

[258] Deepak Rawtan and Yadvendra K Agrawal. Emerging strategies and applications of layer-by-layer self-assembly. *Nanobiomedicine*, 1(Godište 2014):1–8, 2014. 42

[259] Meng Hu and Baoxia Mi. Layer-by-layer assembly of graphene oxide membranes via electrostatic interaction. *Journal of Membrane Science*, 469:80–87, 2014. 42

[260] Vepika Kandjou, Miguel Hernaez, Beatriz Acevedo, and Sonia Melendi-Espina. Interfacial crosslinked controlled thickness graphene oxide thin-films through dip-assisted layer-by-layer assembly means. *Progress in Organic Coatings*, 137:105345, 2019. 43

[261] Hyo Won Kim, Hee Wook Yoon, Seon-Mi Yoon, Byung Min Yoo, Byung Kook Ahn, Young Hoon Cho, Hye Jin Shin, Hoichang Yang, Ungyu Paik, Soongeun Kwon, et al. Selective gas transport through few-layered graphene and graphene oxide membranes. *Science*, 342(6154):91–95, 2013. 43

[262] Seungju Kim, Xiaocheng Lin, Ranwen Ou, Huiyuan Liu, Xiwang Zhang, George P Simon, Christopher D Easton, and Huanting Wang. Highly crosslinked, chlorine tolerant polymer network entwined graphene oxide membrane for water desalination. *Journal of Materials Chemistry A*, 5(4):1533–1540, 2017. 43

[263] Bassel A Abdelkader, Mohamed A Antar, Tahar Laoui, and Zafarullah Khan. Development of graphene oxide-based membrane as a pretreatment for thermal seawater desalination. *Desalination*, 465:13–24, 2019. 43

[264] Yunkyu Choi, Sung-Soo Kim, Ji Hoon Kim, Junhyeok Kang, Eunji Choi, Seung Eun Choi, Jeong Pil Kim, Ohchan Kwon, and Dae Woo Kim. Graphene

oxide nanoribbon hydrogel: Viscoelastic behavior and use as a molecular separation membrane. *ACS nano*, 14(9):12195–12202, 2020. 44

[265] Jie Wang, Minghui Liang, Yan Fang, Tengfei Qiu, Jin Zhang, and Linjie Zhi. Rod-coating: towards large-area fabrication of uniform reduced graphene oxide films for flexible touch screens. *Advanced Materials*, 24(21):2874–2878, 2012. 44

[266] Danial Qadir, Hilmi Mukhtar, and Lau Kok Keong. Mixed matrix membranes for water purification applications. *Separation & Purification Reviews*, 46(1):62–80, 2017. 45

[267] Beatriz Zornoza, Carlos Tellez, Joaquin Coronas, Jorge Gascon, and Freek Kapteijn. Metal organic framework based mixed matrix membranes: An increasingly important field of research with a large application potential. *Microporous and Mesoporous Materials*, 166:67–78, 2013. 45

[268] Libin Yang, Zhan Wang, and Jinglong Zhang. Zeolite imidazolate framework hybrid nanofiltration (nf) membranes with enhanced permselectivity for dye removal. *Journal of membrane science*, 532:76–86, 2017. 45

[269] Rana J Kadhim, Faris H Al-Ani, Muayad Al-Shaeli, Qusay F Alsalhy, and Alberto Figoli. Removal of dyes using graphene oxide (go) mixed matrix membranes. *Membranes*, 10(12):366, 2020. 45, 48, 51, 188

[270] Junjiao Deng, Yi You, Heriberto Bustamante, Veena Sahajwalla, and Rakesh K Joshi. Mechanism of water transport in graphene oxide laminates. *Chemical science*, 8(3):1701–1704, 2017. 45

[271] Baoxia Mi. Graphene oxide membranes for ionic and molecular sieving. *Science*, 343(6172):740–742, 2014. 45

[272] RR Nair, HA Wu, Parthipan N Jayaram, Irina V Grigorieva, and AK Geim. Unimpeded permeation of water through helium-leak–tight graphene-based membranes. *Science*, 335(6067):442–444, 2012. 45

[273] Feng Shi, Jia Niu, Jianlin Liu, Fang Liu, Zhiqiang Wang, X-Q Feng, and Xi Zhang. Towards understanding why a superhydrophobic coating is needed by water striders. *Advanced Materials*, 19(17):2257–2261, 2007. 46

[274] Hongyu Dong, Mengjiao Cheng, Yajun Zhang, Hao Wei, and Feng Shi. Extraordinary drag-reducing effect of a superhydrophobic coating on a macroscopic model ship at high speed. *Journal of Materials Chemistry A*, 1(19):5886–5891, 2013. 46

[275] Hobin Jee, Jaewon Jang, Yesol Kang, Tasnim Eisa, Kyu-Jung Chae, In S Kim, and Euntae Yang. Enhancing the dye-rejection efficiencies and stability of graphene oxide-based nanofiltration membranes via divalent cation intercalation and mild reduction. *Membranes*, 12(4):402, 2022. 46, 153, 182, 187

[276] Kanika Gupta, Sathyam Reddy Yasa, Amzad Khan, Om P Sharma, and Om P Khatri. Charge-driven interaction for adsorptive removal of organic dyes using ionic liquid-modified graphene oxide. *Journal of Colloid and Interface Science*, 607:1973–1985, 2022. 46

[277] Hao Chen, Aiguo Zhong, Junyong Wu, Jie Zhao, and Hua Yan. Adsorption behaviors and mechanisms of methyl orange on heat-treated palygorskite clays. *Industrial & engineering chemistry research*, 51(43):14026–14036, 2012. 47

[278] Alicia Kyoungjin An, Jiaxin Guo, Sanghyun Jeong, Eui-Jong Lee, S Assiyeh Alizadeh Tabatabai, and TorOve Leiknes. High flux and antifouling properties of negatively charged membrane for dyeing wastewater treatment by membrane distillation. *Water Research*, 103:362–371, 2016. 47

[279] Mehdi Mahmoudian and Mahmoud Ghasemi Kochameshki. The performance of polyethersulfone nanocomposite membrane in the removal of industrial dyes. *Polymer*, 224:123693, 2021. 47, 48, 53, 106, 114, 182

[280] Mehran Khansanami and Ali Esfandiar. High flux and complete dyes removal from water by reduced graphene oxide laminate on poly vinylidene fluoride/graphene oxide membranes. *Environmental Research*, 201:111576, 2021. 47, 195

[281] Long Chen, Yanhui Li, Lina Chen, Na Li, Chenglong Dong, Qiong Chen, Beibei Liu, Qing Ai, Pengchao Si, Jinkui Feng, et al. A large-area free-standing graphene oxide multilayer membrane with high stability for nanofiltration applications. *Chemical Engineering Journal*, 345:536–544, 2018. 47, 52

[282] Abdul Ghaffar, Lina Zhang, Xiaoying Zhu, and Baoliang Chen. Porous pvdf/go nanofibrous membranes for selective separation and recycling of charged organic dyes from water. *Environmental science & technology*, 52(7):4265–4274, 2018. 47

[283] Shania Sharif, Khuram Shahzad Ahmad, Fida Hussain Memon, Faisal Rehman, Faheeda Soomro, and Khalid Hussain Thebo. Functionalised graphene oxide-based nanofiltration membranes with enhanced molecular separation performance. *Materials Research Innovations*, pages 1–9, 2021. 47

[284] Yulong Liu, Zhonghua Huang, Zhen Zhang, Xiaolu Lin, Qunxia Li, and Yihang Zhu. A high stability go nanofiltration membrane preparation by co-deposition and crosslinking polydopamine for rejecting dyes. *Water Science and Technology*, 85(6):1783–1799, 2022. 47

[285] AM Hidalgo, M Gómez, MD Murcia, M Serrano, R Rodríguez-Schmidt, and PA Escudero. Behaviour of polysulfone ultrafiltration membrane for dyes removal. *Water Science and Technology*, 77(8):2093–2100, 2018. 48

[286] Yang-ying Zhao, Fan-xin Kong, Zhi Wang, Hong-wei Yang, Xiao-mao Wang, Yue-feng F Xie, and T David Waite. Role of membrane and compound properties in affecting the rejection of pharmaceuticals by different ro/nf membranes. *Frontiers of Environmental Science & Engineering*, 11:1–13, 2017. 48

[287] SS Madaeni. The effect of operating conditions on critical flux in membrane filtration of latexes. *Process safety and environmental protection*, 75(4):266–269, 1997. 48

[288] Erna Yuliwati, Ahmad Fauzi Ismail, Mohd Hafiz Dzarfan Othman, and Mohammad Mahdi A Shirazi. Critical flux and fouling analysis of pvdf-mixed matrix membranes for reclamation of refinery-produced wastewater: Effect of mixed liquor suspended solids concentration and aeration. *Membranes*, 12(2):161, 2022. 48

[289] Patrice Bacchin, Pierre Aimar, and Robert W Field. Critical and sustainable fluxes: theory, experiments and applications. *Journal of membrane science*, 281(1-2):42–69, 2006. 49

[290] Victor F Medina, Christopher S Griggs, Brooke Petery, Jose Mattei-Sosa, Luke Gurtowski, Scott A Waisner, Jay Blodget, and Robert Moser. Fabrication, characterization, and testing of graphene oxide and hydrophilic polymer graphene oxide composite membranes in a dead-end flow system. *Journal of Environmental Engineering*, 143(11):04017072, 2017. 49

[291] Arlindo Caniço Gomes, Isolina Cabral Gonçalves, and Maria Norberta de Pinho. The role of adsorption on nanofiltration of azo dyes. *Journal of Membrane Science*, 255(1-2):157–165, 2005. 50

[292] Jian Huang and Kaisong Zhang. The high flux poly (m-phenylene isophthala-

mide) nanofiltration membrane for dye purification and desalination. *Desalination*, 282:19–26, 2011. 50

[293] Xiuzhen Wei, Songxue Wang, Yingying Shi, Hai Xiang, and Jinyuan Chen. Application of positively charged composite hollow-fiber nanofiltration membranes for dye purification. *Industrial & Engineering Chemistry Research*, 53(36):14036–14045, 2014. 50

[294] Meng Li, Xi Wang, Cassandra J Porter, Wei Cheng, Xuan Zhang, Lianjun Wang, and Menachem Elimelech. Concentration and recovery of dyes from textile wastewater using a self-standing, support-free forward osmosis membrane. *Environmental science & technology*, 53(6):3078–3086, 2019. 50

[295] Lu Shao, Xi Quan Cheng, Yang Liu, Shuai Quan, Jun Ma, Shu Zhen Zhao, and Kai Yu Wang. Newly developed nanofiltration (nf) composite membranes by interfacial polymerization for safranin o and aniline blue removal. *Journal of Membrane Science*, 430:96–105, 2013. 50

[296] Natália Cândido Homem, Natália de Camargo Lima Beluci, Sara Amorim, Rui Reis, Angélica Marquetotti Salcedo Vieira, Marcelo Fernandes Vieira, Rosângela Bergamasco, and Maria Teresa Pessoa Amorim. Surface modification of a polyethersulfone microfiltration membrane with graphene oxide for reactive dyes removal. *Applied Surface Science*, 486:499–507, 2019. 50, 190

[297] Chao Xing, Jing Han, Xin Pei, Yuting Zhang, Jing He, Rong Huang, Suhong Li, Changyu Liu, Chao Lai, Lingdi Shen, et al. Tunable graphene oxide nanofiltration membrane for effective dye/salt separation and desalination. *ACS Applied Materials & Interfaces*, 13(46):55339–55348, 2021. 50

[298] Long Chen, Na Li, Ziyan Wen, Lin Zhang, Qiong Chen, Lina Chen, Pengchao Si, Jinkui Feng, Yanhui Li, Jun Lou, et al. Graphene oxide based membrane interca-

lated by nanoparticles for high performance nanofiltration application. *Chemical Engineering Journal*, 347:12–18, 2018. 50

[299] Weiming Zhong, Yuyu Zhang, Ling Zhao, and Wanbin Li. Highly stable and antifouling graphene oxide membranes prepared by bio-inspired modification for water purification. *Chinese Chemical Letters*, 31(10):2651–2656, 2020. 51

[300] Y You, XH Jin, XY Wen, V Sahajwalla, V Chen, H Bustamante, and RK Joshi. Application of graphene oxide membranes for removal of natural organic matter from water. *Carbon*, 129:415–419, 2018. 51

[301] Khalid Hussain Thebo, Xitang Qian, Qing Zhang, Long Chen, Hui-Ming Cheng, and Wencai Ren. Highly stable graphene-oxide-based membranes with superior permeability. *Nature communications*, 9(1):1–8, 2018. 52

[302] Liang Huang, Ji Chen, Tiantian Gao, Miao Zhang, Yingru Li, Liming Dai, Liangti Qu, and Gaoquan Shi. Reduced graphene oxide membranes for ultrafast organic solvent nanofiltration. *Advanced Materials*, 28(39):8669–8674, 2016. 52

[303] Usman Mohammed Aliyu, Sudesh Rathilal, and Yusuf Makarfi Isa. Membrane desalination technologies in water treatment: A review. *Water Practice & Technology*, 13(4):738–752, 2018. 53

[304] Rohan S Dassanayake, Sanjit Acharya, and Noureddine Abidi. Recent advances in biopolymer-based dye removal technologies. *Molecules*, 26(15):4697, 2021. 53

[305] Gheorghe Falca, Valentina-Elena Musteata, Ali Reza Behzad, Stefan Chisca, and Suzana Pereira Nunes. Cellulose hollow fibers for organic resistant nanofiltration. *Journal of Membrane Science*, 586:151–161, 2019. 53

[306] Anouar Ben Fradj, Ali Boubakri, Amor Hafiane, and Sofiane Ben Hamouda.

Removal of azoic dyes from aqueous solutions by chitosan enhanced ultrafiltration. *Results in Chemistry*, 2:100017, 2020. 53

[307] Teboho Clement Mokhena and Adriaan Stephanus Luyt. Development of multifunctional nano/ultrafiltration membrane based on a chitosan thin film on alginate electrospun nanofibres. *Journal of Cleaner Production*, 156:470–479, 2017. 53

[308] Arfa Iqbal, Emre Cevik, Omar Alagha, and Ayhan Bozkurt. Highly robust multilayer nanosheets with ultra-efficient batch adsorption and gravity-driven filtration capability for dye removal. *Journal of Industrial and Engineering Chemistry*, 109:287–295, 2022. 53

[309] PR Yaashikaa, P Senthil Kumar, and S Karishma. Review on biopolymers and composites–evolving material as adsorbents in removal of environmental pollutants. *Environmental Research*, 212:113114, 2022. 54

[310] Yifan Cui, Qingfen Ma, Zhongye Wu, Hui Lu, Zezhou Gao, and Junqing Fan. A hydrostatic pressure-driven desalination system for large-scale deep sea space station. *International Journal of Chemical Engineering*, 2021, 2021. 54

[311] Xiuqiang Li, Bin Zhu, and Jia Zhu. Graphene oxide based materials for desalination. *Carbon*, 146:320–328, 2019. 54

[312] Francis G Donnan. Theorie der membrangleichgewichte und membranpotentiale bei vorhandensein von nicht dialysierenden elektrolyten. ein beitrag zur physikalisch-chemischen physiologie. *Zeitschrift für Elektrochemie und angewandte physikalische Chemie*, 17(14):572–581, 1911. 55

[313] Frederick George Donnan. The theory of membrane equilibria. *Chemical reviews*, 1(1):73–90, 1924. 55

[314] Cunzhi Zhang, Federico Giberti, Emre Sevgen, Juan J de Pablo, Francois Gygi, and Giulia Galli. Dissociation of salts in water under pressure. *Nature communications*, 11(1):1–9, 2020. 55

[315] Razi Epsztein, Evyatar Shaulsky, Nadir Dizge, David M Warsinger, and Menachem Elimelech. Role of ionic charge density in donnan exclusion of monovalent anions by nanofiltration. *Environmental science & technology*, 52(7):4108–4116, 2018. 55

[316] Amaia Lejarazu-Larrañaga, Juan M Ortiz, Serena Molina, Sylwin Pawlowski, Claudia F Galinha, Vanessa Otero, Eloy García-Calvo, Svetlozar Velizarov, and João G Crespo. Nitrate removal by donnan dialysis and anion-exchange membrane bioreactor using upcycled end-of-life reverse osmosis membranes. *Membranes*, 12(2):101, 2022. 55

[317] Yi Han, Zhen Xu, and Chao Gao. Ultrathin graphene nanofiltration membrane for water purification. *Advanced Functional Materials*, 23(29):3693–3700, 2013. 55, 60, 202, 209

[318] Johan Schaep, Bart Van der Bruggen, Carlo Vandecasteele, and Dirk Wilms. Influence of ion size and charge in nanofiltration. *Separation and Purification Technology*, 14(1-3):155–162, 1998. 55

[319] Gonggang Liu, Hongqi Ye, Antai Li, Chenyuan Zhu, Heng Jiang, Yong Liu, Kai Han, and Yonghua Zhou. Graphene oxide for high-efficiency separation membranes: Role of electrostatic interactions. *Carbon*, 110:56–61, 2016. 55

[320] Chong Luo, Che-Ning Yeh, Jesus M Lopez Baltazar, Chao-Lin Tsai, and Jiaxing Huang. A cut-and-paste approach to 3d graphene-oxide-based architectures. *Advanced Materials*, 30(15):1706229, 2018. 55

[321] Zhenxing Wang, Fang He, Jing Guo, Shaoqin Peng, Xi Quan Cheng, Yingjie Zhang, Enrico Drioli, Alberto Figoli, Yuexiang Li, and Lu Shao. The stability of a graphene oxide (go) nanofiltration (nf) membrane in an aqueous environment: Progress and challenges. *Materials Advances*, 1(4):554–568, 2020. 56

[322] Renlong Liu, Girish Arabale, Jinseon Kim, Ke Sun, Yongwoon Lee, Changkook Ryu, and Changgu Lee. Graphene oxide membrane for liquid phase organic molecular separation. *Carbon*, 77:933–938, 2014. 56

[323] Zhiqian Jia, Yan Wang, Weixing Shi, and Jianli Wang. Diamines cross-linked graphene oxide free-standing membranes for ion dialysis separation. *Journal of Membrane Science*, 520:139–144, 2016. 56, 57

[324] EA Guertal and JA Hattey. A scale model of cation exchange for classroom demonstration. *Journal of Natural Resources and Life Sciences Education*, 25(2):125–127, 1996. 56, 219

[325] Karl W Putz, Owen C Compton, Claire Segar, Zhi An, SonBinh T Nguyen, and L Catherine Brinson. Evolution of order during vacuum-assisted self-assembly of graphene oxide paper and associated polymer nanocomposites. *Acs Nano*, 5(8):6601–6609, 2011. 57

[326] Yinghui Mo, Xin Zhao, and Yue-xiao Shen. Cation-dependent structural instability of graphene oxide membranes and its effect on membrane separation performance. *Desalination*, 399:40–46, 2016. 57

[327] Ruirui Hu, Guoke Zhao, Yijia He, and Hongwei Zhu. The application feasibility of graphene oxide membranes for pressure-driven desalination in a dead-end flow system. *Desalination*, 477:114271, 2020. 57, 215, 218, 219

[328] Baoxia Mi. Scaling up nanoporous graphene membranes. *Science*, 364(6445):1033–1034, 2019. 57

[329] Jijo Abraham, Kalangi S Vasu, Christopher D Williams, Kalon Gopinadhan, Yang Su, Christie T Cherian, James Dix, Eric Prestat, Sarah J Haigh, Irina V Grigorieva, et al. Tunable sieving of ions using graphene oxide membranes. *Nature nanotechnology*, 12(6):546–550, 2017. 57

[330] Hengyu Yang, Naixin Wang, Lin Wang, Hong-Xia Liu, Quan-Fu An, and Shulan Ji. Vacuum-assisted assembly of zif-8@ go composite membranes on ceramic tube with enhanced organic solvent nanofiltration performance. *Journal of Membrane Science*, 545:158–166, 2018. 57

[331] Zhiqian Jia and Yan Wang. Covalently crosslinked graphene oxide membranes by esterification reactions for ions separation. *Journal of Materials Chemistry A*, 3(8):4405–4412, 2015. 57

[332] Takafumi Aizawa and Yoshito Wakui. Correlation between the porosity and permeability of a polymer filter fabricated via co2-assisted polymer compression. *Membranes*, 10(12):391, 2020. 57

[333] Georgy Kagramanov, Vladimir Gurkin, and Elena Farnosova. Physical and mechanical properties of hollow fiber membranes and technological parameters of the gas separation process. *Membranes*, 11(8):583, 2021. 57

[334] Haiwei Dai, Zhijun Xu, and Xiaoning Yang. Water permeation and ion rejection in layer-by-layer stacked graphene oxide nanochannels: a molecular dynamics simulation. *The Journal of Physical Chemistry C*, 120(39):22585–22596, 2016. 58, 211

[335] Qi Chen and Xiaoning Yang. Pyridinic nitrogen doped nanoporous graphene as desalination membrane: molecular simulation study. *Journal of Membrane Science*, 496:108–117, 2015. 58

[336] Hubiao Huang, Zhigong Song, Ning Wei, Li Shi, Yiyin Mao, Yulong Ying, Luwei Sun, Zhiping Xu, and Xinsheng Peng. Ultrafast viscous water flow through nanostrand-channelled graphene oxide membranes. *Nature communications*, 4(1):1–9, 2013. 58, 211

[337] Hubiao Huang, Yiyin Mao, Yulong Ying, Yu Liu, Luwei Sun, and Xinsheng Peng. Salt concentration, ph and pressure controlled separation of small molecules through lamellar graphene oxide membranes. *Chemical Communications*, 49(53):5963–5965, 2013. 58, 59, 209

[338] Wanbin Li, Wufeng Wu, and Zhanjun Li. Controlling interlayer spacing of graphene oxide membranes by external pressure regulation. *Acs Nano*, 12(9):9309–9317, 2018. 59

[339] Yang Li, Wang Zhao, Matthew Weyland, Shi Yuan, Yun Xia, Huiyuan Liu, Meipeng Jian, Jindi Yang, Christopher D Easton, Cordelia Selomulya, et al. Thermally reduced nanoporous graphene oxide membrane for desalination. *Environmental science & technology*, 53(14):8314–8323, 2019. 59

[340] Mingzhan Wang, Xiang He, Eli Hoenig, Gangbin Yan, Guiming Peng, Fengyuan Shi, Julia Radhakrishnan, Grant Hill, David M Tiede, Hua Zhou, et al. Tuning transport in graphene oxide membrane with single-site copper (ii) cations. *Iscience*, 25(4):104044, 2022. 60

[341] Yi Han, Yanqiu Jiang, and Chao Gao. High-flux graphene oxide nanofiltration membrane intercalated by carbon nanotubes. *ACS applied materials & interfaces*, 7(15):8147–8155, 2015. 60

[342] Aaron Morelos-Gomez, Rodolfo Cruz-Silva, Hiroyuki Muramatsu, Josue Ortiz-Medina, Takumi Araki, Tomoyuki Fukuyo, Syogo Tejima, Kenji Takeuchi, Takuya Hayashi, Mauricio Terrones, et al. Effective nacl and dye rejection of

hybrid graphene oxide/graphene layered membranes. *Nature nanotechnology*, 12(11):1083–1088, 2017. 60, 219

[343] Zhanguo Li, Yi Wang, Mengwei Han, Dayong Wang, Shitong Han, Zequn Liu, Ningyu Zhou, Ran Shang, and Chaoxin Xie. Graphene oxide incorporated forward osmosis membranes with enhanced desalination performance and chlorine resistance. *Frontiers in Chemistry*, 7:877, 2020. 60

[344] Bin Liang, Wu Zhan, Genggeng Qi, Sensen Lin, Qian Nan, Yuxuan Liu, Bing Cao, and Kai Pan. High performance graphene oxide/polyacrylonitrile composite pervaporation membranes for desalination applications. *Journal of Materials Chemistry A*, 3(9):5140–5147, 2015. 60, 213

[345] Xiaowei Qian, Na Li, Qinzhuo Wang, and Songcan Ji. Chitosan/graphene oxide mixed matrix membrane with enhanced water permeability for high-salinity water desalination by pervaporation. *Desalination*, 438:83–96, 2018. 61

[346] Xinglin Lu and Menachem Elimelech. Fabrication of desalination membranes by interfacial polymerization: history, current efforts, and future directions. *Chemical Society Reviews*, 50(11):6290–6307, 2021. 61

[347] Dan Li and Huanting Wang. Recent developments in reverse osmosis desalination membranes. *Journal of Materials Chemistry*, 20(22):4551–4566, 2010. 61

[348] Viatcheslav Freger and Guy Z Ramon. Polyamide desalination membranes: Formation, structure, and properties. *Progress in Polymer Science*, 122:101451, 2021. 61

[349] Zi-Ming Zhan, Xin Zhang, Yin-Xin Fang, Yong-Jian Tang, Ka-Ke Zhu, Xiao-Hua Ma, and Zhen-Liang Xu. Polyamide nanofiltration membranes with enhanced desalination and antifouling performance enabled by surface grafting

polyquaternium-7. *Industrial & Engineering Chemistry Research*, 60(39):14297–14306, 2021. 61

[350] Zhiwei Jiang, Santanu Karan, and Andrew G Livingston. Water transport through ultrathin polyamide nanofilms used for reverse osmosis. *Advanced Materials*, 30(15):1705973, 2018. 62

[351] Yue Wen, Ruobin Dai, Xuesong Li, Xingran Zhang, Xingzhong Cao, Zhichao Wu, Shihong Lin, Chuyang Y Tang, and Zhiwei Wang. Metal-organic framework enables ultraselective polyamide membrane for desalination and water reuse. *Science advances*, 8(10):eabm4149, 2022. 62

[352] Mohammed Kadhom and Baolin Deng. Metal-organic frameworks (mofs) in water filtration membranes for desalination and other applications. *Applied Materials Today*, 11:219–230, 2018. 62

[353] Mohammed Kadhom and Baolin Deng. Metal-organic frameworks uio-66 and mil-125 nanoparticles enhance the performance of thin film nanocomposite membrane for water desalination. In *2017 AIChE Annual Meeting*. AIChE, 2017. 62

[354] Yuan Xu, Xueli Gao, Xiaojuan Wang, Qun Wang, Zhiyong Ji, Xinyan Wang, Tao Wu, and Congjie Gao. Highly and stably water permeable thin film nanocomposite membranes doped with mil-101 (cr) nanoparticles for reverse osmosis application. *Materials*, 9(11):870, 2016. 62

[355] Ben Corry. Designing carbon nanotube membranes for efficient water desalination. *The Journal of Physical Chemistry B*, 112(5):1427–1434, 2008. 62

[356] Wai-Fong Chan, Hang-yan Chen, Anil Surapathi, Michael G Taylor, Xiaohong Shao, Eva Marand, and J Karl Johnson. Zwitterion functionalized carbon nanotube/polyamide nanocomposite membranes for water desalination. *Acs Nano*, 7(6):5308–5319, 2013. 62

[357] Shang-Ru Tsai and Michael R Hamblin. Biological effects and medical applications of infrared radiation. *Journal of Photochemistry and Photobiology B: Biology*, 170:197–207, 2017. 70

[358] Glen Fox. The brewing industry and the opportunities for real-time quality analysis using infrared spectroscopy. *Applied Sciences*, 10(2):616, 2020. 70

[359] Sevgi Türker-Kaya and Christian W Huck. A review of mid-infrared and near-infrared imaging: principles, concepts and applications in plant tissue analysis. *Molecules*, 22(1):168, 2017. 70

[360] Wenji Guo, Jianbo Chen, Suqin Sun, and Qun Zhou. In situ monitoring the molecular diffusion process in graphene oxide membranes by atr-ftir spectroscopy. *The Journal of Physical Chemistry C*, 120(13):7451–7456, 2016. 70

[361] Jiang-Bin Wu, Miao-Ling Lin, Xin Cong, He-Nan Liu, and Ping-Heng Tan. Raman spectroscopy of graphene-based materials and its applications in related devices. *Chemical Society Reviews*, 47(5):1822–1873, 2018. 71

[362] John William Strutt. Lviii. on the scattering of light by small particles. *The London, Edinburgh, and Dublin Philosophical Magazine and Journal of Science*, 41(275):447–454, 1871. 71

[363] Chandrasekhara Venkata Raman and Kariamanikkam Srinivasa Krishnan. A new type of secondary radiation. *Nature*, 121(3048):501–502, 1928. 71

[364] Robin R Jones, David C Hooper, Liwu Zhang, Daniel Wolverson, and Ventsislav K Valev. Raman techniques: fundamentals and frontiers. *Nanoscale research letters*, 14(1):1–34, 2019. 71, 72

[365] Horiba Jobin Yvon. Raman spectroscopy for analysis

and monitoring. *nd). Retrieved from http://www. horiba. com/fileadmin/uploads/Scientific/Documents/Raman/bands. pdf*, 2017. 72

[366] Dominique B Schuepfer, Felix Badaczewski, Juan Manuel Guerra-Castro, Detlev M Hofmann, Christian Heiliger, Bernd Smarsly, and Peter J Klar. Assessing the structural properties of graphitic and non-graphitic carbons by raman spectroscopy. *Carbon*, 161:359–372, 2020. 72

[367] Fred A Stevie and Carrie L Donley. Introduction to x-ray photoelectron spectroscopy. *Journal of Vacuum Science & Technology A: Vacuum, Surfaces, and Films*, 38(6):063204, 2020. 73, 75

[368] David Briggs. Practical surface analysis. *Auger and X-Ray Photoelecton Spectroscory*, 1:151–152, 1990. 73

[369] Albert Einstein. Über einem die erzeugung und verwandlung des lichtes betreffenden heuristischen gesichtspunkt. *Annalen der physik*, 4, 1905. 74

[370] Mark A Isaacs, Josh Davies-Jones, Philip R Davies, Shaoliang Guan, Roxy Lee, David J Morgan, and Robert Palgrave. Advanced xps characterization: Xps-based multi-technique analyses for comprehensive understanding of functional materials. *Materials Chemistry Frontiers*, 5(22):7931–7963, 2021. 75

[371] L Torrisi, L Silipigni, M Cutroneo, and A Torrisi. Graphene oxide as a radiation sensitive material for xps dosimetry. *Vacuum*, 173:109175, 2020. 75

[372] Thomas R Gengenbach, George H Major, Matthew R Linford, and Christopher D Easton. Practical guides for x-ray photoelectron spectroscopy (xps): Interpreting the carbon 1s spectrum. *Journal of Vacuum Science & Technology A: Vacuum, Surfaces, and Films*, 39(1):013204, 2021. 75

[373] Donald R Baer, Kateryna Artyushkova, Hagai Cohen, Christopher D Easton, Mark Engelhard, Thomas R Gengenbach, Grzegorz Greczynski, Paul Mack, David J Morgan, and Adam Roberts. Xps guide: Charge neutralization and binding energy referencing for insulating samples. *Journal of Vacuum Science & Technology A: Vacuum, Surfaces, and Films*, 38(3):031204, 2020. 76, 77

[374] De Fang, Feng He, Junlin Xie, and Lihui Xue. Calibration of binding energy positions with c1s for xps results. *Journal of Wuhan University of Technology-Mater. Sci. Ed.*, 35(4):711–718, 2020. 77

[375] R Al-Gaashani, A Najjar, Y Zakaria, S Mansour, and MA Atieh. Xps and structural studies of high quality graphene oxide and reduced graphene oxide prepared by different chemical oxidation methods. *Ceramics International*, 45(11):14439–14448, 2019. 77

[376] Soo-Jin Park and Min-Kang Seo. Solid-gas interaction. In *Interface Science and Technology*, volume 18, pages 59–145. Elsevier, 2011. 78

[377] Yih Horng Tan, Jason A Davis, Kohki Fujikawa, N Vijaya Ganesh, Alexei V Demchenko, and Keith J Stine. Surface area and pore size characteristics of nanoporous gold subjected to thermal, mechanical, or surface modification studied using gas adsorption isotherms, cyclic voltammetry, thermogravimetric analysis, and scanning electron microscopy. *Journal of materials chemistry*, 22(14):6733–6745, 2012. 78

[378] Stephen Brunauer, Paul Hugh Emmett, and Edward Teller. Adsorption of gases in multimolecular layers. *Journal of the American chemical society*, 60(2):309–319, 1938. 78

[379] WA Steele, G Zgrablich, and W Rudzinski. *Equilibria and dynamics of gas adsorption on heterogeneous solid surfaces*. Elsevier, 1996. 78

[380] Michel Che and Jacques C Védrine. *Characterization of solid materials and heterogeneous catalysts: From structure to surface reactivity*. John Wiley & Sons, 2012. 78

[381] Filip Ambroz, Thomas J Macdonald, Vladimir Martis, and Ivan P Parkin. Evaluation of the bet theory for the characterization of meso and microporous mofs. *Small methods*, 2(11):1800173, 2018. 79

[382] Matthias Thommes, Katsumi Kaneko, Alexander V Neimark, James P Olivier, Francisco Rodriguez-Reinoso, Jean Rouquerol, and Kenneth SW Sing. Physisorption of gases, with special reference to the evaluation of surface area and pore size distribution (iupac technical report). *Pure and applied chemistry*, 87(9-10):1051–1069, 2015. 79

[383] Seymour Lowell and Joan E Shields. *Powder surface area and porosity*, volume 2. Springer Science & Business Media, 1991. 79

[384] Simon J Blott, Debra J Croft, Kenneth Pye, Samantha E Saye, and Helen E Wilson. Particle size analysis by laser diffraction. *Geological Society, London, Special Publications*, 232(1):63–73, 2004. 79

[385] Jörg Stetefeld, Sean A McKenna, and Trushar R Patel. Dynamic light scattering: a practical guide and applications in biomedical sciences. *Biophysical reviews*, 8(4):409–427, 2016. 79, 80

[386] Nicolas Bonod and Jérôme Neauport. Diffraction gratings: from principles to applications in high-intensity lasers. *Advances in Optics and Photonics*, 8(1):156–199, 2016. 80

[387] Thomas Wriedt. Mie theory: a review. *The Mie Theory*, pages 53–71, 2012. 80

[388] Craig F Bohren and Donald R Huffman. *Absorption and scattering of light by small particles*. John Wiley & Sons, 2008. 80

[389] David W Hahn. Light scattering theory. *Department of Mechanical and Aerospace Engineering, University of Florida*, 2009. 80

[390] Selda Murat Hocaoglu and Derin Orhon. Particle size distribution analysis of chemical oxygen demand fractions with different biodegradation characteristics in black water and gray water. *CLEAN–Soil, Air, Water*, 41(11):1044–1051, 2013. 80

[391] Albert Einstein. *Investigations on the Theory of the Brownian Movement*. Courier Corporation, 1956. 80

[392] Katherine Kornei. Particles stratify by size in thin films. *Physics*, 9:30, 2016. 81

[393] R Shaw. Dynamic light scattering training achieving reliable nano particle sizing.[online] 149.171. 168.221, 2018. 81

[394] Dennis E Koppel. Analysis of macromolecular polydispersity in intensity correlation spectroscopy: the method of cumulants. *The Journal of Chemical Physics*, 57(11):4814–4820, 1972. 81, 82

[395] Barbara J Frisken. Revisiting the method of cumulants for the analysis of dynamic light-scattering data. *Applied optics*, 40(24):4087–4091, 2001. 82

[396] Veronika Schmiedova, Jan Pospisil, Alexander Kovalenko, Petr Ashcheulov, Ladislav Fekete, Tomas Cubon, Peter Kotrusz, Oldrich Zmeskal, and Martin Weiter. Physical properties investigation of reduced graphene oxide thin films prepared by material inkjet printing. *Journal of Nanomaterials*, 2017, 2017. 82

[397] Matthew A Brown, Guilherme Volpe Bossa, and Sylvio May. Emergence of a stern

layer from the incorporation of hydration interactions into the gouy–chapman model of the electrical double layer. *Langmuir*, 31(42):11477–11483, 2015. 82

[398] Daniel R Grisham and Vikas Nanda. Hydrodynamic radius coincides with the slip plane position in the electrokinetic behavior of lysozyme. *Proteins: Structure, Function, and Bioinformatics*, 86(5):515–523, 2018. 83

[399] Robert J Hunter. *Zeta potential in colloid science: principles and applications*, volume 2. Academic press, 2013. 83

[400] Angel V Delgado, Fernando González-Caballero, RJ Hunter, Luuk K Koopal, and J Lyklema. Measurement and interpretation of electrokinetic phenomena (iupac technical report). *Pure and Applied Chemistry*, 77(10):1753–1805, 2005. 83

[401] James W Swan and Eric M Furst. A simpler expression for henry's function describing the electrophoretic mobility of spherical colloids. *Journal of colloid and interface science*, 388(1):92–94, 2012. 84

[402] DC Henry. The cataphoresis of suspended particles. part i.—the equation of cataphoresis. *Proceedings of the Royal Society of London. Series A, Containing Papers of a Mathematical and Physical Character*, 133(821):106–129, 1931. 84

[403] M von Smoluchowski. Handbuch der elektrizität und des magnetismus. *Band II, Barth-Verlag, Leipzig*, pages 366–427, 1921. 84

[404] Ratna Tantra, Philipp Schulze, and Paul Quincey. Effect of nanoparticle concentration on zeta-potential measurement results and reproducibility. *Particuology*, 8(3):279–285, 2010. 84

[405] Daniel José Pochapski, Caio Carvalho dos Santos, Gabriel Wosiak Leite, Sandra Helena Pulcinelli, and Celso Valentim Santilli. Zeta potential and colloidal

stability predictions for inorganic nanoparticle dispersions: Effects of experimental conditions and electrokinetic models on the interpretation of results. *Langmuir*, 37(45):13379–13389, 2021. 84

[406] Siqi Shen, Shengke Yang, Qianli Jiang, Mengya Luo, Yu Li, Chunyan Yang, and Dan Zhang. Effect of dissolved organic matter on adsorption of sediments to oxytetracycline: An insight from zeta potential and dlvo theory. *Environmental Science and Pollution Research*, 27(2):1697–1709, 2020. 85

[407] Jin Wang, Yanxin Li, Dan Zheng, Hrvoje Mikulčić, Milan Vujanović, and Bengt Sundén. Preparation and thermophysical property analysis of nanocomposite phase change materials for energy storage. *Renewable and Sustainable Energy Reviews*, 151:111541, 2021. 86

[408] Tomáš Sitek, Jiří Pospíšil, Ján Poláčik, and Radomír Chỳlek. Thermogravimetric analysis of solid biomass fuels and corresponding emission of fine particles. *Energy*, 237:121609, 2021. 86

[409] Claudio Ferdeghini, Lorenzo Guazzelli, Christian S Pomelli, Andrea Ciccioli, Bruno Brunetti, Andrea Mezzetta, and Stefano Vecchio Ciprioti. Synthesis, thermal behavior and kinetic study of n-morpholinium dicationic ionic liquids by thermogravimetry. *Journal of Molecular Liquids*, 332:115662, 2021. 86

[410] Manisha Chakraborty, Anubha Dey, and Ashis Bhattacharjee. Insights into the thermal decomposition of organometallic compound ferrocene carboxaldehyde as precursor for hematite nanoparticles synthesis. *Zeitschrift für Physikalische Chemie*, 2022. 86

[411] Amani Al-Othman, Paul Nancarrow, Muhammad Tawalbeh, Ahmad Ka'ki, Karim El-Ahwal, Bassam El Taher, and Malek Alkasrawi. Novel composite mem-

brane based on zirconium phosphate-ionic liquids for high temperature pem fuel cells. *International Journal of Hydrogen Energy*, 46(8):6100–6109, 2021. 86

[412] Dipeshkumar D Kachhadiya and ZVP Murthy. Graphene oxide modified cubtc incorporated pvdf membranes for saltwater desalination via pervaporation. *Separation and Purification Technology*, 290:120888, 2022. 86

[413] Dorothee Liebschner, Pavel V Afonine, Matthew L Baker, Gábor Bunkóczi, Vincent B Chen, Tristan I Croll, Bradley Hintze, L-W Hung, Swati Jain, Airlie J McCoy, et al. Macromolecular structure determination using x-rays, neutrons and electrons: recent developments in phenix. *Acta Crystallographica Section D: Structural Biology*, 75(10):861–877, 2019. 87

[414] Yvonne M Mos, Arnold C Vermeulen, Cees JN Buisman, and Jan Weijma. X-ray diffraction of iron containing samples: the importance of a suitable configuration. *Geomicrobiology Journal*, 35(6):511–517, 2018. 87

[415] RE Dinnebier and SJL Billinge. The bragg equation derived. 2019. 87

[416] Rolf Behling. *Modern diagnostic x-ray sources: technology, manufacturing, reliability*. CRC Press, 2021. 88

[417] Marcus H Mendenhall, Lawrence T Hudson, Csilla I Szabo, Albert Henins, and James P Cline. The molybdenum k-shell x-ray emission spectrum. *Journal of Physics B: Atomic, Molecular and Optical Physics*, 52(21):215004, 2019. 89

[418] Pietro Guccione, Mattia Lopresti, Marco Milanesio, and Rocco Caliandro. Multivariate analysis applications in x-ray diffraction. *Crystals*, 11(1):12, 2020. 89

[419] Maks Merela, Nejc Thaler, Angela Balzano, and Denis Plavčak. Optimal surface preparation for wood anatomy research of invasive species by scanning electron microscopy. *Drvna industrija*, 71(2):117–127, 2020. 90

[420] Anwar Ul-Hamid. *A beginners' guide to scanning electron microscopy*, volume 1. Springer, 2018. 90, 91

[421] Gerwin Dijk, Alexandra L Rutz, and George G Malliaras. Stability of pedot: Pss-coated gold electrodes in cell culture conditions. *Advanced Materials Technologies*, 5(3):1900662, 2020. 91

[422] Azad Mohammed and Avin Abdullah. Scanning electron microscopy (sem): A review. In *Proceedings of the 2018 International Conference on Hydraulics and Pneumatics—HERVEX, Băile Govora, Romania*, pages 7–9, 2018. 91, 93

[423] VV Zabrodsky, SV Zaitsev, V Yu Karaulov, EI Rau, VA Smolyar, and EV Sherstnev. Angular and energy characteristics of backscattered electrons and allowing for them in the three-dimensional visualization of microstructures in scanning electron microscopy. *Bulletin of the Russian Academy of Sciences: Physics*, 83(11):1357–1365, 2019. 91

[424] Vasily N Lednev, Pavel A Sdvizhenskii, Roman D Asyutin, Roman S Tretyakov, Mikhail Ya Grishin, Anton Ya Stavertiy, and Sergey M Pershin. In situ multi-elemental analysis by laser induced breakdown spectroscopy in additive manufacturing. *additive manufacturing*, 25:64–70, 2019. 91

[425] Joseph I Goldstein, Dale E Newbury, Joseph R Michael, Nicholas WM Ritchie, John Henry J Scott, and David C Joy. *Scanning electron microscopy and X-ray microanalysis*. Springer, 2017. 92

[426] Pavel Potocek, Patrick Trampert, Maurice Peemen, Remco Schoenmakers, and Tim Dahmen. Sparse scanning electron microscopy data acquisition and deep neural networks for automated segmentation in connectomics. *Microscopy and Microanalysis*, 26(3):403–412, 2020. 92

[427] Mohammad Yeakub Ali, Wayne Hung, and Fu Yongqi. A review of focused ion beam sputtering. *International journal of precision engineering and manufacturing*, 11(1):157–170, 2010. 94

[428] Lucille A Giannuzzi and Frederick A Stevie. A review of focused ion beam milling techniques for tem specimen preparation. *Micron*, 30(3):197–204, 1999. 94

[429] BI Prenitzer, CA Urbanik-Shannon, LA Giannuzzi, SR Brown, RB Irwin, TL Shofner, and FA Stevie. The correlation between ion beam/material interactions and practical fib specimen preparation. *Microscopy and Microanalysis*, 9(3):216–236, 2003. 94

[430] C Kizilyaprak, J Daraspe, and BM Humbel. Focused ion beam scanning electron microscopy in biology. *Journal of microscopy*, 254(3):109–114, 2014. 94

[431] M Ritter, M Hemmleb, B Lich, P Faber, and H Hohenberg. Sem/fib stage calibration with photogrammetric methods. In *ISPRS Commission V Symp. 2006 (Int. Archives of Photogrammetry, Remote Sensing and Spatial Information Sciences)*, volume 36. Citeseer, 2006. 94

[432] Valentina Baena, Ryan Conrad, Patrick Friday, Ella Fitzgerald, Taeeun Kim, John Bernbaum, Heather Berensmann, Adam Harned, Kunio Nagashima, and Kedar Narayan. Fib-sem as a volume electron microscopy approach to study cellular architectures in sars-cov-2 and other viral infections: A practical primer for a virologist. *Viruses*, 13(4):611, 2021. 95

[433] Che-Ning Yeh, Kalyan Raidongia, Jiaojing Shao, Quan-Hong Yang, and Jiaxing Huang. On the origin of the stability of graphene oxide membranes in water. *Nature chemistry*, 7(2):166–170, 2015. 95

[434] Parisa Sadat Parsamehr, Marzieh Zahed, Maryam Ahmadzadeh Tofighy, Toraj Mohammadi, and Mashallah Rezakazemi. Preparation of novel cross-linked

graphene oxide membrane for desalination applications using (edc and nhs)-activated graphene oxide and pei. *Desalination*, 468:114079, 2019. 95

[435] Thomas Young. Iii. an essay on the cohesion of fluids. *Philosophical transactions of the royal society of London*, (95):65–87, 1805. 96

[436] Robert J Good. Contact angle, wetting, and adhesion: a critical review. *Journal of adhesion science and technology*, 6(12):1269–1302, 1992. 97

[437] John D Bernardin, Issam Mudawar, Christopher B Walsh, and Elias I Franses. Contact angle temperature dependence for water droplets on practical aluminum surfaces. *International journal of heat and mass transfer*, 40(5):1017–1033, 1997. 97

[438] Sanjay S Latthe, Chiaki Terashima, Kazuya Nakata, and Akira Fujishima. Superhydrophobic surfaces developed by mimicking hierarchical surface morphology of lotus leaf. *Molecules*, 19(4):4256–4283, 2014. 97

[439] N Slepickova Kasalkova, Petr Slepicka, Zdenka Kolska, and Vaclav Svorcik. Wettability and other surface properties of modified polymers. *Wetting Wettability*, 12:323–356, 2015. 97

[440] Jaroslaw Drelich. Guidelines to measurements of reproducible contact angles using a sessile-drop technique. *Surface innovations*, 1(4):248–254, 2013. 97

[441] Hailong Liu and Guoxin Cao. Effectiveness of the young-laplace equation at nanoscale. *Scientific reports*, 6(1):1–10, 2016. 97

[442] S Chaiyakun, N Witit-Anun, N Nuntawong, P Chindaudom, S Oaew, C Kedkeaw, P Limsuwan, et al. Preparation and characterization of graphene oxide nanosheets. *Procedia Engineering*, 32:759–764, 2012. 100

[443] Leila Shahriary and Anjali A Athawale. Graphene oxide synthesized by using modified hummers approach. *Int. J. Renew. Energy Environ. Eng*, 2(01):58–63, 2014. 100

[444] Sophia Kenrick and Daniel Some. Wyatt technology corporation. 2014. 103

[445] Sze Yin Chee, Hwee Ling Poh, Chun Kiang Chua, Filip Šaněk, Zdeněk Sofer, and Martin Pumera. Influence of parent graphite particle size on the electrochemistry of thermally reduced graphene oxide. *Physical Chemistry Chemical Physics*, 14(37):12794–12799, 2012. 104

[446] R Sijs, S Kooij, HJ Holterman, J Van De Zande, and D Bonn. Drop size measurement techniques for sprays: Comparison of image analysis, phase doppler particle analysis, and laser diffraction. *AIP advances*, 11(1):015315, 2021. 104

[447] Xiluan Wang, Hua Bai, and Gaoquan Shi. Size fractionation of graphene oxide sheets by ph-assisted selective sedimentation. *Journal of the American Chemical Society*, 133(16):6338–6342, 2011. 104

[448] Ewelina Gacka, Łukasz Majchrzycki, Bronisław Marciniak, and Anna Lewandowska-Andralojc. Effect of graphene oxide flakes size and number of layers on photocatalytic hydrogen production. *Scientific Reports*, 11(1):1–11, 2021. 104

[449] Antoine Thill and Olivier Spalla. Aggregation due to capillary forces during drying of particle submonolayers. *Colloids and Surfaces A: Physicochemical and Engineering Aspects*, 217(1-3):143–151, 2003. 104

[450] MK Rabchinskii, SD Saveliev, SA Ryzhkov, EK Nepomnyashchaya, SI Pavlov, MV Baidakova, and PN Brunkov. Establishing the applicability of the laser diffraction technique for the graphene oxide platelets lateral size measurements.

In *Journal of Physics: Conference Series*, volume 1695, page 012070. IOP Publishing, 2020. 105

[451] Najihah Jamil, Nur Hidayati Othman, Nur Hashimah Alias, Munawar Zaman Shahruddin, Rosyiela Azwa Roslan, Woei Jye Lau, and Ahmad Fauzi Ismail. Mixed matrix membranes incorporated with reduced graphene oxide (rgo) and zeolitic imidazole framework-8 (zif-8) nanofillers for gas separation. *Journal of Solid State Chemistry*, 270:419–427, 2019. 105

[452] Benjamin Diby Ossonon and Daniel Bélanger. Synthesis and characterization of sulfophenyl-functionalized reduced graphene oxide sheets. *RSC advances*, 7(44):27224–27234, 2017. 105

[453] J Scott Beck, Jo C Vartuli, W Jelal Roth, M Eo Leonowicz, CT Kresge, KD Schmitt, CTW Chu, D Hm Olson, EW Sheppard, SB McCullen, et al. A new family of mesoporous molecular sieves prepared with liquid crystal templates. *Journal of the American Chemical Society*, 114(27):10834–10843, 1992. 105

[454] Vijayakumar Paranthaman, Kannadhasan Sundaramoorthy, Balaji Chandra, Senthil Pandian Muthu, Pandikumar Alagarsamy, and Ramasamy Perumalsamy. Investigation on the performance of reduced graphene oxide as counter electrode in dye sensitized solar cell applications. *physica status solidi (a)*, 215(18):1800298, 2018. 105

[455] S Smart, Shaomin Liu, JM Serra, JC Diniz da Costa, A Iulianelli, and A Basile. Porous ceramic membranes for membrane reactors. In *Handbook of Membrane Reactors*, pages 298–336. Elsevier, 2013. 106

[456] Yanhui Li, Jun Ding, Junfeng Chen, Cailu Xu, Bingqing Wei, Ji Liang, and Dehai Wu. Preparation of ceria nanoparticles supported on carbon nanotubes. *Materials research bulletin*, 37(2):313–318, 2002. 106

[457] Abdel-Nasser A El-Hendawy. Influence of hno3 oxidation on the structure and adsorptive properties of corncob-based activated carbon. *Carbon*, 41(4):713–722, 2003. 107

[458] Konghu Tian, Zheng Su, Hua Wang, Xingyou Tian, Weiqi Huang, and Chao Xiao. N-doped reduced graphene oxide/waterborne polyurethane composites prepared by in situ chemical reduction of graphene oxide. *Composites Part A: Applied Science and Manufacturing*, 94:41–49, 2017. 107

[459] Van Chuc Nguyen, Sarah Kheireddine, Amar Dandach, Marion Eternot, Thi Thu Ha Vu, and Nadine Essayem. Acid properties of go and reduced go as determined by microcalorimetry, ftir, and kinetics of cellulose hydrolysis-hydrogenolysis. *Catalysts*, 10(12):1393, 2020. 107

[460] Jiang-Bin Wu, Miao-Ling Lin, Xin Cong, He-Nan Liu, and Ping-Heng Tan. Raman spectroscopy of graphene-based materials and its applications in related devices. *Chemical Society Reviews*, 47(5):1822–1873, 2018. 107

[461] John R Dennison, Mark Holtz, and Greg Swain. Raman spectroscopy of carbon materials. *Spectroscopy*, 11(8), 1996. 107

[462] Vittorio Scardaci and Giuseppe Compagnini. Raman spectroscopy investigation of graphene oxide reduction by laser scribing. *C*, 7(2):48, 2021. 107, 108

[463] Adarsh Kaniyoor and Sundara Ramaprabhu. A raman spectroscopic investigation of graphite oxide derived graphene. *Aip Advances*, 2(3):032183, 2012. 107

[464] Patrick Feicht and Siegfried Eigler. Defects in graphene oxide as structural motifs. *ChemNanoMat*, 4(3):244–252, 2018. 107

[465] David López-Díaz, Marta Lopez Holgado, José L García-Fierro, and M Mercedes Velázquez. Evolution of the raman spectrum with the chemical composition of

graphene oxide. *The Journal of Physical Chemistry C*, 121(37):20489–20497, 2017. 108

[466] Sreekanth Perumbilavil, Pranitha Sankar, T Priya Rose, and Reji Philip. White light z-scan measurements of ultrafast optical nonlinearity in reduced graphene oxide nanosheets in the 400–700 nm region. *Applied Physics Letters*, 107(5):051104, 2015. 108

[467] Andrea C Ferrari. Raman spectroscopy of graphene and graphite: Disorder, electron–phonon coupling, doping and nonadiabatic effects. *Solid state communications*, 143(1-2):47–57, 2007. 108

[468] Ebrahim Akbari, Iman Akbari, and Mohammad Reza Ebrahimi. sp2/sp3 bonding ratio dependence of the band-gap in graphene oxide. *The European Physical Journal B*, 92(4):1–6, 2019. 109

[469] Seon-Guk Kim, Ok-Kyung Park, Joong Hee Lee, and Bon-Cheol Ku. Layer-by-layer assembled graphene oxide films and barrier properties of thermally reduced graphene oxide membranes. *Carbon letters*, 14(4):247–250, 2013. 109, 110

[470] Helio Ribeiro, Wellington Marcos da Silva, Juliana Cardoso Neves, Hállen Daniel Resende Calado, Roberto Paniago, Luciana Moreira Seara, Denise das Mercês Camarano, and Glaura Goulart Silva. Multifunctional nanocomposites based on tetraethylenepentamine-modified graphene oxide/epoxy. *Polymer Testing*, 43:182–192, 2015. 109

[471] Wei Liu and Giorgio Speranza. Tuning the oxygen content of reduced graphene oxide and effects on its properties. *ACS omega*, 6(9):6195–6205, 2021. 110, 111, 114

[472] Victor Rezende Moreira, Yuri Abner Rocha Lebron, Marielle Mara da Silva, Lucilaine Valéria de Souza Santos, Raquel Sampaio Jacob, Cláudia Karina Barbosa

de Vasconcelos, and Marcelo Machado Viana. Graphene oxide in the remediation of norfloxacin from aqueous matrix: simultaneous adsorption and degradation process. *Environmental Science and Pollution Research*, 27(27):34513–34528, 2020. 111

[473] Libin Tang, Xueming Li, Rongbin Ji, Kar Seng Teng, Guoan Tai, Jing Ye, Changsong Wei, and Shu Ping Lau. Bottom-up synthesis of large-scale graphene oxide nanosheets. *Journal of Materials Chemistry*, 22(12):5676–5683, 2012. 111

[474] Loknath Dhar, Saddam Hossain, Md Sajjadur Rahman, Shamshad B Quraishi, Koushik Saha, Farzana Rahman, and Mir Tamzid Rahman. Adsorption mechanism of methylene blue by graphene oxide-shielded mg–al-layered double hydroxide from synthetic wastewater. *The Journal of Physical Chemistry A*, 125(4):954–965, 2021. 112

[475] Karthikeyan Krishnamoorthy, Murugan Veerapandian, Kyusik Yun, and S-J Kim. The chemical and structural analysis of graphene oxide with different degrees of oxidation. *Carbon*, 53:38–49, 2013. 114

[476] R Siburian, DR Sari, J Gultom, H Sihotang, SL Raja, and M Supeno. Performance of graphite and graphene as electrodes in primary cell battery. In *Journal of Physics: Conference Series*, volume 1116, page 042034. IOP Publishing, 2018. 114, 120

[477] Hani Manssor Albetran. Structural characterization of graphite nanoplatelets synthesized from graphite flakes. 2020. 114

[478] Xuan Jiao, Yangshuai Qiu, Lingyan Zhang, and Xudong Zhang. Comparison of the characteristic properties of reduced graphene oxides synthesized from natural graphites with different graphitization degrees. *RSC advances*, 7(82):52337–52344, 2017. 114

[479] KSB De Silva, Seyed H Aboutalebi, Xun Xu, Xiaolin Wang, WX Li, Konstantin Konstantinov, and SX Dou. A significant improvement in both low-and high-field performance of mgb2 superconductors through graphene oxide doping. 2013. 114

[480] Ayrat M Dimiev, Lawrence B Alemany, and James M Tour. Graphene oxide. origin of acidity, its instability in water, and a new dynamic structural model. *ACS nano*, 7(1):576–588, 2013. 116

[481] Safae Sali, Hamish R Mackey, and Ahmed A Abdala. Effect of graphene oxide synthesis method on properties and performance of polysulfone-graphene oxide mixed matrix membranes. *Nanomaterials*, 9(5):769, 2019. 116, 214

[482] Salim Newaz Kazi, Ahmad Badarudin, Mohd Nashrul Mohd Zubir, Huang Nay Ming, Misni Misran, Emad Sadeghinezhad, Mohammad Mehrali, and Nur Ily Syuhada. Investigation on the use of graphene oxide as novel surfactant to stabilize weakly charged graphene nanoplatelets. *Nanoscale research letters*, 10(1):1–15, 2015. 116

[483] Sangiliyandi Gurunathan, Jae Woong Han, Eunsu Kim, Deug-Nam Kwon, Jin-Ki Park, and Jin-Hoi Kim. Enhanced green fluorescent protein-mediated synthesis of biocompatible graphene. *Journal of nanobiotechnology*, 12(1):1–16, 2014. 117

[484] Swarnima Kashyap, Shashank Mishra, and Shantanu K Behera. Aqueous colloidal stability of graphene oxide and chemically converted graphene. *Journal of Nanoparticles*, 2014, 2014. 117

[485] YS Li, TS Zhao, and WW Yang. Measurements of water uptake and transport properties in anion-exchange membranes. *International Journal of Hydrogen Energy*, 35(11):5656–5665, 2010. 124

[486] Hadis Zarrin, Drew Higgins, Yu Jun, Zhongwei Chen, and Michael Fowler. Functionalized graphene oxide nanocomposite membrane for low humidity and high

temperature proton exchange membrane fuel cells. *The Journal of Physical Chemistry C*, 115(42):20774–20781, 2011. 125

[487] Guoxiu Wang, Bei Wang, Jinsoo Park, Juan Yang, Xiaoping Shen, and Jane Yao. Synthesis of enhanced hydrophilic and hydrophobic graphene oxide nanosheets by a solvothermal method. *Carbon*, 47(1):68–72, 2009. 125

[488] Xuebing Hu, Yun Yu, Weimin Hou, Jianer Zhou, and Lixin Song. Effects of particle size and ph value on the hydrophilicity of graphene oxide. *Applied Surface Science*, 273:118–121, 2013. 125

[489] BM Ganesh, Arun M Isloor, and Ahmad Fauzi Ismail. Enhanced hydrophilicity and salt rejection study of graphene oxide-polysulfone mixed matrix membrane. *Desalination*, 313:199–207, 2013. 125

[490] K Noel Jacob, S Senthil Kumar, A Thanigaivelan, M Tarun, and D Mohan. Sulfonated polyethersulfone-based membranes for metal ion removal via a hybrid process. *Journal of Materials Science*, 49(1):114–122, 2014. 127

[491] Amira KM Ali, Mohamed EA Ali, Ahmed A Younes, AB Farag, et al. Proton exchange membrane based on graphene oxide/polysulfone hybrid nano-composite for simultaneous generation of electricity and wastewater treatment. *Journal of Hazardous Materials*, 419:126420, 2021. 129

[492] Sirus Zinadini, Vahid Vatanpour, Ali Akbar Zinatizadeh, Masoud Rahimi, Zahra Rahimi, and Mohsen Kian. Preparation and characterization of antifouling graphene oxide/polyethersulfone ultrafiltration membrane: application in mbr for dairy wastewater treatment. *Journal of Water Process Engineering*, 7:280–294, 2015. 129

[493] Lida Badrinezhad, Sahar Ghasemi, Yashar Azizian-Kalandaragh, and Ali Nematollahzadeh. Preparation and characterization of polysulfone/graphene oxide

nanocomposite membranes for the separation of methylene blue from water. *Polymer Bulletin*, 75(2):469–484, 2018. 130

[494] Maziyar Sabet and Hassan Soleimani. Influence of graphene oxide on the mechanical, thermal and roughness of polyethersulphone. *Bulletin of Materials Science*, 45(1):1–12, 2022. 130

[495] Cheng Peng, Zafar Iqbal, Kamalesh K Sirkar, and Gregory W Peterson. Graphene oxide-based membrane as a protective barrier against toxic vapors and gases. *ACS applied materials & interfaces*, 12(9):11094–11103, 2020. 130

[496] Seungju Kim, Ranwen Ou, Yaoxin Hu, Xingya Li, Huacheng Zhang, George P Simon, and Huanting Wang. Non-swelling graphene oxide-polymer nanocomposite membrane for reverse osmosis desalination. *Journal of Membrane Science*, 562:47–55, 2018. 130, 215

[497] Marjan Farnam, Hilmi Mukhtar, and Azmi Shariff. Investigation of optimum drying conditions for pure pes membranes for gas separation. *Adv Environ Biol*, 9(27):326–331, 2015. 133

[498] K Zahri, KC Wong, PS Goh, and AF Ismail. Graphene oxide/polysulfone hollow fiber mixed matrix membranes for gas separation. *Rsc Advances*, 6(92):89130–89139, 2016. 133

[499] Tahmineh Forati, M Atai, AM Rashidi, M Imani, and A Behnamghader. Physical and mechanical properties of graphene oxide/polyethersulfone nanocomposites. *Polymers for advanced technologies*, 25(3):322–328, 2014. 133

[500] Jigang Wang, Haiyun Jiang, and Nan Jiang. Study on the pyrolysis of phenol-formaldehyde (pf) resin and modified pf resin. *Thermochimica Acta*, 496(1-2):136–142, 2009. 133

[501] Mariana Ionita, Andreea Madalina Pandele, Livia Crica, and Luisa Pilan. Improving the thermal and mechanical properties of polysulfone by incorporation of graphene oxide. *Composites Part B: Engineering*, 59:133–139, 2014. 133

[502] Arun Kumar Shukla, Javed Alam, Mansour Alhoshan, Lawrence Arockiasamy Dass, and MR Muthumareeswaran. Development of a nanocomposite ultrafiltration membrane based on polyphenylsulfone blended with graphene oxide. *Scientific Reports*, 7(1):1–12, 2017. 134

[503] Javed Alam, Arun Kumar Shukla, Mansour Alhoshan, Lawrence Arockiasamy Dass, Muthu Ramamoorthy Muthumareeswaran, Aslam Khan, and Fekri Abdulraqeb Ahmed Ali. Graphene oxide, an effective nanoadditive for a development of hollow fiber nanocomposite membrane with antifouling properties. *Advances in Polymer Technology*, 37(7):2597–2608, 2018. 134

[504] Yehia Manawi, Viktor Kochkodan, Ebrahim Mahmoudi, Daniel J Johnson, Abdul Wahab Mohammad, and Muataz Ali Atieh. Characterization and separation performance of a novel polyethersulfone membrane blended with acacia gum. *Scientific reports*, 7(1):1–12, 2017. 136

[505] Azam Marjani, Ali Taghvaie Nakhjiri, Maryam Adimi, Hassan Fathinejad Jirandehi, and Saeed Shirazian. Effect of graphene oxide on modifying polyethersulfone membrane performance and its application in wastewater treatment. *Scientific reports*, 10(1):1–11, 2020. 136

[506] Hoan Thi Vuong Nguyen, Thu Hong Anh Ngo, Khai Dinh Do, Minh Ngoc Nguyen, Nu Thi To Dang, Tham Thi Hong Nguyen, Vo Vien, and Tuan Anh Vu. Preparation and characterization of a hydrophilic polysulfone membrane using graphene oxide. *Journal of Chemistry*, 2019, 2019. 136

[507] Sirus Zinadini, Ali Akbar Zinatizadeh, Masoud Rahimi, Vahid Vatanpour, and

Hadis Zangeneh. Preparation of a novel antifouling mixed matrix pes membrane by embedding graphene oxide nanoplates. *Journal of Membrane Science*, 453:292–301, 2014. 136, 196

[508] Nader Gholami and Hossein Mahdavi. Nanofiltration composite membranes of polyethersulfone and graphene oxide and sulfonated graphene oxide. *Advances in Polymer Technology*, 37(8):3529–3541, 2018. 136

[509] AM Munshi, VN Singh, Mukesh Kumar, and JP Singh. Effect of nanoparticle size on sessile droplet contact angle. *Journal of Applied Physics*, 103(8):084315, 2008. 137

[510] Yongbo Deng, Dario Mager, Yue Bai, Teng Zhou, Zhenyu Liu, Liping Wen, Yihui Wu, and Jan G Korvink. Inversely designed micro-textures for robust cassie–baxter mode of super-hydrophobicity. *Computer Methods in Applied Mechanics and Engineering*, 341:113–132, 2018. 139

[511] Edward Bormashenko. Why does the cassie–baxter equation apply? *Colloids and Surfaces A: Physicochemical and Engineering Aspects*, 324(1-3):47–50, 2008. 139

[512] Ikuo Taniguchi, Teruhiko Kai, Shuhong Duan, Shingo Kazama, and Hiroshi Jinnai. A compatible crosslinker for enhancement of co2 capture of poly (amidoamine) dendrimer-containing polymeric membranes. *Journal of Membrane Science*, 475:175–183, 2015. 141

[513] Hugo Hernandez-Martinez, Eduardo Coutino-Gonzalez, Fabricio Espejel-Ayala, Francisco Alberto Ruiz-Trevino, Gabriel Guerrero-Heredia, Ana Laura García-Riego, and Lilian Irais Olvera. Mixed matrix membranes based on fluoropolymers with m-and p-terphenyl fragments for gas separation applications. *ACS omega*, 6(7):4921–4931, 2021. 141

[514] Zhengwei Zhang, Jieyu Xian, Hongbin Wu, Meifu Jin, and Zhenyu Shen. Influence of particle concentration on the elemental penetration region and properties of ni-p-sic composite coatings prepared through sandblasting and scanning electrodeposition on 45 steel surfaces. *Coatings*, 11(10):1237, 2021. 142

[515] Lina Nie, Kunli Goh, Yu Wang, Jaewoo Lee, Yinjuan Huang, H Enis Karahan, Kun Zhou, Michael D Guiver, and Tae-Hyun Bae. Realizing small-flake graphene oxide membranes for ultrafast size-dependent organic solvent nanofiltration. *Science advances*, 6(17):eaaz9184, 2020. 142, 184

[516] Daniel R Dreyer, Sungjin Park, Christopher W Bielawski, and Rodney S Ruoff. The chemistry of graphene oxide. *Chemical society reviews*, 39(1):228–240, 2010. 145

[517] Lijuan Wu, Xuewen Liu, Guocheng Lv, Runliang Zhu, Lintao Tian, Meng Liu, Yuxin Li, Wenxiu Rao, Tianming Liu, and Libing Liao. Study on the adsorption properties of methyl orange by natural one-dimensional nano-mineral materials with different structures. *Scientific reports*, 11(1):1–11, 2021. 146

[518] Idrees Khan, Khalid Saeed, Ivar Zekker, Baoliang Zhang, Abdulmajeed H Hendi, Ashfaq Ahmad, Shujaat Ahmad, Noor Zada, Hanif Ahmad, Luqman Ali Shah, et al. Review on methylene blue: its properties, uses, toxicity and photodegradation. *Water*, 14(2):242, 2022. 146

[519] Van-Phuc Dinh, Hung M Le, Van-Dong Nguyen, Vinh-Ai Dao, N Quang Hung, L Anh Tuyen, Sunhwa Lee, Junsin Yi, Trinh Duy Nguyen, LV Tan, et al. Insight into the adsorption mechanisms of methylene blue and chromium (iii) from aqueous solution onto pomelo fruit peel. *RSC advances*, 9(44):25847–25860, 2019. 147

[520] R Nandini and B Vishalakshi. A study of interaction of methyl orange with some polycations. *E-Journal of Chemistry*, 9(1):1–14, 2012. 147

[521] GGRPR McKay, G Ramprasad, and P Pratapa Mowli. Equilibrium studies for the adsorption of dyestuffs from aqueous solutions by low-cost materials. *Water, Air, and Soil Pollution*, 29(3):273–283, 1986. 150, 169

[522] Carolina Quezada, Humberto Estay, Alfredo Cassano, Elizabeth Troncoso, and René Ruby-Figueroa. Prediction of permeate flux in ultrafiltration processes: A review of modeling approaches. *Membranes*, 11(5):368, 2021. 154

[523] Torsten Teorell. An attempt to formulate a quantitative theory of membrane permeability. *Proceedings of the Society for Experimental Biology and Medicine*, 33(2):282–285, 1935. 154

[524] Akbar Elsagh, Omid Moradi, Ali Fakhri, Fahimeh Najafi, Reza Alizadeh, and Vahid Haddadi. Evaluation of the potential cationic dye removal using adsorption by graphene and carbon nanotubes as adsorbents surfaces. *Arabian Journal of Chemistry*, 10:S2862–S2869, 2017. 159

[525] Salwa M Al-Rashed and Amani A Al-Gaid. Kinetic and thermodynamic studies on the adsorption behavior of rhodamine b dye on duolite c-20 resin. *Journal of Saudi Chemical Society*, 16(2):209–215, 2012. 159

[526] Muhammad Yusuf Prajitno, David Harbottle, Nicole Hondow, Huagui Zhang, and Timothy N Hunter. The effect of pre-activation and milling on improving natural clinoptilolite for ion exchange of cesium and strontium. *Journal of Environmental Chemical Engineering*, 8(1):102991, 2020. 161

[527] Soon Poh Lee, Gomaa AM Ali, H Algarni, and Kwok Feng Chong. Flake size-dependent adsorption of graphene oxide aerogel. *Journal of Molecular Liquids*, 277:175–180, 2019. 167

[528] Aida Arabpour, Sasan Dan, and Hassan Hashemipour. Preparation and optimization of novel graphene oxide and adsorption isotherm study of methylene blue. *Arabian Journal of Chemistry*, 14(3):103003, 2021. 169

[529] Sisca O Lesmana, Novie Febriana, Felycia E Soetaredjo, Jaka Sunarso, and Suryadi Ismadji. Studies on potential applications of biomass for the separation of heavy metals from water and wastewater. *Biochemical Engineering Journal*, 44(1):19–41, 2009. 169

[530] JA Mead. A comparison of the langmuir, freundlich and temkin equations to describe phosphate adsorption properties of soils. *Soil Research*, 19(3):333–342, 1981. 170

[531] FO Okeola and EO Odebunmi. Comparison of freundlich and langmuir isotherms for adsorption of methylene blue by agrowaste derived activated carbon. *Advances in Environmental Biology*, pages 329–336, 2010. 170

[532] Philip Bradder, Sie King Ling, Shaobin Wang, and Shaomin Liu. Dye adsorption on layered graphite oxide. *Journal of Chemical & Engineering Data*, 56(1):138–141, 2011. 172

[533] Nimibofa Ayawei, Augustus Newton Ebelegi, and Donbebe Wankasi. Modelling and interpretation of adsorption isotherms. *Journal of chemistry*, 2017, 2017. 172

[534] Mohammad A Al-Ghouti and Dana A Da'ana. Guidelines for the use and interpretation of adsorption isotherm models: A review. *Journal of hazardous materials*, 393:122383, 2020. 172, 173

[535] Chunfang Tang, Yan Shu, Riqing Zhang, Xin Li, Jinfeng Song, Bing Li, Yuting Zhang, and Danling Ou. Comparison of the removal and adsorption mechanisms of cadmium and lead from aqueous solution by activated carbons prepared from

typha angustifolia and salix matsudana. *RSC advances*, 7(26):16092–16103, 2017. 172

[536] Jacek Piekarski, Katarzyna Ignatowicz, and Tomasz Dabrowski. Analysis of selected methods use for calculation of the coefficients of adsorption isotherms and simplified equations of adsorption dynamics with the use of izo application. *Materials*, 14(15):4192, 2021. 173

[537] Varun Dolia, Asha Liza James, Satadru Chakrabarty, and Kabeer Jasuja. Dissimilar adsorption of higher-order aggregates compared with monomers and dimers of methylene blue on graphene oxide: an optical spectroscopic perspective. *Carbon Trends*, 4:100066, 2021. 175

[538] Erik Smith. Experiments in light scattering: Examining aqueous suspensions of graphene oxide and the aggregation behavior of bordeaux dye. 2010. 175

[539] Mohsen Moazzami Gudarzi. Colloidal stability of graphene oxide: aggregation in two dimensions. *Langmuir*, 32(20):5058–5068, 2016. 177

[540] Y Thomas He, Jiamin Wan, and Tetsu Tokunaga. Kinetic stability of hematite nanoparticles: the effect of particle sizes. *Journal of nanoparticle research*, 10(2):321–332, 2008. 177

[541] Zecheng Gan, Xiangjun Xing, and Zhenli Xu. Effects of image charges, interfacial charge discreteness, and surface roughness on the zeta potential of spherical electric double layers. *The Journal of Chemical Physics*, 137(3):034708, 2012. 178

[542] Shi-chuan Wu, Lin-ling Yu, Fang-fang Xiao, Xia You, Cao Yang, and Jian-hua Cheng. Synthesis of aluminum-based mof/graphite oxide composite and enhanced removal of methyl orange. *Journal of Alloys and Compounds*, 724:625–632, 2017. 179

[543] Brennan Mao, Boopathi Sidhureddy, Antony Raj Thiruppathi, Peter C Wood, and Aicheng Chen. Efficient dye removal and separation based on graphene oxide nanomaterials. *New Journal of Chemistry*, 44(11):4519–4528, 2020. 180

[544] E Alventosa-deLara, S Barredo-Damas, MI Alcaina-Miranda, and MI Iborra-Clar. Ultrafiltration technology with a ceramic membrane for reactive dye removal: optimization of membrane performance. *Journal of Hazardous materials*, 209:492–500, 2012. 182

[545] Saif Al Aani, Tameem N Mustafa, and Nidal Hilal. Ultrafiltration membranes for wastewater and water process engineering: A comprehensive statistical review over the past decade. *Journal of Water Process Engineering*, 35:101241, 2020. 182

[546] Selestina Gorgieva, Robert Vogrinčič, and Vanja Kokol. The effect of membrane structure prepared from carboxymethyl cellulose and cellulose nanofibrils for cationic dye removal. *Journal of Polymers and the Environment*, 27(2):318–332, 2019. 182

[547] Yuan Gao, Kunmei Su, Xiaotian Wang, and Zhenhuan Li. A metal-nano go frameworks/pps membrane with super water flux and high dyes interception. *Journal of Membrane Science*, 574:55–64, 2019. 184

[548] Qian Yang, Yang Su, Chenglong Chi, CT Cherian, Kun Huang, VG Kravets, FC Wang, JC Zhang, Andrew Pratt, AN Grigorenko, et al. Ultrathin graphene-based membrane with precise molecular sieving and ultrafast solvent permeation. *Nature materials*, 16(12):1198–1202, 2017. 184

[549] Claudio Adrian Ruiz-Torres, Junhyeok Kang, Kyoung Min Kang, Kyeong Min Cho, Yoon Tae Nam, Chan Byon, Yoon-Young Chang, Dae Woo Kim, and Hee-Tae Jung. Graphene-based ultrafast nanofiltration membrane under cross-flow

operation: Effect of high-flux and filtered solute on membrane performance. *Carbon*, 185:641–649, 2021. 184

[550] Lu Shao, Xi Quan Cheng, Yang Liu, Shuai Quan, Jun Ma, Shu Zhen Zhao, and Kai Yu Wang. Newly developed nanofiltration (nf) composite membranes by interfacial polymerization for safranin o and aniline blue removal. *Journal of Membrane Science*, 430:96–105, 2013. 184

[551] Xiuzhen Wei, Xin Kong, Chengtian Sun, and Jinyuan Chen. Characterization and application of a thin-film composite nanofiltration hollow fiber membrane for dye desalination and concentration. *Chemical engineering journal*, 223:172–182, 2013. 184, 194

[552] Jian Huang and Kaisong Zhang. The high flux poly (m-phenylene isophthalamide) nanofiltration membrane for dye purification and desalination. *Desalination*, 282:19–26, 2011. 184

[553] Ismail Koyuncu. Reactive dye removal in dye/salt mixtures by nanofiltration membranes containing vinylsulphone dyes: effects of feed concentration and cross flow velocity. *Desalination*, 143(3):243–253, 2002. 185

[554] Long Chen, Jung-Hyeon Moon, Xiaoxin Ma, Lin Zhang, Qiong Chen, Lina Chen, Ruiqin Peng, Pengchao Si, Jinkui Feng, Yanhui Li, et al. High performance graphene oxide nanofiltration membrane prepared by electrospraying for wastewater purification. *Carbon*, 130:487–494, 2018. 187

[555] Aoze Miao, Mingjie Wei, Fang Xu, and Yong Wang. Influence of membrane hydrophilicity on water permeability: An experimental study bridging simulations. *Journal of Membrane Science*, 604:118087, 2020. 188

[556] Gil Hurwitz, Gregory R Guillen, and Eric MV Hoek. Probing polyamide mem-

brane surface charge, zeta potential, wettability, and hydrophilicity with contact angle measurements. *Journal of membrane science*, 349(1-2):349–357, 2010. 188

[557] Jiguo Zhang, Zhiwei Xu, Wei Mai, Chunying Min, Baoming Zhou, Mingjing Shan, Yinglin Li, Caiyun Yang, Zhen Wang, and Xiaoming Qian. Improved hydrophilicity, permeability, antifouling and mechanical performance of pvdf composite ultrafiltration membranes tailored by oxidized low-dimensional carbon nanomaterials. *Journal of Materials Chemistry A*, 1(9):3101–3111, 2013. 188

[558] AL Ahmad, AA Abdulkarim, BS Ooi, and S Ismail. Recent development in additives modifications of polyethersulfone membrane for flux enhancement. *Chemical engineering journal*, 223:246–267, 2013. 188

[559] Jacopo Frallicciardi, Josef Melcr, Pareskevi Siginou, Siewert J Marrink, and Bert Poolman. Membrane thickness, lipid phase and sterol type are determining factors in the permeability of membranes to small solutes. *Nature communications*, 13(1):1–12, 2022. 188

[560] Bruno J Zwolinski, Henry Eyring, and Cecil E Reese. Diffusion and membrane permeability. *The Journal of physical chemistry*, 53(9):1426–1453, 1949. 188

[561] Pengcheng Su, Fei Wang, Zhanjun Li, Chuyang Y Tang, and Wanbin Li. Graphene oxide membranes: controlling their transport pathways. *Journal of Materials Chemistry A*, 8(31):15319–15340, 2020. 193

[562] Abhijit Gogoi, Aditya Koneru, and K Anki Reddy. Effect of graphene oxide (go) nanosheet sizes, pinhole defects and non-ideal lamellar stacking on the performance of layered go membranes: an atomistic investigation. *Nanoscale Advances*, 1(8):3023–3035, 2019. 193

[563] Jian Li, Mengyang Hu, Hongchang Pei, Xiaohua Ma, Feng Yan, Derrick S Dlamini, Zhenyu Cui, Benqiao He, Jianxin Li, and Hideto Matsuyama. Improved

water permeability and structural stability in a polysulfone-grafted graphene oxide composite membrane used for dye separation. *Journal of Membrane Science*, 595:117547, 2020. 193

[564] Ji Hoon Kim, Yunkyu Choi, Junhyeok Kang, Eunji Choi, Seung Eun Choi, Ohchan Kwon, and Dae Woo Kim. Scalable fabrication of deoxygenated graphene oxide nanofiltration membrane by continuous slot-die coating. *Journal of Membrane Science*, 612:118454, 2020. 193

[565] Mohammad Fadhil Abid, Mumtaz Abdulahad Zablouk, and Abeer Muhssen Abid-Alameer. Experimental study of dye removal from industrial wastewater by membrane technologies of reverse osmosis and nanofiltration. *Iranian journal of environmental health science & engineering*, 9(1):1–9, 2012. 195

[566] Jing-Long Han, Xue Xia, Muhammad Rizwan Haider, Wen-Li Jiang, Yu Tao, Mei-Jun Liu, Hong-cheng Wang, Yang-Cheng Ding, Ya-Nan Hou, Hao-Yi Cheng, et al. Functional graphene oxide membrane preparation for organics/inorganic salts mixture separation aiming at advanced treatment of refractory wastewater. *Science of the Total Environment*, 628:261–270, 2018. 197

[567] Xin Zhuang, Ying Wan, Cuimiao Feng, Ying Shen, and Dongyuan Zhao. Highly efficient adsorption of bulky dye molecules in wastewater on ordered mesoporous carbons. *Chemistry of materials*, 21(4):706–716, 2009. 198

[568] Efosa Igbinigun, Yaolin Fennell, Ramamoorthy Malaisamy, Kimberly L Jones, and Vernon Morris. Graphene oxide functionalized polyethersulfone membrane to reduce organic fouling. *Journal of Membrane Science*, 514:518–526, 2016. 198

[569] Tadele Assefa Aragaw and Fikiru Temesgen Angerasa. Synthesis and characterization of ethiopian kaolin for the removal of basic yellow (by 28) dye from aqueous solution as a potential adsorbent. *Heliyon*, 6(9):e04975, 2020. 198

[570] Alison E Contreras, Zvi Steiner, Jing Miao, Roni Kasher, and Qilin Li. Studying the role of common membrane surface functionalities on adsorption and cleaning of organic foulants using qcm-d. *Environmental science & technology*, 45(15):6309–6315, 2011. 199

[571] Pengsong Li, Shiyuan Wang, Imran Ahmed Samo, Xingheng Zhang, Zhaolei Wang, Cheng Wang, Yang Li, Yiyun Du, Yang Zhong, Congtian Cheng, et al. Common-ion effect triggered highly sustained seawater electrolysis with additional nacl production. *Research*, 2020, 2020. 203

[572] L Shu, TD Waite, PJ Bliss, Anthony Fane, and V Jegatheesan. Nanofiltration for the possible reuse of water and recovery of sodium chloride salt from textile effluent. *Desalination*, 172(3):235–243, 2005. 203

[573] Arivithamani Nallathambi and Giri Dev Venkateshwarapuram Rengaswami. Industrial scale salt-free reactive dyeing of cationized cotton fabric with different reactive dye chemistry. *Carbohydrate Polymers*, 174:137–145, 2017. 203

[574] Bing Hui Mo, Yu Huai Yu, Rong Ping Hu, Liang Wu, Huan Liao, and Xue Min Cui. The synthesis and characterization of new-style anticorrosive pigment zinc molybdate. In *Advanced Materials Research*, volume 634, pages 467–471. Trans Tech Publ, 2013. 203

[575] Nidal Hilal, H Al-Zoubi, AW Mohammad, and NA Darwish. Nanofiltration of highly concentrated salt solutions up to seawater salinity. *Desalination*, 184(1-3):315–326, 2005. 205

[576] B Achiou, H Elomari, A Bouazizi, A Karim, M Ouammou, A Albizane, J Bennazha, S Alami Younssi, and IE El Amrani. Manufacturing of tubular ceramic microfiltration membrane based on natural pozzolan for pretreatment of seawater desalination. *Desalination*, 419:181–187, 2017. 208

[577] Abdessamad Belgada, Brahim Achiou, Saad Alami Younssi, Fatima Zohra Charik, Mohamed Ouammou, Jason A Cody, Rachid Benhida, and Khaoula Khaless. Low-cost ceramic microfiltration membrane made from natural phosphate for pretreatment of raw seawater for desalination. *Journal of the European Ceramic Society*, 41(2):1613–1621, 2021. 208

[578] Yulong Ying, Luwei Sun, Qian Wang, Zhuangjun Fan, and Xinsheng Peng. In-plane mesoporous graphene oxide nanosheet assembled membranes for molecular separation. *RSC Advances*, 4(41):21425–21428, 2014. 212

[579] Hanaa M Hegab and Linda Zou. Graphene oxide-assisted membranes: fabrication and potential applications in desalination and water purification. *Journal of Membrane Science*, 484:95–106, 2015. 214

[580] Mahdie Safarpour, Alireza Khataee, and Vahid Vatanpour. Thin film nanocomposite reverse osmosis membrane modified by reduced graphene oxide/tio2 with improved desalination performance. *Journal of Membrane Science*, 489:43–54, 2015. 215

[581] Imamdin Chandio, Farooque Ahmed Janjhi, Ayaz Ali Memon, Shahabuddin Memon, Zubair Ali, Khalid Hussain Thebo, Azhar Ali Ayaz Pirzado, Ayaz Ali Hakro, and Waheed S Khan. Ultrafast ionic and molecular sieving through graphene oxide based composite membranes. *Desalination*, 500:114848, 2021. 215

[582] Gonggang Liu, Hongqi Ye, Antai Li, Chenyuan Zhu, Heng Jiang, Yong Liu, Kai Han, and Yonghua Zhou. Graphene oxide for high-efficiency separation membranes: Role of electrostatic interactions. *Carbon*, 110:56–61, 2016. 216

[583] Kecheng Guan, Shengyao Wang, Yufan Ji, Yuandong Jia, Lei Zhang, Kai Ushio, Yuqing Lin, Wanqin Jin, and Hideto Matsuyama. Nanochannel-confined charge

repulsion of ions in a reduced graphene oxide membrane. *Journal of Materials Chemistry A*, 8(48):25880–25889, 2020. 216

[584] Raka Mukherjee, Prasenjit Bhunia, and Sirshendu De. Nanofiltration range desalination by high flux graphene oxide impregnated ultrafiltration hollow fiber mixed matrix membrane. *Journal of Cleaner Production*, 213:393–405, 2019. 218

[585] Berrin Tansel. Significance of thermodynamic and physical characteristics on permeation of ions during membrane separation: Hydrated radius, hydration free energy and viscous effects. *Separation and purification technology*, 86:119–126, 2012. 218

[586] Pengzhan Sun, Miao Zhu, Kunlin Wang, Minlin Zhong, Jinquan Wei, Dehai Wu, Zhiping Xu, and Hongwei Zhu. Selective ion penetration of graphene oxide membranes. *ACS nano*, 7(1):428–437, 2013. 218

[587] Lifen Liu, Xin Xie, Rahul S Zambare, Antony Prince James Selvaraj, Bhuvana NIL Sowrirajalu, Xiaoxiao Song, Chuyang Y Tang, and Congjie Gao. Functionalized graphene oxide modified polyethersulfone membranes for low-pressure anionic dye/salt fractionation. *Polymers*, 10(7):795, 2018. 226

[588] Pengli Chen, Xiao Ma, Zhaoxiang Zhong, Feng Zhang, Weihong Xing, and Yiqun Fan. Performance of ceramic nanofiltration membrane for desalination of dye solutions containing nacl and na2so4. *Desalination*, 404:102–111, 2017. 226

[589] Elena Alventosa-deLara, Sergio Barredo-Damas, Elena Zuriaga-Agustí, María Isabel Alcaina-Miranda, and María Isabel Iborra-Clar. Ultrafiltration ceramic membrane performance during the treatment of model solutions containing dye and salt. *Separation and Purification Technology*, 129:96–105, 2014. 227

[590] Chuyang Y Tang, TH Chong, and Anthony G Fane. Colloidal interactions and

fouling of nf and ro membranes: a review. *Advances in colloid and interface science*, 164(1-2):126–143, 2011. 227

[591] Novin Mehrabi, Haiqing Lin, and Nirupam Aich. Deep eutectic solvent functionalized graphene oxide nanofiltration membranes with superior water permeance and dye desalination performance. *Chemical Engineering Journal*, 412:128577, 2021. 227

[592] Shaojun Huang, Ping Du, Chungang Min, Yaozu Liao, Hui Sun, and Yubo Jiang. Poly (1-amino-5-chloroanthraquinone): highly selective and ultrasensitive fluorescent chemosensor for ferric ion. *Journal of fluorescence*, 23(4):621–627, 2013. 227

[593] Mahir Alkan, Özkan Demirbaş, and Mehmet Doğan. Electrokinetic properties of sepiolite suspensions in different electrolyte media. *Journal of Colloid and Interface Science*, 281(1):240–248, 2005. 227

[594] Kaijie Yang, Baoliang Chen, Xiaoying Zhu, and Baoshan Xing. Aggregation, adsorption, and morphological transformation of graphene oxide in aqueous solutions containing different metal cations. *Environmental science & technology*, 50(20):11066–11075, 2016. 227

[595] Lu Wang, Naixin Wang, Guojun Zhang, and Shulan Ji. Covalent crosslinked assembly of tubular ceramic-based multilayer nanofiltration membranes for dye desalination. *AIChE Journal*, 59(10):3834–3842, 2013. 227

[596] Jieyu Hu, Meng Li, Lianjun Wang, and Xuan Zhang. Polymer brush-modified graphene oxide membrane with excellent structural stability for effective fractionation of textile wastewater. *Journal of Membrane Science*, 618:118698, 2021. 228

[597] Ho Bum Park, Jovan Kamcev, Lloyd M Robeson, Menachem Elimelech, and Benny D Freeman. Maximizing the right stuff: The trade-off between membrane permeability and selectivity. *Science*, 356(6343):eaab0530, 2017. 228

[598] Benny D Freeman. Basis of permeability/selectivity tradeoff relations in polymeric gas separation membranes. *Macromolecules*, 32(2):375–380, 1999. 228

[599] Yesol Kang, Jaewon Jang, Yunho Lee, and In S Kim. Dye adsorptive thin-film composite membrane with magnetite decorated sulfonated graphene oxide for efficient dye/salt mixture separation. *Desalination*, 524:115462, 2022. 228

[600] Meng Li, Jieyu Hu, Bin Li, Shengyuan Deng, and Xuan Zhang. Graphene oxide nanofiltration membrane with trimethylamine-n-oxide zwitterions for robust biofouling resistance. *Journal of Membrane Science*, 640:119855, 2021. 229